NOAA Technical Memorandum ERL SEL-85

SOLAR UV FLUX MEASUREMENTS FROM THE SBUV2 MONITOR ON THE NOAA9 SATELLITE

PART I. Mg II h & k LINE CORE-TO-WING RATIOS FOR 1986-1988

R. F. Donnelly
L. C. Puga
J. Barrett
S. D. Bouwer
J. Pap
D. E. Stevens
W. K. Tobiska

Space Environment Laboratory
Boulder, Colorado
December 1994

noaa NATIONAL OCEANIC AND ATMOSPHERIC ADMINISTRATION / Environmental Research Laboratories

NOAA Technical Memorandum ERL SEL-85

SOLAR UV FLUX MEASUREMENTS FROM THE SBUV2 MONITOR ON THE NOAA9 SATELLITE

PART I. Mg II h & k LINE CORE-TO-WING RATIOS FOR 1986-1988

R. F. Donnelly
L. C. Puga
J. Barrett
S. D. Bouwer
J. Pap
D. E. Stevens
W. K. Tobiska

Space Environment Laboratory
Boulder, Colorado
December 1994

UNITED STATES
DEPARTMENT OF COMMERCE

Ronald H. Brown
Secretary

NATIONAL OCEANIC AND
ATMOSPHERIC ADMINISTRATION

D. JAMES BAKER
Under Secretary for Oceans
and Atmosphere/Administrator

Environmental Research
Laboratories

James L. Rasmussen
Director

NOTICE

Mention of a commercial company or product does not constitute an endorsement by NOAA/ERL. Use of information from this publication concerning proprietary products or the tests of such products for publicity or advertising purposes is not authorized.

For sale by the National Technical Information Service, 5285 Port Royal Road
Springfield, VA 22161

TABLE OF CONTENTS

SOLAR UV FLUX MEASUREMENTS FROM THE SBUV2 MONITOR ON THE NOAA9 SATELLITE

Part I. Mg II h & k Line Core-to-Wing Ratios for 1986-1988

Richard F. Donnelly, Larry Puga, Joan Barrett,
S. David Bouwer,* Judit Pap,* David E. Stevens,* and W. Kent Tobiska*
Space Environment Laboratory, NOAA ERL
Boulder, Colorado 80303

ABSTRACT

Analyses of the discrete-wavelength mode of observations of the solar full-disk Mg II h and k line spectral irradiance measured by the Solar Backscatter UV Monitor (SBUV2) on the NOAA9 satellite are presented. Relative photometry techniques were used to derive a core-to-wing ratio (R_{MgII}). This ratio has been modified, relative to that used by Heath and Schlesinger's (1986) classical Mg II ratio derived for solar UV measurements made by their SBUV experiment aboard the Nimbus-7 satellite, to avoid inter-range instrumentation drifts encountered in the NOAA9 SBUV2 monitor. Prior research of the solar Mg II h and k lines is reviewed. The raw measurements and observational parameters, such as the angle of the Sun as seen at the SBUV2 monitor, are discussed. Temporal interpolations among the sets of discrete-mode measurements are used to account for most of the Sun-angle dependence and to reduce the sensitivity of the results to any errors in the Sun angles. Wavelength "jitter" and long-term drift are studied, and intensity linearity and inter-range drift are analyzed. The NOAA9 results are compared with same-day Nimbus-7 data, the Kitt Peak Ca K 1 Å index, the Canadian 10.7 cm solar radio flux, and observations of the solar H Lyman α line. Rocket- and balloon-flight observations of the Mg II h and k lines, made with fine-wavelength resolution, are analyzed to determine what their characteristics would be like if they were observed with the broad passband of the Nimbus 7 and NOAA9 instruments. R_{MgII} results are presented for 1986-1988.

1. SBUV/2 MONITOR

Progress in research of the solar ultraviolet (UV) spectral irradiance, achieved during 1987-1989 by the NOAA ERL Solar UV Radiation and Climate Research Project, is reported below. The last progress report in this series was published in November 1987 (Puga et al., 1987). Before 1987, our research was dominated by studies of Nimbus-7 solar UV spectral irradiance measurements and AE-E measurements of the solar extreme ultraviolet (EUV) flux measurements (Donnelly, 1987, 1988b; Donnelly et al., 1987; Bouwer et al., 1990; Donnelly,

*Cooperative Institute for Research in Environmental Sciences, University of Colorado at Boulder.

1990a, b; Donnelly and Puga, 1990; and Pap et al. 1990). Prior to 1987, computer programmer Joan Barrett was the main group member working on the new solar UV spectral irradiance measurements from the Solar Backscatter UV Monitor (SBUV2) on the NOAA9 satellite, starting with the Sun-view wavelength-sweep measurements.

We first concentrated on relative photometry of solar spectral lines such as the Mg II h and k lines near 280 nm because quantitative information on the instrument corrections for absolute photometry was being developed elsewhere and was expected to become available only slowly. In early 1987, the results of our studies of the Sun-view wavelength-sweep mode of the Mg II h and k lines were unsatisfactory, because the ratio of solar signal to noise in those data was too small. Correlations of the Mg II core-to-wing ratio (R_{MgII}) for these sweep-mode measurements, with respect to the same-day Nimbus-7 values for April 1985-1986, were smaller than for the solar 10.7 cm radio flux (F10) or for the equivalent-width (EW) of the He I absorption line at 1083 nm with respect to the Nimbus-7 data, even though real differences occur between F10 or EW and R_{MgII}. In other words, it would have been better to extend the Nimbus-7 R_{MgII} results in time by using EW or F10, rather than by using those NOAA9 data.

In the summer of 1987, we abandoned our work on the Mg II sweep-mode data and switched to studying a special set of measurements of the Mg II h and k lines, called the discrete-wavelength mode of Mg II line measurements, which have been made daily starting on May 27, 1986. Most of the rest of the research group started to concentrate on the NOAA9 data. This report discusses those studies of the discrete-mode MG II line and is intended for the small audience of scientists who are either researching data from SBUV2 monitors or are using our results for studying solar physics or stratospheric physics and would like to know the details behind our results.

1.1. Joint NASA and NOAA/NESDIS Program

The SBUV2 monitor on the NOAA9 satellite is part of a joint NASA and NOAA program for monitoring ozone as a function of altitude, latitude, longitude, and time. In this joint program NASA develops and demonstrates the instruments; NOAA continues the operation, performs routine data processing, and disseminates the data to the scientific community. On the Nimbus-4 and Nimbus-7 satellites, respectively, NASA's BUV and SBUV instruments (Heath et al., 1975), which were built by Beckman Instruments, Inc., were predecessors of the joint NASA-NOAA SBUV2 monitors, which were built by Ball Aerospace Systems Group in Boulder, Colorado. Fortunately for our research of solar UV variability, the prototype Nimbus-7 SBUV included solar UV flux measurements, scanning in wavelength from 160 to 400 nm (Heath and Schlesinger, 1986). Similarly, the SBUV2 monitors included solar UV measurements using a diffuser plate to reflect the solar flux into the nadirally pointed SBUV2. The SBUV2 instrument with serial number 2 was launched on the NOAA9 satellite on December 9, 1984.

The NOAA SBUV2 ozone-monitoring program is directed by Walter Planet, Physics Branch, Satellite Experiment Lab., NOAA NESDIS, Camp Springs, Maryland. Dudley

Bowman, of NOAA NESDIS, leads the processing of the SBUV2 data, which mainly derives the terrestrial ozone data but also produces the "1b" data tapes that we use to extract the SBUV2 solar UV measurements. From NOAA NESDIS' viewpoint, our organization functions as one of several data centers to which they send copies of their data tapes. The data tape for April 1985 was the first one available to us for study.

The purpose of the Solar UV Radiation and Climate Research Project (Donnelly et al., 1984) was to answer the following questions:

(1) What are the temporal variations of the solar UV spectral irradiance in the wavelength range 100-400 nm?

(2) Why does the solar UV radiation vary, and can we model the variations?

(3) What are the atmospheric effects of the observed UV variations, and can they significantly affect climate?

To achieve these goals, we have studied solar UV measurements from the SBUV2 monitors and from other available sources (SME, Nimbus 7, UARS, etc.). SBUV2 data processing results, such as the "modified" Mg II core-to-wing ratio, are a by-product of our research and not an end product. Preliminary Mg II ratios have been published in NOAA NESDIS' *Solar Geophysical Data* (1988, 1989, 1991).

1.2 Instrument Description

1.2.1. Optics

Figure 1.1 shows a schematic diagram of the SBUV2 instrument, which is an Ebert-Fastie double monochromator. When ozone measurements are made, the diffuser plate is stowed and the instrument views the radiance from the terrestrial atmosphere; downward toward Earth is to the left of this diagram. For the solar irradiance measurements that we study, the diffuser plate is deployed. Since SBUV2 is mounted on the bottom or Earth side of the satellite, the Sun can be observed only when it lies near or below the bottom plane of the satellite, otherwise the satellite blocks the Sun from being visible at the diffuser plate. The depolarizer is needed for the terrestrial ozone measurements. The solar rays that enter the instrument then pass through the double monochromator, first through a top chamber with two reflections off the first Ebert mirror, before and after one pass off the reflectance grating. The path is then directed by a mirror to pass through the intermediate slit from the top chamber through the scattered-light-blocking separating wall into the bottom chamber, where the light then passes the second monochromator. Identical gratings and Ebert mirrors are used in both chambers, and scattered-light baffles are used to separate the upper and lower portions. One shaft turns the gratings for both chambers; i. e. the two monochromators are tuned to the same wavelength and the grating in the second chamber is rigidly mounted to that in the first.

According to William K. Fowler and Kevin Kelly (1994, private communication) of Ball Aerospace Systems Division, "To relay light from the first to the second monochromator, it is

reflected at 90° off a pair of mirrors in a roof configuration, passes through the intermediate slit, and is then folded an additional 90° by a single diagonal mirror. This has the effect of a cube-corner retro-reflector, with the intermediate slit within the cube. This system turns the direction for dispersion so that the two monochromators are additive in dispersion. The slits can then be twice as wide as for a zero-dispersion double monochromator of equal bandpass, thus aiding thoughput."

The advantage of the Ebert-Fastie double monochromator is that the great reduction of scattered light of a double monochromator is achieved with moderate wavelength resolution and a simple one-shaft grating drive system. This latter aspect lends itself to obtain precise wavelength repeatability, which is very important to the ozone monitoring measurements. Consequently, measurements of solar spectral lines that depend on precise wavelength repeatability benefit greatly from this design strength which is required for the ozone measurements. The primary sources of information about the instrument design and calibration that we have used are Ball References No. 1-4.

1.2.2. Wavelength Drive System

The grating shaft is supported at each end by bearings (Ball Reference 4), which are the only moving parts in the wavelength drive mechanism. There are no cams, gears, chains, or worm drives. An optical shaft encoder is mounted on the grating shaft to determine very accurately the shaft's position. An electromagnetic torque is used to turn the shaft. These two components are included in an electronic feedback control to accurately position the shaft.

Solar irradiance measurements are made with two different wavelength drive programs: the wavelength-scan mode and the discrete-wavelength mode (Ball Reference 1). In the wavelength-scan mode, the instrument scans from about 407 nm down to 160 nm for about two scans of the Sun each day during a 6-minute interval (192 + 168 s). Each step in wavelength is about 0.074 nm, and two steps in wavelength occur ($\simeq$0.15 nm) during each 0.1 s sample of the photomultiplier output (i.e. the wavelength changes slightly during each sample). In the discrete-mode measurements, twelve wavelength positions are used. The instrument uses 0.75 s to settle in on each of the wavelengths and then uses 1.25 s to sample the photomultiplier output. Consequently, we expect less noise to occur in the discrete-wavelength measurements, due to both the longer sample time and the improved wavelength repeatability achieved through the longer time available for the feedback-controlled magnetic torgue drive to settle at a particular wavelength.

According to Frederick et al. (1986), the relation between the wavelength λ to which the double monochromator is tuned and the digital output (g) of the grating shaft-position indicator is given by

$$\lambda = A \sin[\alpha(g + \beta)] \quad (nm) \tag{1.1}$$

where the values A, α, and β can be derived both from preflight calibrations and inflight observations of solar spectral lines. The coefficients we have used are discussed further in section

1.3.3; we have used the coefficients derived by others, and consider our wavelength labels as nominal values. We have not yet studied solar spectral lines to derive our own wavelength scale. Because we have emphasized relative photometry, we have been more concerned with wavelength repeatability than with determining the absolute wavelength scale. Note that these wavelength coefficients will differ slightly more (by about 0.037 nm in wavelength) for the wavelength-scan mode, which smears through two wavelength steps per measurement and therefore has an average effective wavelength between these two steps than for the discrete-wavelength mode, which settles at particular wavelength steps.

Because of the lack of mechanical parts in the wavelength drive system, it is not clear how the wavelength positions might drift with time. The fairly uniform shifts in wavelength with age, caused by the mechanical wear of cam drives in other instruments, have no clear connection to the SBUV2 monitor. Perhaps the edges of the many optical windows of the shaft angle encoder suffer from surface changes that cause a small periodic (one cycle per window) shift in wavelength with age. The friction in the shaft bearings may change with age and affect the magnitude of the random error in how closely the shaft settles to the assigned position, and this may cause a growing amplitude of wavelength jitter with age.

According to W. K. Fowler and K. Kelly, "It is possible that the action of the magnetic torque motor, over long periods of time, somehow causes a small shift in the position of the gratings relative to the grating shaft. The shaft angle signal is the sum of four position sensors that read through the encoder disk. Perhaps thermal or mechanical stress in the shaft housing alters the relative alignment of these sensors, or their output may vary with age, either of which can change the encoder signal. The monochromator housing can also distort due to thermal stress, causing a shift in wavelength calibration."

1.2.3. Detector and Electronic Systems

Figure 1.1 shows that the dynamic range of the output of the photomultiplier is covered by three overlapping electronic range circuits, two in the anode circuit and one in the cathode circuit. In the SBUV2 monitor, the flux levels are high and the photomultiplier operates in a continuous current mode (modulated by the optical chopper). W. K. Fowler and K. Kevin reported: "The cathode circuit uses the tube as though it were a photodiode, having no gain except for the cathode current amplifier (range 3). The anode current is about 500 times the cathode current due to the secondary emission of electrons at each dynode stage within the tube. This multiplication effect is inversely proportional to temperature, and varies with use, depending on the average current through the tube. The exact ratio between cathode and anode (range 2) current varies with wavelength as some photons pass through the photocathode material and strike the first dynode, causing a photoelectric emission from the dynode material. The additional amplifier for range 1 determines the ratio between range 1 and range 2 signals." Figure 6 (in Cebula et al., 1989) indicates that the instrument's overall transfer function degraded with time and that the degradation increased with decreasing wavelength

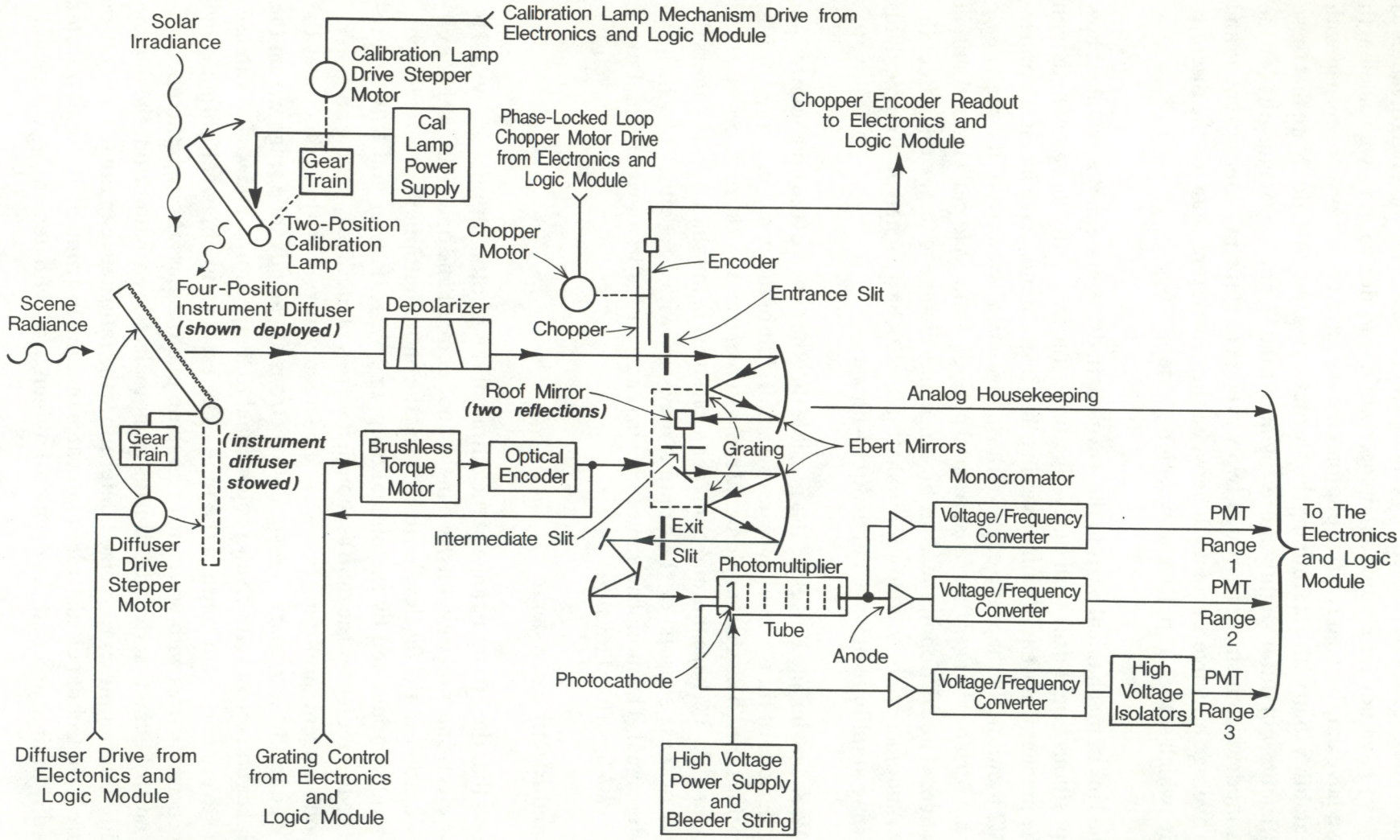

Figure 1.1 Schematic diagram of the solar backscatter UV monitor, based on figure 2-13 of a Ball Aerospace Systems Div. report (Ball Ref. 4). The cloud cover radiometer is not shown here in order to simplify the diagram; it is not relevant to the solar irradiance measurements.

below 280 nm. This can also be due to degradation of optical components in the monochromator.

1.2.4. Instrument Transfer Function

The relationship between the solar irradiance $F(\lambda, t)$ as a function of wavelength λ, time t, and the instrument output $C_r(t)$ for output range r (r=1, 2 or 3) is given by the following equation:

$$F(\lambda,t) = K_F(\lambda,t,\theta,\emptyset)X_{1r}[C_r(t) - C_{or}](Wm^{-2}nm^{-1}) \quad . \tag{1.2}$$

$C_r(t)$ includes a correction for the background output seen when the chopper blocks the incoming solar radiation. $K_F(\lambda,t,\theta,\emptyset)$ is the calibration factor as a function of the position angles (θ, $\emptyset$) of the Sun as seen at the diffuser plate input (Frederick et al., 1986), where θ is the angle between a normal to the diffuser plane and the incident solar ray, and $\emptyset$ is the azimuth angle in the plane of the diffuser between some reference direction within the structure of the instrument and the projection of the solar ray onto the diffuser plane. Frederick et al. point out that the reflectance is a weak function of λ and $\emptyset$ and roughly a cosine function of θ, but the more detailed corrections as a function of λ, θ, and $\emptyset$ are important for accurate absolute-spectral-irradiance measurements. Both θ and $\emptyset$ vary with time during the several minutes of any type of solar irradiance measurements because of the satellite's orbital motion.

C_{or} is a zero offset for the electronics that processes the output of the photomultiplier for range r. The values we have used are C_{o2}=65.4 and C_{o3}= 58.4 (Cebula, 1988; Frederick et al., 1986). Our results for the modified Mg II ratio, discussed later, are only weakly sensitive to errors or drifts in C_{o2} because the smallest range-2 values of C_2 that we use (the center-of-the-line measurements) are above 14,000; a doubling of the offset would cause less than ½% error. Conversely, the wing measurements of the classical Mg II discrete-mode data discussed below are very sensitive to drifts in C_{o3} since the C_3 measurement values are as low as about 700.

X_{1r} is the interrange ratio that converts an output in range r to its equivalent value in range 1.

$$X_{1r} = \frac{C_1 - C_{o1}}{C_r - C_{or}}. \tag{1.3}$$

The calibration factor is expressed by Frederick et al. (1986) as a function of the preflight calibrations as follows:

$$K_F(\lambda,t,\theta,\emptyset) = K_F^c(\lambda)\frac{R(\lambda,t_c,\theta_c,\emptyset_c)}{R(\lambda,t,\theta,\emptyset)}. \tag{1.4}$$

where "c" denotes the preflight calibration values made at time t_c. The relative Sun-angle dependence of the diffuser reflectance (R) has been separated out in the form of a ratio. Note that the variable t in the denominator denotes the expected drift in diffuser reflectance with age and exposure to space. The SBUV2 monitor was designed to test the diffuser after the satellite was launched using a mercury lamp. Frederick et al. (1986) assumed that the diffuser

degradation detected by the mercury lamp for the particular direction angles (θ_{Hg}, $\emptyset_{Hg}$) for the lamp location would give the temporal correction for all the other angles at which the Sun would be viewed. So, they separated the Sun angle-dependent term in (1.4) into a diffuser aging term τ and a time independent Sun-angle term Γ.

$$\frac{R(\lambda, t_c, \theta_c, \emptyset_c)}{R(\lambda, t, \theta, \emptyset)} = \tau(\lambda, t)\Gamma(\lambda, \theta, \emptyset), \qquad \text{where} \qquad (1.5)$$

$$\tau(\lambda, t) = \frac{R(\lambda, t_c, \theta_{Hg}, \emptyset_{Hg})}{R(\lambda, t, \theta_{HG}, \emptyset_{Hg})}, \qquad \text{and} \qquad (1.6)$$

$$\Gamma(\lambda, \theta, \emptyset) = \frac{R(\lambda, t_c, \theta_c, \emptyset_c)}{R(\lambda, t_c, \theta, \emptyset)}. \qquad (1.7)$$

On the basis of data from the Nimbus-4 BUV instrument and the Nimbus-7 SBUV instrument (Heath et al., 1975; Schlesinger et al., 1988), degradation of the diffuser reflectance was expected to be one of the major causes of SBUV2 instrument degradation. The plan was to use the mercury lamp to monitor $\tau(\lambda,t)$. Although Frederick et al.(1986) show K_F^c as being time invariant, there are drifts in the instrument caused by sources other than the diffuser. For example, photomultiplier gains tend to degrade with age. These additional drifts can be approximately separated from the overall solar spectral irradiance drift by using the mercury lamp, placed within the field of view of the rest of the instrument, with the diffuser stowed and removed from the optical path. These age corrections ought to be incorporated into equation 1.2, either as a separate multiplying factor or using the combined effects of diffuser and other sources of degradation in the denominator term of equation 1.6. It appears that Frederick et al. (1986) planned to do the latter.

1.3. Calibrations

1.3.1. Irradiance Calibrations

Ball Aerospace Systems Division calibrated the SBUV2 instrument (Serial No. 002), before it was launched on the NOAA9 satellite, using an FEL lamp, a deuterium lamp and an argon mini-arc, all of which were calibrated by the National Bureau of Standards. Irradiance calibration results are reported for the wavelength- scan mode in Ball Reference 3; however, the copy of that report that we received did not include chapter 7, on the discrete-mode composite calibration. Revision C (Ball Reference 5) of that report series included irradiance calibration constants (K_F^c) for the discrete mode and range-2 outputs for a dozen laboratory calibration lines. K_F^c ranges from about 3.401×10^{-3} mW m^{-2} nm^{-1} count^{-1} at 252 nm, dropping to 2.056×10^{-3} at 340 nm, where the wavelength dependence has a steep linear decrease with increasing wavelength from 283.1 to 312.6 nm. For use with the solar Mg II discrete-mode measurements in the 276-283 nm wavelength range, we fitted a second-order polynomial to these calibrations by forcing it to fit the calibration data at both 273.7 and 283.1 nm and also forcing it to have the same slope with respect to wavelength at 283.1 nm as that defined by a straight line

fit between the calibration data at 283.1 and 287.7 nm. The results are given by the following equation:

$$K_F^c(\lambda) = -51.574 \times 10^{-4} + 0.41049 \times 10^{-4}\lambda - 7.6761 \times 10^{-8}\lambda^2 . \qquad (1.8)$$

This equation should be applied only to wavelengths in the 274-283.1 nm range.

Another calibration of interest is Ball Aerospace Division's preflight goniometric calibration, i. e. the calibration of the Sun-angle dependence of $\Gamma(\lambda, \theta, \emptyset)$ in equation (1.7). Those results are reported in Section 9 of Ball Reference 3. In Section 4.2 of this report, temporal interpolations among the SBUV2 observations of the Mg II line are developed. These interpolations determine the wing and core measurements for the same instant in time, and consequently for the same Sun angles. This combined with the use of relative photometry in determining the Mg II core-to-wing ratio causes most of the $\Gamma(\lambda, \theta, \emptyset)$ dependence to cancel out in the ratio. There is a wavelength dependence that does not cancel, but it is very small because the diffuser reflectance is only a weak smoothly varying function of wavelength and the Mg II index involves a small wavelength range. Consequently, in our exploratory studies of the MgII index, the $\Gamma(\lambda, \theta, \emptyset)$ term was neglected. In section 7.2, we discuss its importance for refinements to the Mg II index.

1.3.2. Intensity Linearity

The photomultiplier is not perfectly linear over the large dynamic range for which it is used (Frederick et al., 1986). Ball Reference 3 (section 2.0) presents preflight laboratory measurements of the linearity of the instrument; their combination of the three ranges provides results by which the non-linearity is within ± 1.5 %. R. P. Cebula (ST Systems Corp., 1987) reanalyzed these data, combining the data from the three ranges in the way they would be used for analyzing measurements covering the whole dynamic range that the SBUV2 instrument can cover. He derived interrange ratios (X_{12}, X_{23}, and $X_{13}=X_{12}\times X_{23}$) from these same calibrations. His results fit the three decades of magnitude of output values for range 2 with two line segments (percent nonlinearity as a function of $\log_{10} C_r$), one for $151 < C_r < 629$ and the other for the range $630 < C_r < 83{,}168$, where the results are referenced to range 1 values. In this scheme, the nonlinearity for range 2 increases from + 1.7% at $C_r = 10{,}000$ to +2.9% at 84,000. The results for the part of range 2 where the discrete-mode measurements of the solar Mg II h and k lines occur are all in this top decade of range 2's dynamic range. Cebula's nonlinearity result is all positive for the small part of the range of interest to the Mg II ratio, which suggests that this small region may be locally more linear (but has a different slope than does the overall dynamic range) than suggested by Cebula's large nonlinearity factors. This issue is discussed further in section 7.1 below.

We can obtain a more optimum linear fit for our special application, namely the discrete-mode Mg II h and k line data, by using the Ball Aerospace Division linearity calibrations and fitting a line just for the range used in these measurements. We are mainly concerned with the precision of the relative temporal variations in the flux ratios that we derive; therefore, we are

more concerned with the linearity over this small portion of the dynamic range than in either the absolute values of the fluxes or the flux ratios that we derive. The latter case applies because, in our final analyses, we use linear regression relations to convert our results to equivalent Nimbus 7 values of the Mg II core-to-wing ratio, which adjusts the zero offset and renormalizes the slope with solar activity of our Mg II ratios.

Cebula's nonlinearity result for range 3 is quite curvy as a function of $\log_{10} C_3$. For the Mg II wing measurements at intensities above the level where range-2 values are designated as the preferred values (i. e. intensities where the range 3 output is designated by the SBUV2 system as the preferred value, which is the case for most of the Mg II wing measurements), the nonlinearity is in the range -2.7% to -3.4%; it is opposite in sign to the nonlinearity in range 2.

One of our main concerns about these nonlinearity results is how they will age, i. e. whether they will shift in amplitude or whether their shape as a function of $\log_{10} C_r$ will shift in position along the C_r scale. We think that most of the nonlinearity comes from the photomultiplier and may relate to the current level and its associated internal heating or a shift in relative influence of the many multiplier grids. In that case, the nonlinearity probably remains at the same current output levels even though the cathode emissivity and photomultiplier gain degrade with age. On the other hand, we suspect that nonlinearities near the ends of the three electronic ranges, such as that at the low-output end of range 3, may be caused by that electronic processing system rather than by the photomultiplier, and may drift in amplitude and C_r position with time. Therefore, the use of low range-3 values and the application of a pre-flight nonlinearity correction for the life of the satellite may not be wise. Such speculation could be reduced through ongoing laboratory testing of the aging of one of the SBUV2 monitors that will not fly on a satellite for some time.

1.3.3. Wavelength Calibrations

Preflight wavelength calibrations were made for the NOAA9 satellite by Ball Aerospace Systems Division (Ball Reference 3) for the wavelength-scan mode, and separately for the discrete mode, for wavelengths in air at standard temperature and pressure. They used laboratory hollow cathode discharge tubes and SBUV2's internal mercury arc lamp. Using wavelengths in air is consistent with an old custom, wherein values in air were used for wavelengths longer than 200 nm and values in vacuum were used for shorter wavelengths. We prefer to use vacuum wavelengths, which are slightly longer (about 0.0825 nm at 280 nm (Allen, 1963)).

Figure 1.2 shows the spectrum of the SBUV2 mercury calibration lamp with its narrow emission lines. The triangular shape of these lines simply reflects the SBUV2 triangular bandpass function; the emission lines are much narrower than SBUV2's bandpass. The observed peaks of these lines and their known wavelengths are used to obtain a best fit to equation 1.1. The wavelength coefficients we have used for equation 1.1 were provided by R. P. Cebula on June 27, 1988 (private communication), where A= 818.865 nm (vacuum), α= -9.59472×10^{-5} radians per encoder count, and β= -4157.03 grating-shaft encoder counts. It is our understanding that these coefficients are based on in-flight wavelength measurements and apply to the discrete-wavelength mode of measurements used in this report. Because we have

not completed our study of wavelength positions of either the mercury lamp lines or solar spectral lines, we consider the wavelengths derived from these coefficients to be nominal values. Our greatest interest lies in the repeatability of these wavelengths with age. The absolute values of the Mg II discrete-mode measurements mainly affect comparisons with early rocket-flight measurements. So far, our studies of such data (See section 6.2) have shown that more serious problems than those due to differences in wavelength scales would hinder any quantitative use of those early results.

1.4. In-Flight Performance

Frederick et al. (1986) examined the performance of the SBUV2 monitor on the NOAA9 satellite during the initial activation and evaluation phase of the operation of the SBUV2 monitor from January through March 1985. Overall, the instrument operated as expected; nevertheless, as in every solar UV spectrometer ever flown, some problems were identified.

1.4.1. Drift in Intensity Range 3 Relative to Range 2

Since the transmittance of the photocathode varies with wavelength, the photomultiplier gain varies with wavelength; this effect is different in the anode circuit (ranges 1 & 2) than in the cathode circuit (range 1). This causes the ratio of range 3 output to the corresponding output for range-2 values X_{23} and also X_{13} to vary with wavelength (Frederick et al., 1986). Furthermore, the small nonlinearity in the system causes X_{23} to be a function of the intensities involved as well as a function of wavelength. Finally, because the photomultiplier degrades with age and the gain in the cathode circuit ages differently from that in the anode circuit, X_{23} drifts with time. For example, Frederick et al. (1986) reported that X_{23} decreased by almost

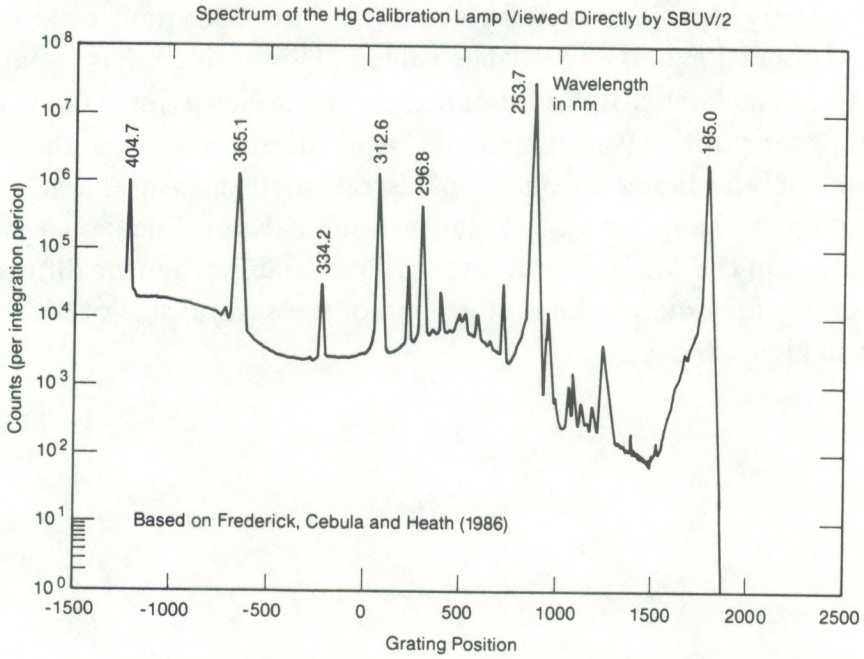

Figure 1.2 Early spectra of the mercury calibration lamp of the SBUV2 monitor aboard the NOAA9 satellite.

2% at 312.6 nm in the first 2 months of operation of the NOAA9 SBUV2 (SN 002). X_{23} rose by about 1% near 282 nm when the output intensity C_T rose from the 500-600 count range to the 600-700 range (Frederick et al., 1986). The wavelength dependence of X_{23} is not clearly defined near the Mg II h and k lines by their results, but it appears to be a smaller problem.

These problems led us to use a modified Mg II ratio later in this report to avoid the range-2 to -3 problems. However, in our early investigations, reported in chapter 3, we attempted to correct for the X_{23} variations. Another problem with range 3 was a high level of noise in C_{o3}.

1.4.2. Unstable Calibration Lamp

Frederick et al. (1986) reported that the output of SBUV2's mercury lamp became unstable starting on March 20, 1985, but that sometimes the lamp is stable. This intermittent loss means that the main system for monitoring drifts in the relative reflectivity of the diffuser and checking for drifts in the wavelength scale was weakened; data that are used must therefore be screened for noisiness. We did not make use of the mercury lamp data during our analyses of NOAA9 data, conducted in 1987-1989.

1.4.3. Diffuser Position

For the solar flux measurements, such as the solar wavelength-scan mode observations and the discrete-wavelength mode for the solar Mg II h and k lines, the Sun is observed at large angles with respect to the normal to the diffuser. This situation could be improved in future flights by changing the angle at which the diffuser is positioned when in its Sun-observing mode. So far as we know, no plans have been made to carry out such an alteration. Another problem with positioning the diffuser was reported by Cebula et al. (1989); the deployment of the diffuser would vary in position angle by about 0.25° from one time to another, which could produce jitter of about 1% in the irradiance values. This problem has apparently been corrected on NOAA11 and later SBUV2 monitors. From the viewpoint of our relative photometry work, this diffuser-position variation should have little effect because the diffuser position needs to be stable only for the 32 s of one set of discrete mode measurements. We do not mind if the instrument's gain changes, as long as the instrument is very linear over the range of measurements involved in the Mg II measurements. Presumably, when the diffuser is deployed it stays at its position (for example, for the duration of the several sets of discrete-mode Mg II measurements made each day).

2. HISTORICAL PERSPECTIVE ON The Mg II *h* and *k* LINES AND CORE-TO-WING RATIO

2.1. Early Spectra of the Mg II *h* and *k* Lines from Rocket and Balloon Flights

Before discussing the NOAA-9 SBUV 2 measurements of the solar Mg II *h* and *k* resonance lines, let us review what is known about these absorption lines. This Mg II doublet involves transitions from the 3^2P electron energy level to the 3^2S ground state: $3s^2S_{1/2}$-$3p^2P^0_{1/2}$ for the *h* line and $3s^2S_{1/2}$-$3p^2P^0_{3/2}$ for the *k* line. These are the same transitions as those in the Ca II H and K lines except for the electron shell number 3 (M shell) for Mg rather than 4 (N shell) for Ca. Because of the similarity of these Mg and Ca ions and doublets, these Mg lines are called *h* and *k* lines (like the Ca H and K lines). Upper-case letters are used for the Ca II lines because of the historical precedent set by Fraunhofer when he labeled them H and K in his list of absorption lines. Lower-case *h* and *k* are used for the Mg II lines because they were not in Fraunhofer's list (since they cannot be observed from the ground) and because of the similarity between these lines and the Ca H and K lines.

First, consider the spectral shape of the lines. Figure 2.1 shows a beautiful, high-resolution spectrum of the Mg II *h* and *k* lines for a quiet region near the center of the Sun (Allen et al., 1978; see also the solar spectrum atlas by Tousey et al., 1974). The numerous vertical lines near the left side and also near the right side of the figure are not noise; they are weak solar absorption lines that are present throughout the middle (200-300 nm) and near (300-400 nm) ultraviolet wavelength ranges. The most conspicuous features in Figure 2.1 are the *h* and *k* chromospheric emission cores near 280.27 and 279.56 nm, respectively. The emission core for the *h* line has a half-maximum width of about 0.043 nm, and that for the *k* line is about 0.047 nm. The largest features are the strong, overlapping *h* and *k* absorption lines, including the following:

(1) The long-wavelength wing of the *h* line, which causes the general decrease in high values between the weak absorption lines from 281.7 nm down to 280.3 nm.

(2) The overlapping short-wavelength wing of the *h* line and the long-wavelength wing of the *k* line, which causes the low, broad peak at 279.96 nm between the *h* and *k* emission cores.

(3) The short-wavelength wing of the *k* line, which causes the general increase in intensity from 279.5 nm down to 278.5 nm. The two emission cores each include a central reversal.

The nomenclature used to describe the spectral features for these lines is analogous to that used for the Ca II H and K lines at 397 and 393 nm, respectively (See Fig. 9-9 of Foukal, 1990). For example, the minimum of the central reversal of the Mg II *k* line is called k_3. The peak at a wavelength longer than k_3 is called $k_{2\text{-long}}$, and the peak to the short wavelength side is called $k_{2\text{-short}}$. The minima between the emission core and the absorption wings are called $k_{3\text{-short}}$ and $k_{3\text{-long}}$, respectively.

During a rocket flight in 1957, Purcell et al. (1958) first observed the solar Mg II *h* and *k* lines with enough wavelength resolution to see the structure of the emission cores. Purcell et al. (1963) identified a number of the weaker absorption lines near the Mg II *h* and *k* lines, including many lines from Fe I and Fe II, as well as Mg II lines (Multiplet No. 3) near 279.1 nm

and 279.8 nm. Lines that appear to be broader than the typical weak absorption lines in the wings of the Mg II *h* and *k* lines at 278.3, 281.1, and 281.3 nm, in Figure 2.1, are groups of overlapping lines rather than a single line with broad wings. Only the line at 278.8 nm is classified as a line with wings (Moore et al., 1982). The stronger the absorption line, the higher in the solar atmosphere is the source for emission at the center of the line. Since the percent variation with solar activity rises with the height of the observed source region, we expect weak absorption lines from the upper photosphere and temperature-minimum region to have very small variations. The emission cores of the Mg II *h* and *k* lines come from the chromosphere, and are therefore expected to have large-percentage variations with solar activity.

Rocket and balloon flight measurements of the solar Mg II *h* and *k* lines established the following:

(1) The Mg II line intensity decreases near the solar limb, and there is a greater limb darkening of the wings than for the emission cores (Kohl and Parkinson, 1976).

(2) The short-wavelength k_2 and h_2 peaks are higher than their respective long-wavelength peaks.

(3) The wavelength of k_3 (h_3) is slightly longer than the midpoint of the two k_2 (h_2) peaks (Tousey et al., 1974; Allen et al., 1978).

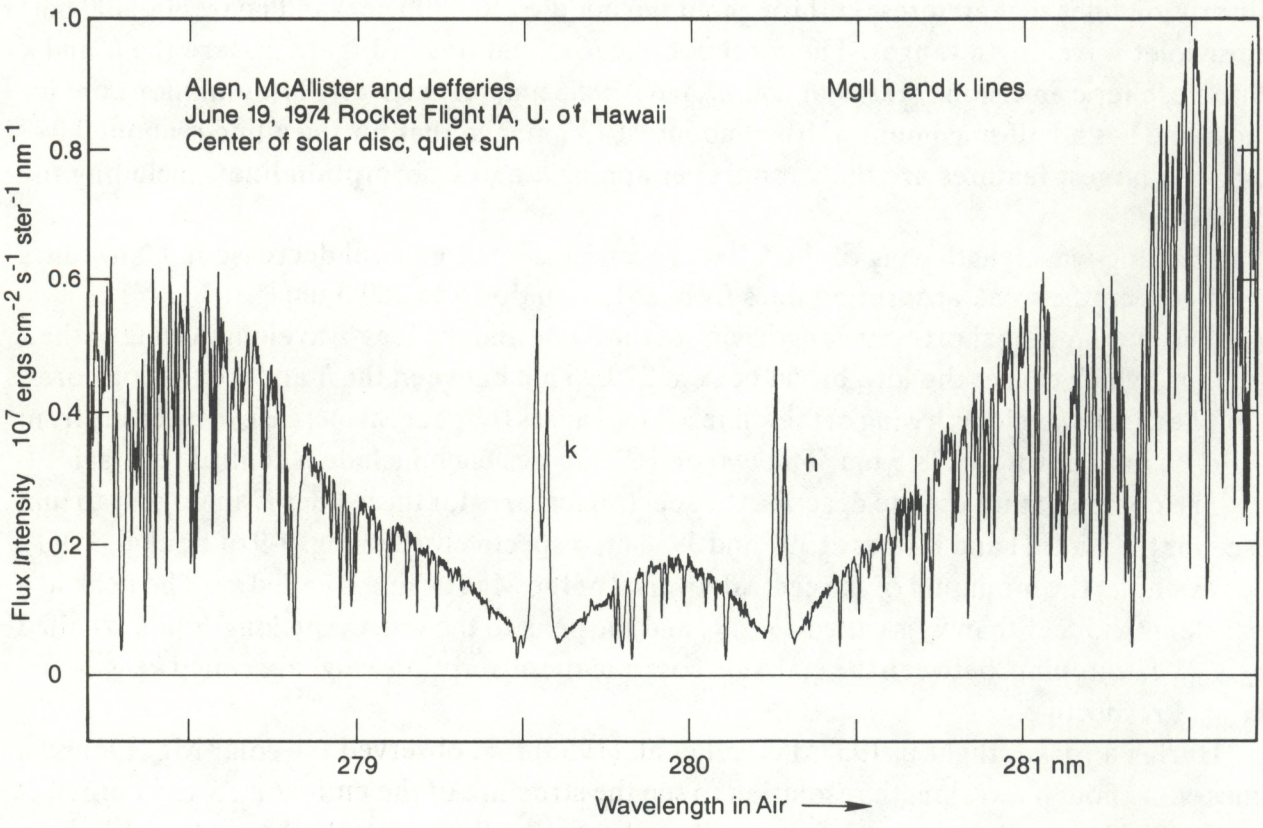

Figure 2.1. Solar spectrum of the Mg II h and k lines with wavelength resolution of 0.002 nm.

(4) The wavelength separation between the k_2 (h_2) peaks increases slightly and their peak intensities become more equal as the observed solar spatial region is moved toward the solar limb (Lemaire, 1970).

(5) The net energy flux in the k emission core above the absorption line background is about three-halves that in the h emission core for full-disk and central-disk measurements (Tousey et al., 1974; Allen et al., 1978).

(6) The emission cores are greatly enhanced (+160%) over bright plages (Lemaire, 1970).

(7) The emission core wavelength shape can vary appreciably with changing solar position for small fields of view (<7" of arc), a phenomenon that has been interpreted by Gouttebroze (1977) to be caused by velocity gradients along the line of sight within the source region for the radiation observed.

Fredga (1969) used a rocket-flight experiment on May 20, 1968, to photograph filtergrams of the Sun in the Mg II k line with a 0.21 nm bandpass. Fredga (1971) compared the relative intensity, as a function of position on the Sun, of her Mg II k-line data with Ca K line spectroheliograms recorded at the McMath-Hulbert Observatory with a slit width of 0.01 nm about 10 minutes later than the Mg II data . The spatial resolution was about 2 to 3″ of arc for the Ca K data and about 8″ of arc for the Mg II measurements; the latter appeared slightly smeared in the direction of the film advance. The correlation of the Mg II intensity with the Ca K line data over one active region was 0.92 and over a second region was again 0.92. Spatially filtering the Ca K data to compensate for the lower spatial resolution and the smear in the Mg II data increased these correlations to 0.94 and 0.95. If the spatial structure in the Ca K and the Mg II k lines are highly correlated, and if the temporal changes of full-disk flux measurements are caused mainly by changes in the brightness and area of plages, plage remnants, and the active network, then we would expect the temporal variations of full-disk Ca-K line and Mg II k line measurements to be highly correlated.

On the other hand, Zirin (1966, 1988) emphasizes that, for a small field of view and average time of observation of the quiet Sun, the Ca K line tends to have one or the other K_2 peaks, but not both. The K_2 peaks are simultaneously bright only in plages and network elements. The K_1 valleys are also enhanced in plages and network elements relative to the quiet Sun. The K_3 central-reversal valley is deep relative to the K_2 peaks in the network ele- ments and relatively weaker in plages. Similar behavior occurs in the Mg II h and k lines (Gouttebroze, 1977). Since the Mg II h and k line cores are from slightly higher chromospheric altitudes than the source of the Ca-K line core, there probably are differences in the dissymmetry of the Mg II k line relative to those of the Ca-K line for observations with small fields of view. Consequently, the correlation between Mg II k line intensity and the co-spatial Ca-K line intensity probably would decrease from Fredga's 0.92 as the field of view was decreased.

2.2. Satellite Measurements with Fine Spatial and Wavelength Resolution

Lemaire (1984) reported on wavelength-profile measurements from the OSO-8 satellite for the Ca K and H, Mg II h and k, and the Lyman alpha and beta lines with 0.002 nm wavelength resolution (except 0.006 nm for Lyman beta) and a field of view of 3 by 13 arcsec.

The intensity versus wavelength was integrated over a 0.1 nm interval, centered on each emission core or line, except in the case of *h* Lyman alpha, where a 0.2 nm interval was used. Figure 2.2 shows several comparisons of line intensities. Each point in these scatter diagrams involves the intensities of the two lines for their concurrent and cospatial measurements. The variation over the dynamic range shown comes more from different spatial regions having different brightnesses than from temporal variations.

The graph in the upper left of Figure 2.2 shows very little deviation from a straight line; therefore, the correlation is very high for Mg II *k* versus *h*. The slope of that line is 1.43. The scatter diagram for the Ca II K-line emission core versus that for the H line has a little more scatter but still a very high correlation, probably in the high 0.9s (Lemaire did not report the correlation coefficient). The slope for Ca II K versus H is near unity. There is a small negative intercept (-3.6×10^4 ergs cm^{-2} s^{-1} $ster.^{-1}$) that is caused by the higher H_1 intensities for the H line than the K_1 levels for the K line since the continuum background decreases with decreasing wavelength from the H line to the K line. The correlation of the Mg II *k* emission core with respect to that for the Ca K line is lower than for the above cases but still quite high, probably in the low 0.9s. One might suspect an observational problem, since the scatter is increasing with increasing wavelength separation of the lines being compared; but apparently most of this scatter is real and probably is produced by the same physical processes that cause the spatial variations in line shapes discussed earlier. Averaging over many spatial regions should reduce the scatter, and full-disk observations offer the largest possible spatial average. Lemaire (1984) pointed out that the Mg II *k* line is a more sensitive tracer of solar chromospheric activity than is the Ca K line; the Mg II *k* emission-core intensity increases over the minimum values shown by 12.6, while the Ca K line varies by 3.7.

In Figure 2.2, the scatter for Mg II *k* versus H Lyman alpha is very large and particular groups of points appear to be uncorrelated. Lemaire (1984) concludes that Lyman alpha and Mg II brightenings are not cospatial. Lyman alpha contains emission from above the sources of the Mg II emission, including the top of the chromosphere and the base of the chromosphere-corona transition region. The solar atmosphere in these regions deviates further from a horizontally stratified medium, and some Lyman-alpha-emitting magnetic flux tubes have a large horizontal component to their direction. Averaging over larger spatial regions should reduce the average scatter. The scatter of H Lyman beta versus alpha is a little larger than might be expected, since they involve the same ion. On the other hand, the beta line is much weaker than the alpha line; the depth to which the beta line's core emission is observed is probably deeper than for the alpha line, and the consequent lack of cospatiality must contribute some of the scatter. Lemaire (1984) notes that some of the scatter for Lyman beta may be real because the signal for this line is much weaker than for the others.

The conclusions (and comments) derived from Figure 2.2 that are important for our studies of the Mg II *h* and *k* lines are the following:

(1) The *h* and *k* emission cores brighten spatially together, therefore, they should also vary temporally together.

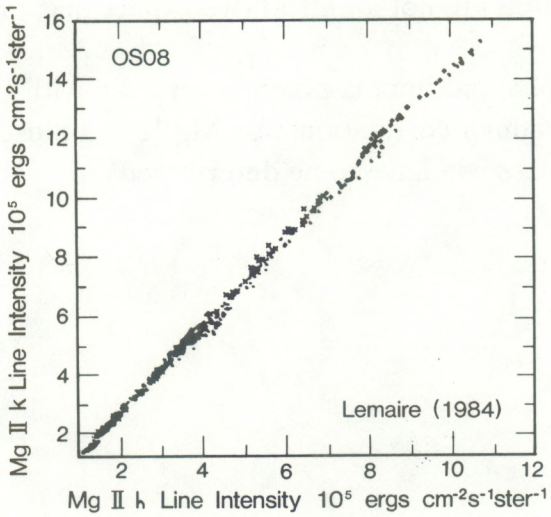

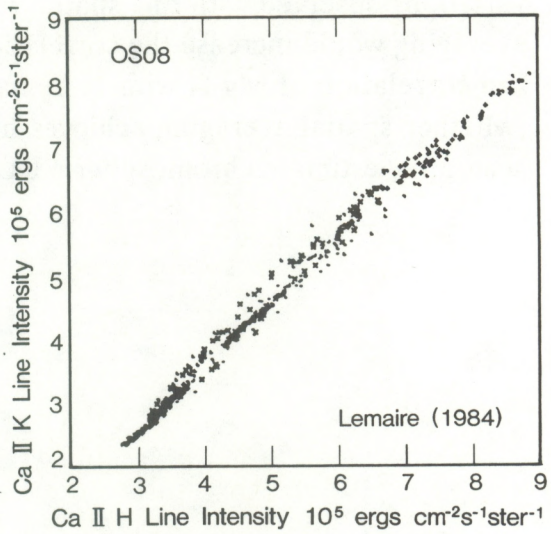

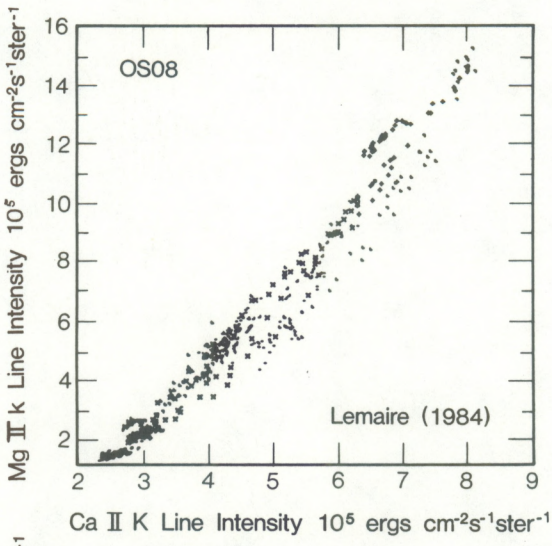

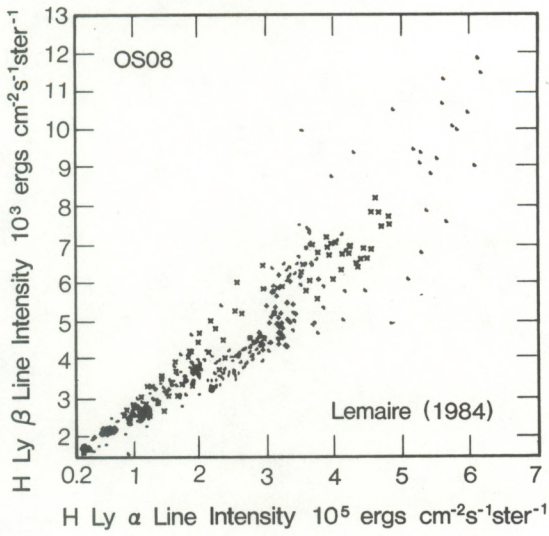

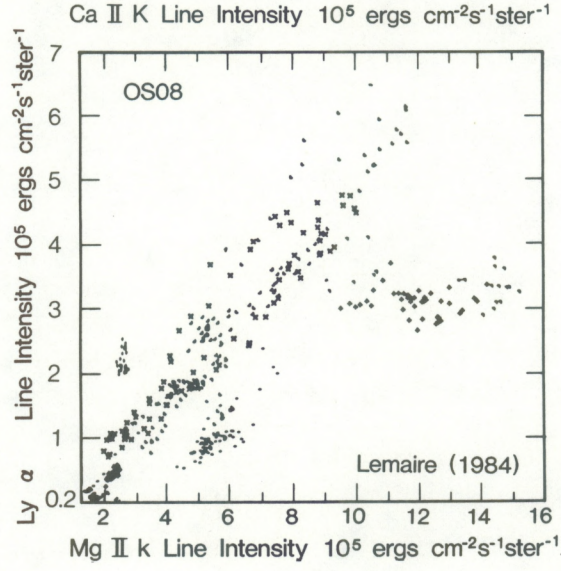

Figure 2.2 Scatter plots of the chromospheric emission cores of major solar spectral lines, where the concurrent intensity pairs involve the same spatial region. These figures are based on Lemaire (1984).

(2) The Mg II *k* (and *h*) emission is highly correlated with the Ca-K emission but their spatial variations observed with fine spatial resolution are not identical (we expect that spatial averaging would increase the correlation).

(3) The correlation of Mg II with H Lyman alpha and beta is much lower than with Ca K (whether spatial averaging achieves high enough correlations for Mg II to be used to accurately estimate chromospheric EUV fluxes will have to be determined).

2.3. Nimbus-7 Core-to-Wing Ratio for the Mg II *h* and *k* Lines

The Solar Backscatter Ultraviolet (SBUV) experiment aboard the Nimbus-7 satellite was the predecessor of the SBUV 2 monitors on the NOAA satellites; research of those measurements is very pertinent to research of the NOAA-9 data. Heath and Schlesinger (1986) first derived the core-to-wing ratio for the Mg II *h* and *k* lines for the Nimbus-7 satellite. Consider the physical principles involved in their ratio. Figure 2.3 shows a spectrum measured by Hall and Anderson (1988) after being filtered by a triangular wavelength filter with the 1.1 nm half-maximum width of the NIMBUS-7 SBUV experiment. In other words, the complicated spectrum shown in Figure 2.1 forms one smooth, blended absorption line when viewed by the NIMBUS-7 SBUV experiment. Solar-activity-induced variations in the *h* and *k* emission cores combine to form small differences in the center of the blended lines. Heath and Schlesinger (1986) took the ratio of the flux measured at three wavelengths at the center of the line to the average of measurements in the short- and long-wavelength wings of the line. Their basic idea was to use a ratio of fluxes in the center of these blended lines, where the solar activity signal was strong, to an average of flux measurements in the wings, where the solar activity signal was very weak. Their ratio would then have a strong solar signal. All the wavelengths involved were close together, so any multiplicative instrumentation drift that was weakly dependent on wavelength would cancel out in the ratio.

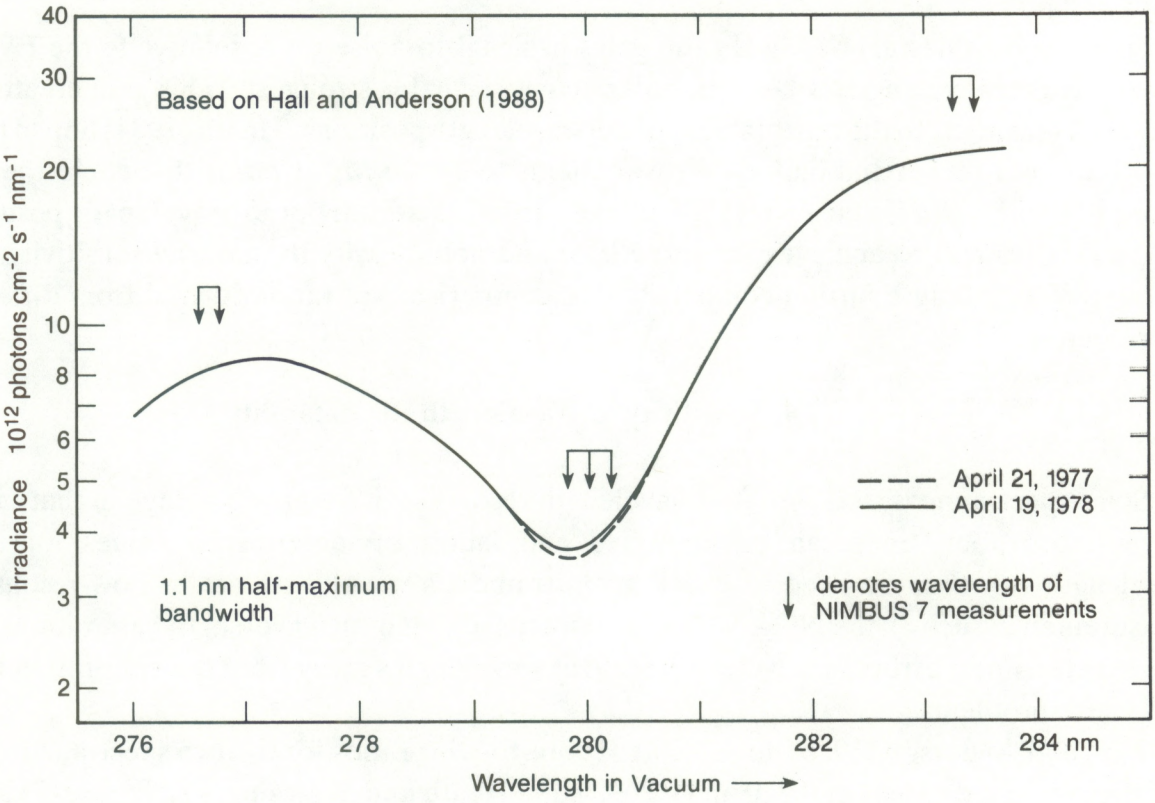

Figure 2.3. Solar UV spectrum of the Mg II h and k lines for the low-wavelength resolution of the Nimbus-7 SBUV observations (Hall and Anderson, 1988).

Using three measurements near the center of the line provided some averaging to improve the signal-to-noise ratio. If the center wavelength were nearest to the minimum of the blended *h* and *k* lines, small drifts in wavelength would have a compensating effect, assuming that the spacing between wavelengths remained the same. As the flux increased in one of the outer core wavelengths due to wavelength drift, the flux in the other outer wavelength would decrease, considering the shape of the line. Two wavelengths were used in each wing to reduce noise, and the pairs were equally spaced in wavelength, relative to the core wavelengths, to provide an estimate of the background flux at the center wavelength. If the wings were of equal intensity, the ratio would be insensitive to multiplicative instrumentation drifts that were a linear function of wavelength. Figures 2.1 and 2.3 show that the short-wavelength wing is weaker than the long-wavelength wing.

Heath and Schlesinger's (1986) ratio is similar to the astronomer's relative photometry technique of measuring the equivalent width (EW) of an absorption line at optical wavelengths. If the spectrometer is good enough to maintain a uniform intensity gain and rate of change in wavelength for a short time while scanning across the line, the line's equivalent width can be adequately measured, i. e. the wavelength width that when multiplied by the estimated continuum intensity gives the same area as that between the estimated background continuum and the observed intensity. Assuming sufficient wavelength resolution, the wavelength of weak absorption lines can be identified and the local wavelength scale can be calibrated.

Heath and Schlesinger's Mg II ratio gains in signal-to-noise ratio, relative to the EW, by using only the wavelengths where the solar activity signal is strongest. This gain creates an increased sensitivity to the repeatability of the wavelength positions. Heath (1984) hoped to be able to use old rocket and balloon measurements to derive Mg II ratios that could then be compared with the Nimbus-7 results but the increased sensitivity to wavelength positions makes this difficult to achieve. Scattered light and nonlinearity in intensity sensitivity as a function of wavelength further complicate intercomparisons of ratios derived from different instruments.

2.4. Sensitivity to Wavelength Repeatability

Solar spectra measured with fine wavelength resolution have an advantage in that small, narrow absorption lines can be identified and laboratory-determined values for their wavelength can then be used to check an instrument's wavelength scale. Low-resolution measurements, such as the NOAA 9 measurements, depend on wavelength calibrations at a few selected lines; errors in wavelength scale at wavelengths away from the calibration lines may cause problems.

Hall and Anderson (1988) derived Mg II core-to-wing ratios for the two spectra in Figure 2.3; they obtained values of 0.270 and 0.266, while Heath and Schlesinger's Nimbus-7 values for those same dates were 0.280 and 0.272, respectively. Since the maximum solar-cycle increase in this ratio is of the order of 10% of the solar minimum level for daily values and 7% for 365-day smoothed data (Heath and Schlesinger, 1986; Donnelly, 1991), the differences

between these same-day values, (3.6 %, 2.2%) from two instruments, is prohibitively large. Hall and Anderson (1988) showed that an error of 0.1 nm in wavelength scales could explain much of the discrepancy. In Figure 2.3, if the wavelength arrows for Nimbus-7 were moved 0.1 nm to shorter wavelengths, the center wavelength would better fit the minimum. Comparisons of the intensities of the three core wavelengths for Nimbus-7 show that the minimum is close to the center wavelength; there definitely is an error in the Nimbus-7 wavelength scale relative to that of Hall and Anderson (1988). Careful intercomparisons of the line shapes for concurrent measurements from two instruments, to correct the wavelength and intensity scales of one relative to the other, may permit more accurate comparison of Mg II ratios. Hall and Anderson (1988) have shown that it is impossible to compare Mg II ratios from different instruments when line-shape intercomparisons cannot be made.

Temporal overlap in satellite measurements is essential when Mg II ratios from one satellite are to be compared with those from the next satellite in the series. Because of the high sensitivity of the Mg II ratio to the wavelength positions used to derive the ratio, it is very important that the satellite instrument accurately repeat these wavelengths. Using Nimbus-7 measurements of emission lines in an in-flight calibration lamp showed that the spectrometer's grating-step positions drifted in wavelength by less than 0.05 nm in 5 years (Heath and Schlesinger, 1986). Using the shape of the solar UV flux measurements at the bottom of the Mg II *h* and *k* lines to estimate the wavelength of minimum flux, Donnelly (1988) estimated that the NOAA 9 measurements near the Mg II lines were repeatable in wavelength position to within about 0.003 nm over 2 years, and the day-to-day jitter (small fluctuations in wavelength from one spectral scan to another) was less than 0.002 nm. One of the strengths of the SBUV 2 monitors is their wavelength repeatability, especially for measurements made in the discrete-wavelength mode such as those discussed in this report.

3. RAW MEASUREMENTS FROM SBUV2 ON THE NOAA9 SATELLITE

3.1. Discrete-Wavelength Mode

The NOAA9 SBUV2 measurements of solar UV irradiance discussed in this report were made in the discrete-wavelength mode at 12 wavelengths in and near to the solar Mg II h and k absorption lines. The diffuser is deployed to scatter the solar irradiance upward into the nadir-pointed instrument. Figure 3.1 shows the wavelength order and timing of one such group of measurements and the start of a second group. The intensity output of the spectrometer is sampled 2 seconds apart for each group of 12 wavelengths. During the first 0.75 seconds of these 2 second steps in wavelength, the instrument changes wavelength and the feedback-loop wavelength sensor and magnetic torque drive system adjust to precisely the same assigned wavelength; the intensity output is sampled during the remaining 1.25 seconds. Therefore, the time between the intensity measurements at these different wavelengths is an integer multiple of 2 seconds, i. e. $2n$ seconds for $n=1, 2, \ldots 11$. After each 12-wavelength group is completed, the instrument resets in 8 seconds to start another similar group of 12-wavelength measurements; so the time between the measurements at a given wavelength in one 12-wavelength group to the next is 32 seconds. About 20 such groups of measurements are made in sequence. Typically, only nine provide usable data from the time span in which the diffuser is illuminated by solar irradiance (just 4.8 minutes).

3.2. Satellite Time and Location

Measurements of the solar Mg II h and k lines using the discrete-wavelength mode are made on one orbit per day. Figure 3.2.1 shows the time of day at the start of each of the nine sunlit sets of 12-wavelength groups for the daily Mg II discrete-wavelength measurements; the daily time span is so short that it contributes only a slight unevenness in the nearly straight line connecting several days in a row. The gap in August 1987 is a consequence of problems encountered in reading that particular data tape when this figure was made. Since then, some of those data have been recovered. The measurements are made between 6.00–8.75 UT, when the terrestrial subsolar point is in the longitude range from 90°E to 48°E and the sunlit terrestrial hemisphere includes much of Europe, Africa, U.S.S.R., India and most of the rest of Asia.

As the measurements are made, the satellite orbits progress relative to the planned solar zenith angles; consequently the times of the measurements also show a day-to-day progression. The main pattern in Figure 3.2.1 includes triangular curves about 7 days in duration, two of

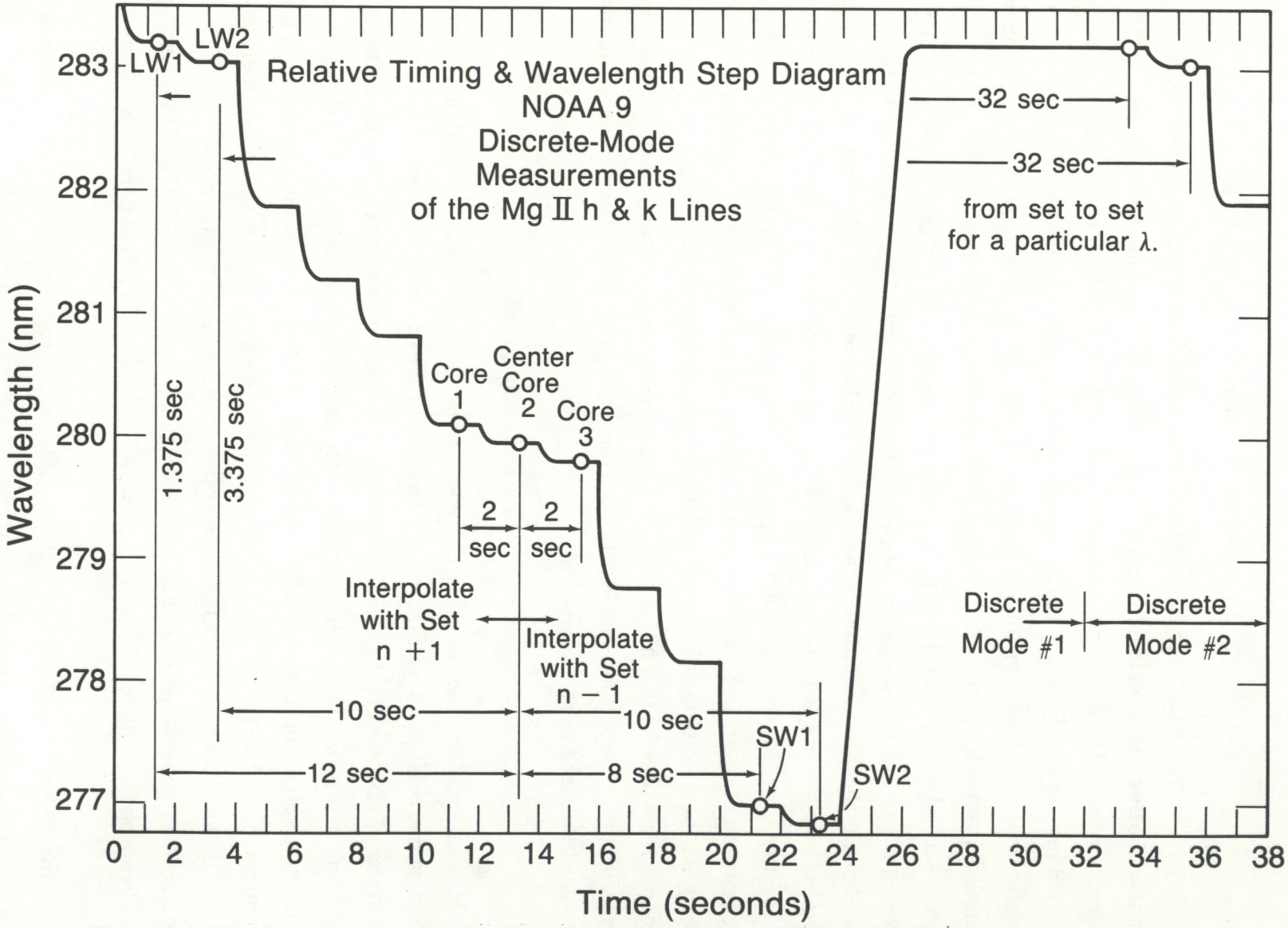

Figure 3.1. Wavelength versus time for discrete-wavelength measurements of the solar Mg II *h* and *k* lines.

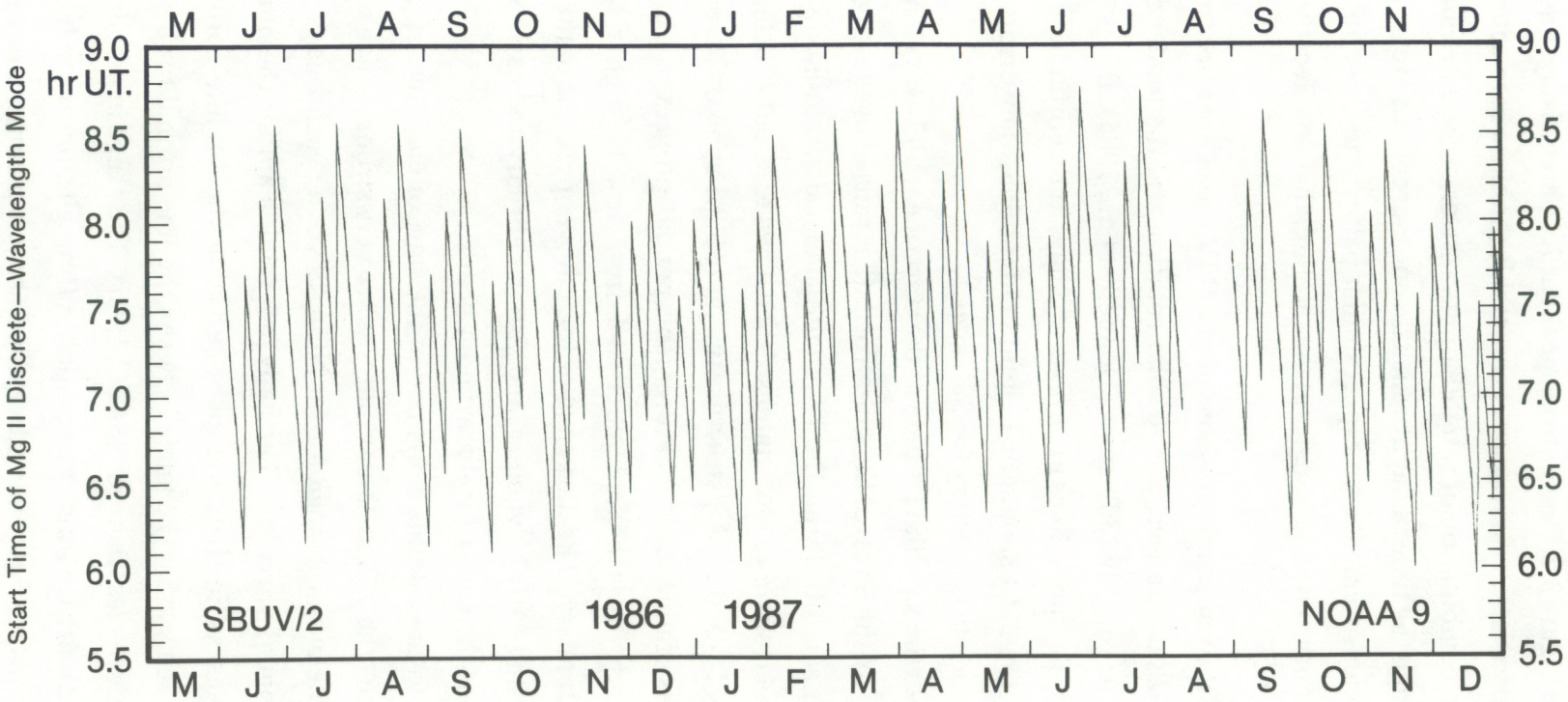

Figure 3.2.1. Start time for the first daily measurements in the discrete-wavelength mode of the solar Mg II *h* and *k* lines.

which combine with a longer-lasting triangle to form a group with a 28-day periodicity. Power spectra of the data in Figure 3.2.1 have strong peaks at 7, 14 and 28 days and their harmonics. A much weaker annual variation also occurs. Presumably the close connection with 1 week and 4 weeks results from a combination of satellite operator work schedules and the satellite orbit progressions. Although the time of day at which the measurements are made does not directly affect the solar flux measurements, we expect similar patterns to show up in other quantities, such as the solar azimuth and zenith angles at the satellite, that do affect the instrument output.

Power spectra of the temporal variations of solar UV fluxes are also strong at periods in the 13–14 day and 27–28 day ranges, due to solar rotation and the tendency for two groups of active regions to occur roughly 180° apart (Donnelly et al., 1985). But power spectra of solar UV fluxes are usually devoid of lines at periods of 7 days and shorter, and so the strong 7-day structure seen in Figure 3.2.1 should be helpful in identifying any errors in our results associated with inaccuracies in correcting for Sun angles.

Figure 3.2.2 shows the satellite latitude at the start of each 12-wavelength group when the diffuser was sunlit. The thickness of the ribbon of data is caused by the large change in latitude for the polar-orbiting satellite during the 4–minute span in discrete-mode start times, ranging from a 16° interval near summer and winter solstice down to about 4° in late February and October. The strong 7-, 14- and 28-day structure in Figure 3.2.1 appears here as a very small, subtle feature. The series of nine sunlit measurements per day progresses from high to lower latitude from mid-March through September and from low to higher latitiude from mid-November through January. The darkened or folded-over portions of the ribbon seen in Figure 3.2.2 in October and early November, and also in February and early March, involve daily progressions that pass through a local maximum near 81°.

Figure 3.2.3 shows the satellite longitude at the start of each set of discrete-wavelength measurements. Here, the 7- and 28-day patterns are very strong, which is consistent with the progression of satellite orbits in longitude for NOAA9's Sun-synchronous polar orbit. There is also a very strong annual variation. The daily progression among the nine sunlit data sets is always from east to west as Earth rotates to the east while the satellite's orbit maintains a direction, relative to the Sun so that the angle between the line normal to the orbit plane and the Sun-satellite line is always less than 68° (SASC, 1986). The range in longitude during these Mg II measurements is moderate from spring equinox through summer to fall equinox, with very large daily variations in October, November, and February through mid-March (in some cases as large as 80°).

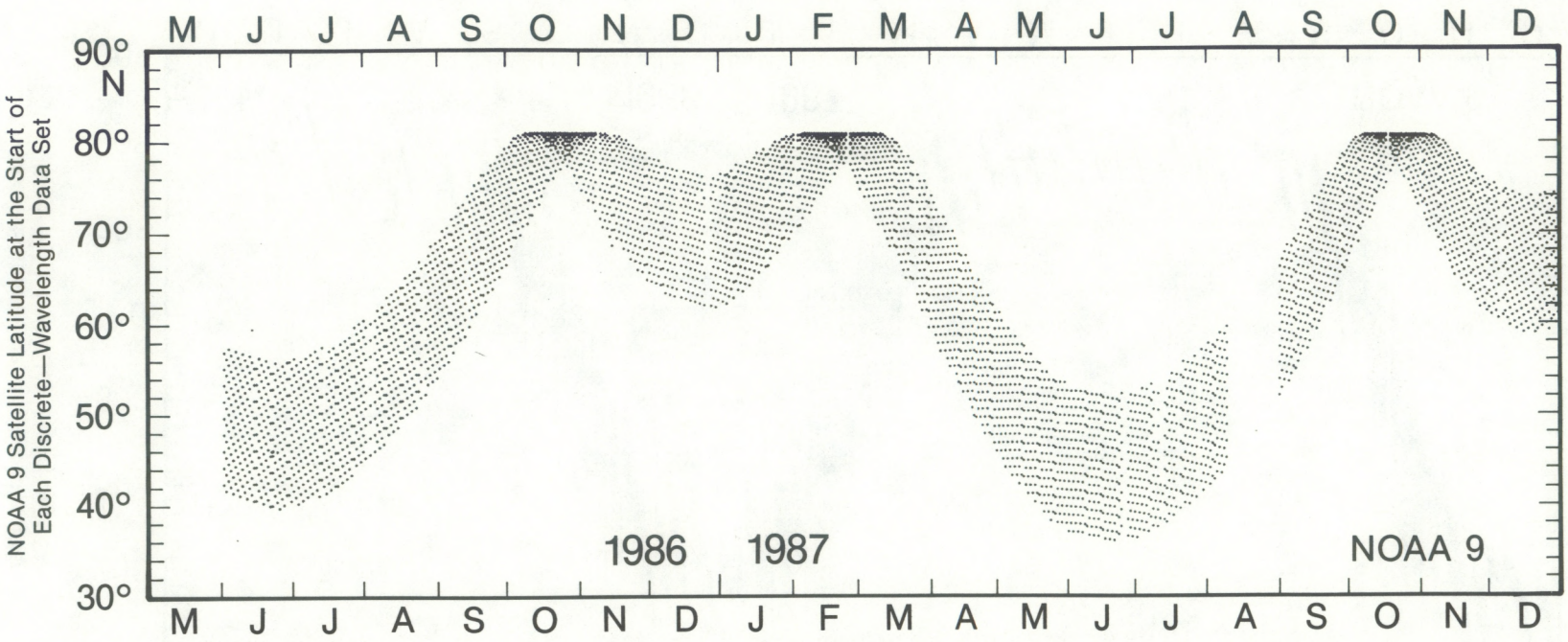

Figure 3.2.2. Satellite latitude at the start of each group of measurements for 12 wavelength steps for the first daily set of solar Mg II line measurements.

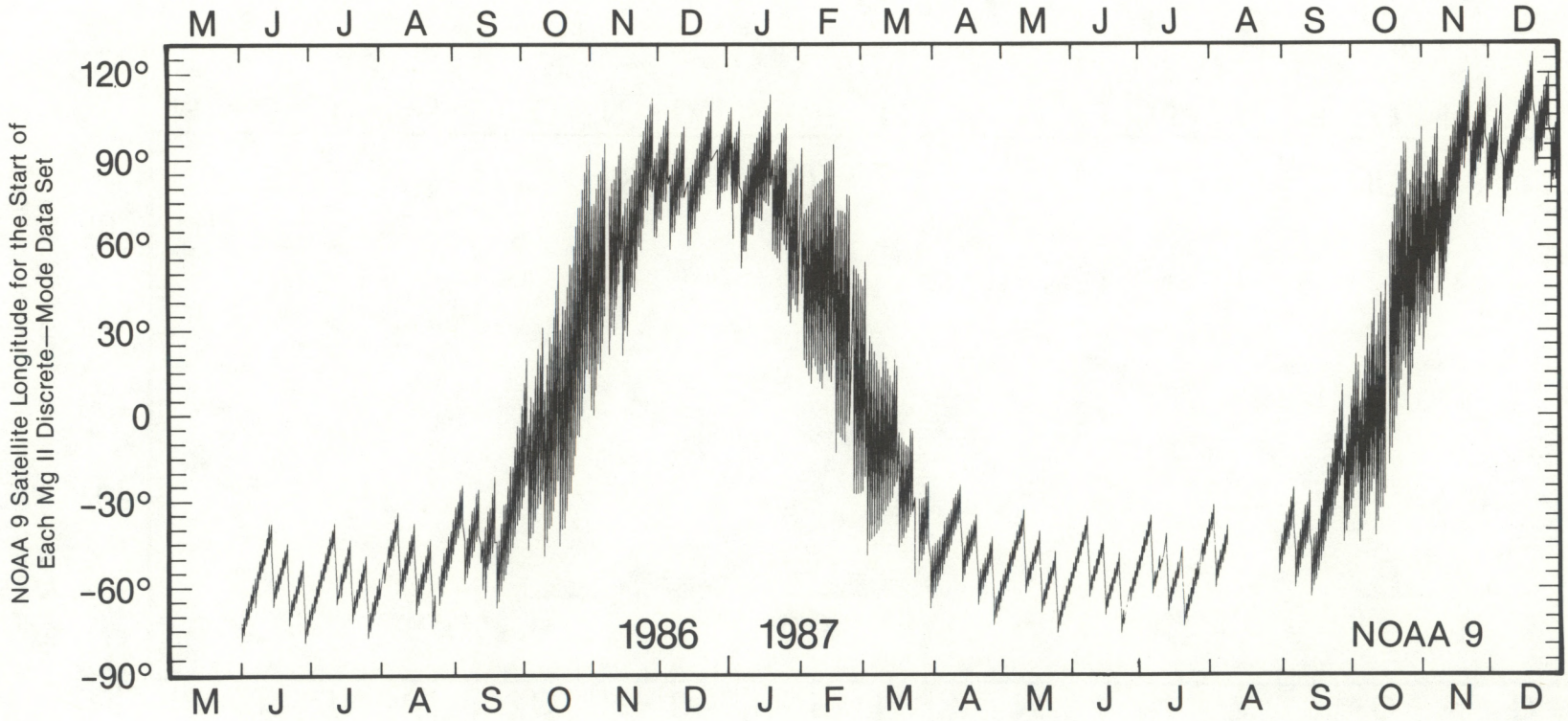

Figure 3.2.3. Satellite longitude at the start of each group of measurements for 12 wavelength steps for the first daily set of solar Mg II line measurements.

The combination of Figures 3.2.2 and 3.2.3 shows Mg II solar measurements are made when the satellite is over the region including Hudson Bay, Toronto, Nova Scotia, Newfoundland, and southern Greenland from spring equinox through summer to fall equinox. This means that the terrestrial atmosphere below the satellite is in nighttime, and the brightest terrestrial emission and scattered light near 280 nm would be the dayglow near the terrestrial limb at the azimuth of the Sun as seen at the satellite. In November–January, the satellite is over Northern Siberia and the Artic Sea, where the sunlit hemisphere is mostly to the south of the satellite. Again, the atmosphere below the satellite is not sunlit and the brightest atmospheric emission visible at the satellite would be the atmosphere near the southern limb.

Figure 3.2.4 shows that the altitude of the satellite at the time of the Mg II measurements is between 847 and 879 km. The rows of points are caused by 1 km resolution in the values in the 1B data tapes, not an important limitation for our purposes. Quasi-sinusoidal variations in altitude occur with a period about 5 months from June through November, followed by a first period of about 3.6 months and then about 4 months, a sequence more frequent than annually. We currently view these altitude variations as unimportant for the solar flux measurements. The important thing is that the atmospheric limb at an altitude of 50 km, as seen by the satellite, has a great-circle ground range of about 3,000 km from the subsatellite location. Even more important is that the terrestrial limb at 50 km altitude is at a zenith angle as seen from the satellite of no less than about 117° and the ground-level limb is at about 118°. The diffuser plate is oriented to exclude directly incident rays from atmospheric emissions below the satellite and from the bright terrestrial limb.

3.3. Sun-Diffuser Angle Data

Figure 3.3.1 shows the approximate azimuth angle of the Sun as seen at the satellite, based on what the SESC User's Guide (SASC, 1986) calls the "field of view solar azimuth angle". We have encountered an inconsistency in the various time, location, and Sun-angle information, and have concluded that the sign must be reversed on these azimuth angles compared to the usual convention of having zero as due north and +90° as due east, etc. Sign ambiguity is a typical problem in computing solar azimuth angle. We conclude that −90° is due east for these values. This means that in December the Sun is viewed looking roughly toward the south-southwest to south and there is a moderate change in azimuth during the nine groups of measurements at 12 wavelengths. In April through August, the Sun is seen to the northeast and there is very little change in azimuth during the nine sets of sunlit discrete-mode measurements taken when the satellite is over the region from Hudson Bay to Newfoundland. From mid-October

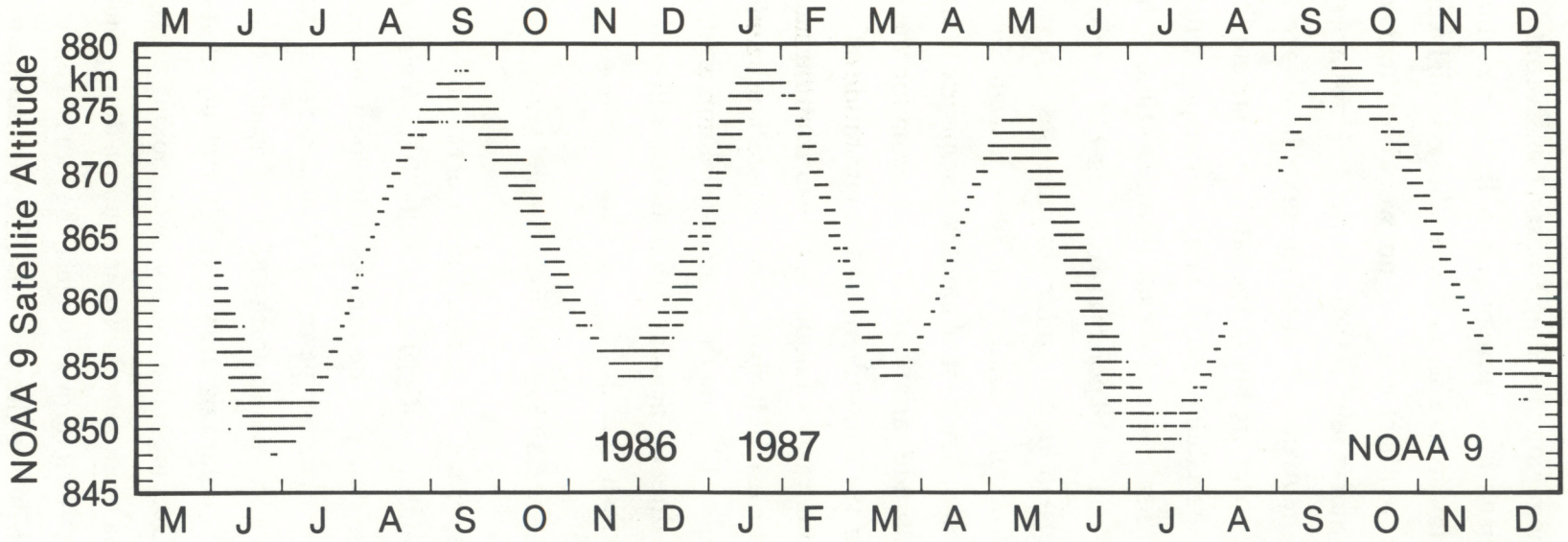

Figure 3.2.4. Satellite altitude at the start of each group of measurments for 12 wavelength steps for the first daily discrete-mode Mg II measurements.

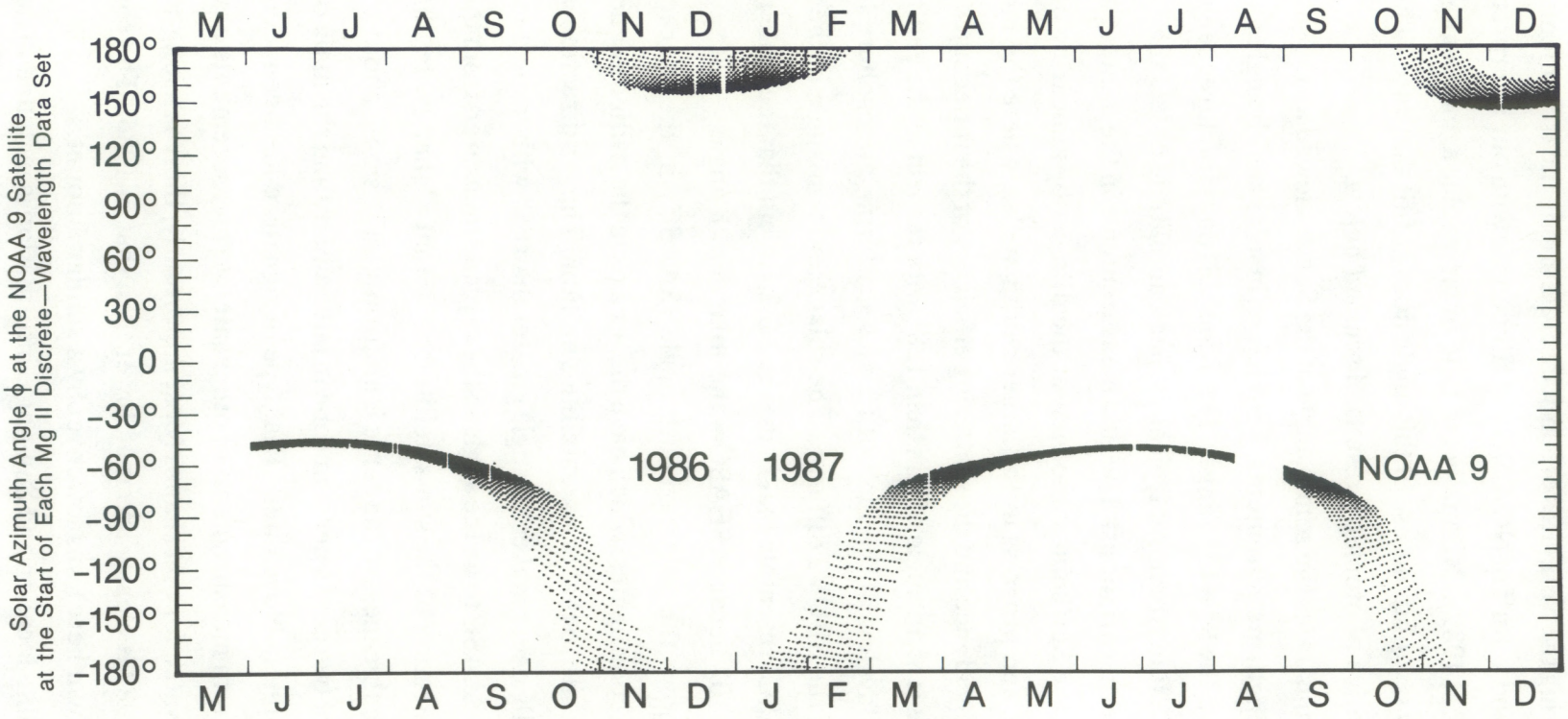

Figure 3.3.1. Solar azimuth angle of the satellite at the start of a 12-wavelength group for the first set of discrete-wavelength mode measurements of the solar Mg II *h* and *k* lines for each day.

through mid-November and from early February through early March, the change in the solar azimuth angle during the 5 minutes of sunlit discrete-mode measurements is very large, almost 90°. J. Lienesch and I. Ruff of NOAA/NESDIS concur with our interpretation that this sign is incorrect (Lienesch, 1989). Normally the field of view solar azimuth angle is used when the nadir field of view is sunlit; our use of this angle does not fit that case. This sign problem does not affect our relative photometry results, discussed below.

Figure 3.3.2 illustrates the zenith angle of the Sun as viewed at the satellite during the Mg II discrete-wavelength measurements. The change in solar zenith angle during each set of daily measurements is in the $9° - 15°$ range. The 7-and 28- day structures seen in Figures 3.2.1 can be seen here in the fine structure; typically a peak amplitude of less than a degree is superimposed on longer-term variations. The first measurements in the data set are at the smaller zenith angles, when the Sun comes into view at the diffuser by appearing below the edge of the satellite structure, and progress to the larger zenith angles, where the incoming solar ray approaches grazing incidence and the scattering efficiency of the reflectance diffuser is quite low. The diffuser plane is at an angle of less than 128° with respect to the zenith axis; this prohibits the atmospheric dayglow at the limb of Earth's scattering atmosphere to be directly visible from the plane of the SBUV2 diffuser. The solar elevation angle in the spacecraft-centered coordinates (SEASC) resemble that in Figure 3.3.2, except that the scale runs from $-5°$ to 20° instead of 85° to 110° because SEASC= the solar zenith angle $\chi - 90°$.

Figure 3.3.3shows the solar azimuth angle (SAASC) in the spacecraft-centered right-handed Cartesian coordinates, which have the $+x$ axis in the nadir direction and the $+y$ axis in the direction opposite to that of the satellite's motion. The $+z$ direction is roughly toward the Sun and supposedly never makes an angle greater than 68° with respect to the satellite-to-Sun line. We interpret SAASC to be the angle in the xy plane measured from the $+z$ axis toward the $+y$ axis to the projection of the sun-satellite line in that plane. Note that the daily range of values given by the thickness of the curve is uniformly quite small, about 1° wide. Note also the annual structure of two peaks per year (one in late January and the main one in early July) and the annual minimum in November. That type of signature has been identified as a source of error in the long-term measurements of other satellite measurements of solar irradiance, and it is important to watch for that shape. Most importantly, there is a long-term downward drift; the peak in July 1987 is clearly about 6° lower than that in 1986. The corresponding peak in July 1988 (not shown here) was lower yet by a similar amount.

All of the satellite location and Sun-angle information is included in the 1B data tapes used in the analyses discussed here by deriving the information from satellite tracking information

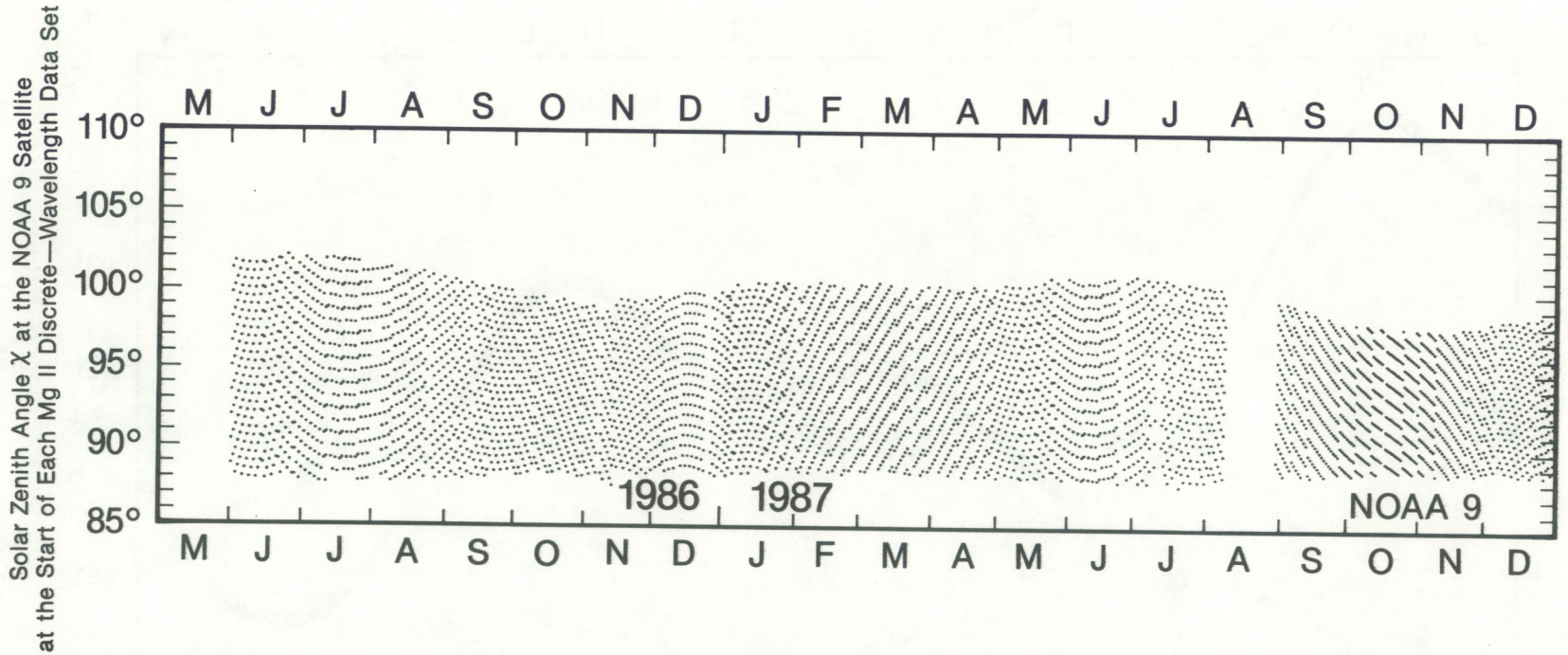

Figure 3.3.2. Solar zenith angle at the satellite at the start of a 12-wavelength group for the first set of discrete-wavelength mode measurements of the solar Mg II *h* and *k* lines for each day.

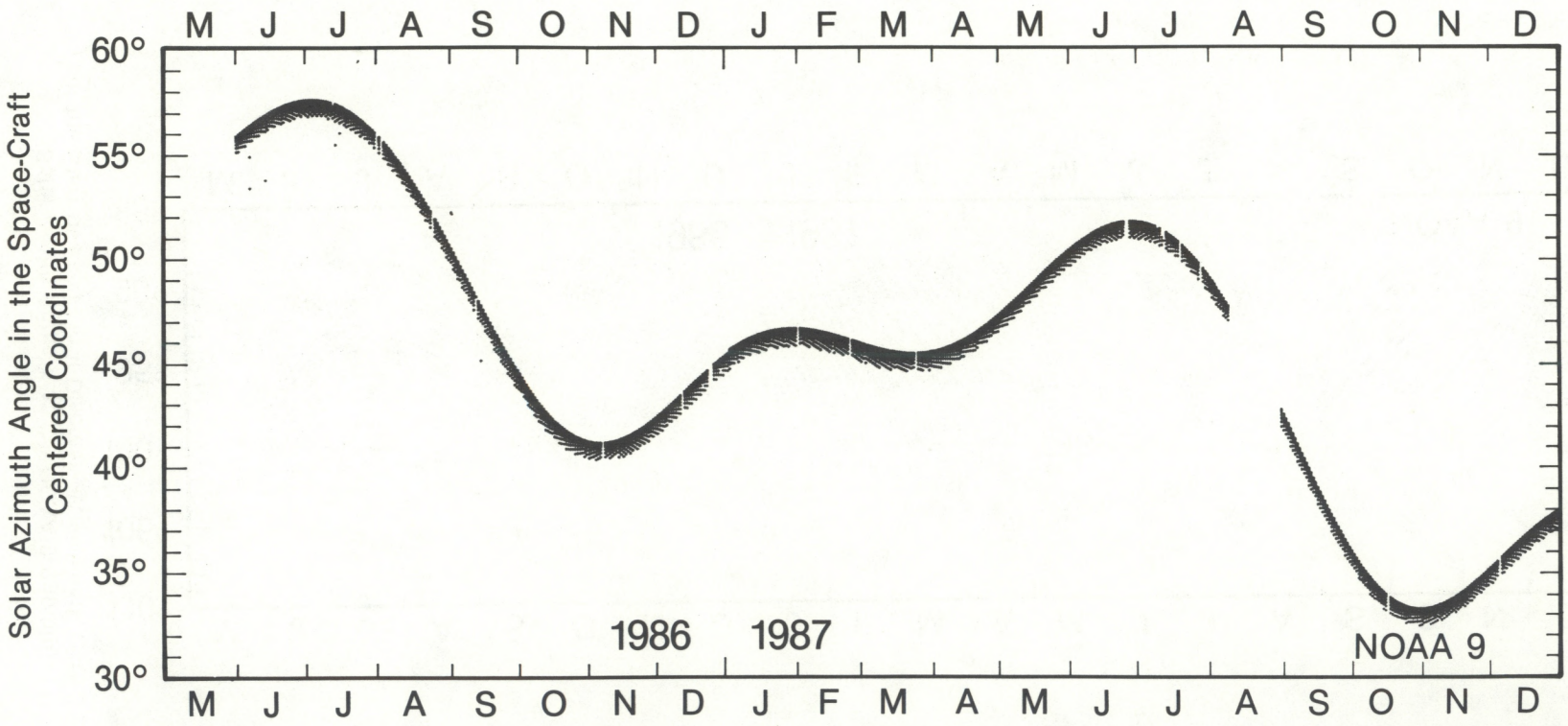

Figure 3.3.3. Solar azimuth angle in the spacecraft-centered coordinate system at the start of a 12-wavelength group for the first set of discrete-wavelength mode measurements of the solar Mg II *h* and *k* lines for each day.

when the tapes are assembled at NOAA's NESDIS facilities in Suitland, Maryland. These data are not telemetried from the satellite as satellite measured data. It is our understanding that these values are estimated from previous-day orbit measurements and do not include fine corrections for small deviations in actual orbital behavior; we have not yet seen any documentation of the size of these small corrections. In the relative photometry analyses discussed below, these missing corrections are not important. The figures presented so far are used here only for general understanding of how the measurements are taken not for quantitative corrections to the data. For later absolute photometry analyses, corrections for Sun-satellite angles will be required.

In summary, the above time, satellite location, and Sun-angle information are consistent with the following: The NOAA9 SBUV2 measurements of solar UV flux in the Mg II h and k absorption lines near 280 nm are made in the discrete-wavelength mode, starting at the end of a satellite pass over the sunlit terrestrial hemisphere. Most of the measurements are then made while the satellite is still sunlit but the area of Earth below the satellite is dark. The first few 12-wavelength sets may occur before the Sun comes into the direct view of the diffuser. Typically, eight to nine sets of measurements at the 12 preselected wavelengths are then made of the solar radiation between the time the solar rays are visible below the satellite to when the Sun passes out of the view of the diffuser. The diffuser plane is oriented so as to keep terrestrial radiation, including the bright terrestrial limb, out of its direct view. These measurements occur between 6 and 9 UT, and the 7-, 14-, and 28-day structure in the schedule of observations shows up as a very small, fine structure in the solar zenith angle. While the solar zenith angle has large daily and small annual variations, the solar azimuth angle in the spacecraft-centered coordinates has small daily and large annual variations.

3.4. Photometer Intensity Output

Figure 3.4.1 shows the raw output for SBUV2 measurements of the flux near the Mg II h and k lines in the discrete-wavelength mode at the longest wavelength of the 12 wavelength steps, the first step at which flux measurements are made in each series of 12 wavelengths. The gaps in May and August are caused by problems in reading the data tapes at the time these figures were made. Most of the data for May has been recovered but the data for August 10–31, 1987 have not. The measurements made daily at this wavelength typically include eight measurements. Measurements before and after the diffuser was sunlit are not included. The first sunlit measurement usualy has the highest raw output because the solar zenith angle is smallest, the angle of incidence on the diffuser is smallest, and the diffuser reflectance effi-

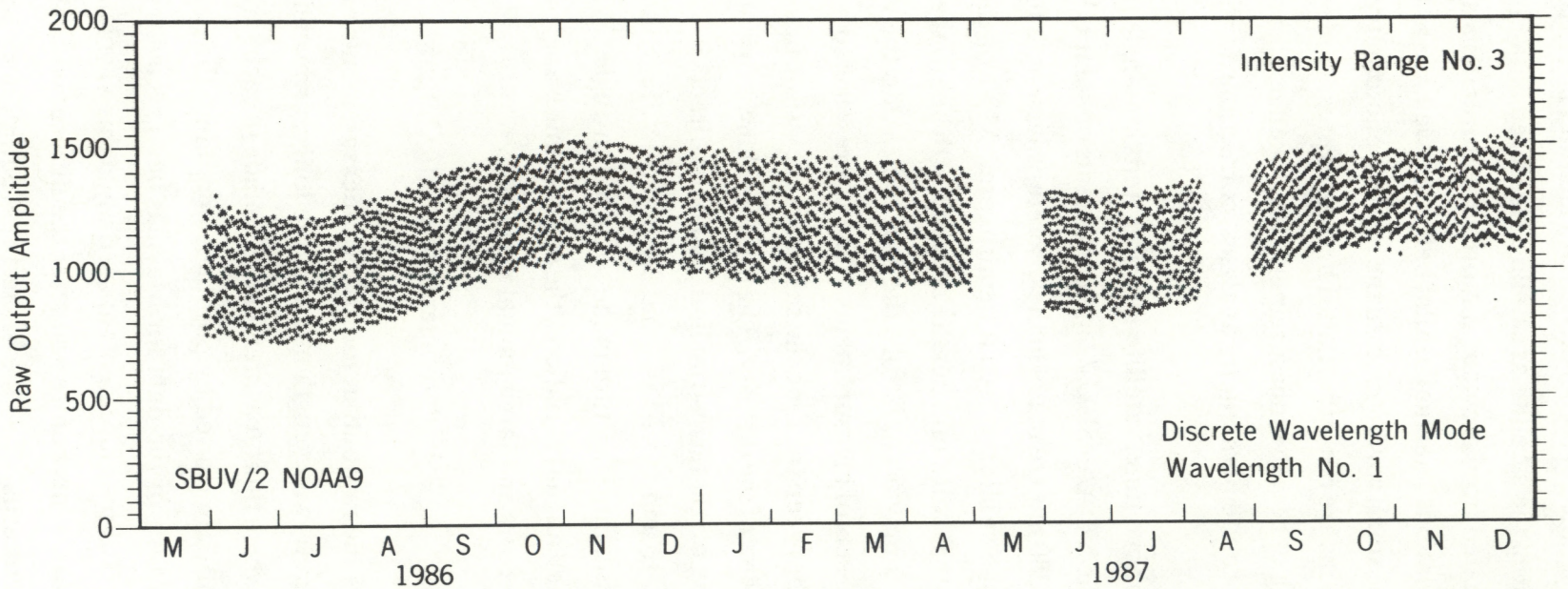

Figure 3.4.1. Raw output versus time for wavelength No.1, the longest wavelength, for the discrete-wavelength mode measurements of the solar flux in the Mg II h and k lines. The gaps in the data were caused by problems in reading the data tapes; these problems were solved later, in most cases.

ciency is highest. The raw output decreases monotonically for the other measurements, the last being the lowest as the solar zenith angle increases and the diffuser reflectance decreases. So the daily changes in angle of incidence on the diffuser during the time span (< 5 minutes) of these measurements cause the thickness of the group of data in Figure 3.4.1 and similarly in Figures 3.4.2-3.4.18.

There is an annual variation in the raw output seen in all of the figures in this section. A maximum occurs in November and a minimum occurs near summer solstice (near the end of June); the maximum is more than 20% higher than the minimum. Only 6.7 % of the variation can be due to the annual variation in the Sun-Earth distance; most of the observed annual variation is caused by the annual changes in angle of incidence on the diffuser (see Figure 3.3.3). The peak azimuth angle in the spacecraft-centered coordinates occurs in late June and early July, which fits with the annual minima seen in Figures 3.4.1–3.4.18. The rapid decrease in azimuth seen in Figure 3.3.3 from August through October would cause an increase in the solar angle of incidence on the diffuser, which is consistent with the rapid rise in output intensity at those times as seen in Figures 3.4.1–3.4.18. The longer-term drift in azimuth angle, evident in Figure 3.3.3 by the lower values in October–November 1987 compared to those months in 1986, also shows up in Figures 3.4.1 in the form of slightly higher raw output values, especially for the last or lowest value each day.

All the values plotted in Figures 3.4.1–3.4.17 are the recommended-range values, the only values available in the wavelength sweep mode, but we also have available in the data tapes the separate concurrent outputs for ranges 1, 2, and 3 in these discrete-mode data. Sometimes the recommended-range values are range-3 values, while at other times they are range-2 values; for certain wavelengths they switch back and forth from range-2 to range-3 values. The range labels in Figures 3.4.1–3.4.17 apply to the main group of data points, well displayed in the figures and may not apply to some of the scattered isolated points.

The main group of points in Figures 3.4.1–3.4.3, 3.4.5, 3.4.13, 3.4.14, and 3.4.16 are intensity-range-3 values. No values below 700 are shown because range-3 values are no longer recommended in those cases, although they exist in the separate file of range-3 values. Most of the scattered, isolated points in these figures are range-2 values that have overflowed their digitizer; they should be corrected by adding $2^{16}-1$ to them. This switch in pre-programmed recommended values clips off the bottom of the data pattern; however, in our analyses of these data in the next chapter we have avoided using the recommended-range values and have used both range-2 and range-3 values regardless of whether they were recommended. The scattered, overflowed range-2 points in the graphs showing primarily recommended range-3 values occur

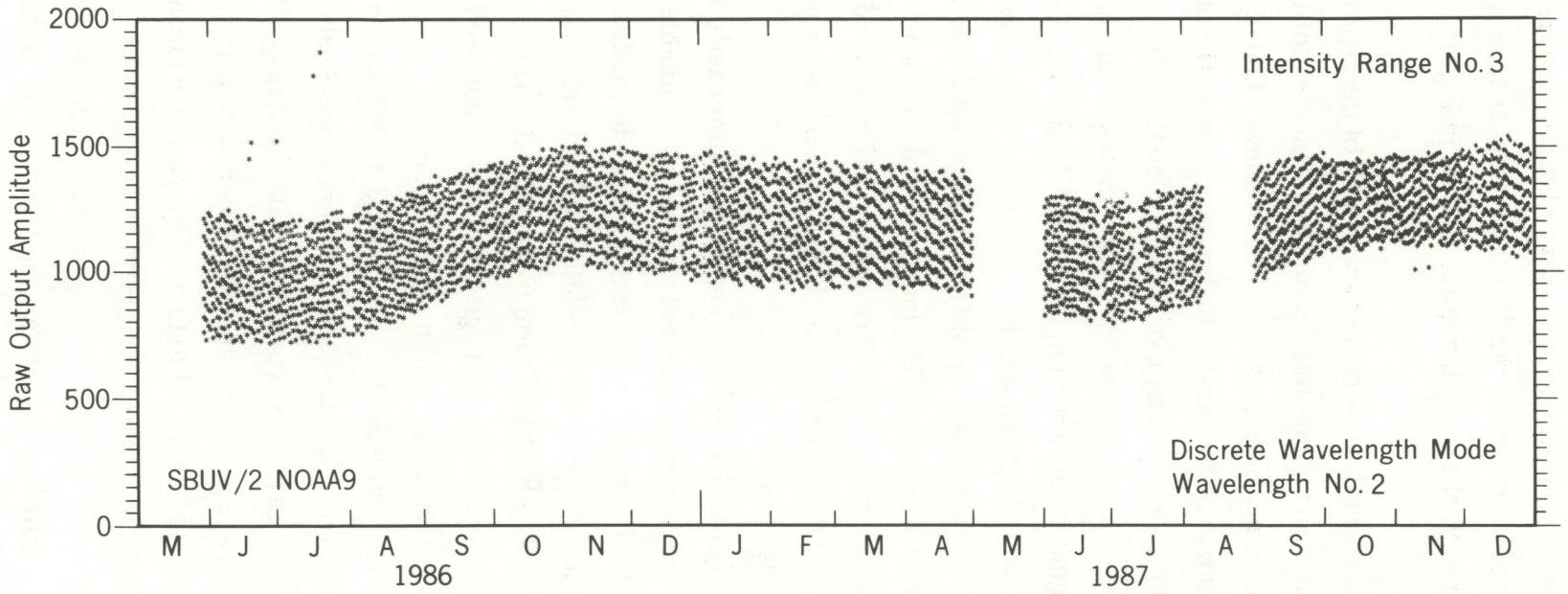

Figure 3.4.2. Output intensity versus time for wavelength No. 2 in the quasi-continuum at wavelengths just longward of the Mg II *h* and *k* absorption lines.

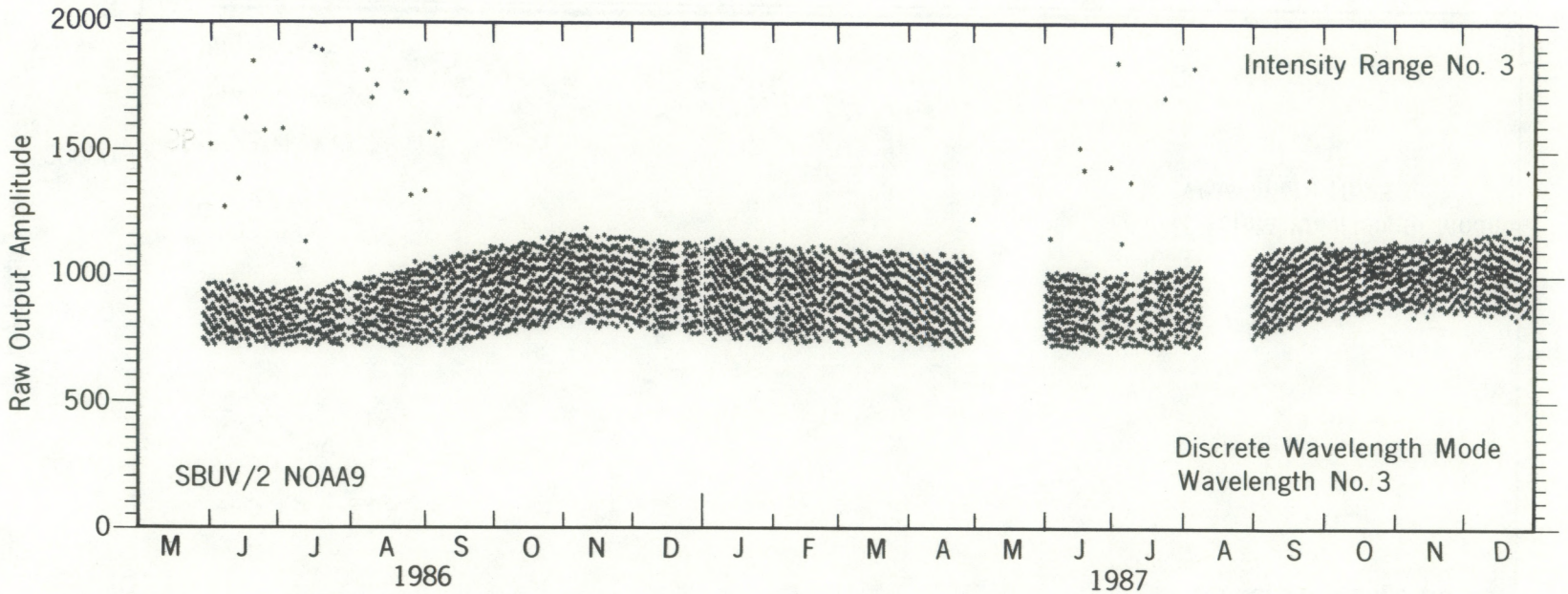

Figure 3.4.3 Output amplitude versus time for wavelength No. 3 in the upper portion of the long-wavelength wall of the solar Mg II *h* and *k* absorption lines. The amplitude scale was chosen to illustrate the range-3 values.

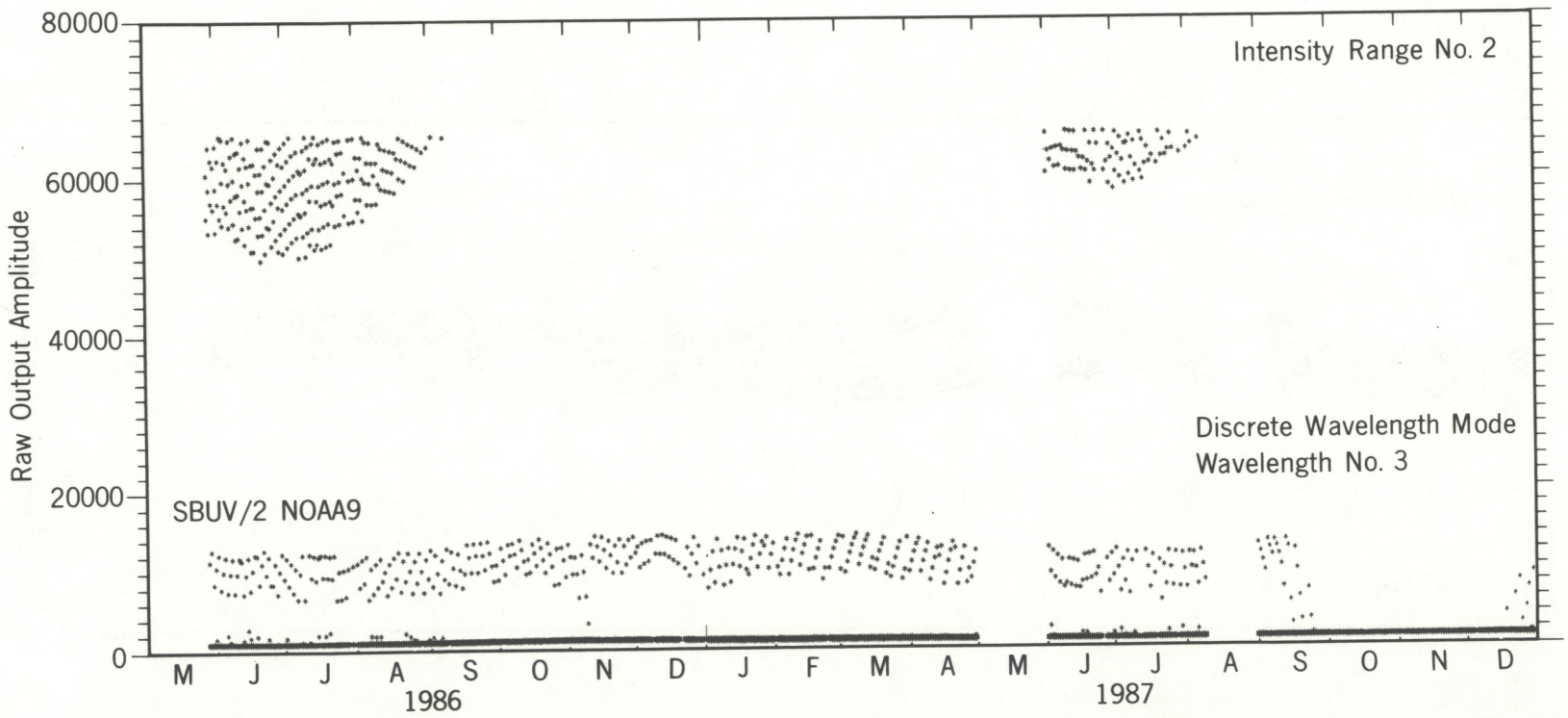

Figure 3.4.4. Output counts versus time for wavelength No. 3. This amplitude scale was chosen to illustrate the range-2 values. The range-3 values shown in the previous figure form the thick, flat line just above the bottom border of this figure. The group of points in the 5,000–14,000 range constitute mystery group *X*.

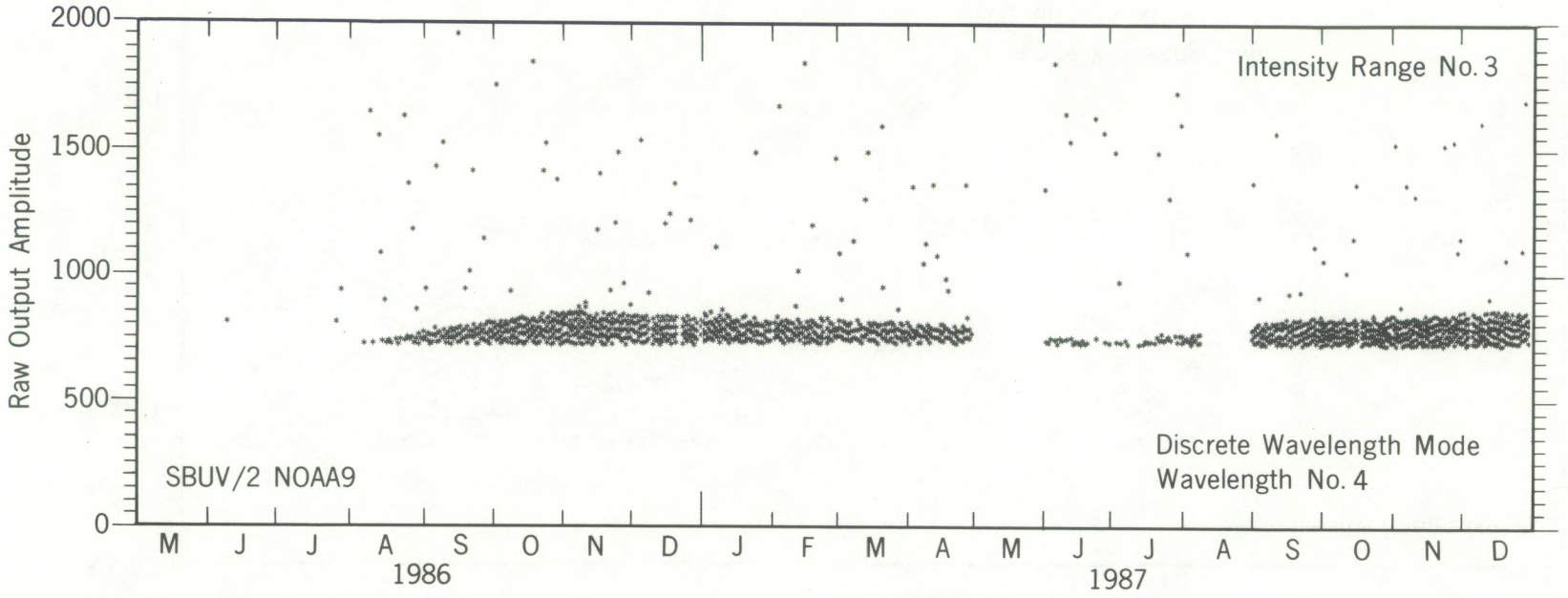

Figure 3.4.5. Output versus time for wavelength No. 4, which is located near the middle of the long-wavelength wall of the Mg II *h* and *k* absorption lines, where the amplitude variation is quite steep. The nearly solid groups of points are range-3 values. The highly scattered points are range-2 values where the range-2 counter has overflowed and started over.

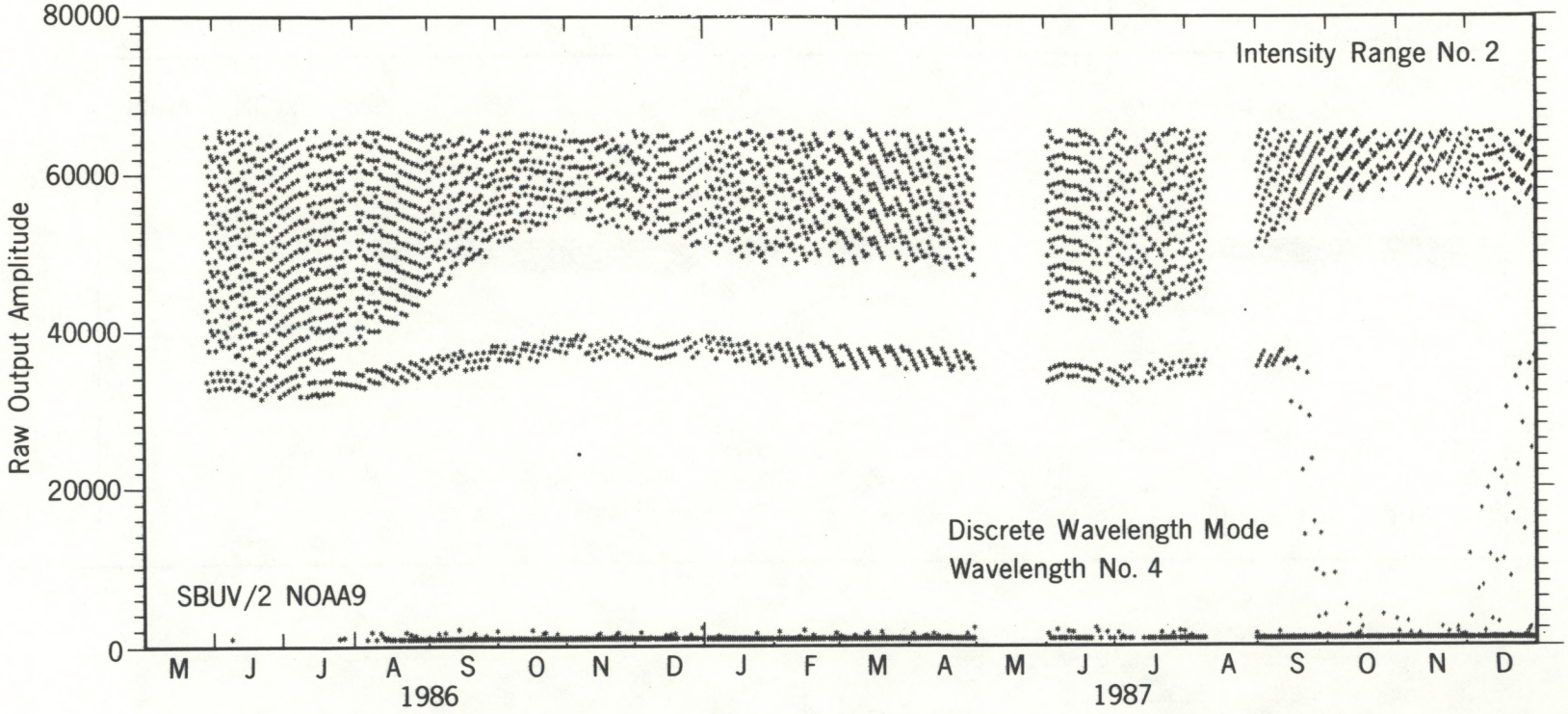

Figure 3.4.6. Raw output versus time for wavelength No. 4 with an amplitude scale for illustrating range-2 values. The row of points with amplitudes near 35,000 are mystery group *Y*. Note that this group drops to low values in October and November 1987.

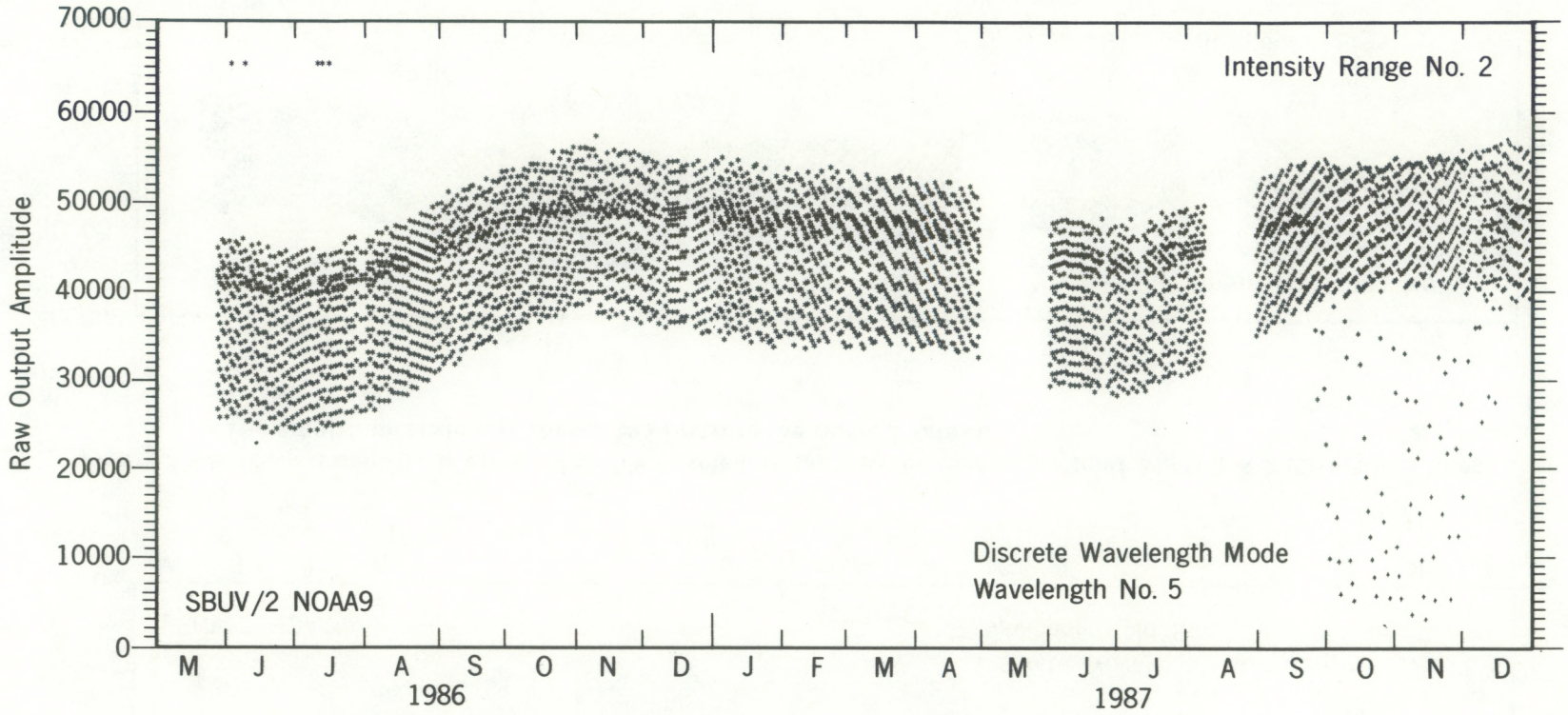

Figure 3.4.7. Output versus time for wavelength No. 5, which is near the steepest variation with respect to wavelength in the long-wavelength wall of the Mg II *h* and *k* absorption lines. The darkened group of points ranging from 1/3–1/5 down from the top of the main set of data points are mystery group *Z*. This latter group breaks into a scatter of low values in October through mid-December 1987.

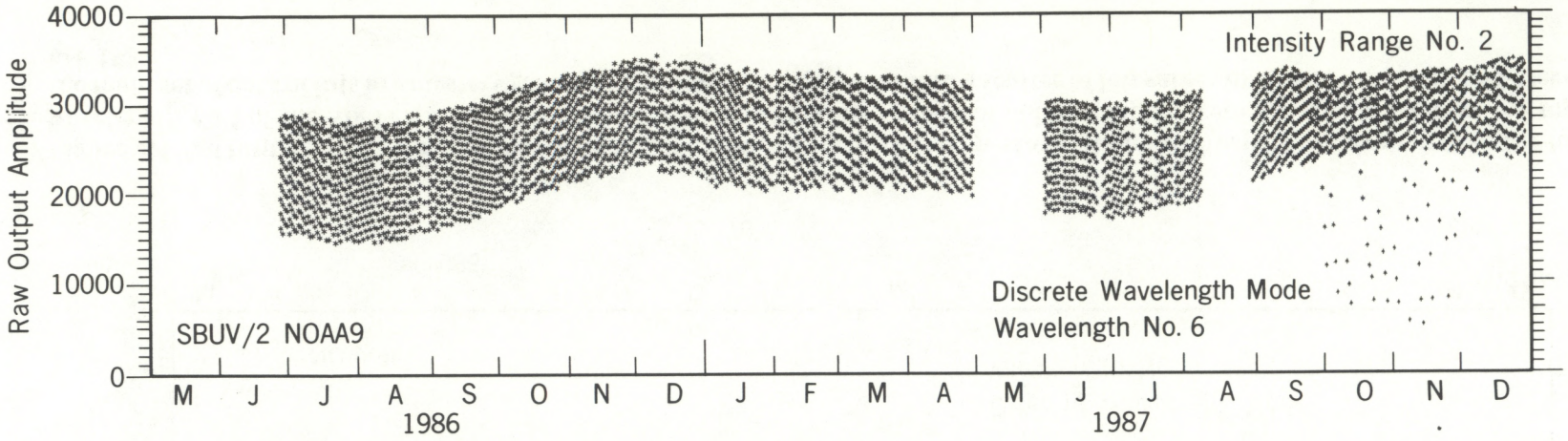

Figure 3.4.8 Output amplitude versus time for wavelength no. 6 in the core of the solar Mg Ii h & k absorption lines. The amplitude scale was chosen to illustrate the range 2 values.

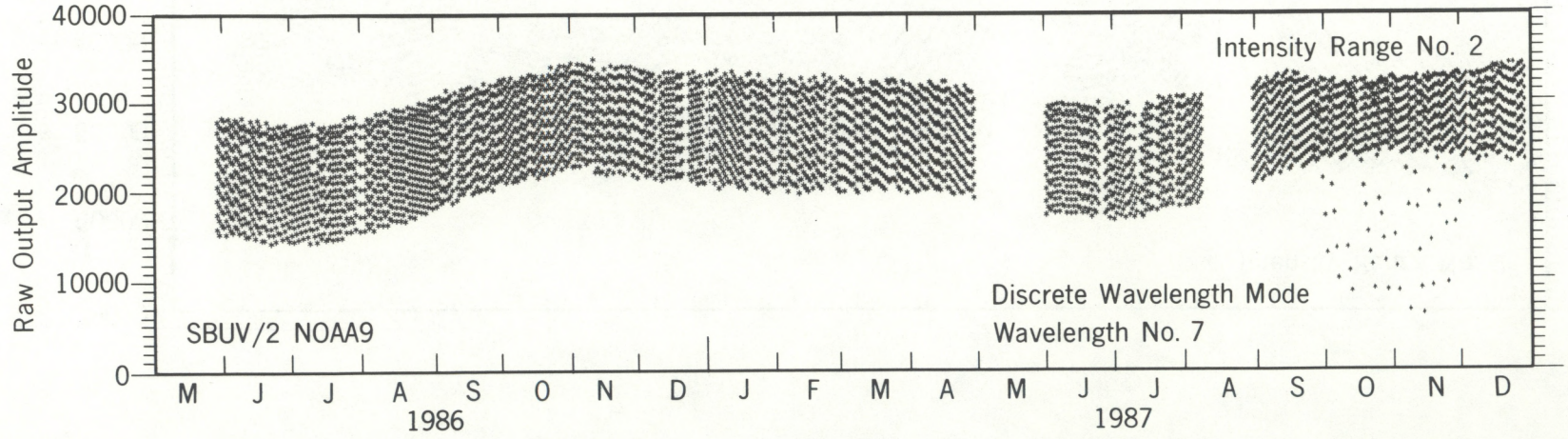

Figure 3.4.9. Output counts versus time for wavelength No. 7 at the center of the Mg II *h* and *k* absorption lines.

mainly during times when the truncation near 700 at the lower edge of range-3 values is occurring.

Figures 3.4.7–3.4.11 show only range-2 values. All of the recommend measurements at these wavelengths are range-2 values. The range-1 values are saturated and the range-3 values are small and noisy. Figures 3.4.4, 3.4.6, 3.4.12, 3.4.15, and 3.4.17 show a mixture of range-2 and range-3 values; the data that are well displayed are range-2 values and the solid, flat lines just above the bottom border are range-3 values that are better displayed in adjacent figures. The range-2 values in these figures do not rise above $2^{16} - 1 = 65{,}535$ because the digitizer for range-2 had overflowed. A few of these overflowed values appear as isolated points near the range-3 lines along the bottom border but do not extend higher than that because the recommended-range values are then switched to range-3 values. In Figures 3.4.7, 3.4.11, and 3.4.17 there are a few isolated bad-data points at the digitizer overflow level of 65,535. We do not know why this rare fault occurs, but these bad points are easily identified.

Keeping in mind the approximately $\times 104$ relation between range-2 and range-3 values, the digitizer overflow effect on range-2 values, and the switch near this overflow level from range-2 to range-3 as the recommended-range values, when viewing Figures 3.4.3–3.4.6 and 3.4.12–3.4.17, then the main patterns common to Figures 3.4.1–3.4.17 are the following: (1) a large daily decrease among the daily values caused mainly by the change in solar zenith angle (Figure 3.3.2) during the 4–5 minute recording period; (2) a large annual variation and a long-term increase caused mainly by the annual variations and long-term trend in the solar azimuth angle in the spacecraft-centered coordinates (Figure 3.3.3) and secondly by the annual Sun-Earth distance variation and instrument sensitivity drift, respectively; and (3) a small 7- and 14-day structure seen in the fine structure, caused by the similar structure in the solar zenith angle that is generated by the combination of observing schedules and orbit progressions.

The most important thing about these figures is what they do not show. There is no large, long-term decrease caused by diffuser degradation; any such effects are small, although not necessarily negligible. The daily and annual variations were described as large because they are large in comparison to the solar variations we are trying to measure, based on knowledge gained from NIMBUS7 (Heath and Schlesinger, 1986).

The remaining puzzles in these data involve the following features:

(1) In Figures 3.4.1 – 3.4.3, 3.4.7–3.4.11, 3.4.14, and 3.4.16, following along the top edge of the main ribbon of data, the top edge appears to be missing from mid-September through November in 1987, i. e. the first values of the daily set of measurements are lower than the

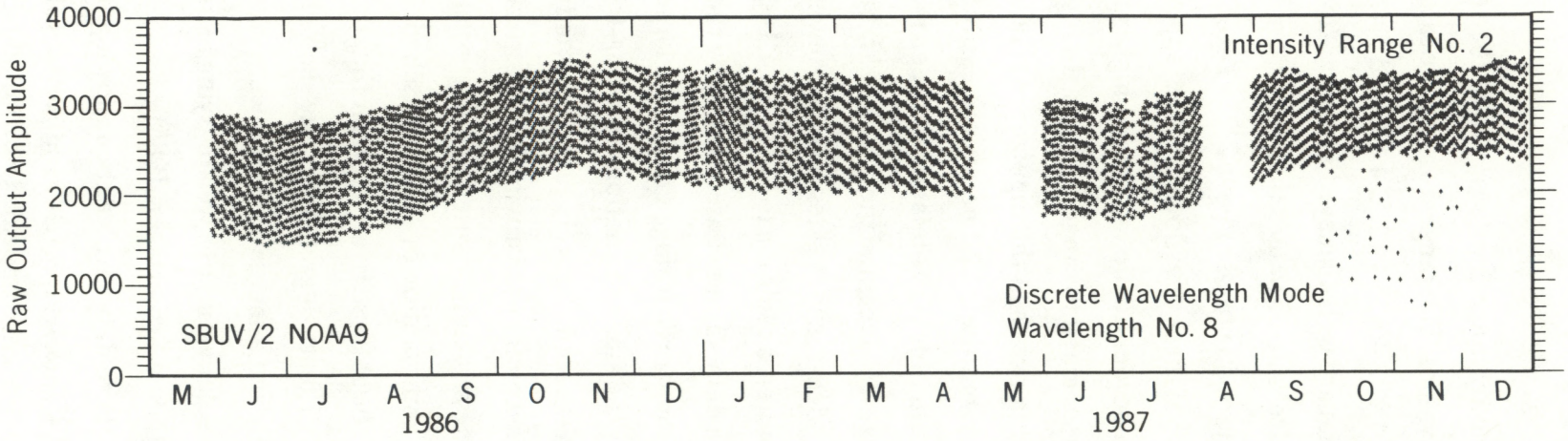

Figure 3.4.10. Output intensity versus time for wavelength No. 8 in the core of the Mg II *h* and *k* absorption lines.

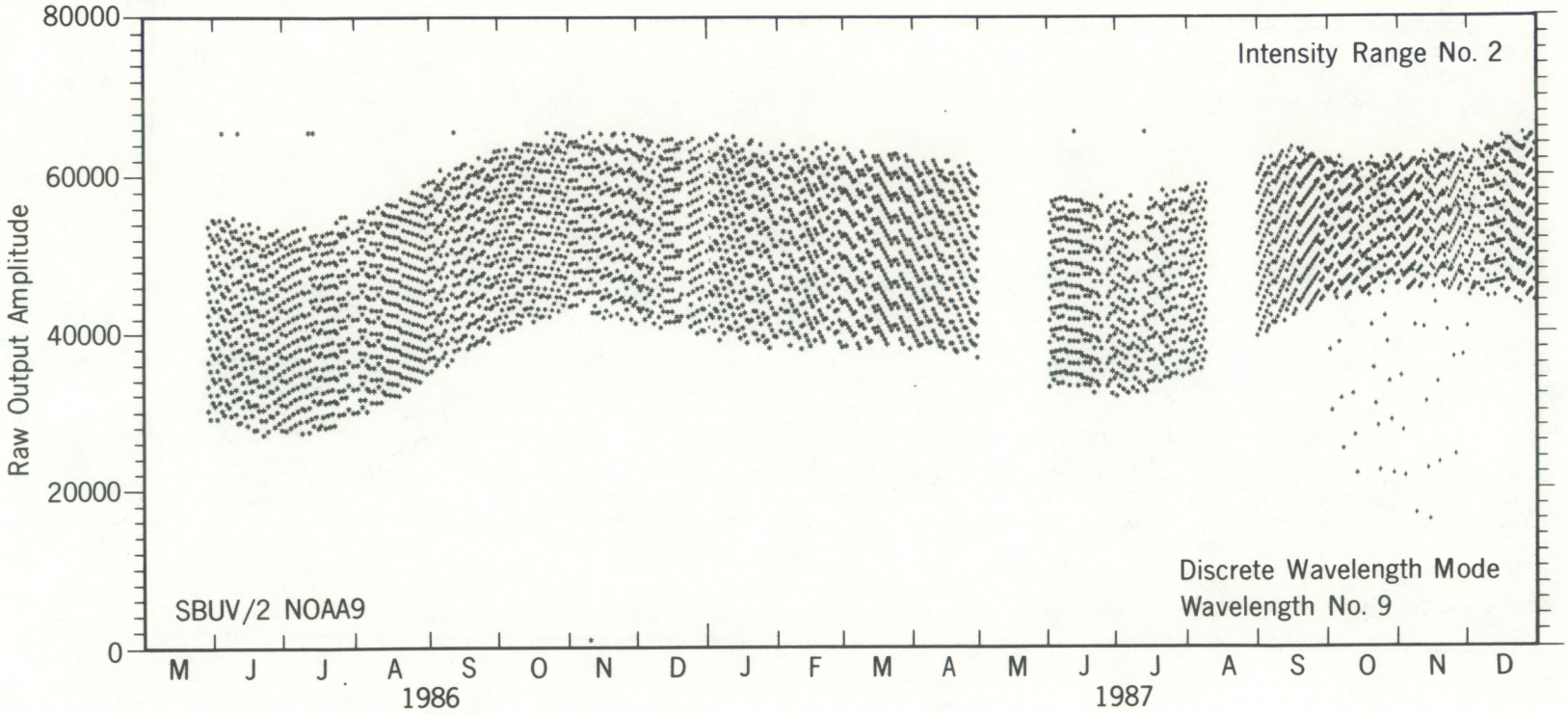

Figure 3.4.11. Raw output versus time for wavelength No. 9 near the middle of the short-wavelength wall of the Mg II *h* and *k* absorption lines.

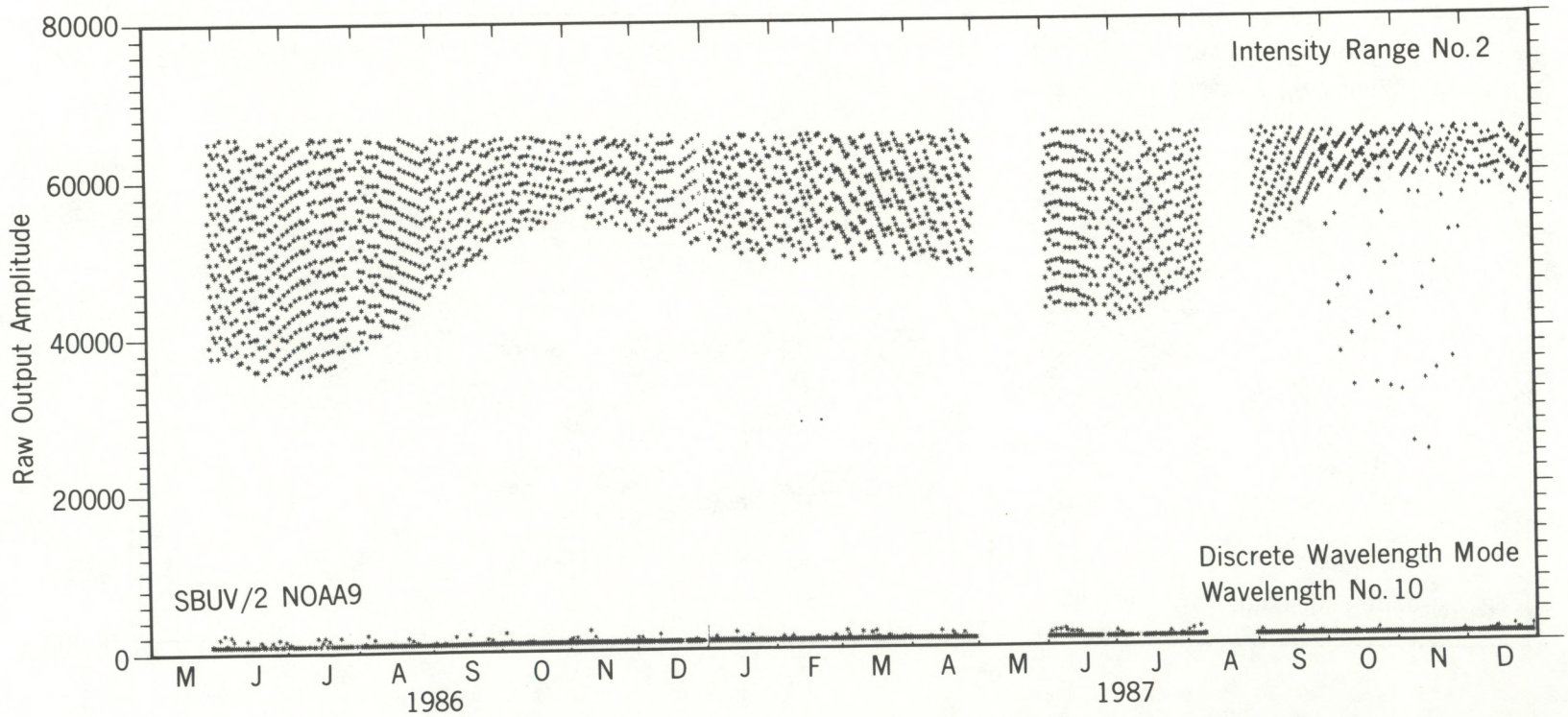

Figure 3.4.12. Output amplitude versus time for wavelength No. 10 in the short-wavelength wall of the Mg II h and k absorption lines. This intensity range illustrates the range-2 values. The range-3 values form the thick solid lines just above the bottom border.

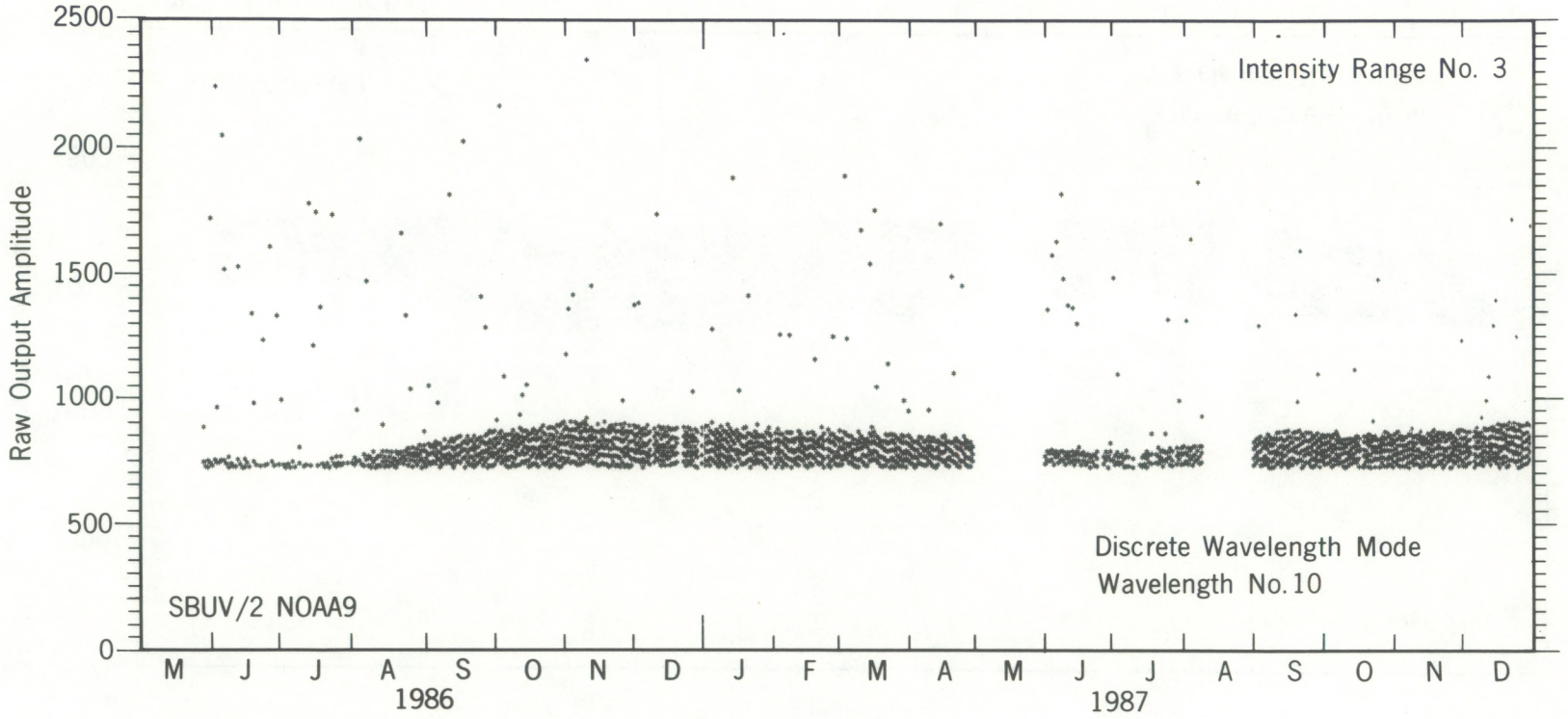

Figure 3.4.13. Output intensity versus time for wavelength No. 10. The nearly solid groups of points are range-3 values. The scattered isolated points are range-2 values where the counter overflowed.

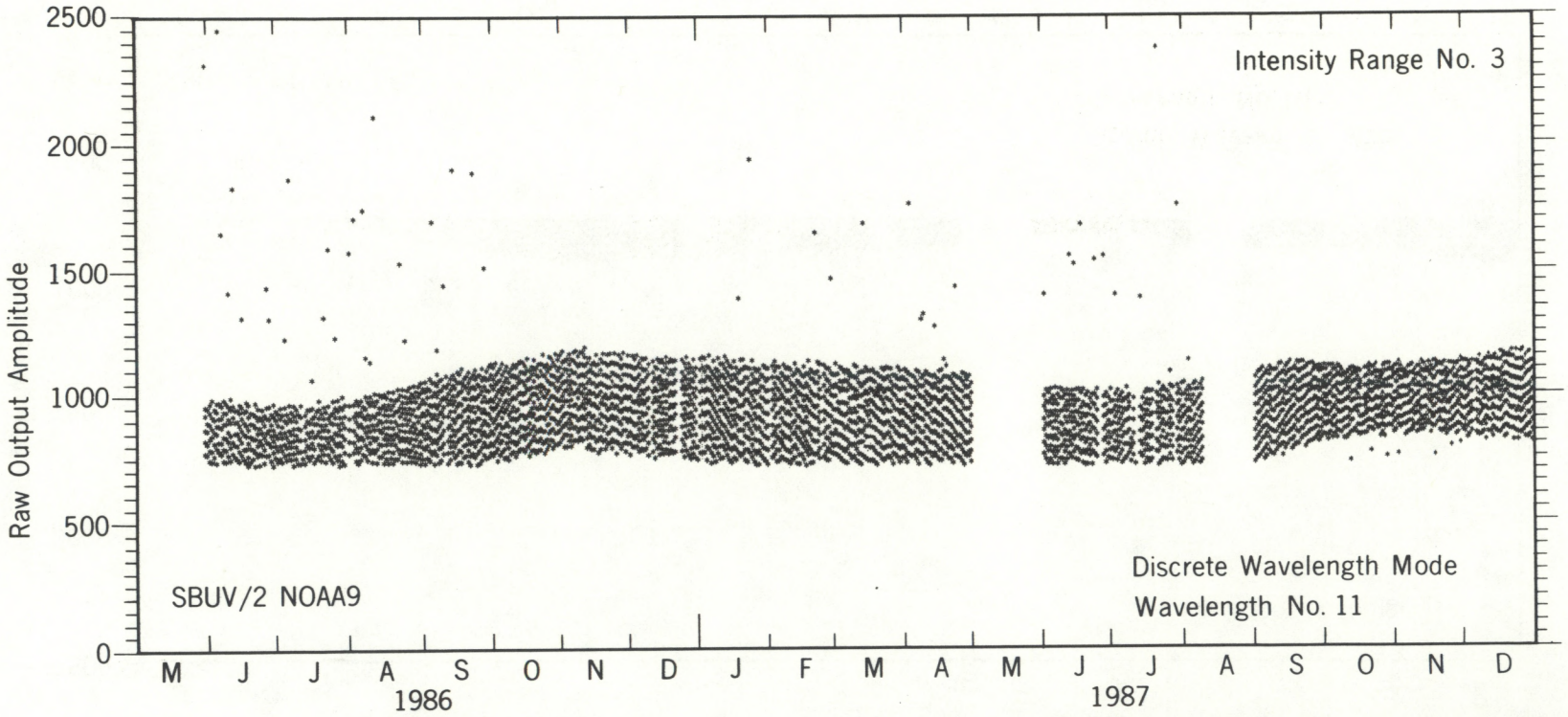

Figure 3.4.14. Raw output counts versus time for wavelength No. 11 in the far short-wavelength wing of the Mg II h and k lines and quasi-continuum adjacent to the lines. While the nearly solid groups of data points are range-3 values, again the scattered isolated points are range-2 values where the counter overflowed.

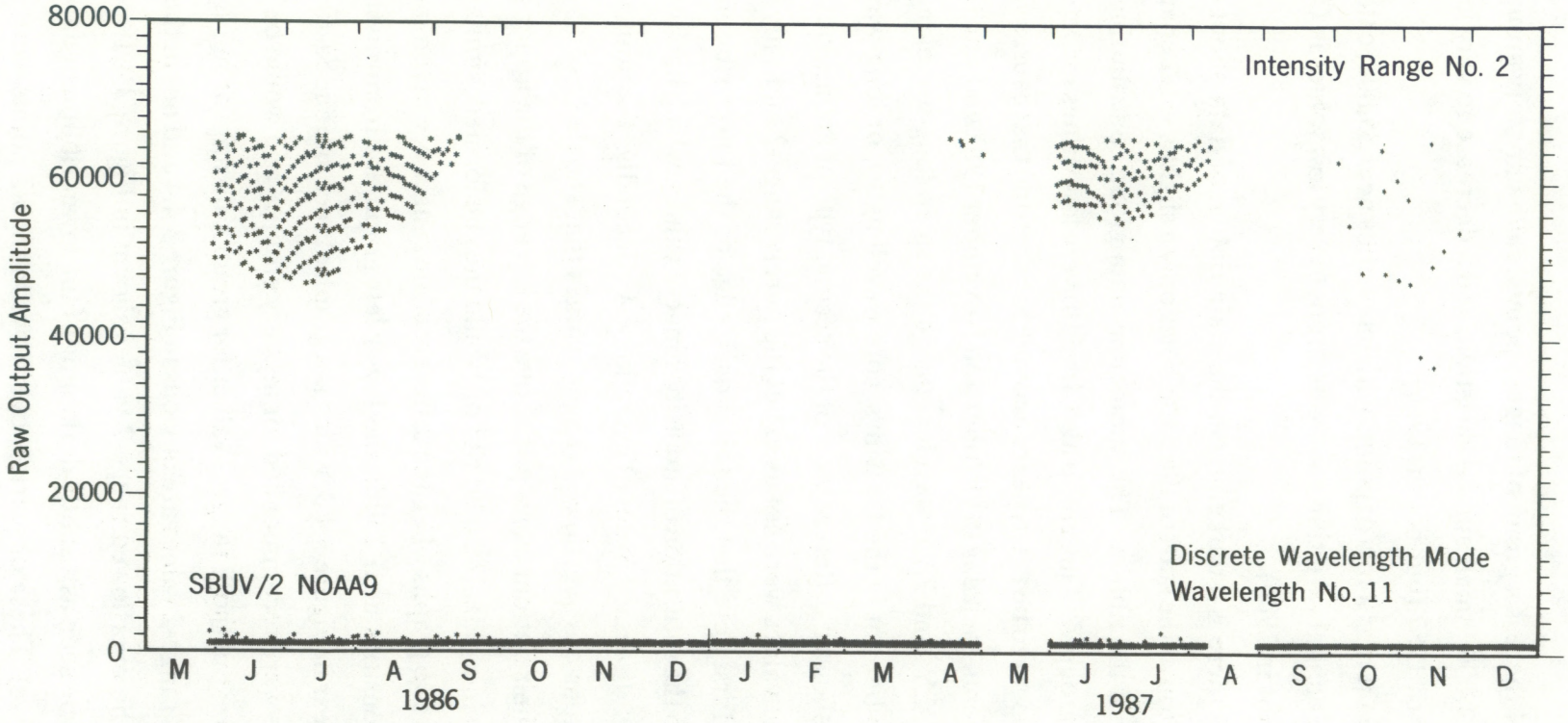

Figure 3.4.15. Output amplitude versus time for wavelength No. 11, where the ordinate scale was selected to display the range-2 values that were offscale above the top of the previous figure. The solid, flat lines just above the bottom border are the range-3 values that are displayed much better in the previous figure. The scattered points from range-2 values that appear in Figure 3.4.14 are seen here as isolated points just above the solid lines of range-3 values. Adding the counter overflow value of 65,535 to these points would place them at the top edge of the main group of range-2 points.

second values and sometimes appear as isolated scattered points below the main ribbon of data.

(2) In Figure 3.4.4 there is a group of range-2 points, called mystery group *X*, with intensities from 5,000 to 14,000, small annual variation, and a decrease to very low levels in October and November of 1987 (but not in 1986).

(3) In Figure 3.4.6 there is a row of points with intensities near 35,000, called mystery group *Y*, that has a small annual variation and again drops to very low values in October and November 1987 (but not in 1986).

(4) In Figure 3.4.7 there is a darkening in the main ribbon of data about one-fifth of the way down from the top at the start of the data; it has only a slightly weaker annual variation than that of the rest of the ribbon. The anomalous data group contributing to the darkening is called mystery group *Z*. This group also drops to very low values in October and November 1986. There appear to be two types of anomalies here: one that causes very low values in the first measurements each day in October and November 1987 and one that causes early values to be low (X,Y, and Z) at wavelengths on the steep long-wavelength wall of the solar absorption line but not in the far wings, core wavelengths, or long-wavelength wall.

Figure 3.4.18 shows a different view of the second type of anomalous data, where the recommended-range values were not used but the purely range-2 and only range-3 values were used separately. First note that the thick, dark edge of the lower ribbon in the graph at the upper left is due to the saturation of intensity-range-2 values, which has not been shown in previous graphs but is discussed in detail in section 4.4. Secondly, the points in the lower groups in the top two graphs are overflowed range-2 values that should have 65,535 added to them; this would place their bottom edges just above the top edge of the upper groups of points. A wide and roughly sinusoidaal shaped ribbon would thus be formed, similar in shape to the ribbon in the bottom two graphs when the different scale ranges are taken into account. The row of points with intensities near 150 in the lower left graph are from mystery group *X*. These points do not appear in Figure 3.4.3, which is a graph of recommended-range values, because the range-2 values were recommended for mystery group *X* and would be far off the top of the scale for that figure; but those range-2 values for group *X* do appear in Figure 3.4.4. The reason these group-*X* range-2 values are obvious in Figure 3.4.4 and not in the upper left graph in 3.4.18 is that all the overflowed range-2 values shown in Figure 3.4.18 obscure the group-*X* points, which can be seen as a subtle darkening of the lower ribbon of data points at about the 10,000 intensity level. These obscuring, overflowed range-2 points were not shown in Figure 3.4.4 because their range-3 counterparts were the recommended-range values. No compara-

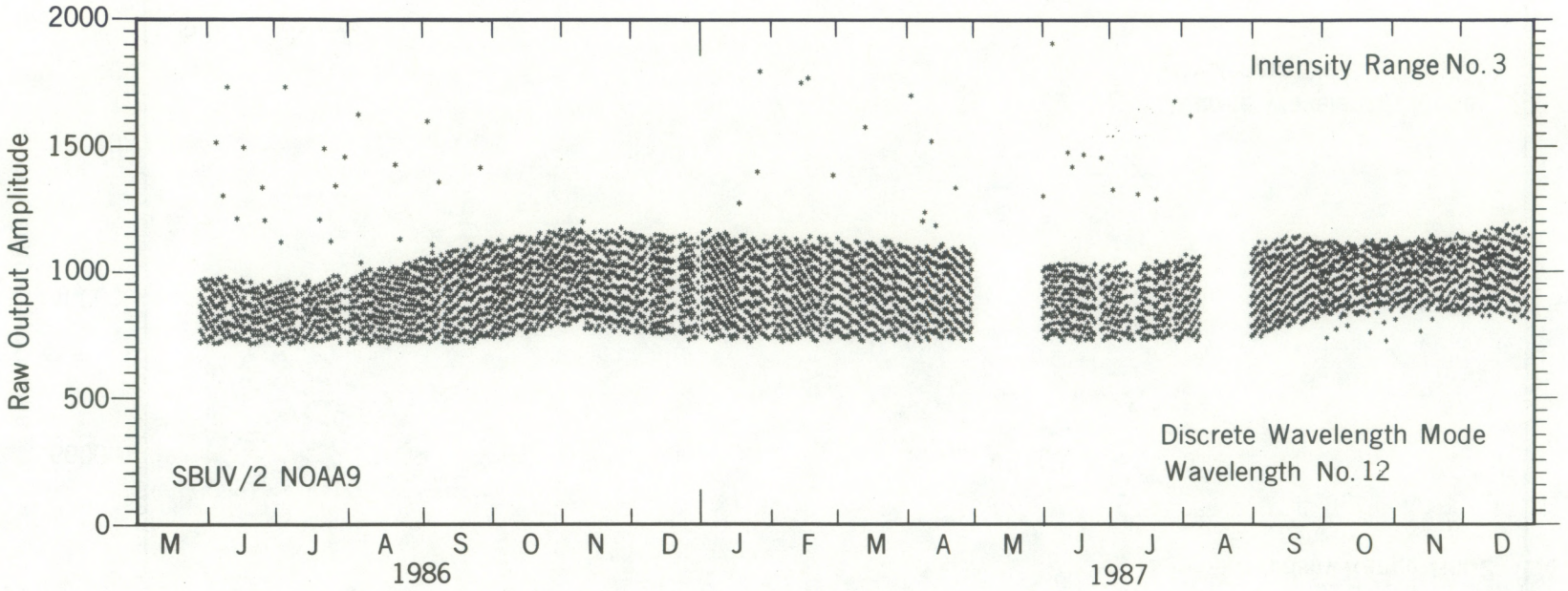

Figure 3.4.16. Temporal dependence of the output magnitude for wavelength No. 12 in the quasi-continuum at shorter wavelength than the Mg II *h* and *k* lines.

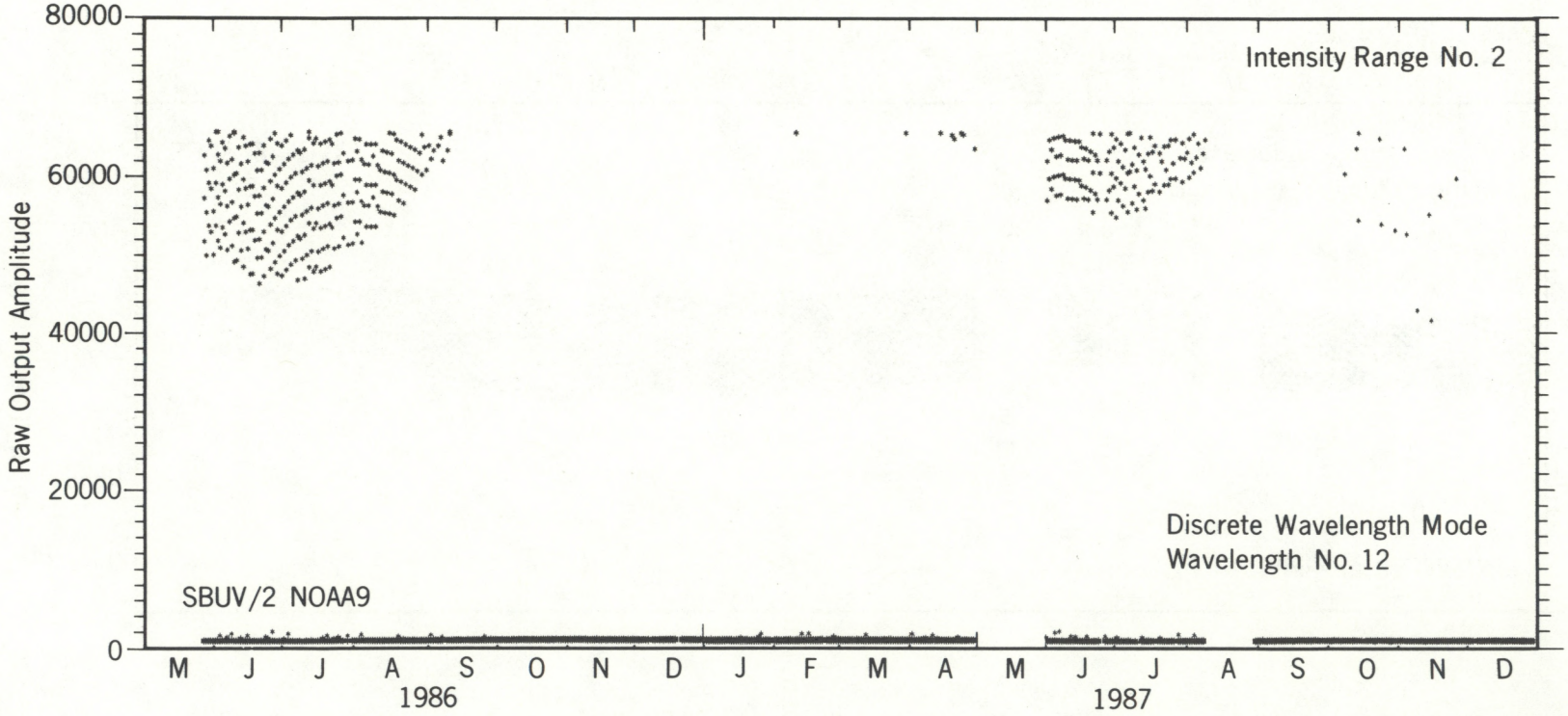

Figure 3.4.17. Temporal dependence of the output intensity for wavelength No. 12, showing the range-2 values that were off scale in the previous figure.

ble anomalous points are evident for wavelength 10, which is located at nearly as high intensity in the short-wavelength wing of the combined Mg II h and k absorption lines as wavelength 3 is in the long-wavelength wing.

The explanation for both of these anomalies comes from their timing, rather than from their wavelength dependence; from the partial occultation of the Sun for the first few measurements; and from our selection of what data to consider as solar radiation and what data to plot. Our current qualitative explanation of the *XYZ* mystery groups is as follows. As the Sun begins to clear the edge of the satellite or the baffles near the diffuser (it is not known which edges limit the view of the spectrometer), the intensity value is not plotted until the recommended range switches from range-1 to 2. This consistently happens after wavelengths 1 and 2 have been sampled, so those low values for LW1 and LW2 are not plotted and are never used because they are interpreted as not being observations of solar radiation. Consequently, Figures 3.4.1 and 3.4.2 have no anomalous low points. Usually the first daily sample interpreted as solar radiation because the recommended range has switched to range-2 is on wavelength No. 3; but apparently the full Sun is not yet in view and the output is consequently anomalously low, which contributes a point to mystery group *X* in Figure 3.4.4. The first sample for wavelength No. 4 occurs 2 seconds later, and the Sun is less occulted but still enough so that the raw output is low compared to that during the next set of 12 wavelengths. This explains why mystery group *Y* is significantly higher relative to the main group of points in Figure 3.4.6 than is group *X* relative to the main group of points in Figure 3.4.4. Similarly the first value interpreted as solar radiation for wavelength 5 is 2 seconds later; the Sun is nearly in full view; and the values in group *Z* are only slightly lower than the highest values in Figure 3.4.7, where the highest values are measured in the next discrete-mode set. By the time the sixth and later wavelengths are measured, the Sun is in full view and there are no anomalously low points. So the apparent peculiar wavelength dependence of the *XYZ* mystery groups is interpreted as a consequence of the time sequence of the measurements. The uniformity of the *XYZ* mystery points is a consequence of the consistent scheduling of these solar discrete-wavelength measurements to achieve quite specific ranges in solar angles in the spacecraft-centered coordinates.

It is our understanding that a solar panel unexpectedly occulted the Sun in October and November 1988. Those months correspond to the annual minimum in the solar azimuth angle in the spacecraft-centered coordinates(see Figure 3.3.3). Considering the year-to-year downward trend in that angle, then if all the solar measurements were blocked for azimuth angles near 26° perhaps this same structure caused a change in the solar rays reaching the diffuser plate for azimuth angles near 33° and zenith angles near 88° in October and November 1987.

The scattered low points in October and November 1987 may have occurred because some satellite structure, perhaps this same solar panel, occulted part of the Sun in the first set of the measurements of the Mg II *h* and *k* lines in the discrete wavelength mode but did not obscure later sets. This would explain why the *X*, *Y* and *Z* mystery points are so strongly affected in October and November 1987; they are, respectively, the first three measurements interpreted as solar radiation and are therefore more affected than wavelengths 1 and 2, which come from a later 12-wavelength set. The reduction of the number of discrete-mode data sets not affected by the solar panel causes the main ribbon of data in Figures 3.4.1–3.4.3, 3.4.7–3.4.11, 3.4.14, and 3.4.16 to decrease in width, the top edge coming downward in October and November 1987. So there is a progression in how low these anomalous scattered points are from wavelength 3 through 12, then to 1, and finally 2, because of the order in timing of the measurements and our selection of which data are measures of solar radiation.

Both types of problem data can simply be deleted from further analyses. If our qualitative interpretations are correct, the causes of the problem data should not affect what we have identified here as the normal group of data; but these interpretations have not been proven quantitatively because we lack information on the satellite structure outside of the SBUV2 instrument.

In summary, studying the raw data has helped improve our understanding of the measurements, including distinguishing between good solar measurements and problem data that should be excluded from further analyses of solar flux. It is now easy to identify which range-2 values have overflowed the digitizer and should have $2^{16}-1$ added to their values. In the future, we will avoid using the recommended-range values and we will use both the separate range-2 and range-3 values and decide which is best for a particular application. The large daily variation in the good raw output is caused mainly by the daily change in solar zenith angle and the consequent change in angle of incidence on the reflectance diffuser and reflection efficiency. The annual variation and at least part of the long-term upward trend in raw- data output is caused by annual and long-term changes in the solar azimuth angle in the spacecraft-centered coordinates.

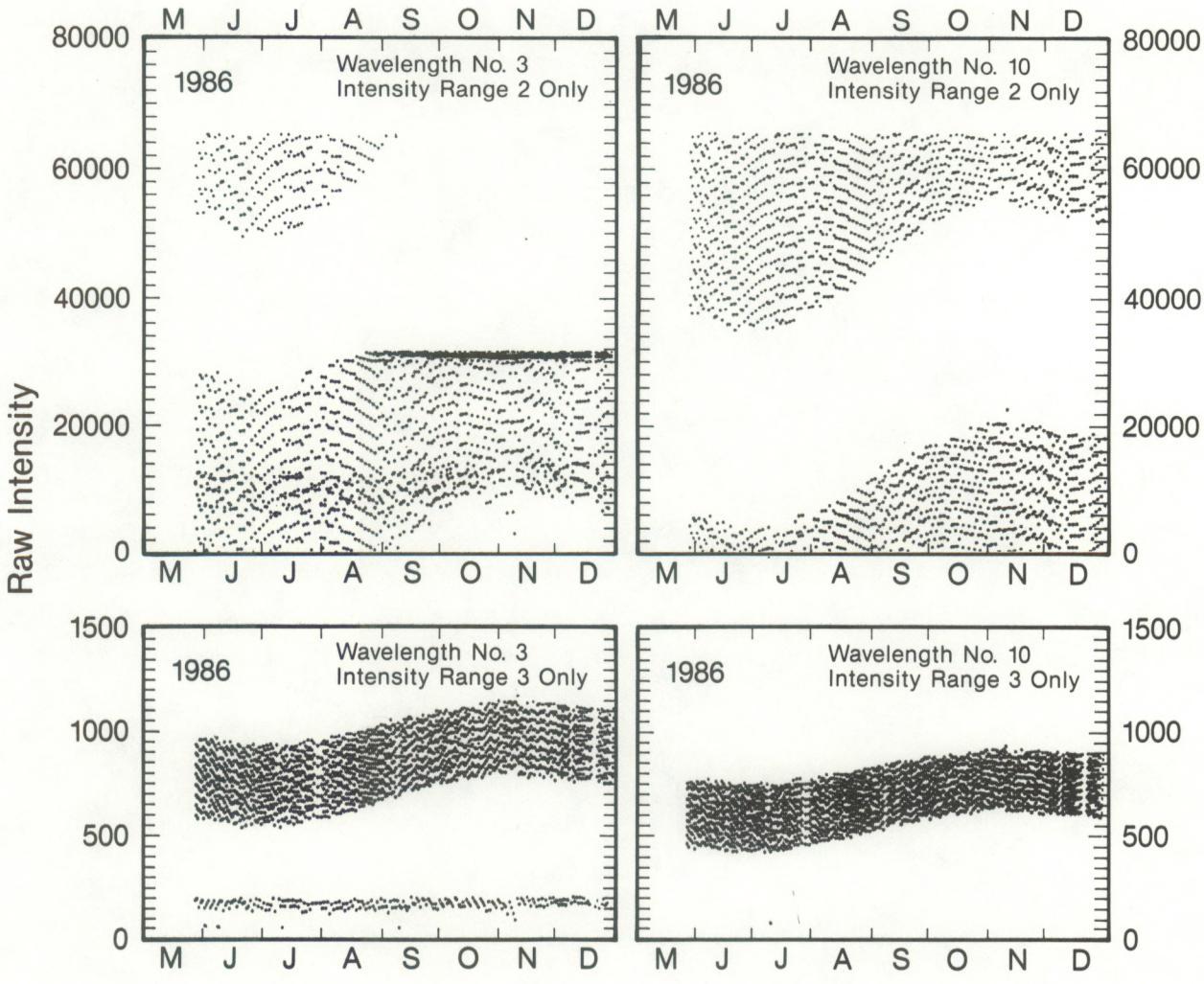

Figure 3.4.18. Output amplitudes for wavelengths 3 and 10 in the long- and short-wavelength walls of the Mg II h & k absorption line pair. Only range-2 values are shown in the top and only range-3 values in the bottom two figures. For both of the top figures, the group of data points in the lower half of the figure have overflowed a digital counter and should have 65,535 added to them, which would move the group upward so their bottom edge fits just above the top edge of the group of points in the 40,00–65,535 range. The row of low points in the range-3 values for wavelength-3 are mystery group X.

4. ANALYSIS OF Mg II h and k LINE MEASUREMENTS IN THE DISCRETE-WAVELENGTH MODE

4.1. Definition of the Mg II Core-to-Wing Ratio

Heath and Schlesinger (1986) defined, by the following equation, the center-to-wing ratio for the Mg II h and k solar absorption lines (not resolved into two lines because the spectrometer bandwidth is too broad) for solar flux measurements made by the SBUV experiment aboard the Nimbus-7 satellite:

$$\frac{R(t)}{MgII} = \frac{4[F(279.8\ nm,t) + F(280.0\ nm,t) + F(280.2\ nm,t)]}{3F(276.6,t) + F(F276.8,t) + F(283.2,t) + F(283.4,t)]} \qquad (4.1)$$

where $F(\lambda,t)$ is the measured solar flux at wavelength λ and time t. The ideas behind this equation include the following:

(a) The core wavelengths in the numerator were selected to have a strong signal of solar variability from the large-percentage variations of the h and k emission cores with changes in solar activity.

(b) The far-wing measurements in the denominator were selected to be close in wavelength to the core of the line and still have very weak solar signals; the combination of (a) and (b) causes the ratio to have a strong solar signal while being insensitive to drifts in instrumentation throughput that are weak functions of wavelength over the range involved in (1).

(c) Three wavelengths at the core provide a small amount of averaging to improve the ratio of the solar variation signal and noise.

(d) For the slight shifts in wavelength that are similar for all three of these wavelengths, the increase in flux output from the outer wavelength that shifts away from the center of the combined h and k lines is partially compensated for by a decrease in flux output of the other outer wavelength, which reduces noise caused by wavelength jitter.

(e) The four wavelengths in the wings provide some reduction of random noise.

(f) The wavelength pairs in the short- and long-wavelength far wings are equally spaced with respect to the center wavelength of the core measurements. This provides an accurate estimate of the background continuum at the center of the combined lines, assuming the background continuum varies approximately linearly with wavelength between these lines.

Figure 4.1.1 shows the approximate wavelength positions for the NOAA9 discrete-wavelength mode measurements for the Mg II h and k lines, in comparison with the higher resolution spectra of Hall and Anderson, after being filtered with a triangular wavelength filter with a half-maximum width of 1.14 nm to approximate the NOAA9 passband. We consider the NOAA9 wavelength scale used here as preliminary; we have not yet completed our analysis of the wavelength algorithm. There may be a slight discrepancy in the wavelength scale for NOAA9 used here, relative to that of Hall and Anderson or to an absolute wavelength scale. Comparing the relative intensities of the three core wavelengths indicates that the cen-

ter wavelength, number 7, counting from the longest to the shortest, must be very close to the minimum or center of the combined h and k lines. The approximate vacuum wavelengths for the discrete-mode measurements of the solar Mg II line are given in Table 4.1.1.

Table 4.1.1. Vacuum Wavelengths in nm for NOAA9 Solar Discrete-Wavelength Mode

No.	Wavelength	No.	Wavelength	No.	Wavelength	No.	Wavelength
1	283.16	4	281.24	7	279.92	10	278.14
2	283.01	5	280.80	8	279.77	11	276.96
3	281.83	6	280.06	9	278.73	12	276.81

Since the wavelength step size for NOAA9 (0.148 nm) differs from that for the Nimbus-7 satellite (0.2 nm), and since their wavelength scales probably are slightly shifted, the wavelengths available in the NOAA9 measurements cannot match those for Nimbus-7 for all the wavelengths in (4.1). Note that the longest wavelength in Table 4.1.1 is closest to the second-longest wave-length in equation (4.1), and the shortest wavelength in Table 4.1.1 is closest to the second-shortest wavelength in (4.1). The wavelength halfway between the shortest and

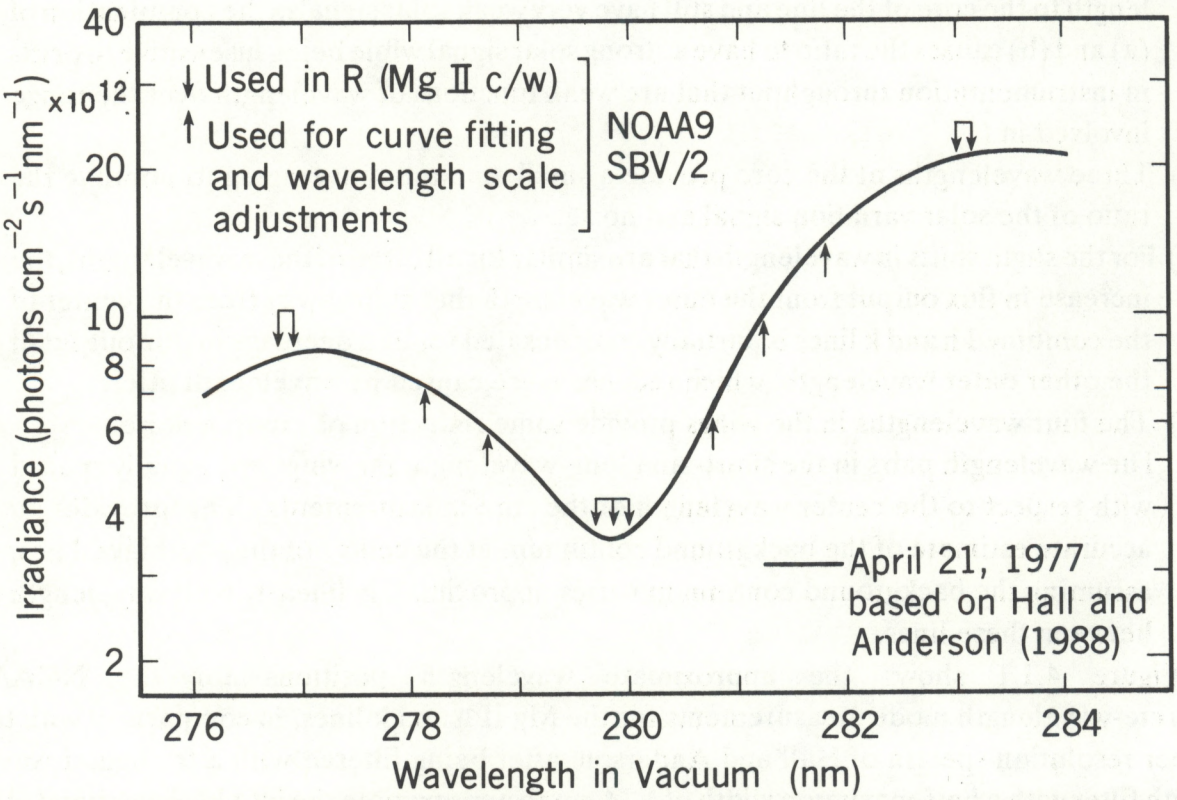

Figure 4.1.1. A spectrum of the Mg II h and k lines filtered with a passband like that on the NOAA9 satellite. The vertical arrows mark the approximate locations of the 12 wavelengths used in the NOAA9 discrete wavelength mode observations. The solid line may be lower in intensity in the short-wavelength wing, relative to that in the long-wavelength wing, than is consistent with the Nimbus-7 or NOAA9 observations. (See §4.6 and 6.2)

longest wavelengths in Table 4.1.1, namely 280.0 nm, matches the center core wavelength for Nimbus-7 (280.0 nm) and is close to wavelength No. 6 in Table 4.1.1; but it does not match wavelength No. 7, the center-of-line wavelength for NOAA9, which is about 0.1 nm shorter than the average of the outer wavelengths. Wavelengths 2 and 12 are approximately equally spaced about No. 7. We have neglected these small offsets in wavelength relative to the original Nimbus-7 values and have used equation (4.2) to approximate (4.1) for the NOAA9 discrete-mode measurements and to explore the quality and characteristics of the NOAA9 data. Later in this chapter we encounter much larger problems than the less than ideal spacing of wavelengths, and eventually adopt a greatly modified ratio. We call the following the Classical Ratio:

$$\frac{R(t)}{MgII} = \frac{4[F(279.8\ nm,t) + F(279.9\ nm,t) + F(280.1\ nm,t)]}{3[F(276.8,t) + F(277.0,t) + F(283.0,t) + F(283.2,t)]} \tag{4.2}$$

4.2. Temporal Interpolation

Figure 4.2.1 shows the spectrometer output counts after converting the "preferred" range-3 values (C_3) to equivalent range-2 values (C_{2E}) as follows:

$$C_{2E} = X_{23}(C_3) + C_{02} \tag{4.3}$$

where X_{23} is the factor for converting a range-3 value to its equivalent range-2 value and C_{30} is the range-3 background noise output based on Frederick et al. (1986), i.e. $X_{23}=104.22$ for the Sun view and C_3 in the range of 600-700 counts (Figure 2 of Frederick et al., 1986), $C_{03} = 59.5$ and $C_{02} = 65.4$ (Table 1 of Frederick et al., 1986). All of the values shown in Figure 4.2.1 were range-3 outputs. Note that the output for each wavelength is nearly a linear function of time. This linear variation in intensity must result from the time-varying angles of incidence of the incoming solar radiation on the reflectance diffuser; the solar flux at these UV wavelengths should be fairly constant during the 3.7 minutes of these observations.

Figure 4.2.2 similarly shows a linear trend for the core wavelength, No. 7. All of these values involve range-2 outputs. No conversion of range-3 values to range-2 equivalent values is involved for wavelengths No. 6, 7 and 8. Note that these are the lowest range-2 values for the 12 wavelengths. These values are very large compared to C_{02}, so uncertainties in C_{02} are not important to C_2. Uncertainties in X_{23} and C_{03} are very important for wavelengths with range-3 values that must be converted to range-2 values, (for example for wavelengths No. 1, 2, 3, 11 and 12, as seen in Figures 3.4.1, 3.4.2, 3.4.3, 3.4.14, and 3.4.16).

Figure 4.2.3 again shows a linear trend for wavelength 12, where the deviation of about 2% above the linear trend of the fifth point is larger than in the previous figures. In this case, the first five points are range-3 outputs converted to their equivalent range-2 values, while the last three values are range-2 output values. Figure 4 appears to have one linear trend for the first five points and another for the last three. This may be a consequence of not yet including the

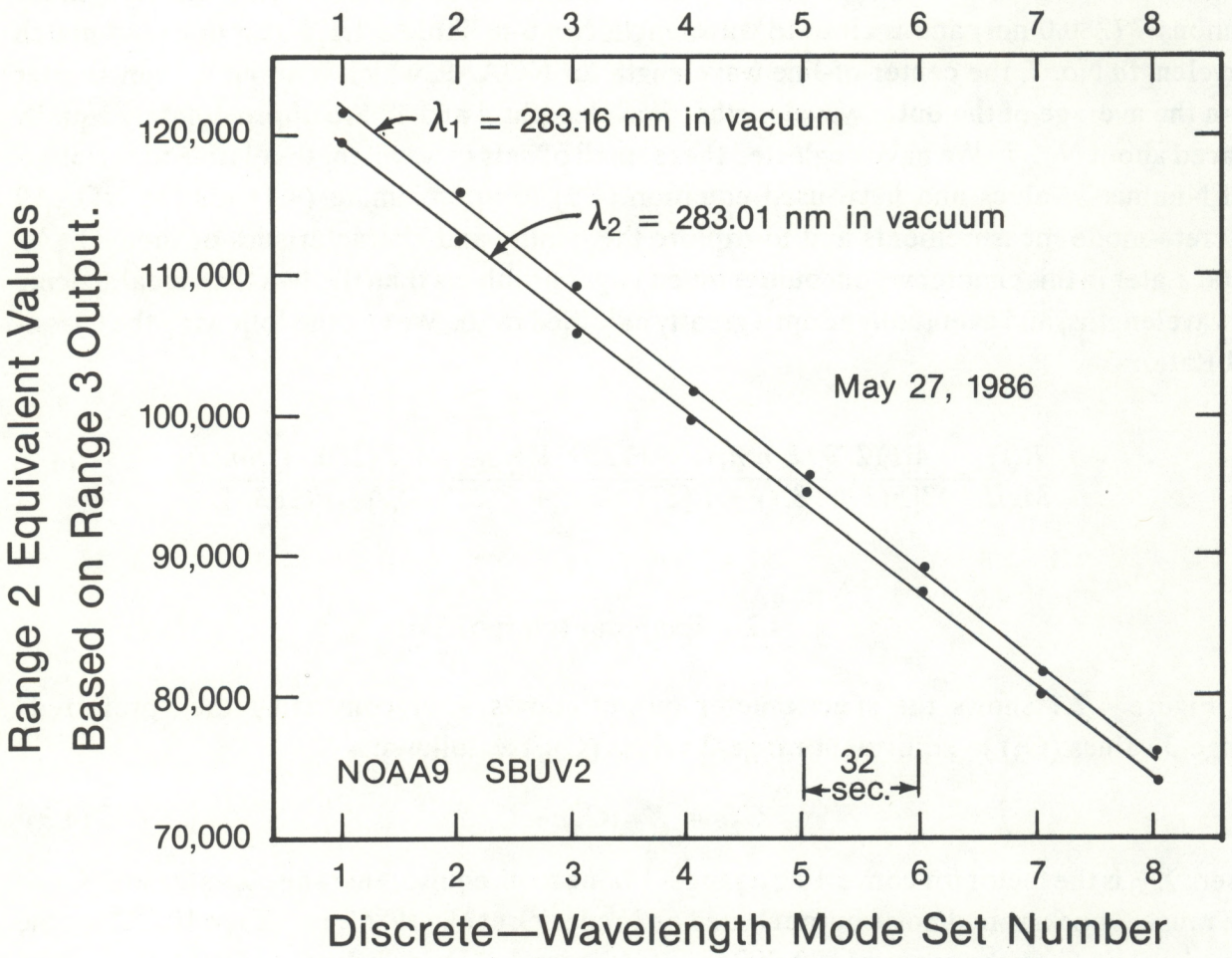

Figure 4.2.1. Spectrometer output counts for wavelength positions No. 1 and 2.

small correction for nonlinearity, where those corrections are largest for the low-intensity portion of range-3.

Figure 4.2.4 shows a problem for wavelength 11, where the fifth point is very low. The straight-line fit for the original set of points misses all of the other points by about 10%. The cause of the problem for the fifth point is that it is so low in its range-3 value that its range-2 value is identified as the "preferred" value; yet the range-2 value is so high that the output counter has overflowed and started over after reaching $2^{16} - 1 = 65,535$. Correcting the fifth point by adding 65,535 establishes the close-fitting linear trend.

After conducting such linear-trend fits to about a year's worth of data, we learned the following:

(1) The largest deviations from a linear trend occur during the first set of data; this is especially true for the first few wavelengths, when only part of the Sun is illuminating the diffuser and part is occulted by the spacecraft. This caused us to exclude from further analysis the very first data set , which would correspond to set No. 0 which are not shown in Figures 4.2.1 to 4.2.4.

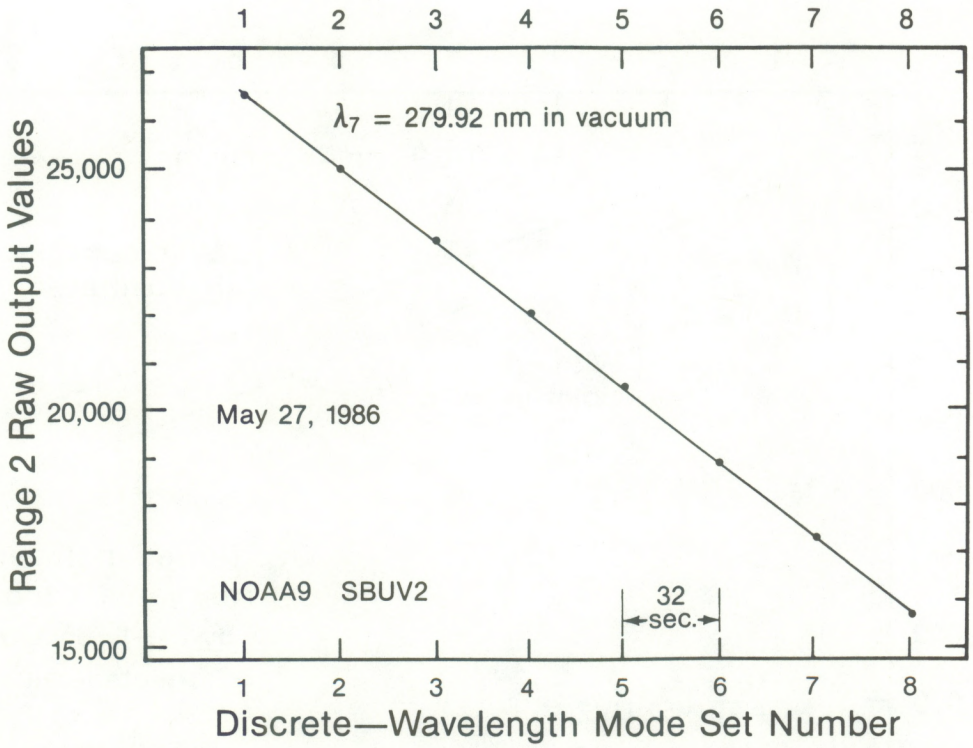

Figure 4.2.2. Linear trend in range-2 output for the NOAA9 discrete-mode wavelength nearest to the center of the unresolved Mg II h and k lines.

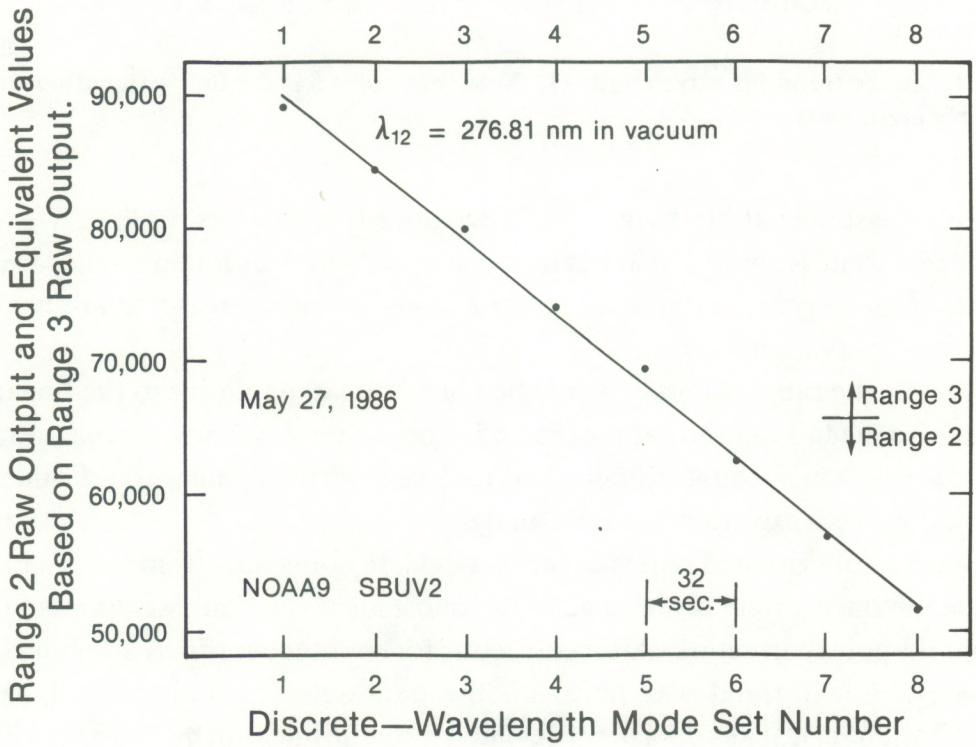

Figure 4.2.3. Linear trend for wavelength 12. Note that point 5 deviates more from the line than do other points and more than it does in previous figures.

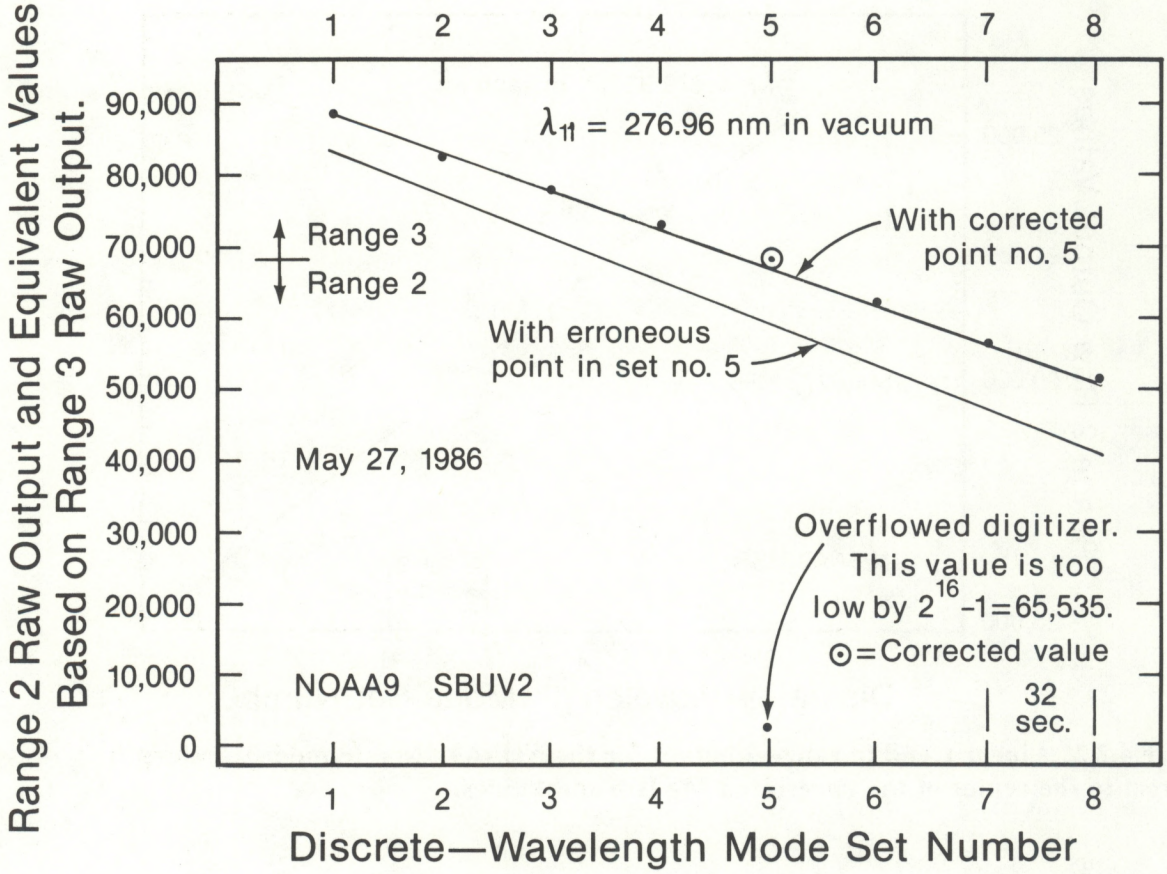

Figure 4.2.4. Linear trend for wavelength 11. Note that point 5 is far below the other points and is clearly erroneous.

(2) There is a seasonal pattern to the small deviations from the best fit line. We assume that the real trend is nearly linear but includes weak higher-order terms that are real; i. e., most of the very small deviations from a straight line are real and are not simply caused by observational noise.

(3) Occasionally the range-2 output would be much too large relative to the linear trend and equal to the full counter value of 65,535. Consequently we now search the range-2 values for this "stuck-counter" value and replace it with the linear trend value found when that point is excluded from the analysis.

(4) On rare occasions isolated points occur that deviate noticeably from the linear trend. Because the linear trend is such a good fit almost all of the time, we adopted the following wild-point correction. After correcting for counter overflows and stuck-counter cases, a linear trend was fit to all the data sets (excluding set 0, the Sun de-occultation set). If any data point deviated from the linear fit by more than 2% (see point 5 in Figure 4.2.3), a new linear fit was derived, excluding the deviant point, and used to determine a "corrected" value for that point.

(5) Wavelengths 1 and 2 were always "preferred" range-3 outputs. Wavelengths 5, 6, 7, and 8 were always "preferred" range-2 outputs, and No. 9 was almost always "preferred" range-2 as well. Wavelengths 3, 4, 10, 11, and 12 tended to switch from "preferred" range-3 to "preferred" range-2 during each day's group of measurements. Linear curve fits for a day's set of points, such as those shown in Figures 4.2.1 to 4.2.4, were used only to correct for isolated wild points and were not used for the piece-wise temporal interpolations described below.

After correcting for counter overflows, stuck full-counter values, and isolated wild points, we computed effective range-2 output values at the time of the measurement for wavelength No. 7 for each of the data sets. The effective range-2 output at wavelength n (n=1- 12, $\neq$ 7) at the time of measurement No. 7 was computed using a linear interpolation between the two nearest measurements at wavelength n. During our early exploratory studies, data sets 0, 1, and 8 were included. For the studies that led to early published values of the relative temporal variations of R_{MgII} (Donnelly, 1988), calculations were made for data sets 2 through 7. For the early exploratory studies, extrapolations were involved for some of the end sets.

For example, for wavelength No. 1, the measurement $C(1, i)$ in set No. i, (i=1 to 7), precedes that of wavelength No. 7 [$C(7, i)$] by 6 wavelength steps or $2\times6=12\,s$. The second measurement at wavelength No. 1 nearest to that at wavelength No. 7 is in the next set of measurements $C(1, i+1)$, which is 32 seconds later than $C(1, i)$ or 32-12= 20s later than $C(7, i)$. Using linear interpolation to determine $CE7(1, i)$, the effective range-2 output at wavelength 1 at the time of the measurement of wavelength 7 leads to the following:

$$C_{E7}(1,i) = \frac{5}{8}\,C(1,i) + \frac{3}{8}\,C(1,i+1) \tag{4.4}$$

In general, for n=1 to 6,

$$C_{E7}(n,i) = \frac{(9+n)C(n,t) + (7-n)C(n,t+1)}{16} \tag{4.5}$$

Similarly, for n=8 to 12

$$c_{E7}(n,i) = \frac{(n-7)C(n,i-1) + (23-n)C(n,i)}{16} \tag{4.6}$$

In the equation for converting the spectrometer output to UV flux values, equation 1.1 in Chapter 1, the variable causing the large changes with time (evident by the vertical thickness of the raw output graphs in Chapter 3) is the diffuser reflectance term because the solar elevation and azimuth angles are changing with time. Using the above temporal interpolations provides a set (i) of range-2 outputs where the solar elevation and azimuth angles on the diffuser are the same for all wavelengths. Using piecewise linear interpolations between two values at the same wavelength at adjacent times may provide a slight improvement over using group linear trend fits, such as those in Figures 4.2.1 – 4.2.4, by partly taking into account that the real trend of the group is a little more complicated than one linear trend.

Neglecting the weak wavelength dependence of the K and Rd terms in 1.1 (derived during the early exploratory work) and canceling out like terms, equation (4.2) becomes

$$\text{CLASSICAL RATIO} = \underset{\text{MgII}}{R(i)} = \frac{4[C_{E7}(6,i) + C(7,i) + C_{E7}(8,i)]}{3[C_{E7}(1,i) + C_{E7}(2,i) + C_{E7}(11,i) + C_{E7}(12,i)]} \quad (4.7)$$

For $i=1$, the $C(11)$ and $C(12)$ values from set 0 may be used in the interpolation. For $i=7$, special end-set extrapolations are used rather than interpolations for wavelengths 1 and 2.

Later in this report, a modified ratio is employed that uses wavelengths 4 and 10 from the walls of the absorption line in order to use only range-2 values with no conversions from range-3 values. For this exploratory phase, that ratio is given by

$$\text{MODIFIED RATIO} = \underset{\text{MgII}}{R(i)} = \frac{2C(7,i)}{[C_{E7}(4,i) + C_{E7}(10,i)]} \quad (4.8)$$

Equation (4.7) was used initially to derive eight values of R_{MgII} without using the temporal interpolations in equations 4.5 and 4.6, or corrections for isolated bad points. Figure 4.2.5 shows the results (dotted line) of comparing the results as a function of the set number in the series of eight daily values. We expect that the real R_{MgII} would be nearly constant over the 4-minute time span of the eight sets of measurements. So, if all were well, we would expect the results in Figure 4.2.5 to be near the unity line for all eight cases. The dotted line monotonically decreases over the eight sets, an undesirable result. First consider the magnitude of these deviations. The solar cycle amplitude of R_{MgII} is of the order of a 10% variation (Heath and Schlesinger, 1986). We would like our observational errors to be less than 1% of that signal, which means within the upper- to-lower horizontal lines in Figure 4.2.5, sets 1, 2, 6, 7, and 8 are outside of this range. This was one of the first indications that we were having problems with the classical ratio. Including the piecewise temporal interpolations and the correction of isolated bad points produced the solid-line results; this provides a small improvement, but the values of sets 1, 2, 7, and 8 are still undesirably far from unity. Probable causes include the lack of correction for nonlinearity in the relation of range-3 values to range-2 values and, possibly, second-order wavelength dependences of K and R that were neglected in our exploratory survey. These solar flux measurements are made after the satellite has passed from the sunlit hemisphere to the night side of Earth (where the instrument is located on the bottom side of the satellite, i. e., toward Earth). These measurements are made during the several minutes that the instrument diffuser is lit by the Sun and from the time the Sun is unocculted at the diffuser by the overlying satellite to when the terrestrial atmosphere occults the Sun. Because the illumination of the SBUV2 instrument and its side of the satellite change rapidly during these measurements, thermal transient effects may cause changes in the instruments' gain or wavelength positions.

Figure 4.2.6 presents similar results except for the standard deviation with respect to the mean of sets 3, 4 and 5. Except for the reference sets (3-5) used in the mean, the standard deviations are not much larger than the deviations from unity of the means in Figure 4.2.5, so there

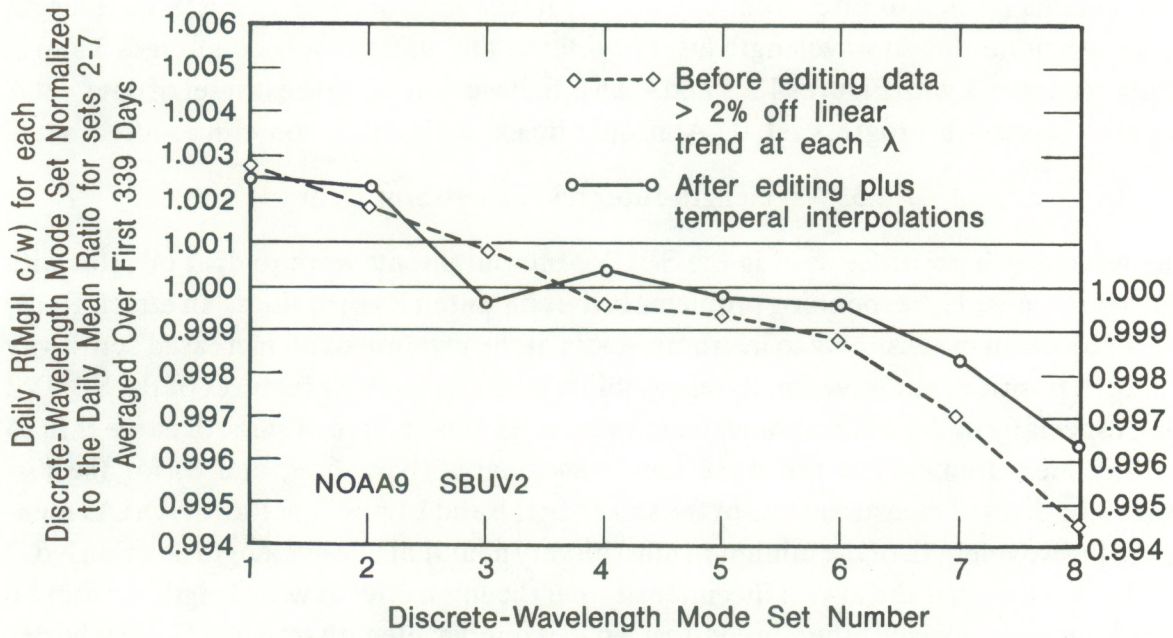

Figure 4.2.5. On average, RMgII is highest for the first discrete-wavelength mode measurements of the daily set of measurements and lowest for the last set, decreasing monotonically with increasing set number (with the exception of set 3) after isolated bad points have been corrected and the temporal interpolations applied.

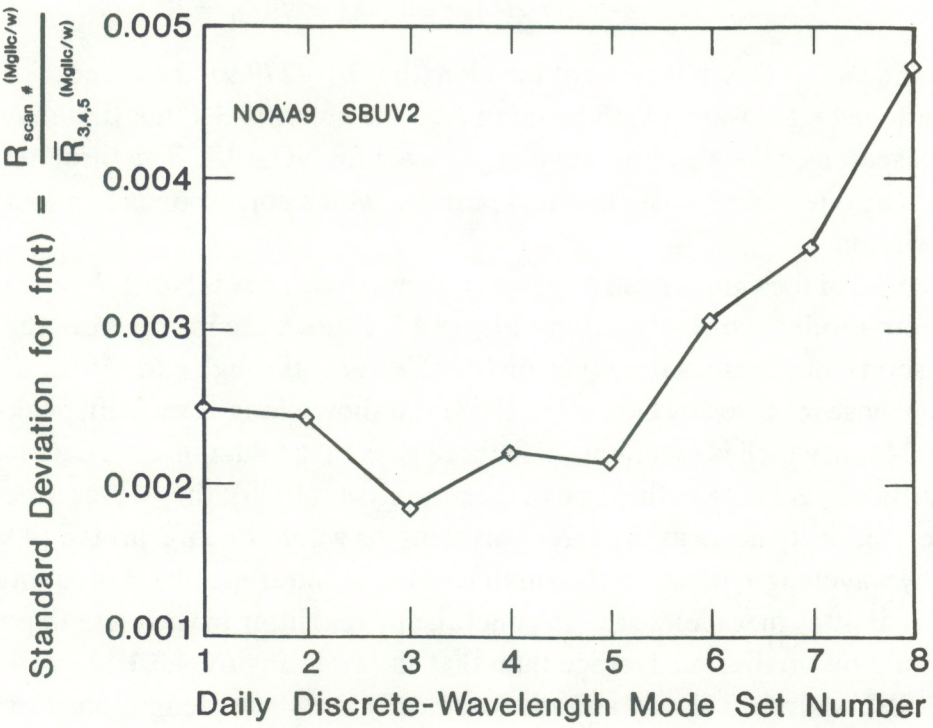

Figure 4.2.6 Deviations of each daily R_{MgII} value for set no. i (i = 1 - 8) with respect to the daily mean for sets 3-5 rms averaged over 339 days of observations.

are few problems related to jitter from one minute to the next of these discrete-wavelength mode measurements due to wavelength jitter or jitter in the relation between ranges 3 and 2. One result of our work with Figures 4.2.5 and 4.2.6 is that we quit using the last set of data, set 8, as well as the sunrise-in-progress set, 0. Atmospheric extinction may sometimes affect set 8.

4.3. Wavelength Jitter and Long-Term Drift

If the wavelength positions used in the SBUV2 measurements were to drift or jitter with time, that could cause corresponding problems in the computed R_{MgII} values. In effect, R_{MgII} achieves a reduction in sensitivity to instrument gain at the expense of an increased sensitivity to wavelength position; but wavelength repeatability is one of the best features of the SBUV2 monitors, especially in the discrete-wavelength mode. In this section, a smooth curve is fit to the intensity measurements at the three core wavelengths (Nos. 6, 7, and 8) for the discrete-wavelength set of measurements of the solar Mg II h and k lines. For these NOAA9 measurements, the wavelength of the minimum must be very near that of wavelength position No. 7 because that position has the lowest flux intensity and the intensities at wavelength positions 6 and 8 are about equal to each other; in contrast No. 8 is one wavelength step (0.149 nm) shorter than that of No. 7 and No. 6 is one step longer in wavelength. For the case of the minimum wavelength being very close to wavelength No. 7, a quadratic equation was used for the smooth curve fit and the wavelength of minimum flux λ_{min} was then computed from

$$\lambda_{min} = \lambda_0 - \frac{\Delta\lambda}{2} \cdot \frac{\Phi(\lambda_0 + \Delta\lambda) - \Phi(\lambda_0 - \Delta\lambda)}{\Phi(\lambda_0 + \Delta\lambda) - 2\Phi(\lambda_0) + \Phi(\lambda_0 - \Delta\lambda)} \quad , \tag{4.9}$$

where $\Phi(\lambda)$ is the energy flux measured at wavelength λ, $\lambda_0 \approx 279.9152$ nm and $\Delta\lambda \approx 0.148$ nm. The wavelength given for wavelength position No. 7 is a nominal value that may be revised after further research of the absolute wavelength scale for NOAA9. The three-term denominator in (4.9) is also tested to verify that it is positive, which corresponds to a local minimum and not a maximum.

A daily median of the values from (4.9) was computed using sets No. 2-7, for each day having eight discrete-mode records available. Figure 4.3.1 shows the results from the start of the solar Mg II discrete-mode measurements, on May 27, 1986, through early 1988. These results are the same as those reported by Donnelly (1988) and show a long-term drift, peak-to-peak, of only about 0.004 nm, which is excellent. The three gaps in the data involve data tapes that we were having difficulty reading at the time of these analyses (1988); they were successfully read at a later date. Intensity noise at the three wavelengths would be interpreted (4.9) as having been caused by wavelength jitter; so the small day-to-day jitter may be due to intensity noise rather than a real jitter in wavelength. In general, any real jitter in wavelength position from day to day should be smaller on average than that shown in Figure 4.3.1.

Nimbus-7 SBUV drifted slowly and monotonically in its wavelength positions, by about half an angstrom (0.05 nm), over 9 years of observations (Schlesinger, 1989); the drift was presumably due to the slow, steady wear of the cam drive. In the case of SBUV2's optical encoder of shaft-rotation position and electromagnetic torque drive system, combined in a feedback

loop-control system, it is not clear what the nature of wavelength drift might be. For example, does part of the wavelength scale drift upward while another section drifts downward? Or does the random error at each wavelength position tend to increase with time, when the worn shaft bearing requires more torque to change positions (or more time to achieve a certain error level)? This latter case should cause an increase in day-to-day jitter with time.

Figure 4.3.2 shows that large errors occurred in the solutions for the minimum wavelength in the first full discrete-wavelength set of measurements made following sunrise on the diffuser (after set 0); thus the first set was not included in deriving the daily median. The spike in July 1986 is due to an uncorrected, isolated bad point. The group of points in October and November 1987 correspond to the sprinkling of low points during that same time, seen in Figures 3.4.8–3.4.10 in the previous chapter, which were interpreted as anomalously low measurements caused by an unexpected partial obstruction of the Sun by some part of the satellite. In the case of the minimum values for the second full set, another uncorrected, isolated bad point caused a large spike in July 1987. Figure 4.3.3 shows that the minimum for the third set has a day-to-day jitter of about 0.001 nm and is lower than the daily median by about 0.002 nm in June 1986, and by about 0.001 nm from November 1986 through March 1988. Figure 4.3.4

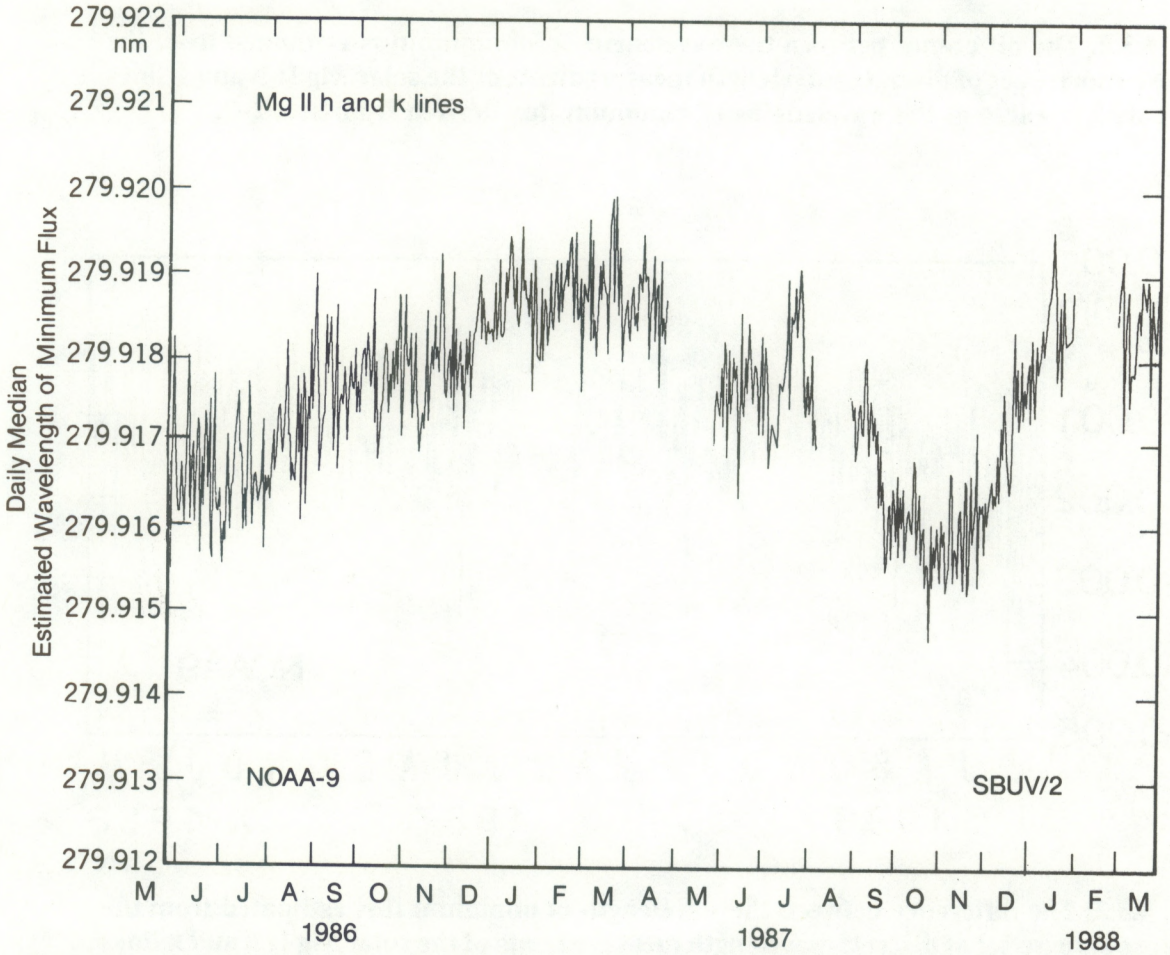

Figure 4.3.1. A consistency test of wavelength position stability, based on estimates of the wavelength of minimum flux for the unresolved Mg II h and k lines.

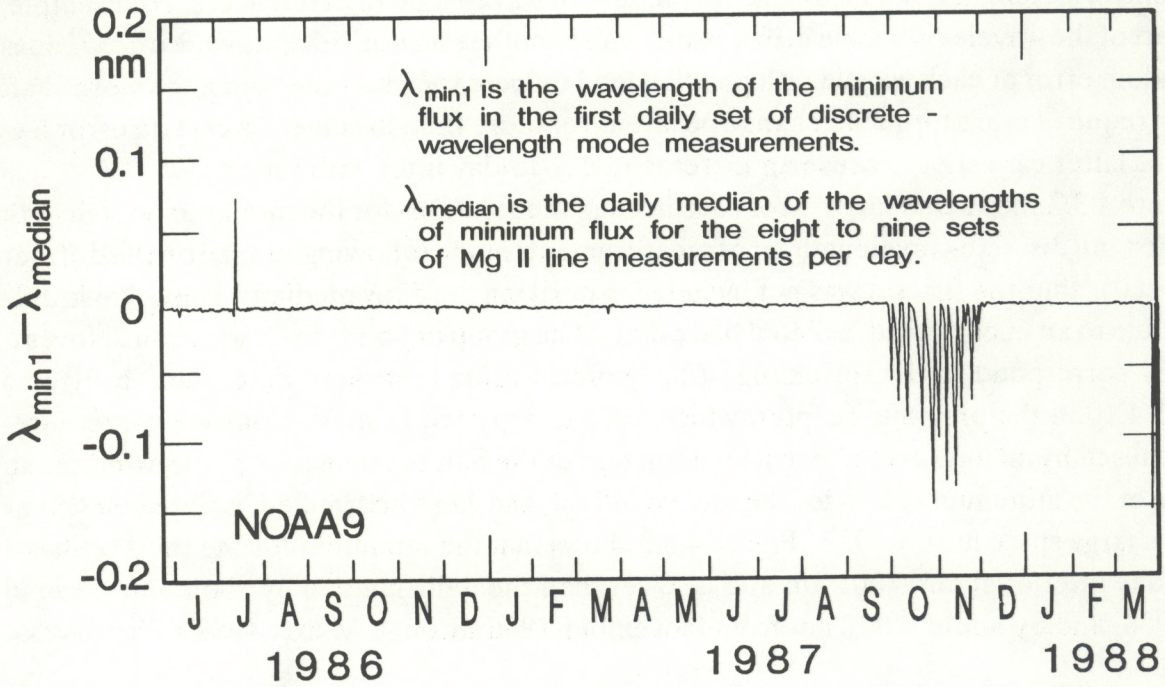

Figure 4.3.2. The difference between the wavelength of minimum flux estimated from the first post-sunrise set of discrete-wavelength measurements of the solar Mg II h and k lines and the daily median of the wavelengths of minimum flux derived from sets 2–7.

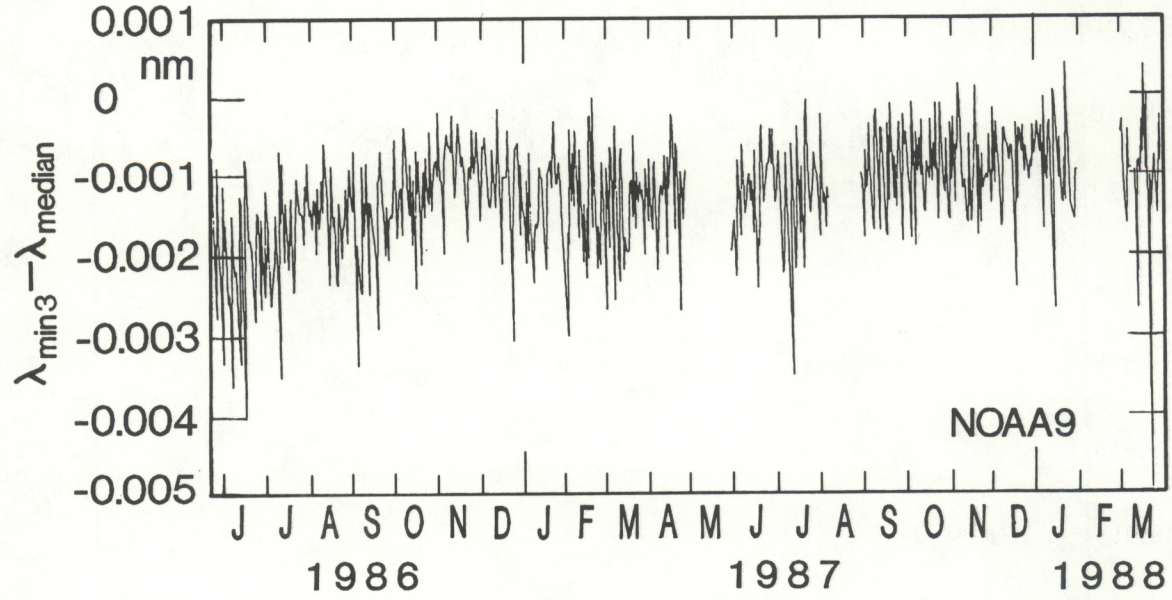

Figure 4.3.3. The difference between the wavelength of minimum flux estimated from the third post-sunrise set of discrete-wavelength measurements of the solar Mg II h and k lines and the daily median of the wavelengths of minimum flux derived from sets 2–7. Note that the very small values are consistently negative.

shows that the wavelength of the minimum flux for the fifth discrete-mode set is almost identical to the daily median yet consistently slightly higher in wavelength. Figure 4.3.5 shows larger differences for set 7 in June and July of 1986 and small positive values after August 1986. The results seen in Figures 4.3.3 - 4.3.5 do not show a pattern like that in Figure 4.3.1. The minima for each discrete-wavelength mode set have the same pattern as that in Figure 4.3.1, so that pattern isn't present in the graphs of differences with respect to the daily median. The main results seen in Figures 4.3.3–4.3.5 are that the greatest differences occurred in the first 2 months, then there was a convergence to very small differences. The trend in which the minima for set 3 are smaller than the daily median, the minima for set 5 are larger, and the differences for set 7 are even more positive, is analogous to the trend from high to low seen in Figure 4.2.5; this implies some residual bias due to some uncorrected Sun angle or non-linearity effect.

The main results are that the drifts seen in Figure 4.3.1 and the offsets seen in Figures 4.3.3–4.3.5 are so small that the errors they cause in R_{MgII} are negligible. For example, the corrections for a drift in the Nimbus 7 data of 0.05 nm amounted to changes in the fourth decimal place for R_{MgII}, i.e., small but not negligible corrections (Schlesinger, 1989). Model results of the sensitivity of R_{MgII} to drifts in wavelength are discussed in Chapter 6.

Figure 4.3.6 shows an extension of the use of equation 4.9 through 1988 and 1989. The data gap in September to November 1988 is due to data loss from occultation of the Sun as seen at the instrument diffuser by part of the satellite. (We have recovered some of the data at the beginning and end of the gap by using fewer than eight Sun-lit discrete-wavelength sets per day.) The other data gaps were caused by data tapes that had not been successfully read at the time of this analysis, but were successfully read at a later date. Note that the scale size (0.01 nm) between major tick marks along the scale at the left side corresponds to the entire height of the graph in Figure 4.3.1. Figure 4.3.6 shows that there were much larger deviations in the minimum wavelength after the fall occultation gap in 1988 through March 1989, and then large deviations to longer wavelengths in October 1989. These drifts (+0.01 nm) were smaller than the Nimbus-7 drifts but they occurred in the fifth year of operation. Although these deviations were small for the classical Mg II core-to-wing ratio, we later switched to using a modified ratio that may be more sensitive to these possible wavelength deviations. Further research is needed on the sensitivity of the modified ratio to wavelength drifts the size of those indicated in 1989.

4.4. Intensity Linearity

One desirable feature of the discrete-wavelength mode is that the output is available separately for each of the three intensity ranges as well as the output of the range the instrument selects as the "preferred" range. (The wavelength-scan mode provides only the preferred range output.) We often use the output of range-2 when range-3 is the preferred range; this practice is explained below.

From Figure 2 of Frederick et al. (1986), we know that the ratio of range-2 output to range-3 output is a weak function of wavelength and also of range-3 intensity. From their Figure 3, we know that the ratio is also a slow function of time (< 2% decrease in 60 days). Conse-

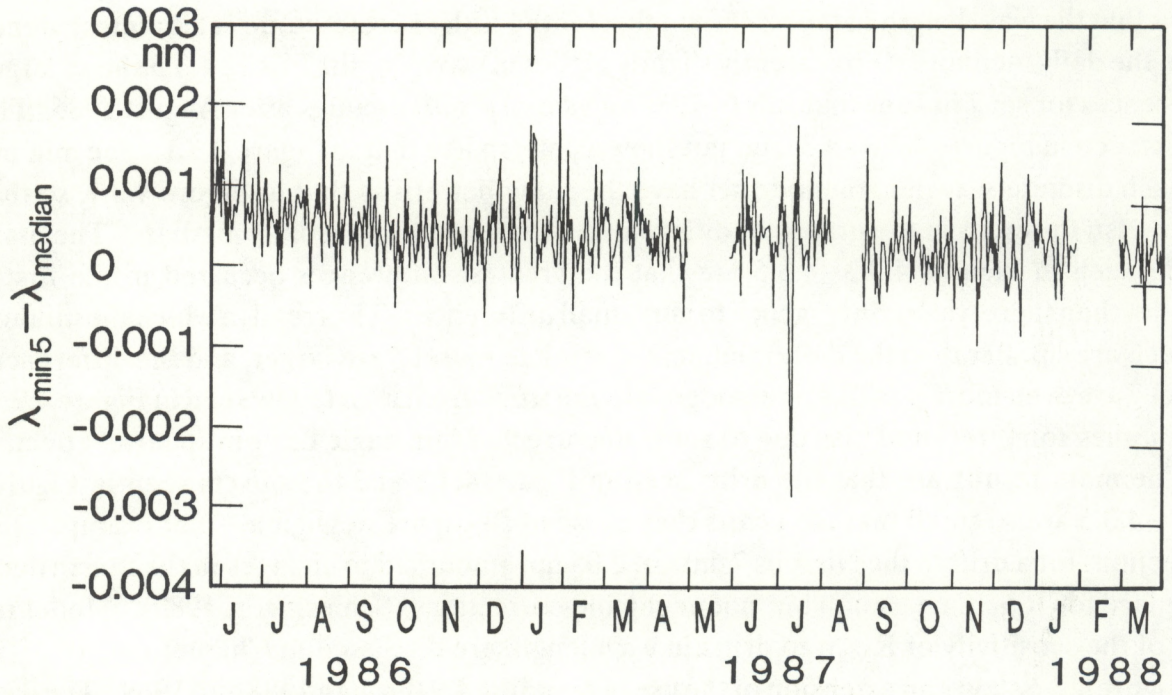

Figure 4.3.4. The difference between the wavelength of minimum flux estimated from the fifth post-sunrise set of discrete-wavelength measurements of the solar Mg II h and k lines and the daily median of the wavelengths of minimum flux derived from sets 2–7. Note that the extremely small values are mostly positive.

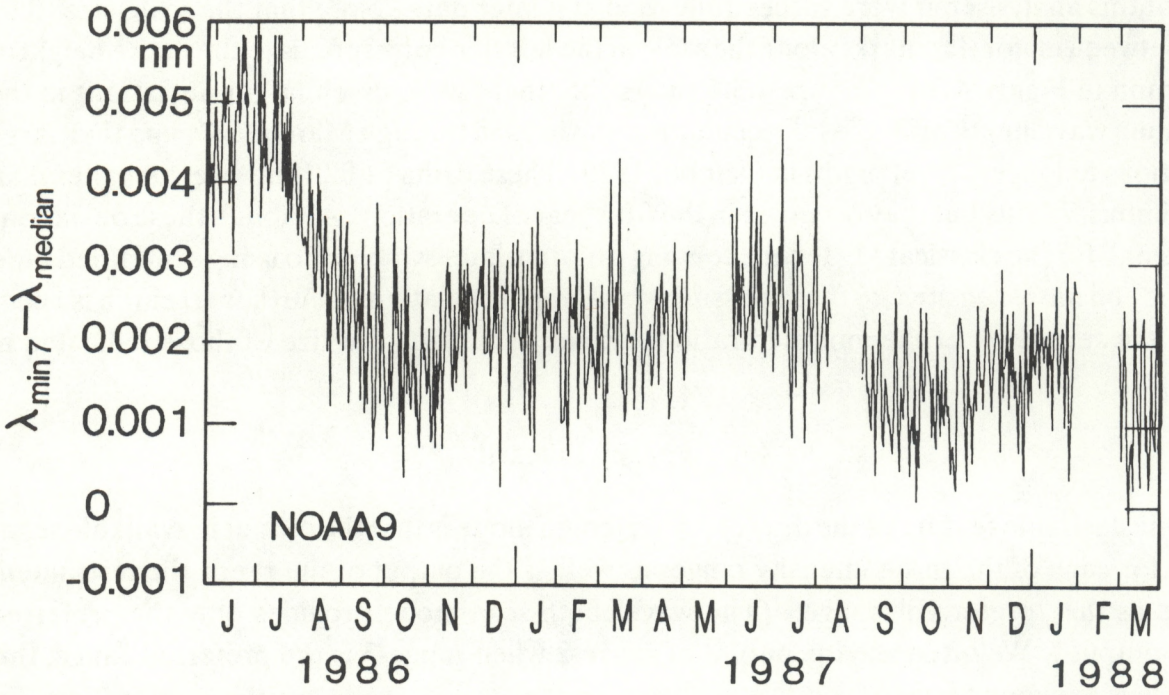

Figure 4.3.5. The difference between the wavelength of minimum flux estimated from the seventh post-sunrise set of discrete-wavelength measurements of the solar Mg II h and k lines and the daily median of the wavelengths of minimum flux derived from sets 2–7. Note that the small values are consistently positive.

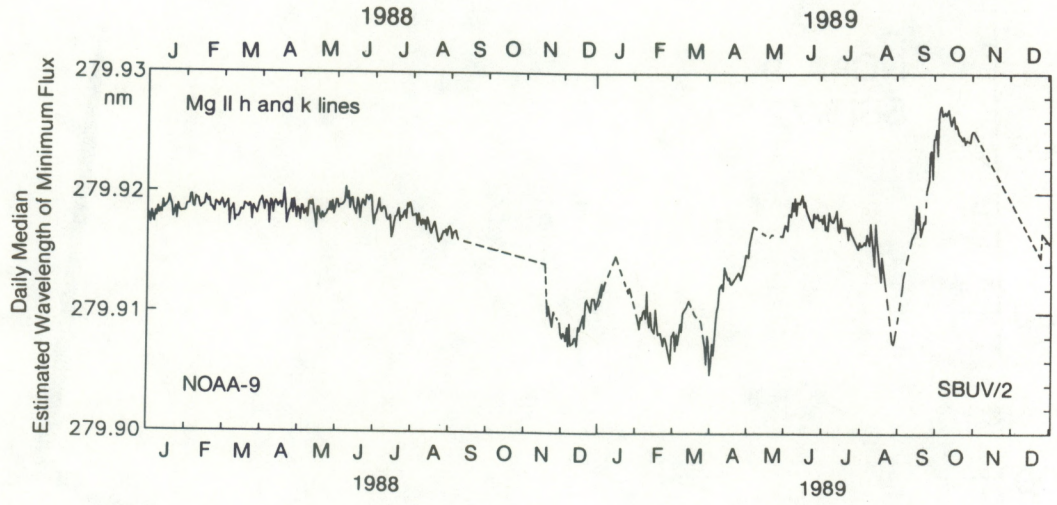

Figure 4.3.6. The estimated minimum wavelength during 1988 and 1989.

quently, the concurrent range-2 and -3 outputs for the Mg II discrete-mode data were studied at the wavelengths important for the core-to-wing ratio of the Mg II h and k lines. Figure 4.4.1 shows the locus of these points for wavelength 1. All of the range-2 values shown here have overflowed the intensity output counter once, so they have had 2^{16} - 1 or 65,535 added to their value. For range-3 values increasing above 1020, the range-2 values decrease slowly; clearly those intensities are too high for range-2 values to be useful. There is also a clear deviation from linearity for range-3 values above 970; we would not want to use this nonlinear region for range-2. For range-3 values below 970, the relation is satisfactorily linear, with separate points showing at the left tip because sunlit wavelength-1 outputs rarely get to such low values. The results for wavelength 2 are the same as in Figure 4.4.1, so they are not shown here.

The linearity found in the lower part of Figure 4.4.1 is not the same as that calibrated by Ball Aerospace in their overall system calibration. The small deviations from linearity that were found in their calibration are of unknown origin. The consistency tests we are considering here involve the combination of the photomultiplier and the electronic output ranges.

Figure 4.4.2 shows very similar results for wavelength Numbers 3 and 12, which had quite similar output ranges during 1986 (May 27–December 31, 1986). These results overlay each other; i. e., no wavelength dependence is seen for the small range in wavelength involved (5 nm). The wavelength affects the intensity range involved, however. For example, both wavelengths 3 and 12 include much lower intensities than do wavelengths 1 and 2; for the intensity ranges they have in common, however, all four results fit each other. For wavelength No. 3, there are some points that are not shown in Figure 4.4.2 that correspond to the points labeled "mystery group X" in Figure 3.4.4. Those points have range-2 values below 15,000 and range-3 values below 210 and are interpreted as resulting from the Sun still being partially occulted by the satellite. They are roughly consistent in their range-2 and range-3 values with the low end of the combined-wavelength result presented below.

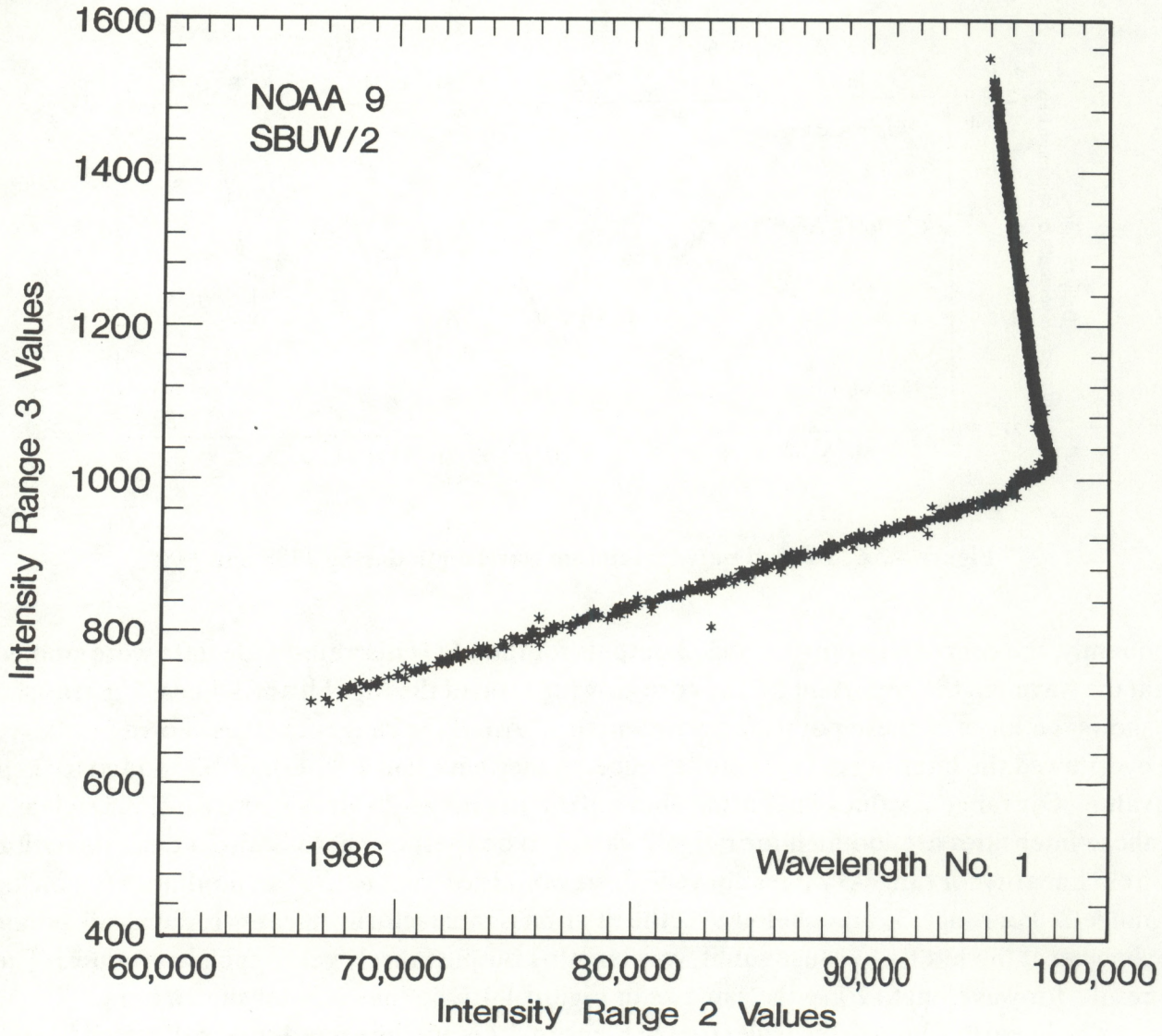

Figure 4.4.1. The range-3 and range-2 output relationship for wavelength No. 1.

Figure 4.4.3 shows results for wavelength 4, where the intensity range is always below the saturation elbow for range-2, or always in the linear portion of the range-2 and range-3 relation. Note the peculiar, offset second line segment in the 32,000–38,000 section for range-2. Those points are the same as the "mystery group-Y" points, in Figure 3.4.6, which are interpreted as partially occulted Sun observations. The slight offset between this short segment and the main line is probably caused by the portion of the diffuser viewed by the instrument being only partially illuminated, and the rest of the optics being illuminated with a different range of rays than normal; this may result in a small difference in the photomultiplier gain in the anode circuit relative to that in the cathode circuit. The other points near 35,000 to 40,000 come from the end of sets of Mg II measurements, when the Sun-to-diffuser angles are much different than for the group-Y points.

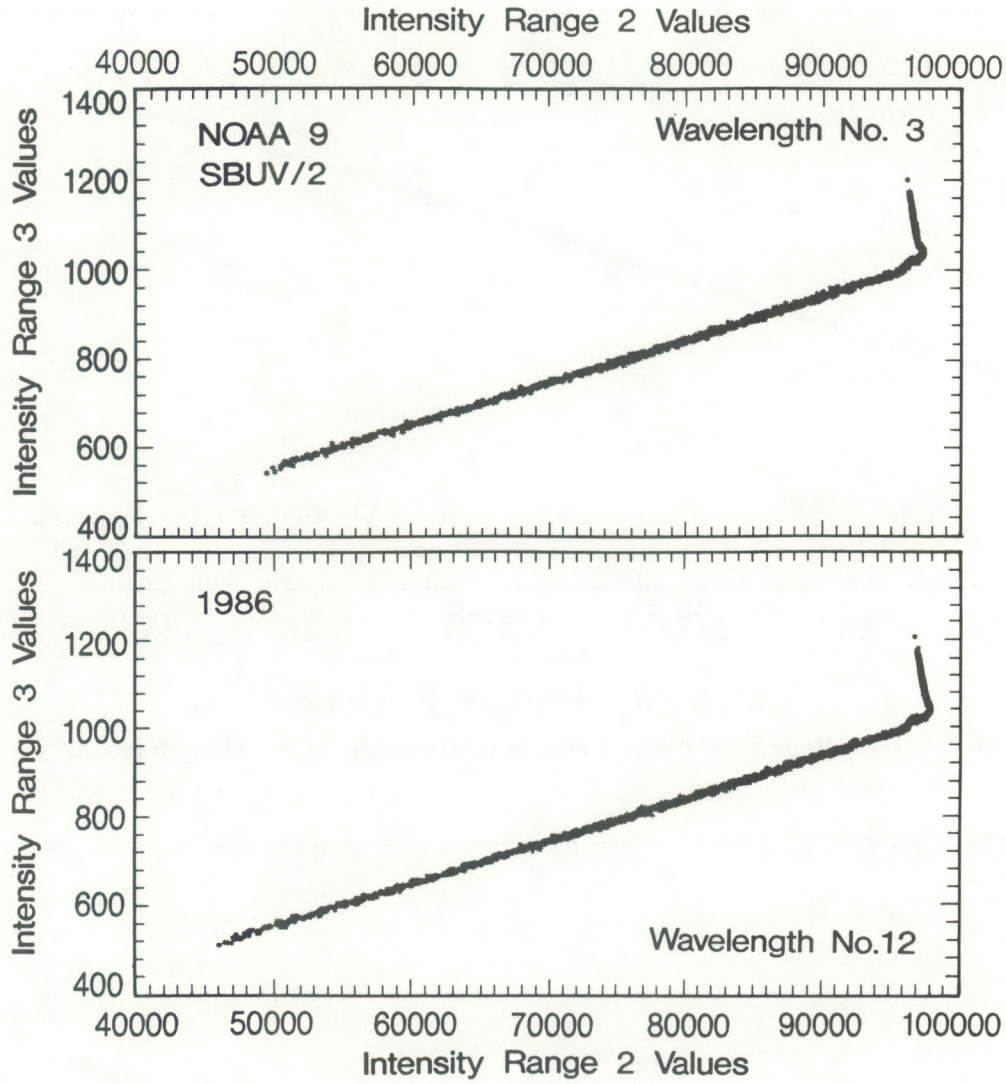

Figure 4.4.2. The range-3 and range-2 output relationship for wavelengths Numbers 3 and 12.

Figure 4.4.4 shows similar intensity ranges as those in Figure 4.4.3 but with no partial-sunrise values and, correspondingly, no offset segment in the 30,000–40,000 range. The results for wavelength 10 (not shown) look like those for No. 9 but are closer to the range of No. 4.

Figure 4.4.5 shows results for wavelength No. 5. The range-3 scale has been expanded in comparison to previous figures, and the scatter of points consequently appears to be fuzzier. The top side of the fuzziness appears to be slightly higher for range-2 values between 40,000–50,000; this is caused by group-Z points that were first identified in Figure 3.4.7. Figure 4.4.6 shows the results for wavelength No. 7, the wavelength nearest minimum flux for the unresolved Mg II h and k lines. The results for wavelengths 6 and 8 look just like those for wavelength 7, so they are not shown here. Similarly, the results for wavelength 11 look just like those for wavelength 12, shown in Figure 4.4.2.

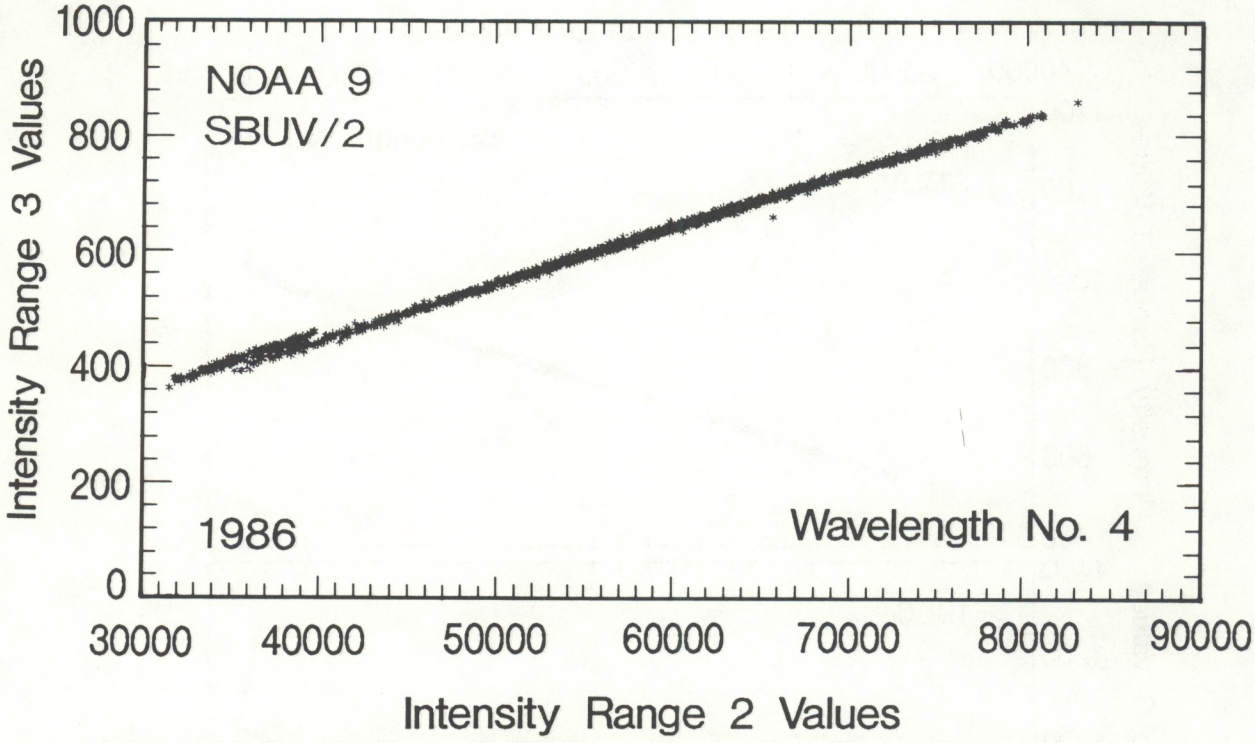

Figure 4.4.3. The range-3 and range-2 output relationship for wavelength No. 4.

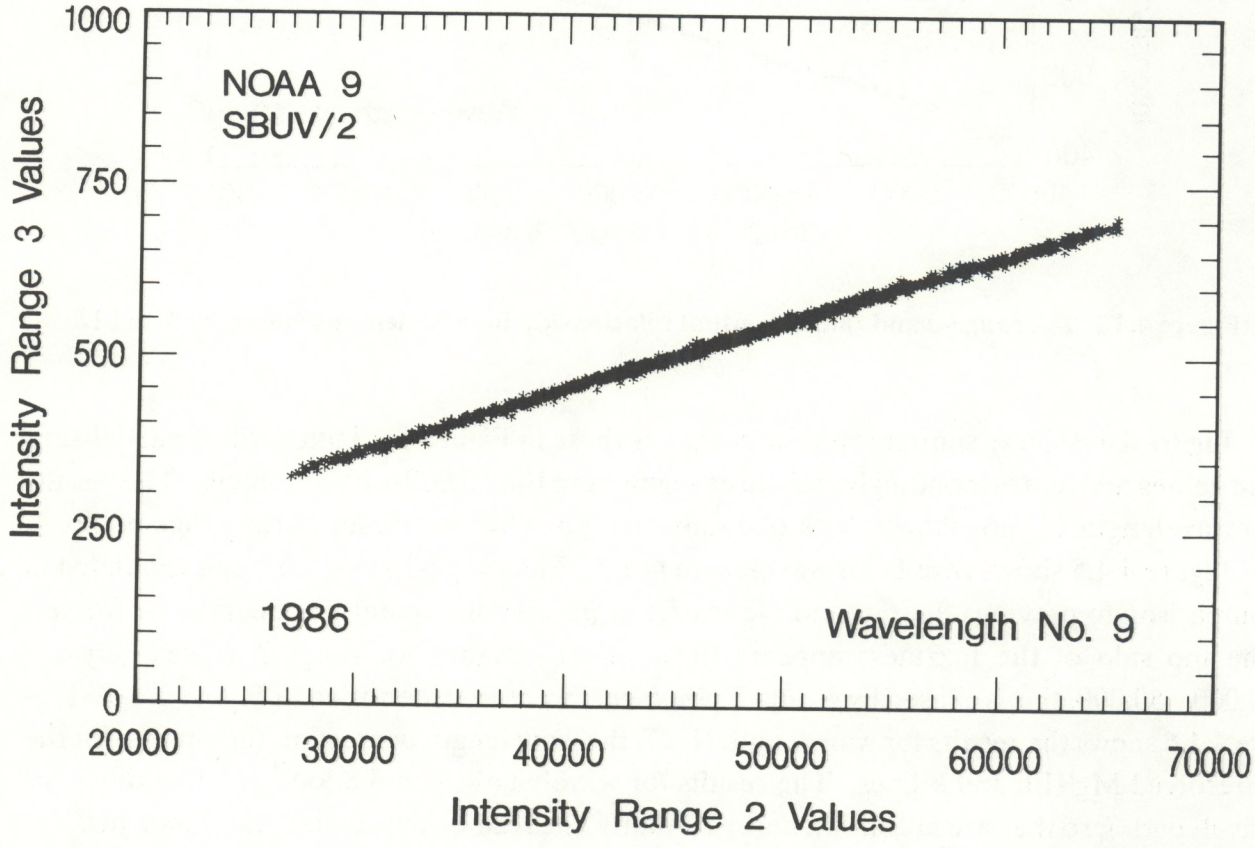

Figure 4.4.4. The range-3 and range-2 output relationship for wavelength No. 9.

The thickness of the scatter in Figure 4.4.6 is desirable from the following viewpoint. Assume for the moment that this spread is probably in the range-3 values (± 10) and is noticeable because we are looking at very low range-3 values. This spread would not be a problem for wavelengths 6, 7, and 8, the core wavelengths used in R_{MgII}, because we would use only the large range-2 values, which presumably contain little of this spread. For wavelengths 1 and 2, where the range-2 values are saturated, we would have to use range-3 values where this same spread would produce a small but not negligible (± 1%) noise level in R_{MgII}. Suppose the scatter in Figure 4.4.6 were not in the range-3 values but in the range-2 values (perhaps due to changes in the photomultiplier gain for its anode circuit). In that case, we would expect the spread in values to increase with increasing intensity and produce a larger spread in Figure 4.4.1 than in 4.4.6. These figures show a rather uniform spread (± 800 in range-2 values), not one that increases with intensity. In this case, the error for the core-wavelength measurements would be about ± 3%, which is even more undesirable for R_{MgII}. Whatever the cause of this spread, it does not appear to be a significant function of wavelength or intensity for the range of wavelengths and intensities involved in the discrete-wavelength mode measurements of the MgII h and k lines.

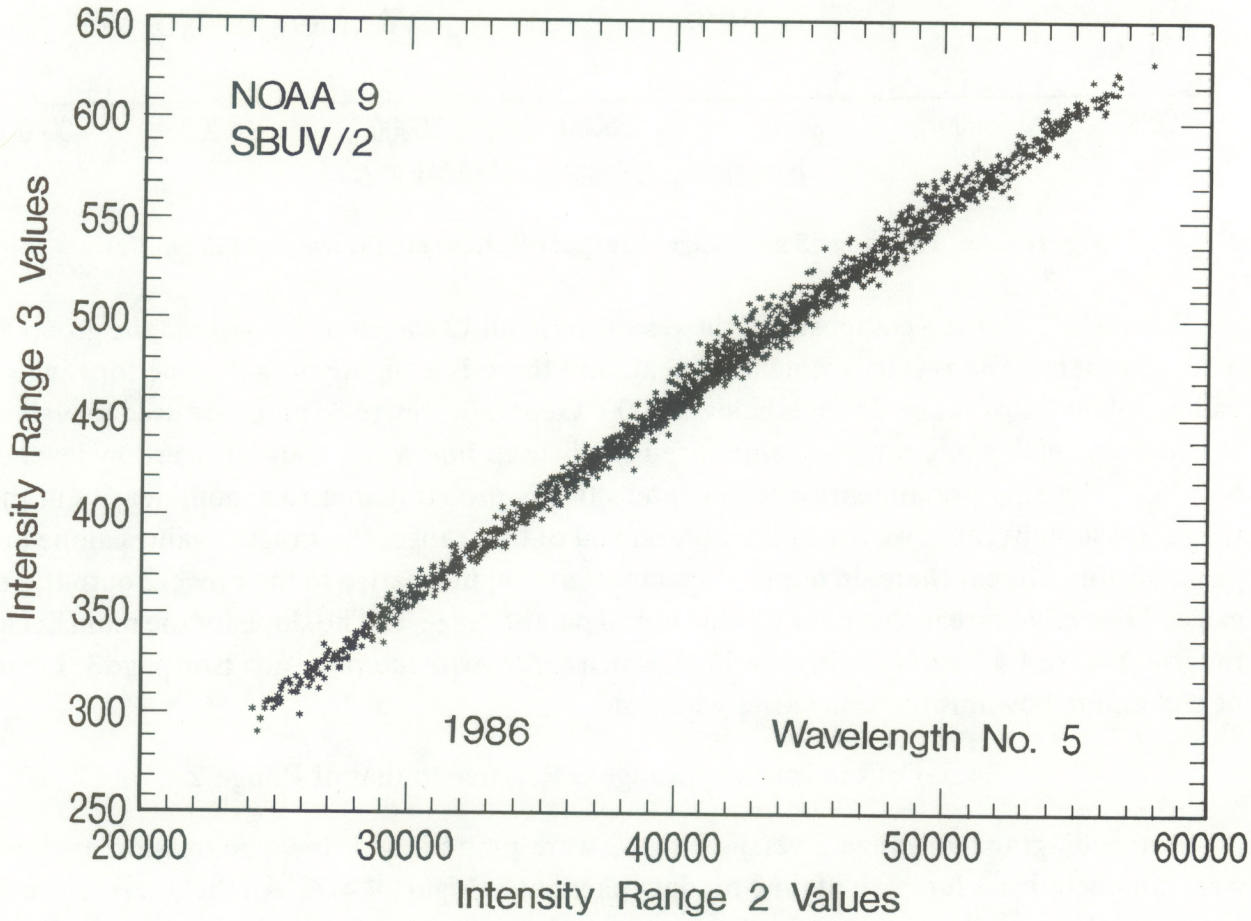

Figure 4.4.5. The range-3 and range-2 output relationship for wavelength No. 5.

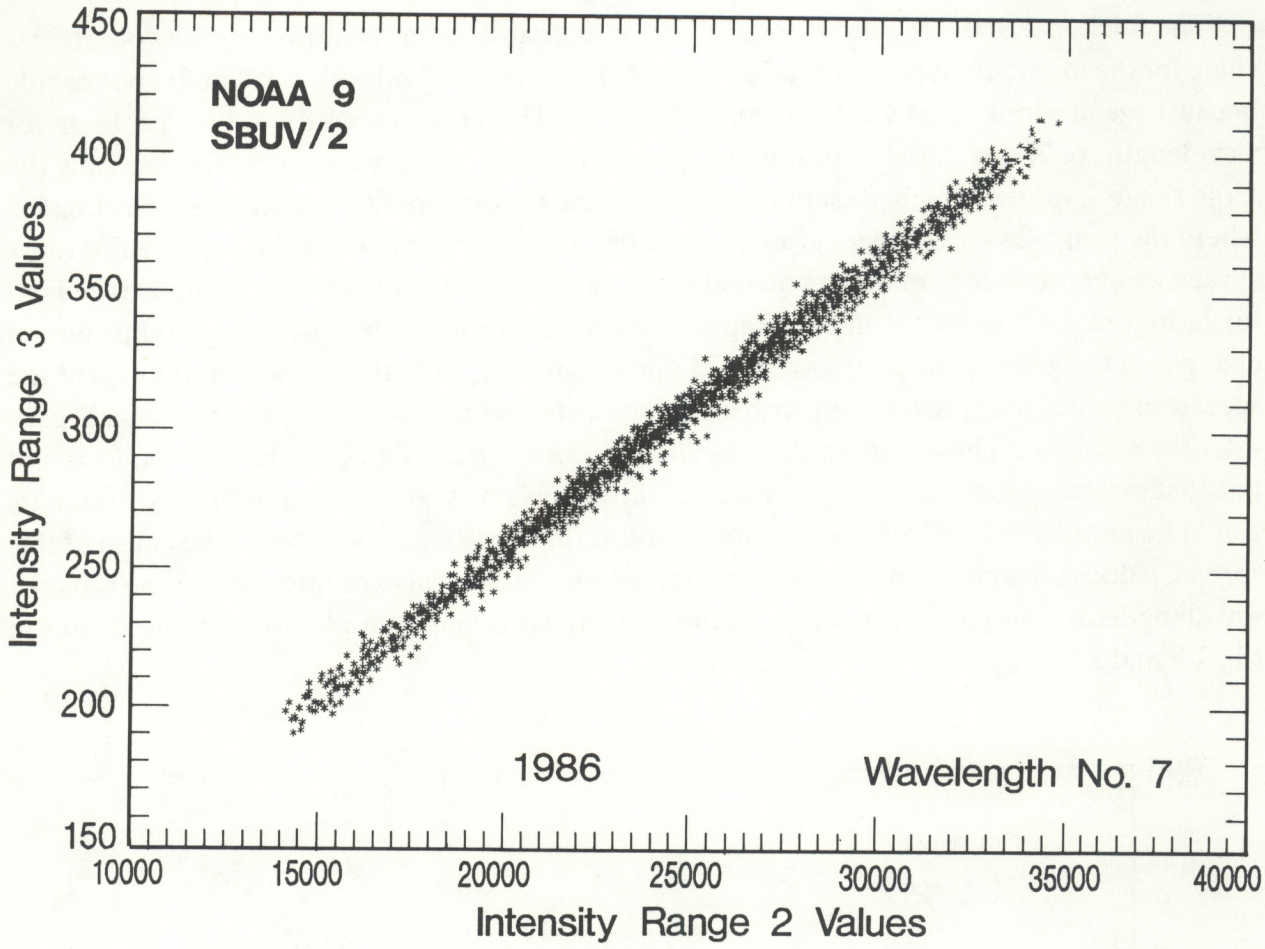

Figure 4.4.6. The range-3 and range-2 output relationship for wavelength No. 7.

Figure 4.4.7 shows a composite of the results from all 12 wavelengths without the group X, Y, or Z points. The results are nearly linear, and there is a slightly larger slope for range-3 values below 400 or range-2 values below 33,000. Generally, range-3 values are used for values above about 600, while range-2 values are usually used below the counter overflow level of 65,535. The slight nonlinearity at low intensities is probably due to a nonlinearity in the range-3 system because we are at the bottom end of that range; the range-2 values alone are probably quite linear there, in terms of spectrometer input relative to the range-2 output, because these values are in the middle of the useful part of range-2. The slope for the main linear range in Figure 4.4.7 is $104.2 = X_{23}$ for 1986, which agrees with the value given on page 3. Let us next examine how this relation varies with time.

4.5. Drift in Intensity Range-3 Relative to that of Range-2

Scatter diagrams of range-3 versus range-2 were plotted, and linear regression analyses were conducted as a function of time for data like that in Figure 4.4.7. All the discrete-wavelength-mode measurements for the observations of the solar Mg II h and k lines for each day were used for all 12 wavelengths combined, except for the following:

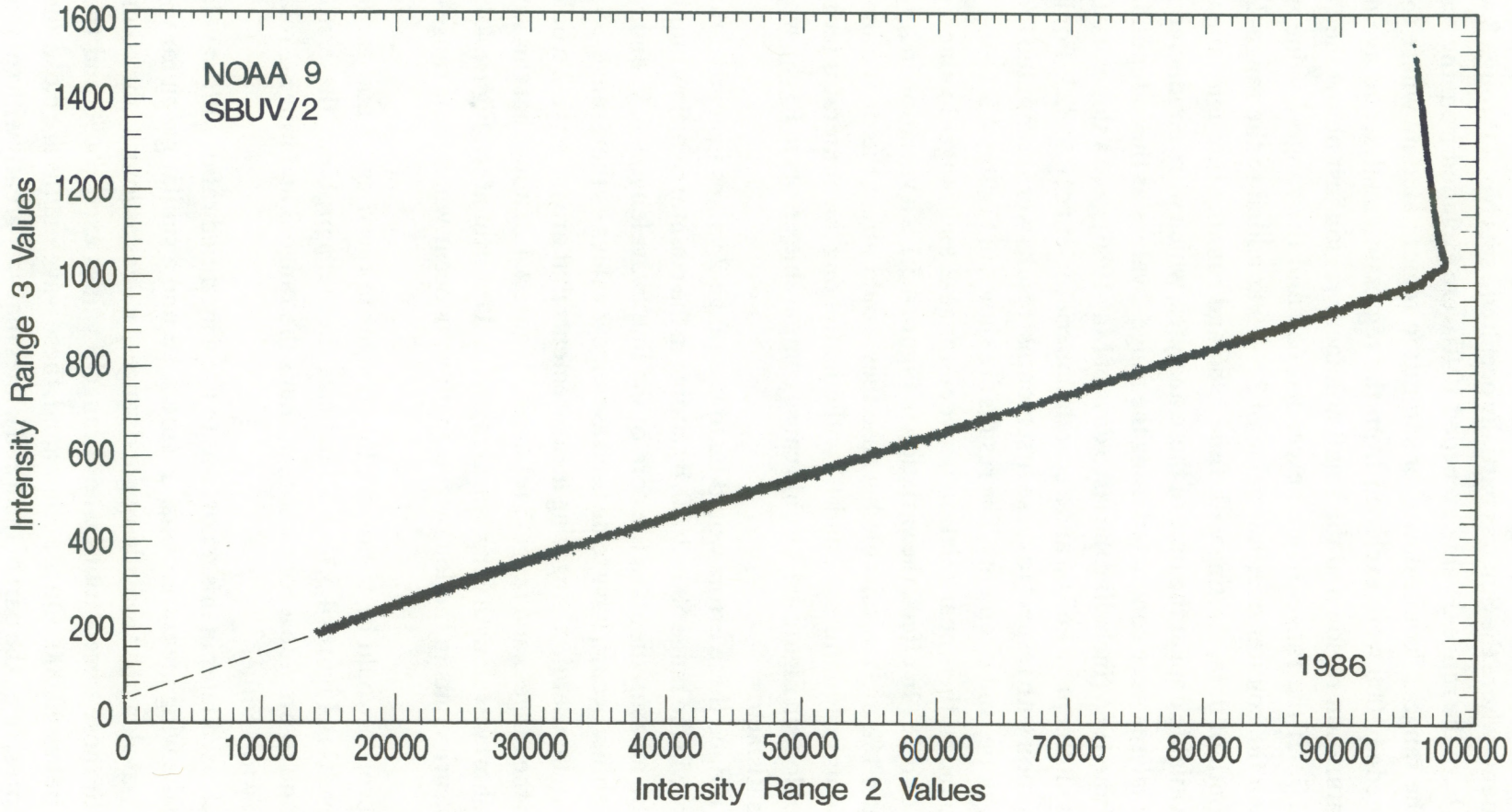

Figure 4.4.7. Range-2 and range-3 intensities for all 12 Mg II wavelengths.

(1) The first two sunlit sets of measurements (sets No. 0 and 1) were excluded to avoid all measurements where the Sun was partially occulted.; sets No. 2 through 8 were used.

(2) All data where the range-3 value exceeded 1040 were excluded from the scatter plots to avoid the range-2 "count-down" or saturation region; all data where the range-3 value exceeded 1000 were excluded from the regression analyses to avoid both the range-2 saturation region and the small nonlinear region just below the "elbow" in Figure 4.4.7. If the range-3 value exceeded 650 and the range-2 value was below 60,000, then the counter overflow value of 2^{16}-1 was added to the range-2 value.

For each month of data, starting with June 1986 and running through January 1989 (the most recently available data at the time of these analyses, which were conducted in 1989), linear regression analyses were conducted using the range-2 values as the independent variable. The results for June 1986 (including the last 5 days of May 1986) gave a slope of 0.0096057 with a range-3 Y-axis intercept of +68.66 and a correlation coefficient of 0.99823. For later months, the percent deviation with respect to these first months' results were computed for the correlation coefficient, slope, and intercept. The results are shown in Figures 4.5.1–4.5.3. Too much variation was found in the linear relation between range-2 and range-3 values, especially in late 1987 and late 1988. In effect, the variation in Figure 4.5.1 is a variation in X_{23}. Variations in X_{23} larger than 1% are undesirable because they would affect the denominator terms or wing measurements in equations 4.2 and 4.7 without affecting the numerator terms. Thus, the deviations in the slope in Figure 4.5.1 would cause comparable errors in R_{MgII}, which would be too large to be satisfactory.

One way to reduce these errors would be to use range-2 values instead of range-3 values when the latter are in the range 600–1000, by adding in the counter overflow number when it is appropriate. The measurements in the core of the line (wavelengths 6, 7, and 8), where the strong solar variability occurs, have to be used as range-2 values – their range-3 values are too small and noisy to be useful. Using wing measurements that are in range-2 would help avoid the variations in the range-3 and range-2 relations. Figure 4.4.2 shows that this would often be possible for the short wavelength wing, wavelength 12. Unfortunately, Figure 4.4.1 shows that most of the measurements in the long-wavelength wing occur when their range-2 values are saturated.

Another approach would be to correct for changes in the range-3 and range-2 relation. Although the results in Figures 4.5.1–4.5.3 indicate there is a problem, these monthly results may be inadequate to provide a correction; perhaps the range-3 and range-2 relationship varies from one day to another.

The approach used later in this report was to use a modified ratio, with wavelengths 4 and 10 representing the wing measurements. Figure 4.4.3 and a similar graph for wavelength 10 show that these wavelengths always have good range-2 values as long as the counter overflow value is added to those observations whose range-3 values exceed 650 and the concurrent range-2 value is below 60,000. On the other hand, these wavelengths are close enough to the h and k emission cores, (i. e., the part of the h and k lines that vary greatly with solar activity), that a small solar signal is included in these absorption-line wall measurements. This is particularly

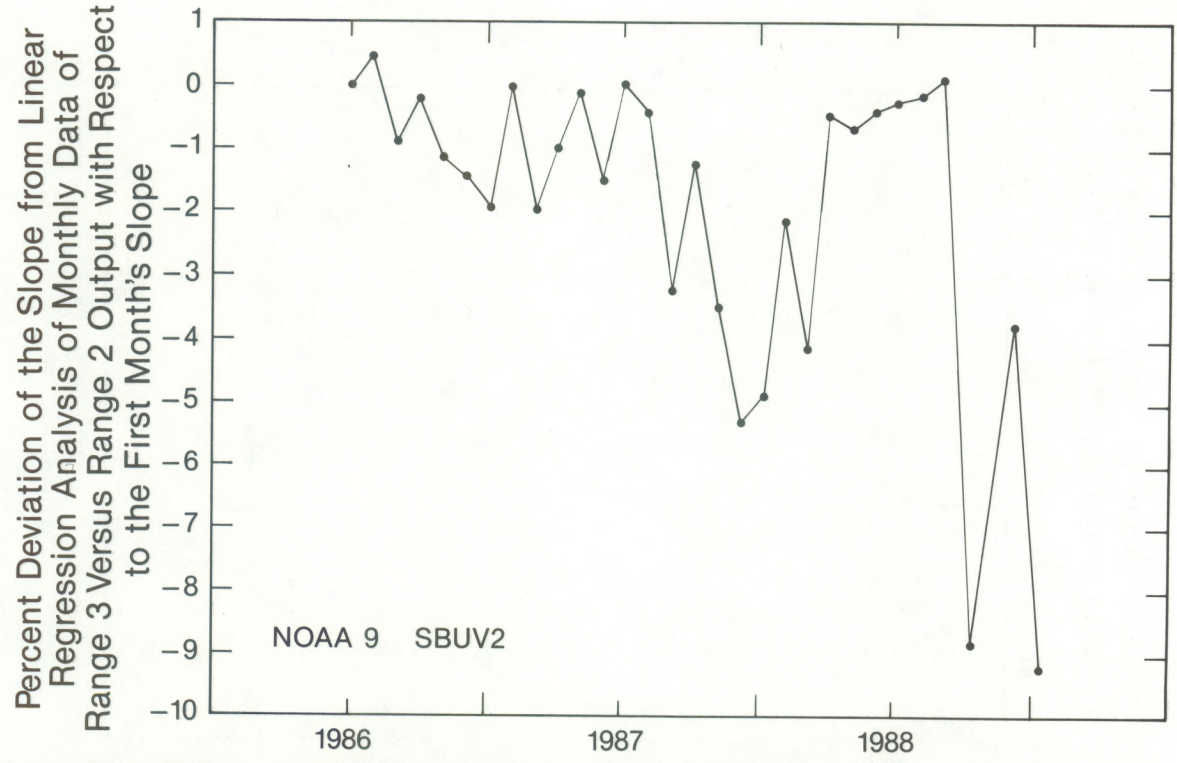

Figure 4.5.1. Changes in the slope of the linear regression of range-3 values as a function of range-2 values.

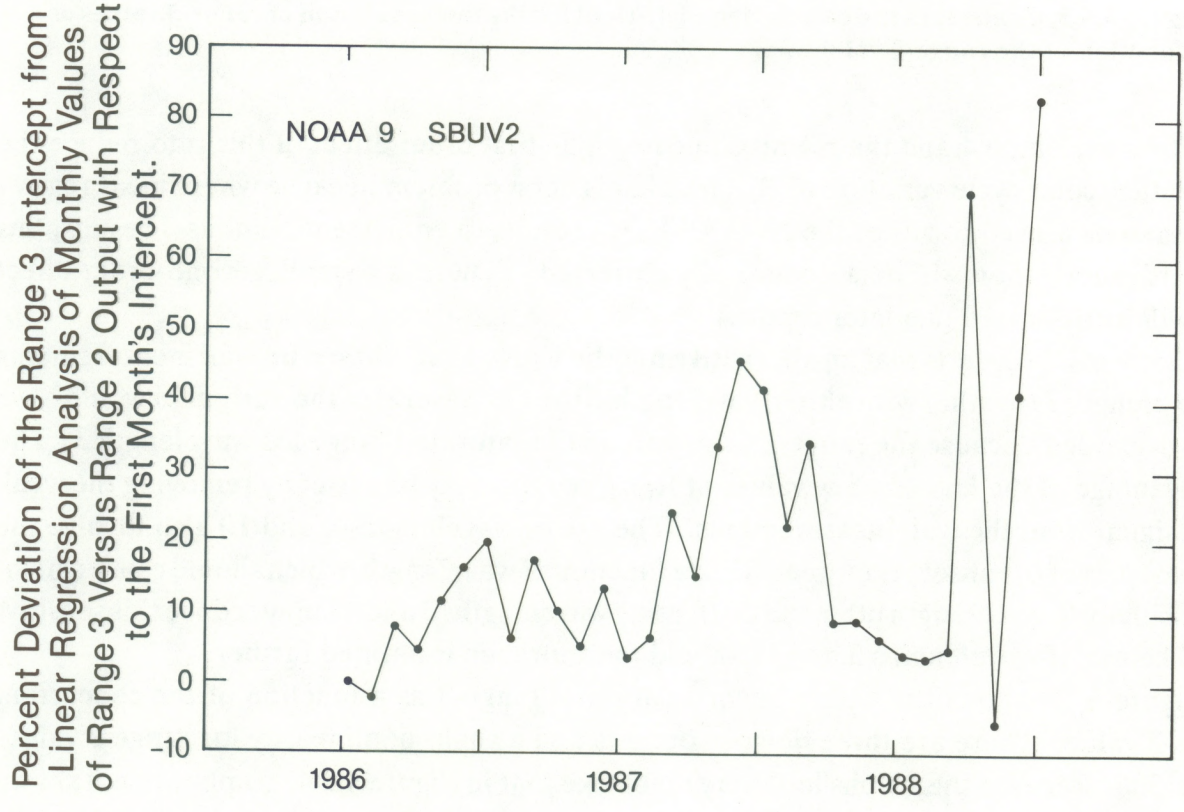

Figure 4.5.2. Changes in the intercept of the linear relation of range-3 as a function of range-2.

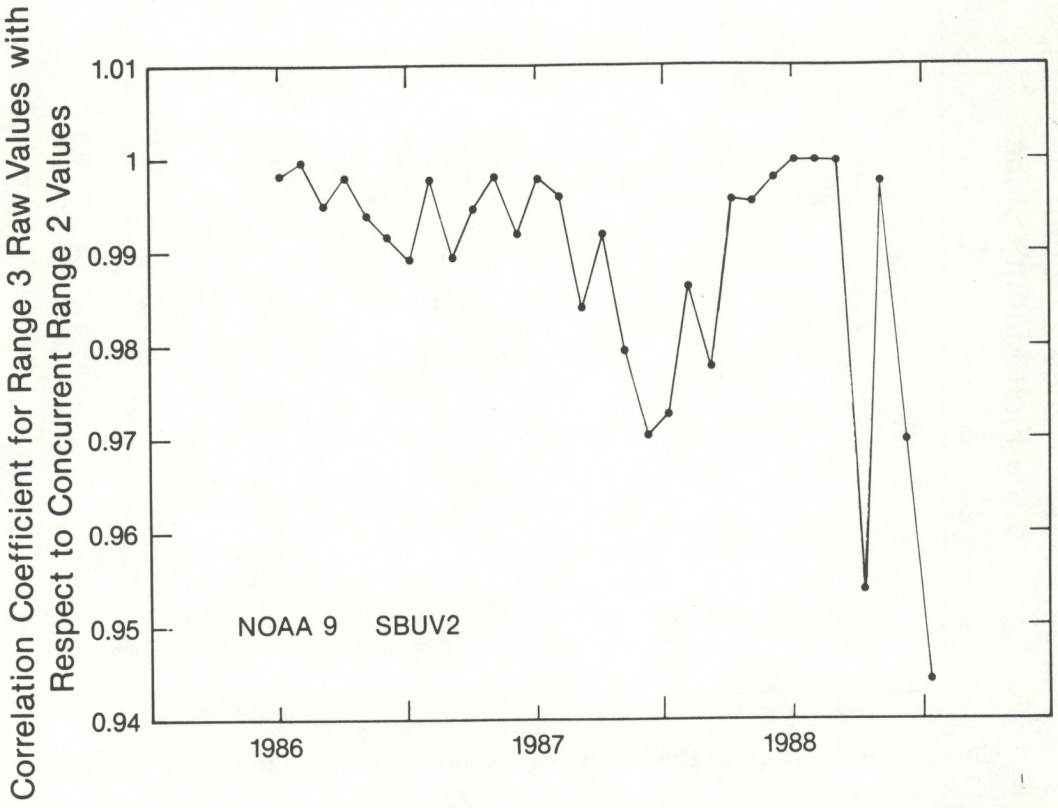

Figure 4.5.3. Changes in the correlation coefficient for the linear relation of range-3 values as a function of the range-2 values.

true for wavelength 4 and the h emission core. The first order effect of this is to reduce the percentage solar cycle variation of R_{MgII}. That is not a problem because when linear regression analysis is used to adjust the NOAA9 R_{MgII} results to equivalent Nimbus-7 results, this first-order reduction will be automatically corrected. (There is a small, second-order effect that will be discussed in a later report.)

Figure 4.4.2 suggests that an alternative may be to use a ratio based on wall measurements at wavelength 3 together with either wavelength 10 or 11. Several of the early data would have to be discarded because the range-2 values are in the saturated range for wavelength 3. The disadvantage of the loss of a few values of R_{MgII} per day may be offset by removing the weak solar signal from the wall measurements. The use of wavelengths 4 and 10 also involve the steepest part of the absorption-line wall as a function of wavelength, which should cause a higher sensitivity to wavelength jitter and drift; using wavelengths 3 and 11 may reduce this sensitivity. The use of wavelengths 3 and 11 should therefore, be examined further.

Figure 4.5.4 shows the nearly linear relation of range-3 as a function of the concurrent range-2 value. There are three obvious outliers and a slight nonlinearity for range-3 values below 300. Because the graphs look very much like that in Figure 4.5.4, graphs are not shown here for the following periods: (1) northern-hemisphere fall equinox, September and October, 1986; (2) winter solstice, December, 1986 and January, 1987; (3) spring equinox, March and

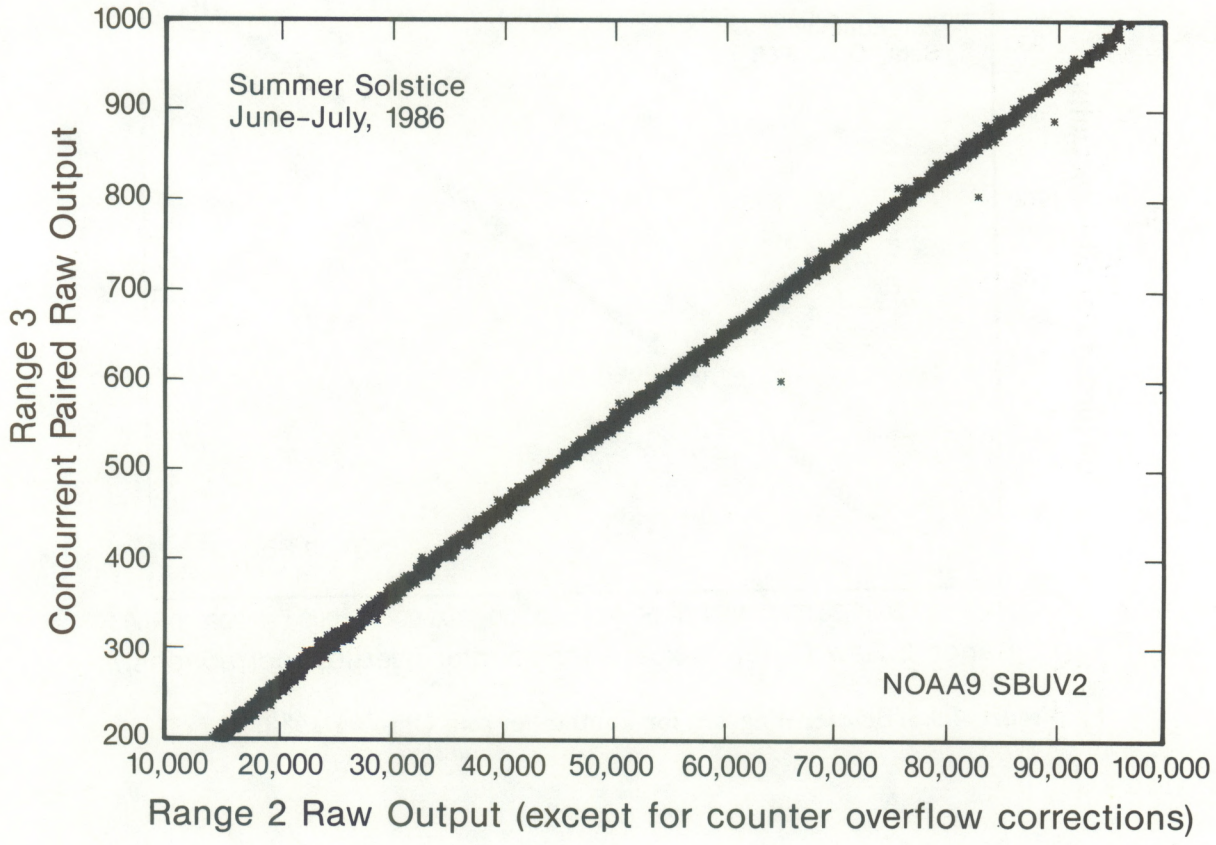

Figure 4.5.4. Scatter diagram of range-3 versus range-2 values for summers solstice, June and July, 1986.

April, 1987; (4) summer solstice, June and July, 1987; (5) fall equinox, September and October, 1987; (6) winter solstice, December, 1987 and January, 1988; (7) spring equinox, March and April, 1988; and (8) summer solstice, June and July, 1988. The main differences in those graphs were the absence of the three outliers seen in Figure 4.5.4 and a tendency toward fewer data points for range-3 values below 250 and near-range-3 values equal to 400. Using viewgraph overlays, it is possible to see a shift upward by about half the data-trace height in the curve for case 6 above; so the shifts indicated in Figures 4.5.1–4.5.3 are quite subtle as compared to the scatter plots themselves. Figures 4.5.5 and 4.5.6 show two of the most extreme changes in these scatter plots. There are fewer points in Figure 4.5.5 because of the loss of solar data for many of the days in those months (caused by the unexpected occultation of the Sun by part of the satellite). Nevertheless, the curve in figure 4.5.5 lies just above that shown in Figure 4.5.4 at the high-intensity end of the graph. In Figure 4.5.6, the data trace is much thicker than in Figure 4.5.4, which suggests undesirable day-to-day variations in the relation between range-3 and range-2 values during December 1988 and January 1989.

The analyses discussed above in Sections 4.1–4.5 were conducted by J. Barrett and interpreted by R. F. Donnelly.

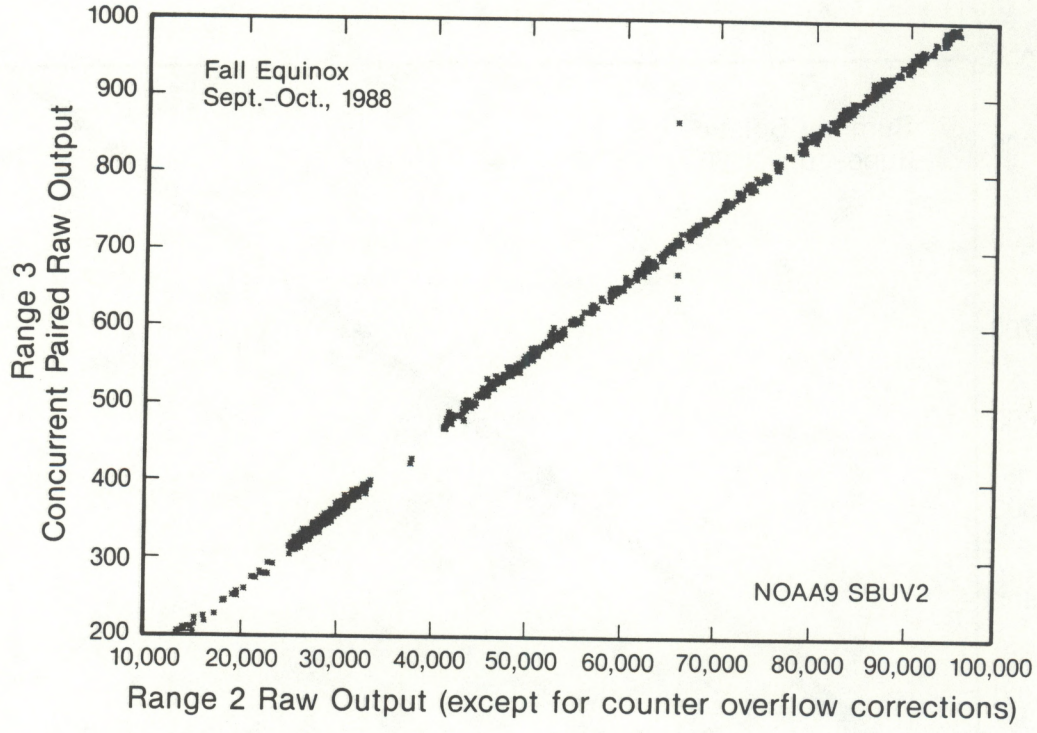

Figure 4.5.5. Scatter diagram for September and October 1988.

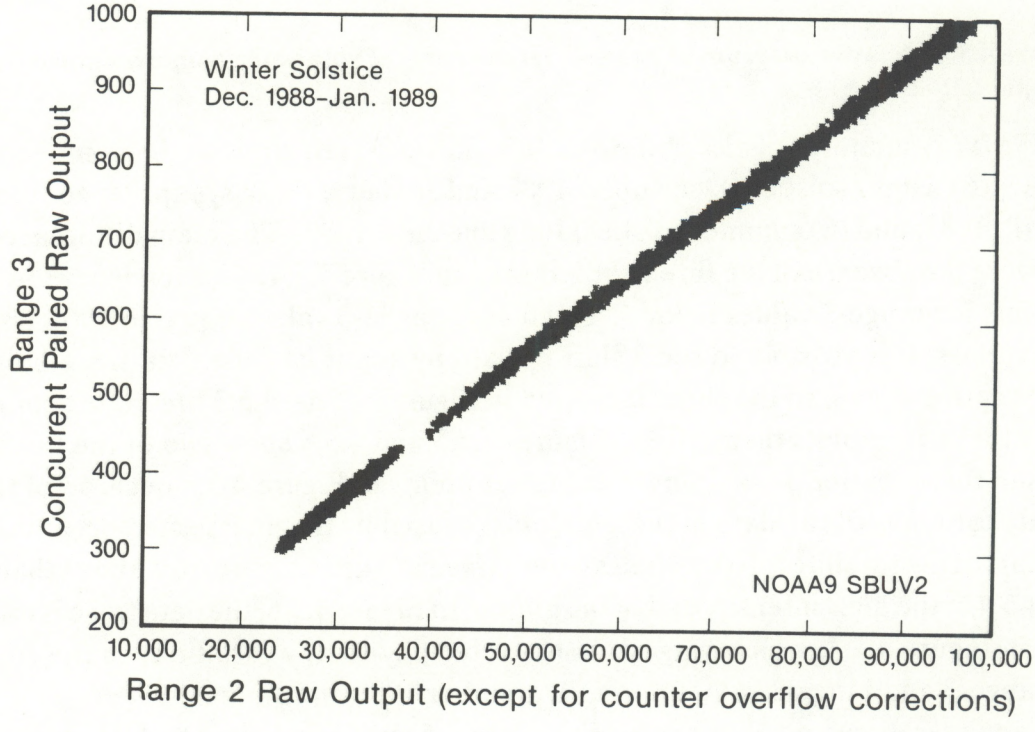

Figure 4.5.6. The thickened trace at high intensities indicates fluctuations.

4.6. The Mg II h and k Line Shape

4.6.1. Ratios to the Core and Near-Walls of the Absorption Line

As an exploration of the wavelength jitter and drift problem discussed in Section 4.4, ratios of raw range-2 outputs to that at the center-of-the-line wavelength (No. 7) were studied for the other core wavelengths and lower-wall wavelengths. The daily median values and their monthly mean were computed for the following range-2 output ratios: $C(5)/C(7)$, $C(6)/C(7)$, $C(8)/C(7)$, $C(9)/C(7)$, and $C(9)/C(5)$. The number within the parentheses is the wavelength number, counting from the top downward in Figure 3.1 and from the right to the left side in Figure 4.1.1. The ratios are approximately equal to the incoming flux ratios for these wavelengths; this is evident for the following reasons: $C_{02} = 65.4$ is negligible in equation (1) (Chapter 1), for this crude look at the data, since all these measurements exceed 14,000 in the digitized range-2 output values. The variation of goniometric angles over the $\pm 4s$ interval for these ratios, with respect to wavelength 7, are small. The variation of the instrument-transfer functions with wavelength over the +.9 to -.12 nm range relative to wavelength 7 is also small. So the angle- and wavelength-dependent terms of the equation converting range-2 outputs to fluxes approximately cancel in these ratios. In Figure 4.6.1, variations related to solar activity appear with increasing activity, causing decreases in the ratio because the solar signal is strong

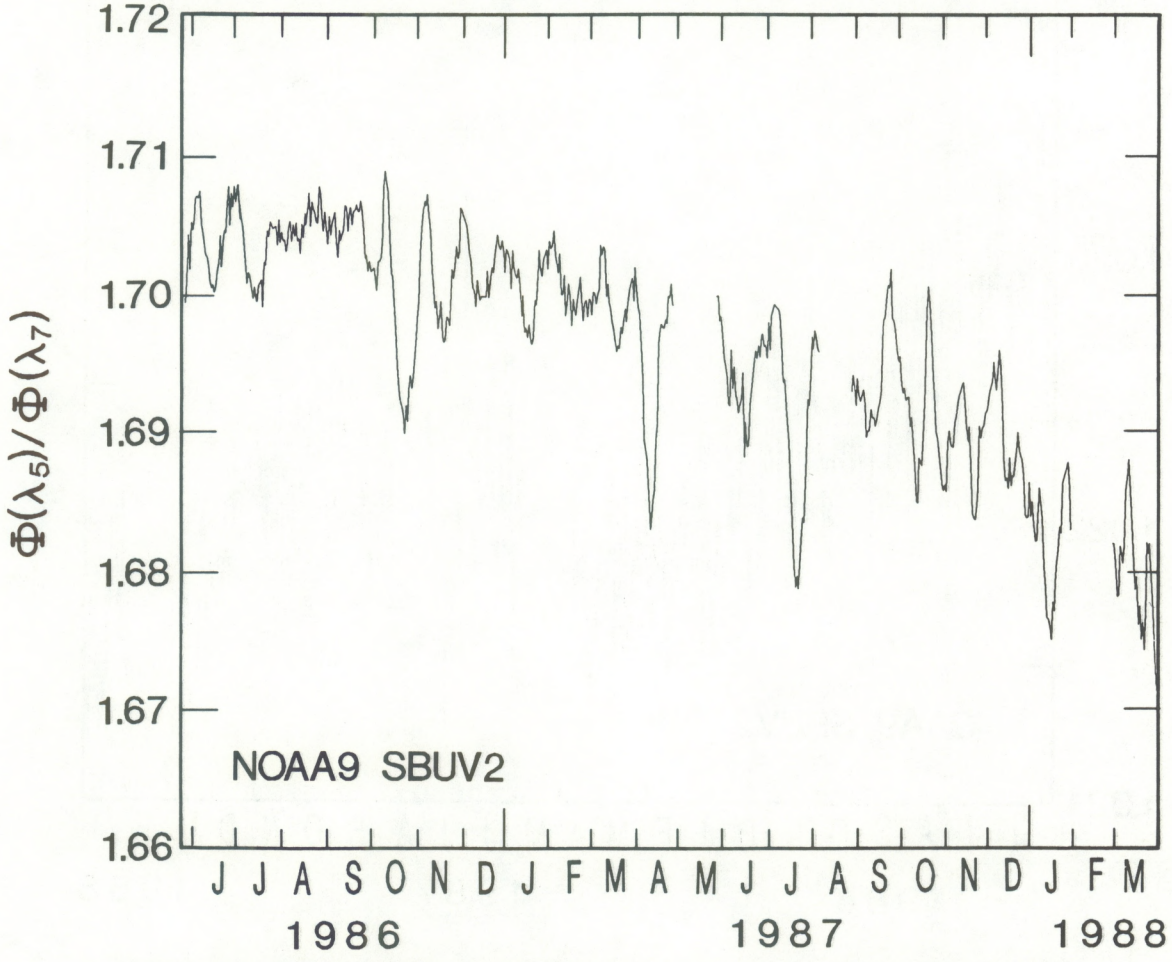

Figure 4.6.1. Daily median ratio of solar flux at wavelength 5 to that in No. 7.

in the denominator term (i. e. wavelength No. 7) and much weaker in wavelength No. 5. For example, the sharp valleys in late October 1986 and early April and mid-July in 1987 correspond to solar-rotational peaks in solar activity seen at Earth. The long-term downward trend with increasing time corresponds to the long-term increase of solar activity during the rise of solar cycle 22. Considering Figure 4.1.1, it is clear that we do not have to move very far away from the core wavelengths (6, 7, and 8) to have the solar signal appear as a dominant feature of the flux ratio. The monthly mean ratio for September 1986, the month of the solar cycle minimum between cycles 21 and 22, was 1.705. Since the solar signal is so strong in this ratio, instrumentation effects are not as clear. The small day-to-day jitter, for example during July-September 1986, is probably caused by instrumental effects.

Figure 4.6.2 shows the ratio for the flux in the longest core wavelength to that at the wavelength nearest the center of the line. The relative solar signal is strong and almost equal in both the numerator and the denominator, so this ratio does not show a strong solar signal. If one uses a viewgraph of Figure 4.6.1 and overlays it on Figure 4.6.2, the latter's weak solar signal becomes more evident; for example the large solar rotational variations of October 1986 and

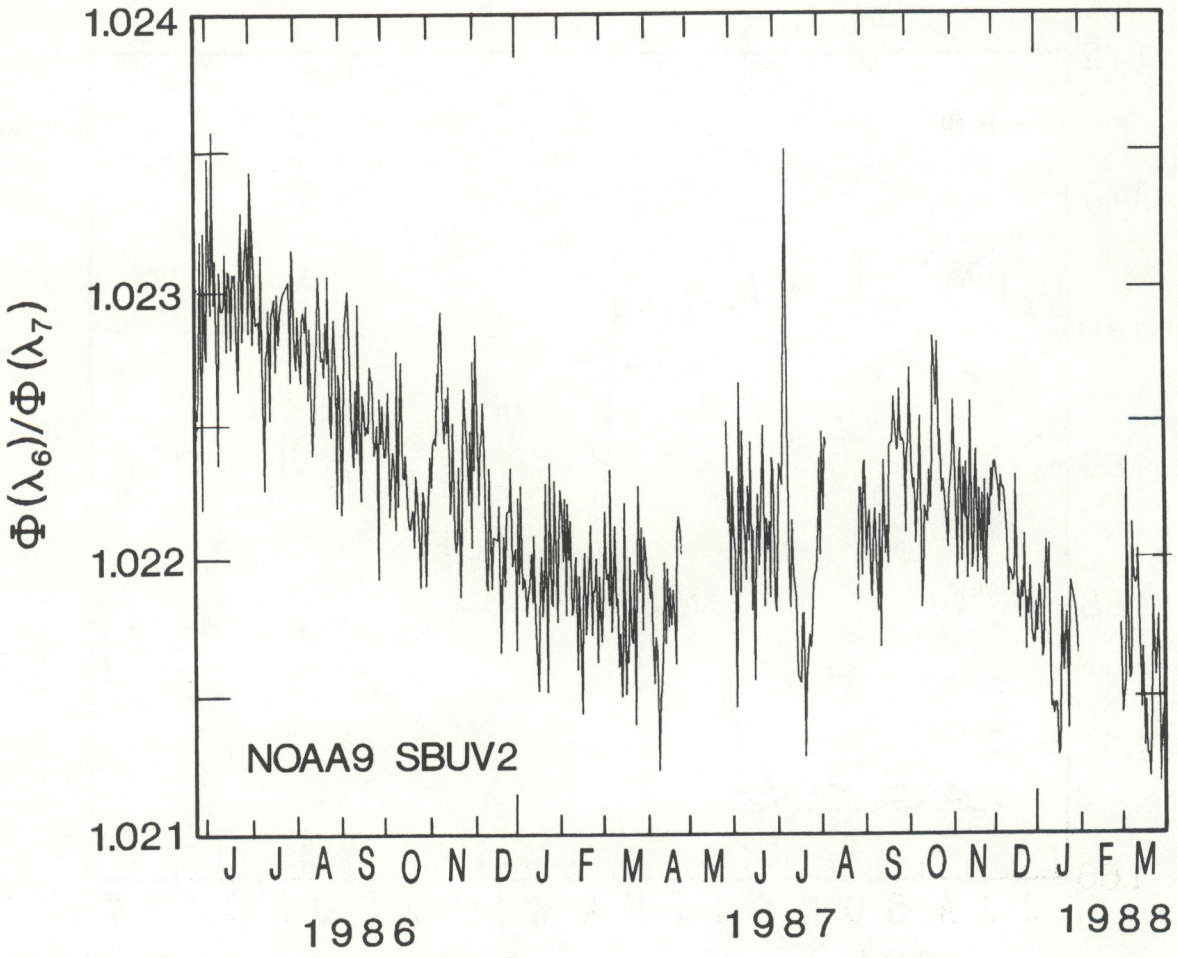

Figure 4.6.2. Daily median range-2 output ratio of core wavelengths 6 to 7.

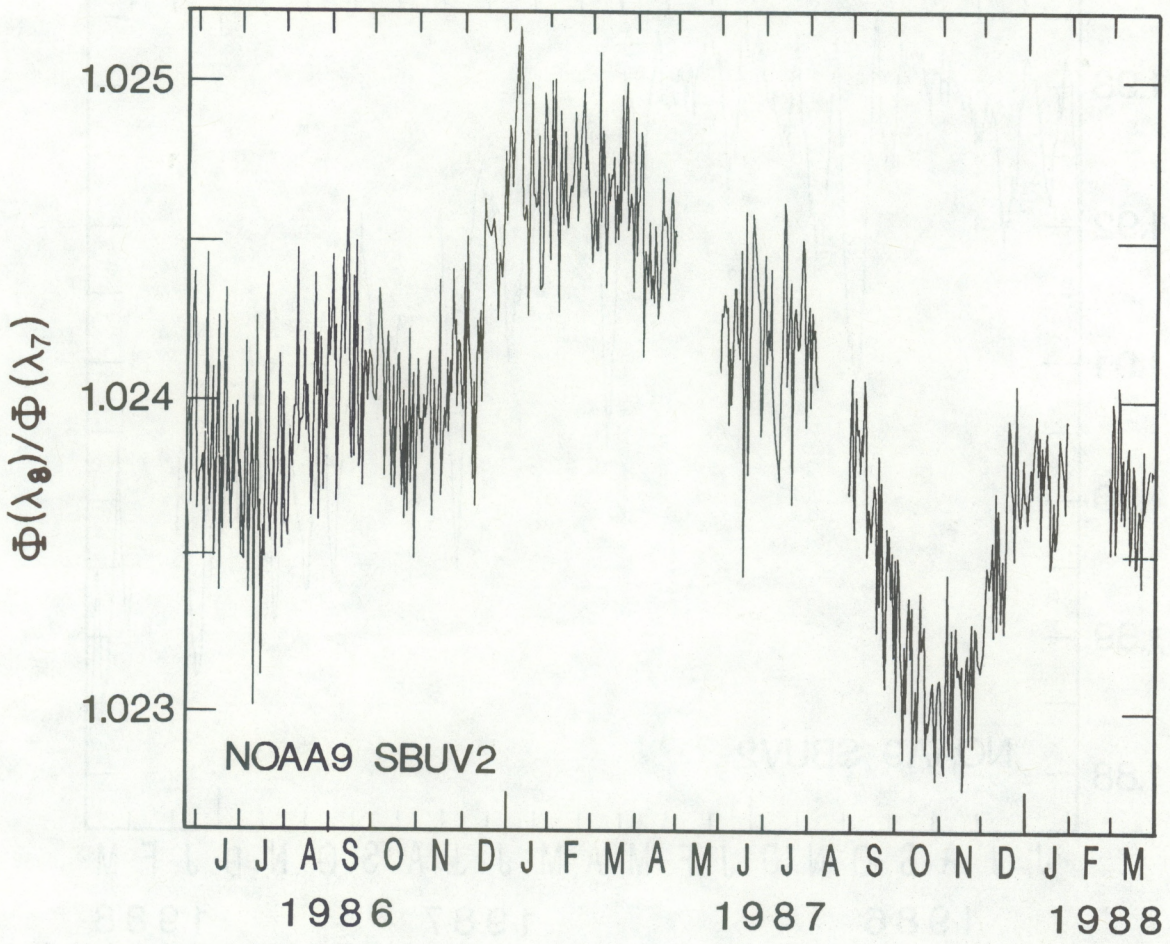

Figure 4.6.3. Daily median range-2 output ratio of core wavelengths 8 to 7.

April and July 1987 become evident as dips, consistent with the solar signal being larger for wavelength 7 than for wavelength 6. The three large solar rotational variations discussed above are a little less than 0.1% of the average ratio in Figure 4.6.2 but a little more than 1% of that in Figure 4.6.1. The solar signal is about 13 to 14 times stronger in Figure 4.6.1 than in Figure 4.6.2. Note that the range of values in Figure 4.6.2 is about 0.2% of the average value, while it is about 2.2% in Figure 4.6.1. The long-term trend in Figure 4.6.2 appears to be inversely related to that of the estimated wavelength of minimum flux shown in Figure 4.3.1. The monthly mean value for September 1986 is 1.0226. The three gaps in all the figures of this section were caused by tapes too difficult to read at the time of this analysis (June 1988); those tapes were successfully processed later.

Figure 4.6.3 has a scale similar to that in Figure 4.6.2. The solar signal is not evident in this ratio of the range-2 outputs for wavelength 8 to that for wavelength 7; the relative solar signal must be about the same for wavelength 8 as it is for wavelength 7. This is consistent with the wavelength of maximum solar signal being a little shorter than that for the minimum flux; wavelength 7 is closer to the latter. We expect the wavelength of strongest relative solar signal to be a little shorter because the change in flux with solar activity is about 1.43 times stronger in

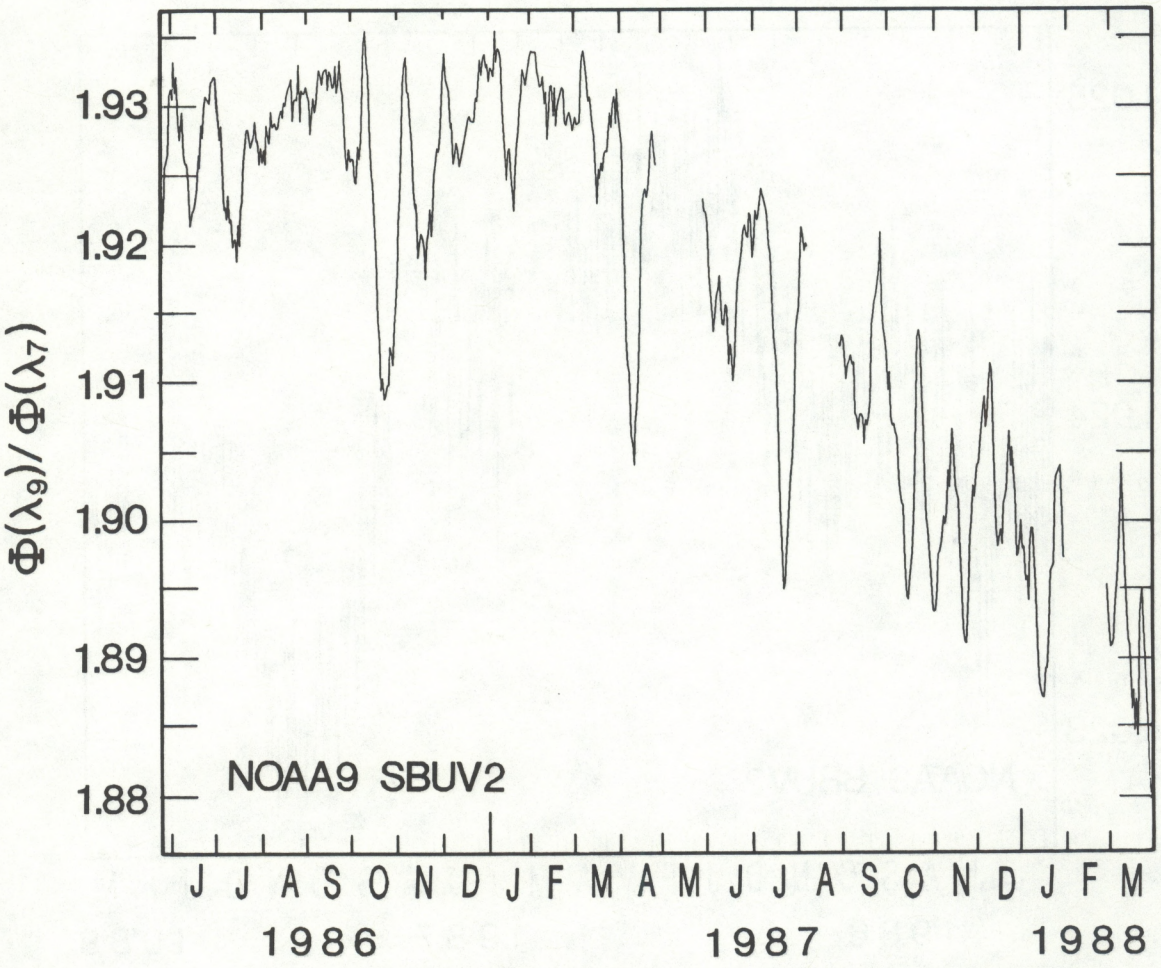

Figure 4.6.4 .Daily median range-2 output ratio of core wavelengths 9 to 7.

the k emission core than in the h emission core (see Figure 2.2.) The monthly mean ratio for September 1986 is 1.0241. The long-term trend, about 0.2%, in Figure 4.6.3 is roughly similar to that in Figure 4.3.1 and inversely related to that in Figure 4.6.2.

Figure 4.6.4 is similar to Figure 4.6.1; a strong inverted solar signal is caused by the strong relative solar signal at wavelength 7 relative to that at wavelength 9. The monthly mean value for September 1986 was 1.932, which is higher, relative to the result for Figure 4.6.1, than would be expected from Figure 4.1.1. This discrepancy in Section 6.2.1 seems to be a problem of atmospheric absorption affecting the spectrum of Hall and Anderson (1988), causing the short-wavelength wall and wing of their spectra to be too low in Figure 4.1.1. The higher values of Figure 4.6.4 relative to 4.6.1 are consistent with wavelength 9 being an additional 0.3 nm, or two wavelength steps of the spectrometer, away from wavelength 7 than is wavelength 5. The overall variation in Figure 4.6.4 is a little less than 3%; the three strongest solar rotational variations each have an amplitude near 1.4%, about 1.3 times larger than for Figure 4.6.1. The larger solar signal here is consistent with wavelength 9 being further from wavelength 7 than is wavelength 5. This means that the side of the passband response for wavelength 9 picks up less

of the solar signal from the h and k emission cores than in the case of wavelength 5; therefore, less solar signal in the numerator subtracts from the strong solar signal of wavelength 7 in the denominator for wavelength 9 than it does for wavelength 5. Figure 4.6.5 differs from the preceding figures because it involves two wavelengths from the two main walls of the unresolved h and k absorption lines and none from the core of the line. It includes a weak solar signal, evident by the three strong solar rotational dips in Figure 4.6.1 also seen in 4.6.5. Their amplitude here is about 0.35%, much smaller than in Figures 4.6.1 and 4.6.4. The solar signal is inverted and in agreement with our expectations that the relative solar signal is stronger for wavelength 5 than for wavelength 9; wavelength 5 is 0.3 nm closer to the h and k emission cores, and the side of the passband picks them up a little more strongly. The long-term trend shown in Figure 4.6.5 looks much like that in Figure 4.6.3 but is larger in amplitude, about 1.1%. This follows the long-term trend in wavelength seen in Figure 4.3.1. Note that the calculations used to estimate the wavelength of minimum flux involved measurements at wavelength positions 6, 7, and 8, and did not involve data from wavelengths 5 or 9. In March 1987 (Figure 4.6.5), when the wavelength of the minimum increased to a peak, the wavelength scale of the NOAA9 SBUV2 monitor must have shifted slightly to lower wavelengths so that the actual wavelength observed at

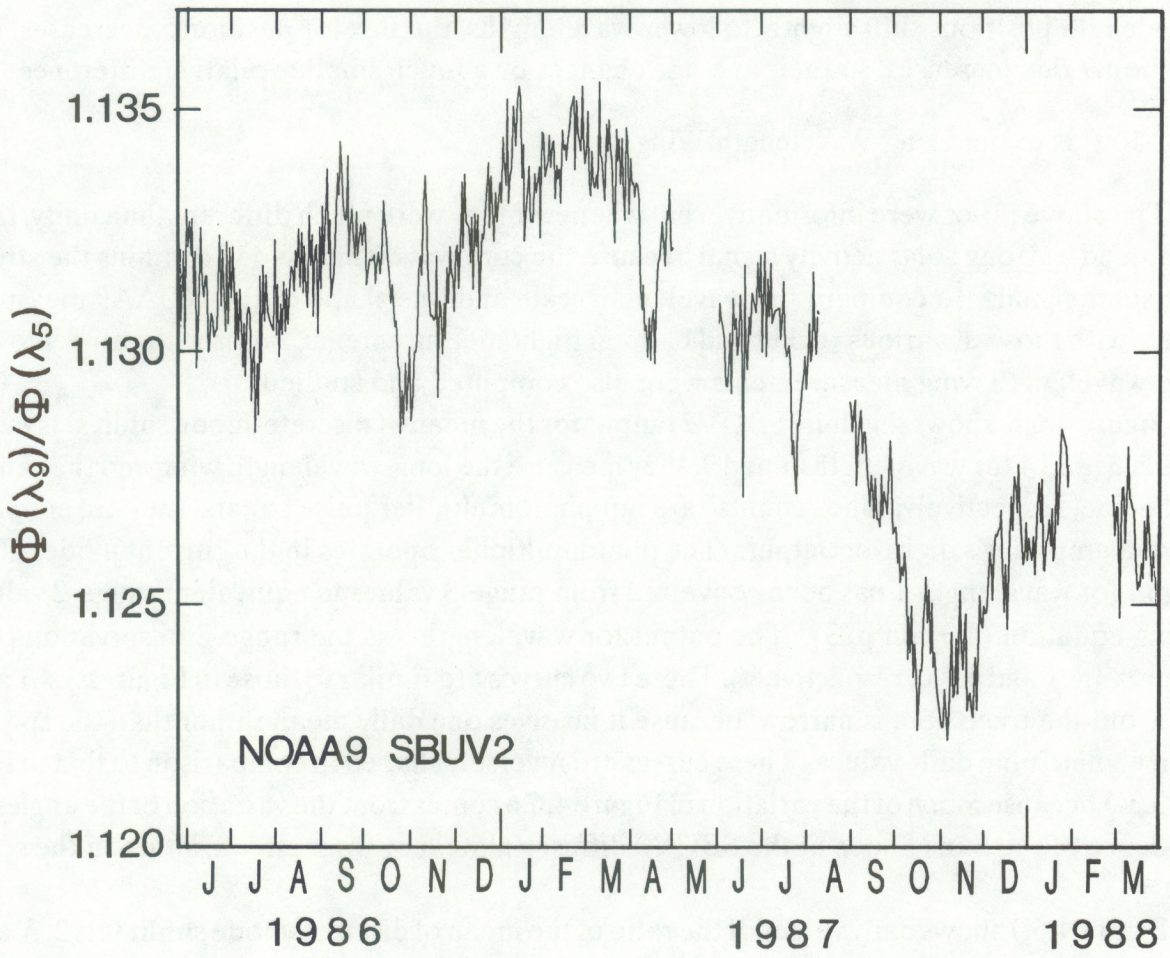

Figure 4.6.5. Daily median range-2 output ratio of core wavelengths 9 to 5.

position No. 7 was about 0.003 nm shorter than it had been at the end of May 1986. If this same shift applied to positions Numbers 5 and 9, then 5 would have moved downward on the long-wavelength wall and 9 would have moved upward on the short-wavelength wall. Consequently, the ratio of the flux at position 9 to that at 5 would have increased from May 1986 to a peak near March 1987, as it did. The steepness of the walls, with respect to wavelength, and the changes in opposite directions for wavelengths 5 and 9 cause a much larger variation of the wavelength drift signal seen in Figure 4.6.5 than in any of the other figures. Similarly, the long-term drift to a minimum in October to November 1987 observed in Figure 4.3.1, predicts the concurrent minimum seen in Figure 4.6.5. The lower values of March 1988 observed in Figure 4.6.5, relative to the March 1987 values seen in Figure 4.3.1, result from the presence of the inverted solar signal evident in Figure 4.6.5. The main point is that the long-term trend of the wall wavelengths (after discounting the weak solar signal) is in agreement with the wavelength drift results derived solely from the core wavelength positions.

If wavelengths 5 and 9 were used to form a ratio of the core flux measurements to the average of two wall wavelengths, the effect of the wavelength drift signal would be much smaller than is shown in Figure 4.6.5 because of the compensating effect of the drift in the average of the two wall wavelengths versus the amplifying effect of the ratio in Figure 4.6.5. When the wavelength positions shift slightly to lower wavelengths, the flux for position 5 decreases, but position 9 flux increases, so their average changes by a much smaller relative difference.

4.6.2 Ratios to the Long-Wavelength Wing

The above ratios were informative, but whenever they were much different than unity, they contained a strong solar activity signal because the core wavelength No. 7 contains the strongest solar signal. To compare the wavelength scale and line shape of the NOAA9 measurements with those of various rocket and balloon flight measurements, ratios with respect to the long-wavelength wing measurements were also computed and studied.

Figure 4.6.6 shows the daily SBUV2 output for the mean of discrete-mode sunlit sets numbers 2, 3, and 4 for wavelengths 1 and 7; they measure the long-wavelength wing and the center of the line, respectively. The "counts" are not photomultiplier pulse counts; they are simply a current amplifier's digitizer output. The photomultiplier operates in the current mode. The output for wavelength 1 has been converted from range-3 values to equivalent range-2 values (using equation (4.3) on p. 3). The output for wavelength 7 is the range-2 observation (see Figures 4.4.1 and 4.4.6, respectively). These two curves are similar to those in Figures 3.4.1 and 3.4.9, but the trace here is narrow because it involves one daily mean rather than the spread from eight to nine daily values. These curves are inversely shaped in comparison to that in Figure 3.3.3 because much of the variation in Figure 4.6.6 comes from the variation of the angles of incidence of the Sun as seen at the SBUV2 diffuser plate, not from any variation in the solar flux.

Figure 4.6.7 shows daily values of the ratio of the mean of discrete-mode sunlit sets 2, 3, and 4 of the equivalent range-2 output at wavelength 2 to that for wavelength 1 in the top graph. The Sun-angle (or goniometric) signal present in both of these outputs (see Figure 4.6.6) can-

cels out in this ratio. The output is fairly constant (as it should be) near 0.988 except for some short-term noise. This noise is not small enough to be negligible; it is larger than expected, probably because the low range-3 outputs used for these wavelengths has too low a signal-to-noise ratio. Some of the short-term structure may be a consequence of not including the Sun-angle corrections.

The center graph of Figure 4.6.7 shows a roughly sinusoidal long-term trend. Considering Figures 3.4.1, 4.4.1, 3.4.4, 3.4.5, and 4.4.2 (where most of the range-2 output values are above the counter overflow level, 65,535), most of the values shown would be based on range-3 output values for both wavelengths 1 and 3. Therefore, the range-3 to range-2 drifts, discussed in Section 4.5, would not affect this ratio. The short-term noise in this ratio is similar in size and structure to that in the top graph, but the percentage variation is largest in the middle graph.

The bottom graph in Figure 4.6.7 shows the Sun-diffuse- angle signal evident in Figures 4.6.6 and in Figure 3.3.3 (with an inverted pattern). Comparing the bottom panel with the

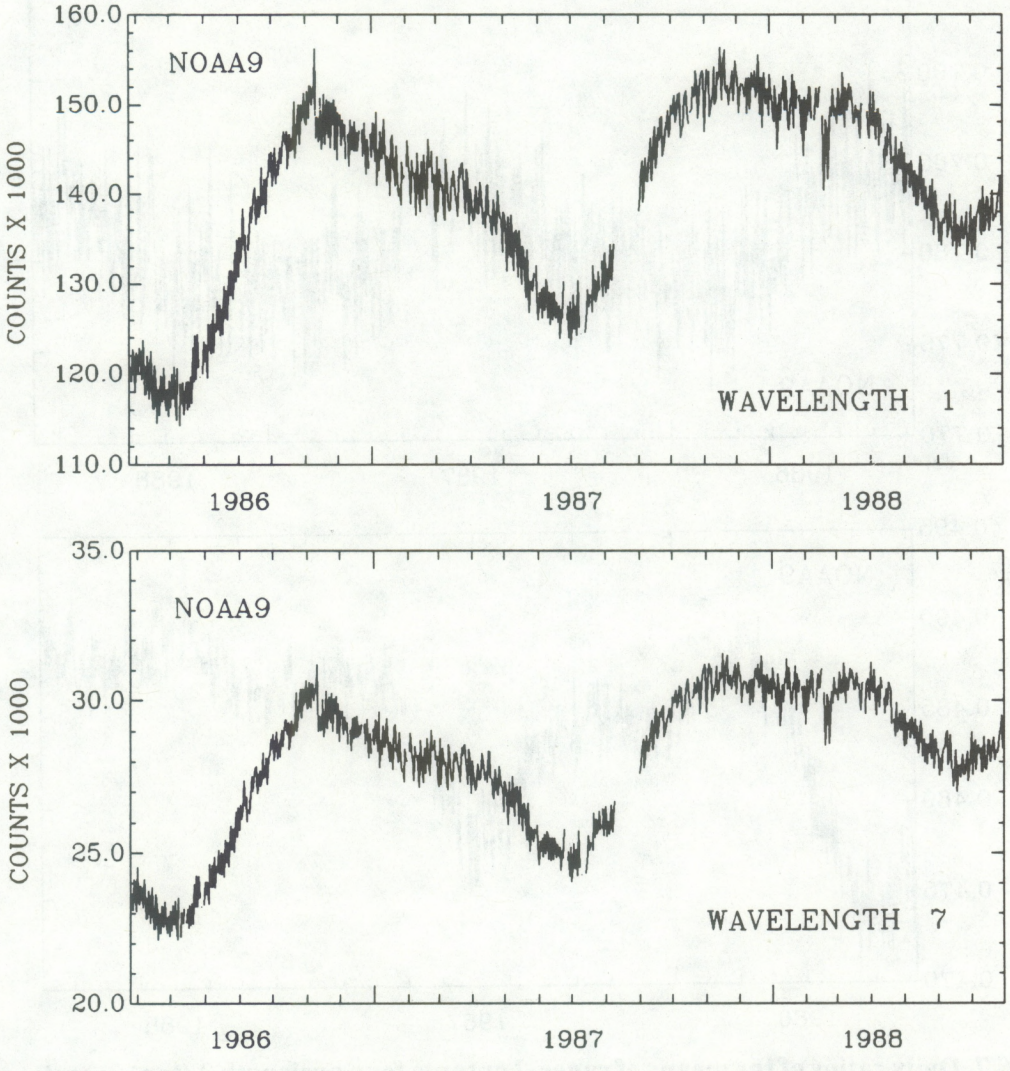

Figure 4.6.6. Daily means of range-2 outputs for wavelength 1 (top) and wavelength 7 (bottom), from the discrete-wavelength mode sunlit sets 2, 3 and 4.

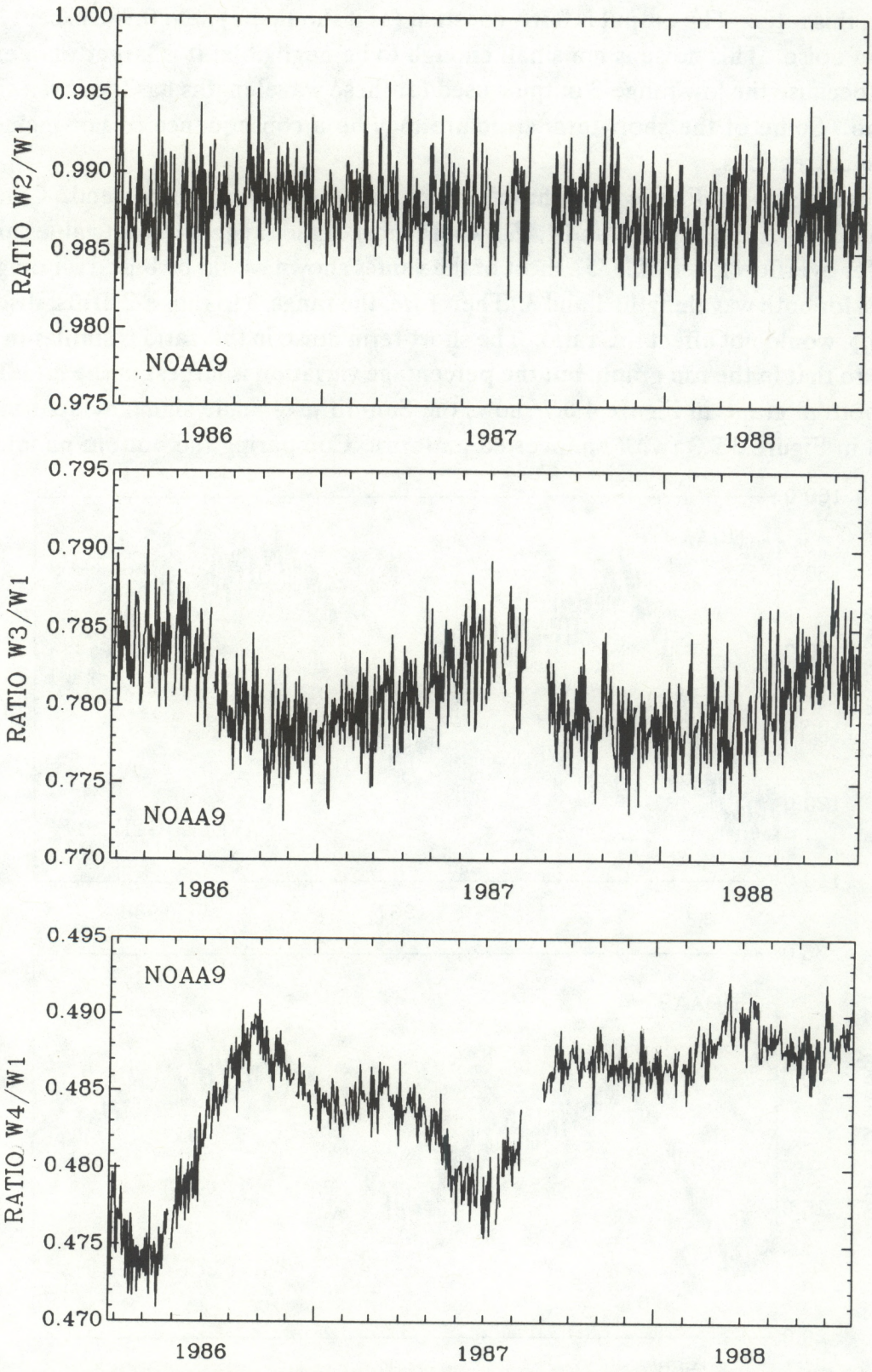

Figure 4.6.7. Daily ratios of the means of range-2 outputs for wavelength 2 (top), wavelength 3 (middle), and wavelength 4 (bottom), relative to wavelength 1, for the discrete-wavelength mode sunlit sets 2, 3, and 4.

middle graph in Figure 4.6.7, the long-term pattern in the middle graph can be interpreted as a weak Sun-diffuser-angle signal, where the ratio increases with increasing Sun azimuth angle, (the inverse of the relation in the bottom graph). In all the graphs in this section, *Wn* stands for the equivalent range-2 output for wavelength position n, $n=1, 2, \ldots 12$.

The top graph in Figure 4.6.8 includes a strong solar signal as well as the Sun-diffuser-angle signal (about 3% in amplitude). The solar signal is expected because wavelength 7 is from the center of the line and includes the strong solar signal from the h and k emission cores. The ratios for the output at wavelength 6 relative to that at wavelength 1, and also for wavelength 8 relative to wavelength 1, closely resemble the graph for wavelength 7 except that the curve is higher by about 0.005; those graphs are not shown here.

The middle graph in Figure 4.6.8 shows a strong Sun-diffuser-angle signal but very little solar signal. In terms of fractional variations, the Sun-diffuser-angle signal is again about 3% for this wavelength-10 case, which is also true for the wavelength-4 case shown at the bottom of Figure 4.6.7. The bottom graph in Figure 4.6.8 shows very small variations like those at the top of Figure 4.6.7. The graph for wavelength 11 looks just like that for wavelength 12, so it is not shown here. Most of the values for wavelength 12 would be equivalent range-2 values derived from range-3 outputs. Figure 4.4.2 shows that most of the wavelength-12 values lie above the range-2 counter-overflow level of 65,535; therefore the values labeled as "preferred" would be range-3 values.

The ratios involving range-3 outputs, namely W2/W1, W3/W1, W11/W1, and W12/W1, have small-to-negligible Sun-diffuser-angle signals despite the large signals present in individual outputs like those in Figure 4.6.6. Ratios involving range-2 values in the numerator and range-3 values for W1, such as W4/W1, W6/W1, W7/W1, W8/W1, W10/W1, and, presumably W5/W1 and W9/W1, have a large Sun-diffuser-angle signal of about 3%. In Section 4.6.1, where the ratios studied involve range-2 outputs with no range-3 values, the Sun- diffuser-angle signal was not evident. To check the consistency of this puzzle, ratios W7/W4 and W7/W10 are shown in Figure 4.6.9. These ratios involve only range-2 values. A strong solar signal is evident. No Sun-diffuser-angle signal is evident. The 1-day noise spike next to the left-side intensity scales in both of these figures is the consequence of using a mean rather than a median when isolated bad points were not removed.

The above suggests that the relation varies between range-3 values and their concurrent range-2 values, where part of that variation includes the Sun-diffuser-angle signal. It may be suggested that the problem lies in taking ratios of raw outputs without correcting for the Sun-diffuser-angles. The above analysis could be improved as follows:

(a) Use piecewise linear interpolation of the denominator values, similar to those used in equations 4.4 - 4.6 on page 4 - 7, so that the numerator values and denominator values are for the same instant in time or for the same Sun-diffuser-angles.

(b) Compute the ratios for each discrete-mode set before averaging.

(c) Compute the median for discrete-mode sets 2–7, where the median is good for removing the effect of isolated bad points.

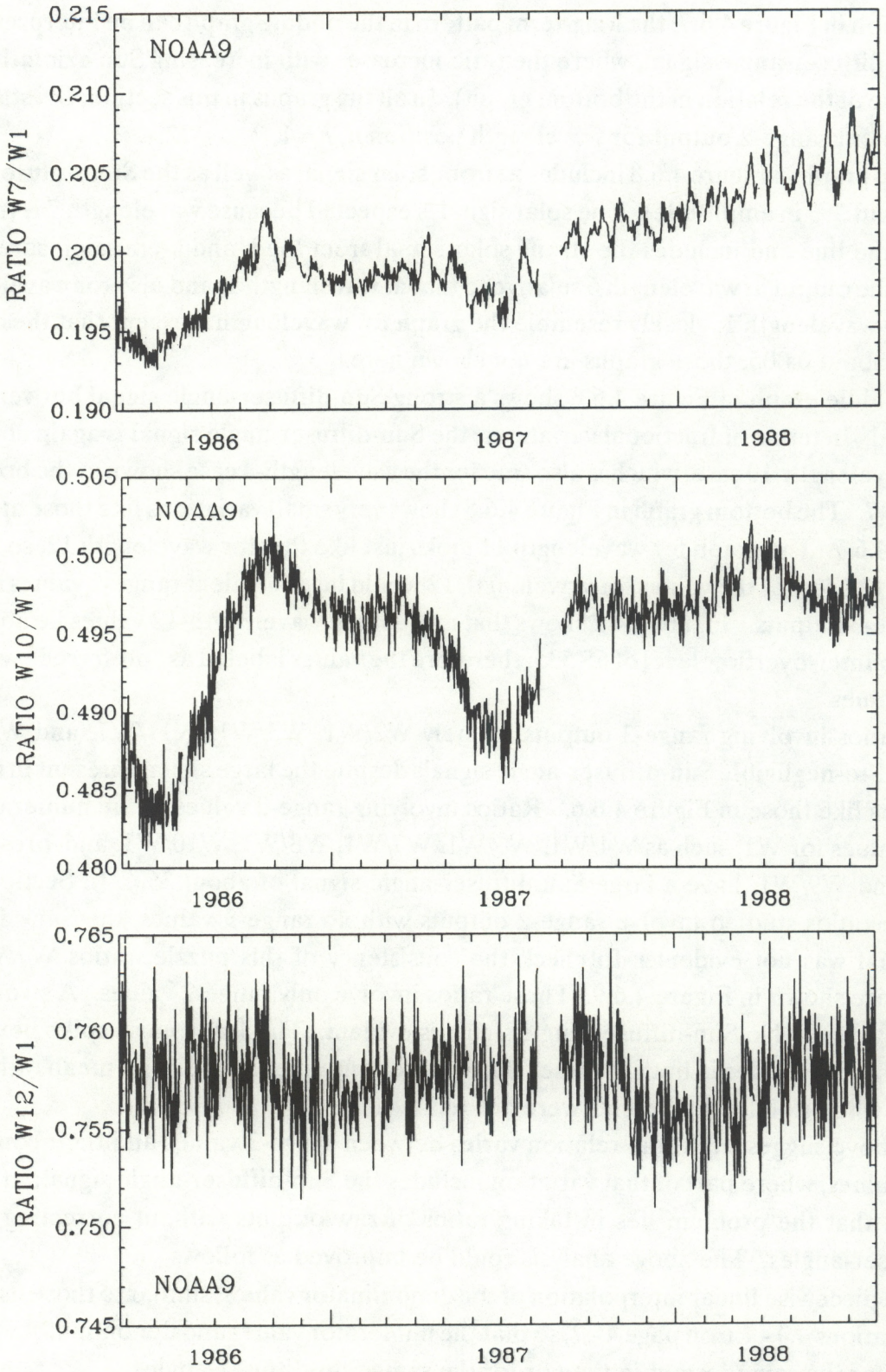

Figure 4.6.8. Daily ratios of the means of range-2 outputs for wavelength 7 (top), wavelength 10 (middle), and wavelength 12 (bottom), relative to wavelength 1, for the discrete-wavelength mode sunlit sets 2, 3, and 4.

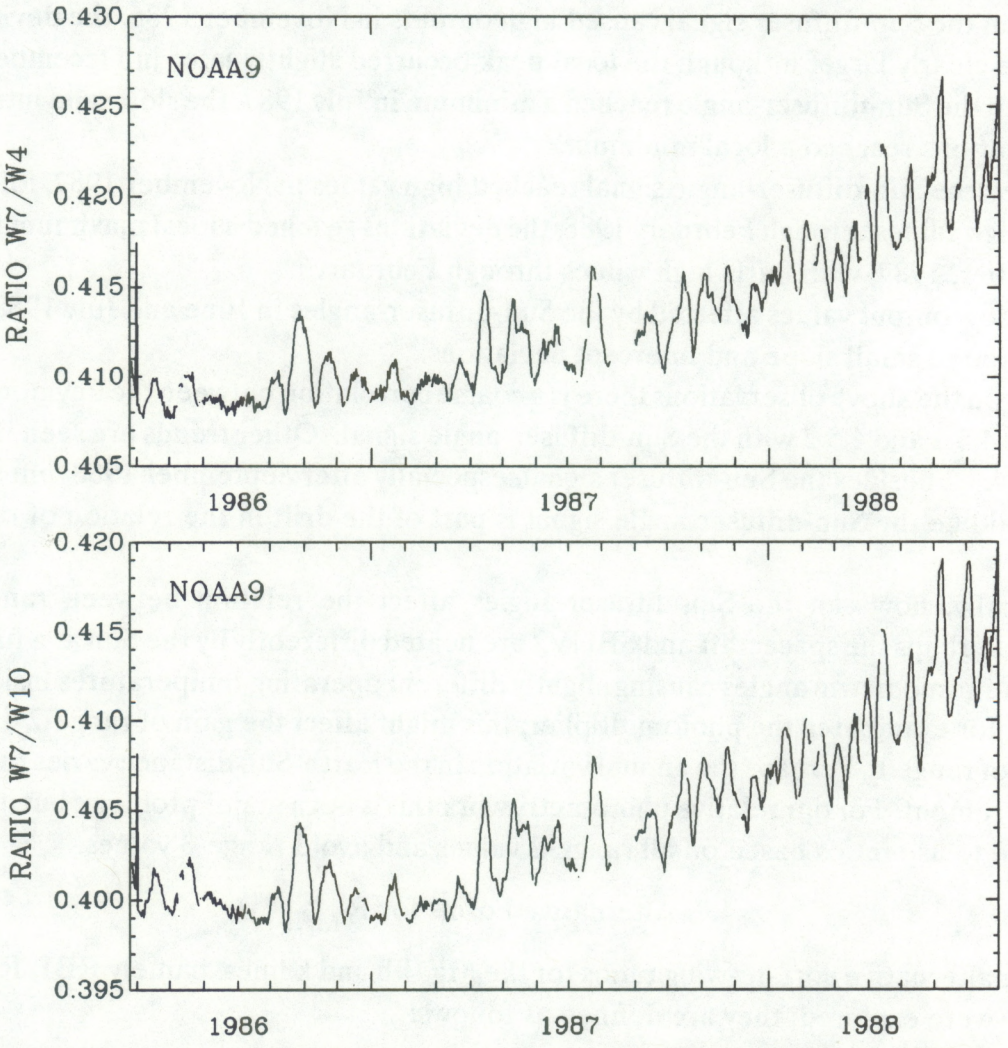

Figure 4.6.9. Range-2 output ratios for center-of-the-line wavelength 7 to wavelength 4 (top) and to wavelength 10 (bottom). The relative variations are nearly identical. A strong solar signal is present. There is no evidence of a Sun-diffuser-angle signal being present.

Such an analysis would avoid criticism of the above ratios having a leakage of the Sun-diffuser-angle signal into the ratio because of the lack of corrections for the Sun-diffuser-angles.

We already have some evidence of the Sun-diffuser-angle signal being a source of error in the relation between range-3 and range-2 values in Figures 4.5.1 and 4.5.2. Those results are based only on concurrent range-3 and range-2 values, where the Sun-diffuser-angles are the same for both the range-2 and range-3-outputs. Comparing Figures 4.5.1 and 4.5.2 with Figure 4.6.6 (Figure 4.4.6. is dominated by the Sun-diffuser signal), one can see that the magnitude of both the slope and intercept deviate from the initial months' measurements in the following ways:

(1) When the Sun-diffuser signal gave low outputs in June-July 1986, the deviations were small.

(2) When the Sun-diffuser signal caused high outputs in November 1986, the deviations were clearly larger although the local peak occurred slightly later in December.

(3) When the Sun-diffuser-angle reached a minimum in July 1987, the slope and intercept deviations reached a local minimum.

(4) When the Sun-diffuser-angle signal reached high values in November 1987, followed by high values through February 1988, the deviations reached a local maximum in December, 1987, with fairly high values through February.

(5) The low output values affected by the Sun-diffuser-angles in June and July 1988 were related to small slope and intercept deviations.

Based on the above observations there is a coarse correlation between the deviations found in Figures 4.5.1 and 4.5.2 with the Sun-diffuser-angle signal. Other trends are seen in Figures 4.5.1 and 4.5.2 besides the Sun-diffuser signal, especially after September 1988; but some annual signal like the Sun-diffuser-angle signal is part of the drift in the relation of range-3 to range-2.

Physically, how can the Sun-diffuser-angles affect the relation between range-3 and range-2? Perhaps the spacecraft and SBUV2 are heated differently by the Sun as a function of these same goniometric angles causing slightly different operating temperatures inside the instrument, for example in the photomultiplier; this might affect the gain of range-2 differently than that of range 1. Perhaps the annual variation in the Earth-Sun distance varies the heating of the instrument. For our relative photometry work this is not a major problem, but it is clearly preferable to use ratios based on all range-2 values and avoid range-3 values.

4.7. Alternative Forms for R_{MgII}

Four alternative core-to-wing ratios for the Mg II h and k lines, namely RB1, RB2, RB3, and RB4 were explored; they are defined as follows:

$$R_{B1}(t) = \frac{4C(7,t)}{[C(1,t) + C(2,t) + C(11,t) + C(12,t)]} \tag{4.10}$$

$$R_{B2}(t) = \frac{2C(7,t)}{[C(1,t) + C(12,t)]} \tag{4.11}$$

$$R_{B3}(t) = \frac{2C(7,t)}{[C(1,t) + C(10,t)]} \tag{4.12}$$

and

$$R_{B4}(t) = \frac{2C(7,t)}{[C(4,t) + C(10,t)]} \tag{4.13}$$

Only the "preferred" range values were used in this analysis, except for wavelengths 4 and 10, where only range-2 values were used. The fact that the 1B data tapes listed range-3 values as "preferred" values for wavelength 4 and 10 when the range-2 value exceeded the counter-overflow value (65,535) was ignored. Consequently, the values used for wavelengths 1, 2, 11, and 12 were range-3 values; those used for wavelengths 4, 7, and 10 were range-2 values. In this

exploratory study, no attempt was made to correct for isolated bad points or to interpolate the wing values with time to estimate the wing values at the same instant as the core measurement. Similarly, a simple average of the wing measurements was used, rather than a linear interpolation, to take into account the unequal wavelength spacing of the wing measurements with respect to the center of the line. A daily mean was computed from the ratios derived from the second, third, and fourth discrete-mode data sets.

The first ratio was an attempt to see whether using only one core wavelength instead of the average of three would significantly increase the noise in the ratio. The second ratio was an attempt to determine whether the short-term noise would increase significantly if we used only two wing measurements instead of four. The third ratio investigated whether the low range-3 values for wavelength 12 were the major source of noise by replacing those values with wavelength 10's range-2 values. The fourth ratio moved the long-wavelength wing to wavelength 4 in the steep wall of the line in order to have all range-2 values.

Figure 4.7.1 shows the results for these four test ratios in comparison with the classical ratio reference. The solid-line reference was based on equation (4.7), but it was applied here for the mean from only sets 2−4 with no correction of isolated bad points or temporal interpolations in order to provide an appropriate comparison with the four test ratios. A few 1-day spikes caused by isolated bad points are evident and should be ignored; Section 4.2 has shown us how to identify and correct them. Note that the extensive day-to-day jitter is greatly reduced in the B4 results in the top curve. We see no significant difference in the B1, B2, B3, and reference results.

Using only range-2 values in the B4 ratio made a marked improvement. It also resolved a long-term difference that had arisen between our comparisons of the classical ratio with the Ca-K 1A index, which will be discussed in Section 6.3. Finally, it also resolved long-term differences between the classical Mg II ratio results from the NOAA9 and NOAA11 SBUV2 measurements. Because of these improvements, we adopted the "Modified Ratio" given by equation (4.8). Only range-2 values are used, including corrections for counter overflows for wavelengths 4 and 10; corrections for isolated bad points were included. The temporal interpolations described by equations (4.5) and (4.6) were used for the outputs at wavelengths 4 and 10 to obtain estimates of their values at the same instant in time (and at the same Sun-diffuser-angles) as the core or wavelength 7 measurement. The daily average was then derived from the median of the ratios from the sunlit discrete-mode measurements 2 through 7.

Refinements that should be evaluated include the following:

(1) Use a linear interpolation between the wing measurements to take into account their unequal wavelength spacing relative to the wavelength-7 measurement.

(2) Include the small wavelength dependent weightings for wavelengths 4 and 10, relative to that for wavelength 7, derived from the preflight K and R factors in equation (1.1).

(3) Reconsider whether wavelengths 6 and 8 should be included with wavelength 7 in an average of the core measurements.

(4) Examine the value of using range-2 outputs for wavelength 3 (and possibly range-2 values from wavelength 11) in lieu of wavelength 4 (and 10) at the cost of forfeiting the

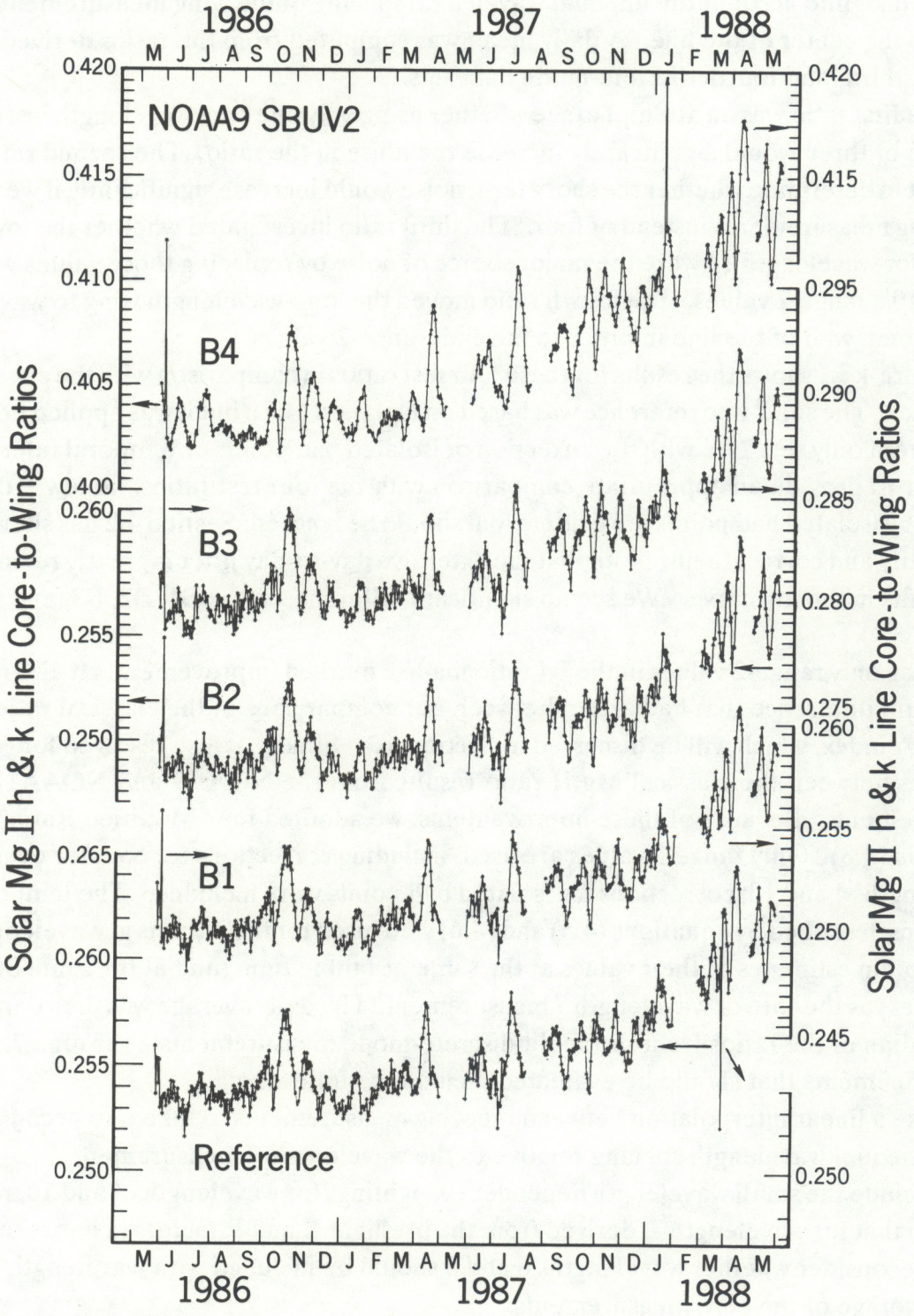

Figure 4.7.1. Test cases for alternative Mg II ratios in reference to the classical Mg II ratio.

range-3-dominated (or range-2-saturated) early sets of daily discrete mode measurements.

(5) Possibly correct for the small nonlinearity for the range-2 levels based on the overall system linearity calibrations performed before the instrument was launched.

In the last case, it is not clear where in the system those small nonlinearities occurred or how they would shift as the instrument aged. Using solely range-2 values, including those from the linear range above the counter overflow level, avoids the nonlinearities that occur for low range-3 values.

The above analysis led to a discovery of the value of the modified ratio. We had previously expected that moving the wing measurements into the steep walls of the wings would cause the resultant modified ratio to be too sensitive to wavelength drift and jitter. Fortunately, excellent wavelength repeatability is one of the best features of the SBUV2 instruments in the discrete-wavelength mode. Such a modified ratio would not have worked well for the Nimbus-7 measurements, where the wavelength jitter and drift were larger. Studies of SBUV2's drift in wavelength positions, such as those in Section 4.3 are essential, as are studies of the sensitivity of this modified ratio to drifts in wavelength.

4.8. Vacuum Wavelength Scale

The equation used to calculate the wavelengths of the 12 SBUV2 grating positions, for the solar Mg II h and k line discrete-wavelength mode observations, recommended by Cebula (1988), is:

$$\lambda_{vac.} = A_0 \sin[A_1(G + A_2)], \tag{4.14}$$

where G is the grating-angle encoder readout from the 1B data tapes. Cebula's (1988) values were the following:

A_0 = 818.865 (nm);
A_1 = -9.59472 x 10^{-5} (radians/encoder-counts);
A_2 =-4157.03 (grating-shaft angle encoder counts).

These values produced the "nominal" values listed in Table 4.1.1, at the beginning of this chapter. Although the old tradition was to use vacuum wavelengths for wavelengths shorter than 200 nm, and wavelength in standard air pressure and humidity for wavelengths longer than 200 nm, we now use the more fundamental wavelengths in vacuum.

The NOAA9 wavelengths of prominent solar lines will be compared with other solar observations, and the wavelength scans of SBUV2's mercury calibration lamp will be analyzed. Our goal is to determine an absolute-vacuum wavelength-scale for NOAA9 and also to determine the relative wavelength-scale corrections needed to compare data with other specific solar observations such as the UARS measurements. (The only results related to wavelength scale in the current study are discussed in Section 6.2).

4.9. Noise and Power Spectra Analysis

A technique is described for evaluating whether some of the eight sets of sunlit, Sun-view, discrete-wavelength-mode measurements are more noisy than others, and which technique is

optimum for averaging the daily set of core-to-wing ratios. The long-term trend of the classical core-to-wing ratio for each sunlit set was removed by subtracting a long-term average. Both long-term instrumentation drifts and solar flux changes were thereby removed. The residuals were rich in 27-day solar rotational variations. Power spectra were computed using the techniques described by Repoff (Heath et al., 1984; Lean and Repoff, 1987). The results are shown in Figure 4.9.1. The spectra all have a strong 27-day line caused by the solar rotation of an inhomogeneous distribution of active regions as a function of solar longitude. Besides the 27-day line, there is a weak line at 13 to 14 days, which may be a solar signal; there is also a low, flat continuum. Removing the long-term trends avoided a high background continuum or one that is a function of frequency. Part of that continuum is caused by real solar variations, such as the sudden emergence of a strong active region over 2–3 days, and some of it is due to observational noise. The higher the continuum level relative to the 27-day solar signal, the noisier the data set or averaging technique will be.

Each graph in Figure 4.9.1 is drawn so the peak of the 27-day line is at the top of the graph, and the height of the graph is the same in each case. Each power spectrum is normalized to unity area over the whole grid of frequencies used in the analyses; the same time interval and frequency grid are used for each case being compared. If the 27-day solar signal is very strong relative to the background continuum, then the scale number at the top of the y-axis is higher. For example, the strongest solar signal to background continuum is the daily mean of sets 2, 3, and 4, shown in the graph at the top left side of the figure; the scale ranges from 0–11%.

One main result is that there are no lines in that graph for periods shorter than 13 days; no solar signal at UV wavelengths is expected there from the Nimbus-7 results (Donnelly and Puga, 1990). The 7-day structure found in the time of the observations (Figure 3.2.1) did not cause an observational error signal line at that period. The Nimbus-7 data had a three-days-on then one-day-off structure in its measurement schedule, which did produce a small line in its power spectra at 4 days.

This analysis was originally conducted to determine an optimum way to compute the daily average. The pre-analysis favorites were the mean of sets 2–7, the median of sets 2–7, and the mean of sets 3–5. Note the low values of the y-axis range (5 to 6%) for the power spectra for the first, sixth, and seventh set per day. The second, third, and fourth sets have a high scale range (8%). Consequently it is not surprising that the mean of sets 2–4 gave the highest ratio of solar signal to observational noise. The median of sets 2–7 almost tied for the highest line to continuum ratio. (Because the median of sets 2–7 is more robust relative to isolated noise problems, it has been used for the modified ratio results in this report). One reviewer thought the mean of sets 2–5 would be best; but that was not one of the cases we tried. However, these particular results are for the classical Mg II core-to-wing ratio, which has now been superseded by the less-noisy modified ratio. Our main purpose here was to demonstrate the technique. One disturbing result was that the 13–14 day solar line was not clearly present in some of these results; this was probably a consequence of the fairly large short-term noise in these classical ratio results.

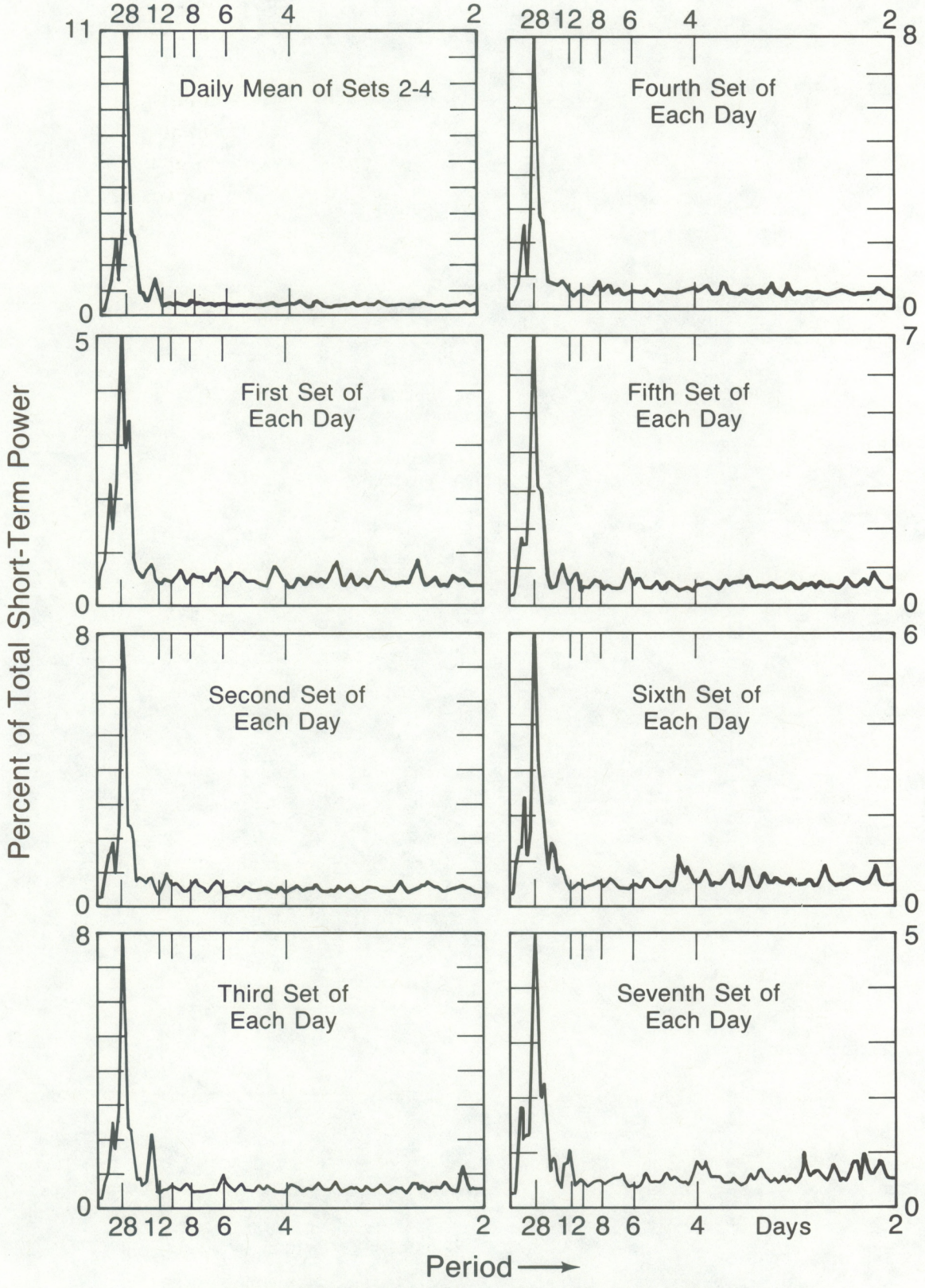

Figure 4.9.1. Power spectra of short-term variations.

5. R_{MgII} DURING THE MINIMUM AND EARLY RISE OF SOLAR CYCLE 22

Our analyses of the SBUV2 solar UV spectral irradiance measurements are not an end product of our work but are a by-product of our research of the temporal variations of the solar UV spectral irradiance. The main results of our research in the latter area have been published elsewhere, so in this section we will briefly discuss those publications and some minor unpublished results.

The first Mg II index data published for NOAA9 were those for May–December 1986. They were published in *Solar Geophysical Data* (SGD) in 1988. Similar data for 1987 were published in the September 1989 issue of SGD. Those preliminary data were based on equation (4.7), where the daily median values were divided by the monthly average of daily values for the month of September 1986, which was near the solar cycle minimum flux. This solar cycle minimum normalization was used to roughly account for all the effects of K_F^c, X_{23}, and R in equations (1.2) and (1.4), except for their weak wavelength dependence over the small wavelength range in the discrete-wavelength mode of Mg II line measurements.

Further studies of those data identified the numerous problems discussed in Chapter 4 and in Section 6.3, which led to a search for improvements and eventually to equation (4.8). These modified ratios, together with the factor for converting them to equivalent Nimbus-7 MgII core-to-wing ratios based on comparisons with the Ca K 1A index (Sect. 6.3), produced the 1986–1988 results published in SGD in 1991 (which supersede those published in 1988 and 1989).

A revised set of results, including some based on the "reprocessed" data tapes, are presented here in Appendix 1. Our values for November 1978–October 1984, based on Donald F. Heath's Nimbus-7 observations, were published in SGD in October 1989. Now let us consider what we have learned about the solar UV flux and its variability from these results.

5.1. Solar Rotational Variations

Donnelly (1988a, c, 1989, 1990b) and Livingston et al. (1991) showed graphs of the solar rotational variations of R_{MgII} from May 1986 through 1988, during the rise of solar cycle 22, using the (now superseded) results based on equation (4.7). Those results were quite noisy, and the four rotational peaks with nearly equal heights in mid 1988 (Donnelly, 1989) should not have been so nearly equal. The graph shown in Donnelly (1990a, 1991) and repeated here in Figure 5.1 is based on the modified Mg II index and supersedes the results discussed above.

Some weak 13–day periodicity (two peaks per solar rotation occurred in early 1988, but the amplitude was too weak to be very useful for extending our knowledge of 13–day periodicity reported by Donnelly and Puga (1990), except for future studies of any solar cycle dependence of the occurrence of predominantly 13–day solar-rotational variations. These NOAA9 data complement the Nimbus-7 Mg II results, since NOAA9 observed the rise of a solar cycle, whereas Nimbus–7 did not. However, for such a study more cases of strong 13–day periodicity can be obtained from Ca K plage data back to 1958, and possibly even earlier, from digitizing photographic plates of Ca K spectroheliograms.

5.2. Minimum Between Solar Cycles 21 and 22

The minimum of a solar cycle is influenced by the slow decline of old activity at low solar latitudes, where "old" means its magnetic polarity is consistent with that of the preceding cycle, and also by the rise of new-cycle activity at mid to high solar latitudes. Since solar activity observations at various wavelengths can involve different solar sources as a function of temperature and spatial location, which evolve similarly yet not identically with time, the balance between the influence of rising new-cycle activity and declining old cycle activity can cause the minimum of the solar cycle to differ as a function of wavelength and also as a function of the temporal smoothing applied. For example, solar UV fluxes are highly persistent (Donnelly, 1987) and appear to be very sensitive to the remnants of active regions, to the evolution of numerous small plagettes, to the active network, and to the evolution of major active regions. Solar radio emission at wavelengths of a few centimeters is sensitive to the more rapidly evolving strong magnetic regions associated with sunspots. So we might expect the solar cycle minimum to differ slightly with respect to spectral irradiance at 200 nm as opposed to that at 2 cm.

Is there any detectable difference in the minimum for the chromospheric Mg II core-to-wing ratio compared to the photospheric 200 nm flux? We don't know yet. The 13–day periodicity at most UV wavelengths longer than 180 nm is stronger than for the Mg II index (Donnelly and Puga, 1990), which indicates that the average center-to-limb function for active region emission is slightly broader, with respect to the region's solar central meridian distance, for the chromospheric Mg II lines than for the upper photospheric UV fluxes. This in turn implies a smaller ratio of short-term variations (13 d, 27 d) to long-term solar cycle variations for the chromospheric Mg II index than for the upper photospheric solar UV fluxes. So there may be a small difference in their solar cycle minimum times.

The size of the averaging interval that is applied to the data before determining the solar cycle minimum also has a slight effect on the magnitude and time of the minimum. The decay of a solar cycle is slower than its rise; as the averaging interval increases, the minimum time would tend to shift to earlier times. Donnelly (1988a) reported that for both 21-day and 81-day running averages the minimum for the NOAA9 Mg II index was in January 1987 and the lowest monthly mean was in September 1986; those results were based on the early classical R_{MgII} results normalized to the solar cycle minimum flux represented by the average value for September 1986 (whose problems were discussed in Chapter 4). The improved R_{MgII} results, based on the modified ratio and converted to equivalent Nimbus-7 values via comparisons with Ca-K .1nm index data, gave the following results for triangular filters with half maximum widths: 27 d width; September 18, 1986; 81 d width, September 2, 1986; and 365 d width, September 2, 1986. So we generally refer to solar cycle minimum between cycles 21 and 22 regarding solar UV radiation as having occurred in September 1986.

5.3. Early Rise of Cycle 22

The highest solar rotational peak in 1986 (See Figure 5.1) occurred in October and marked the beginning of the rise of solar cycle 21. The larger solar rotational variations in 1987 and 1988 were of medium size and were comparable in magnitude (relative to their local rotational minima) to the October 1986 variation. The main effect was the rise in the solar-rotational local minima throughout 1987 and 1988; large solar rotational variations did not occur until 1989. In summary, the rise of solar cycle 22 involved medium to small solar rotational variations combined with a rapid rise in the rotational minima flux.

Donnelly (1991) showed that the long-term solar cycle variation of the Canadian 10.7 cm solar radio flux (F10) is very similar to that for the Mg II core-to-wing ratio (R_{MgII}), despite the marked differences between F10 and $R_{Mg\,II}$ that occur during short-term variations (days, weeks, a couple of months) (Donnelly, 1987). Comparisons of R_{MgII} and F10 are discussed further in Section 6.4. In the early 1980s, our comparisons of Nimbus-7 UV measurements of solar UV flux temporal variations with those of F10, which were dominated by solar-rotational variations with little evidence of the solar cycle variations, led to the conclusion there were marked differences in temporal variations between the data sets (Donnelly et al., 1983).

When the Nimbus-7 data ended, it was clear that the long-term solar cycle variations of F10 and R_{MgII} were quite similar in relative temporal shape; however, those results did not include the main rise of a solar cycle (Donnelly, 1988b). So the addition of the NOAA9 results includes all phases of

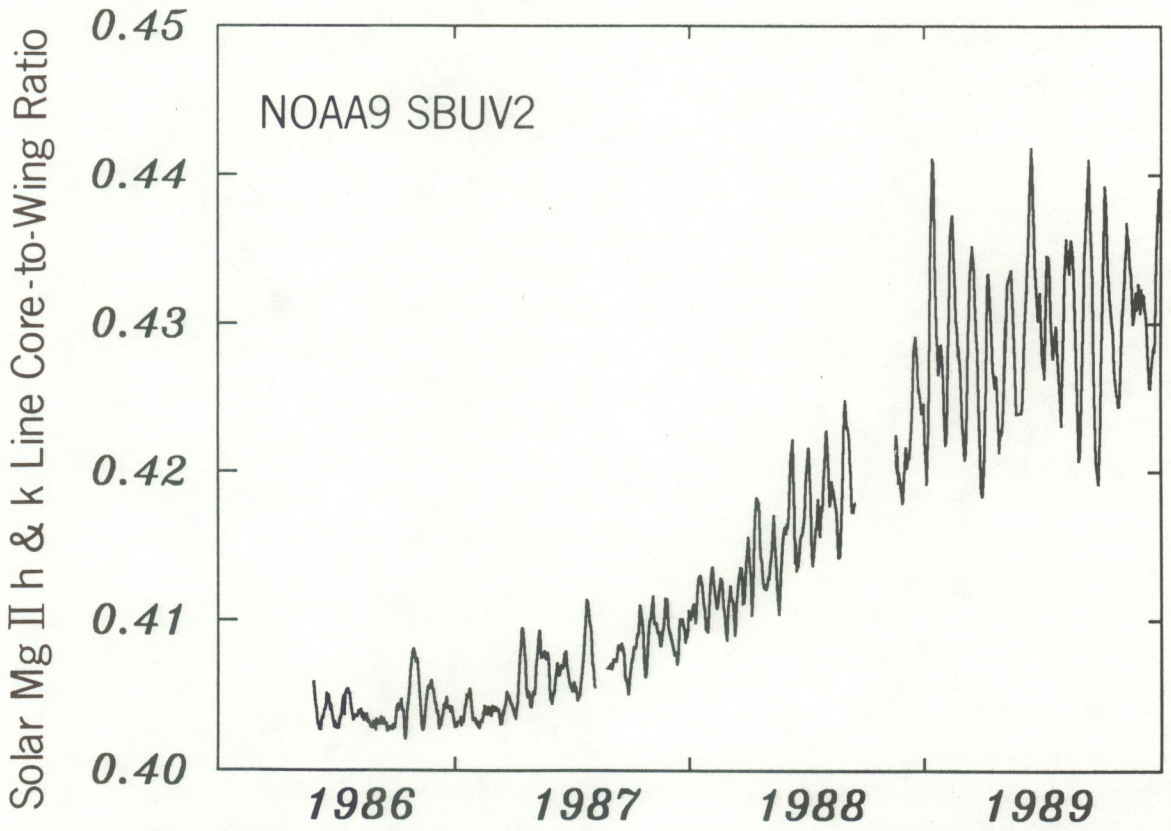

Figure 5.1 The NOAA9 modified Mg II core-to-wing ratio (Donnelly, 1990a, 1991)

the solar cycle, confirming that the long-term solar cycle variations of F10 and R_{MgII} are quite similar for all phases of the solar cycle. On the other hand, a small hysteresis loop effect in those results appears to be related to the long-term variations of F10, which lead those of R_{MgII} by about a solar rotation (Donnelly, 1991).

Bouwer et al. (1990), Pap et al. (1990b) and Bouwer (1992) studied the power spectra of the time series of the Mg II core-to-wing ratio and that of several other measures of solar variability or irradiance. They observed a 51–52 day periodicity that was weak but clearly present in R_{MgII} and that was relatively stronger in solar indices more closely related to emerging magnetic flux on the Sun. This 51–d periodicity appears to be phase stable.

6. COMPARISONS OF R_{MGII} WITH OTHER SOLAR MEASUREMENTS

6.1. NOAA9 and NIMBUS7 Data

J. Barrett and D. E. Stevens

The Nimbus-7 solar UV spectral irradiance measurements from the Solar Backscatter UV (SBUV) experiment provided the first extensive set of core-to- wing ratios (R_{MgII}) for the Mg II h and k lines (Heath and Schlesinger, 1986). The set was composed of more than 8 years of data, starting on November 7, 1978 (see Figure 6.1.1). Because those R_{MgII} results were first and were of very high quality, and because Heath and Schlesinger had derived a high-quality wavelength-scaling function for use in estimating the UV flux variations at other wavelengths based on the time dependence of R_{MgII}, we accepted the Nimbus-7 R_{MgII} values as a reference data set.

We wanted to determine the relation between the NOAA9 results and those for Nimbus 7 so that the NOAA9 results could be converted to equivalent Nimbus 7 values in order to extend the Nimbus-7 time series of R_{MgII} results to later times and to be able to use the Nimbus-7 wavelength scaling function. We do not assume that the Nimbus-7 results are perfect; there probably are unknown errors (for example, absolute flux errors in the reference flux spectrum

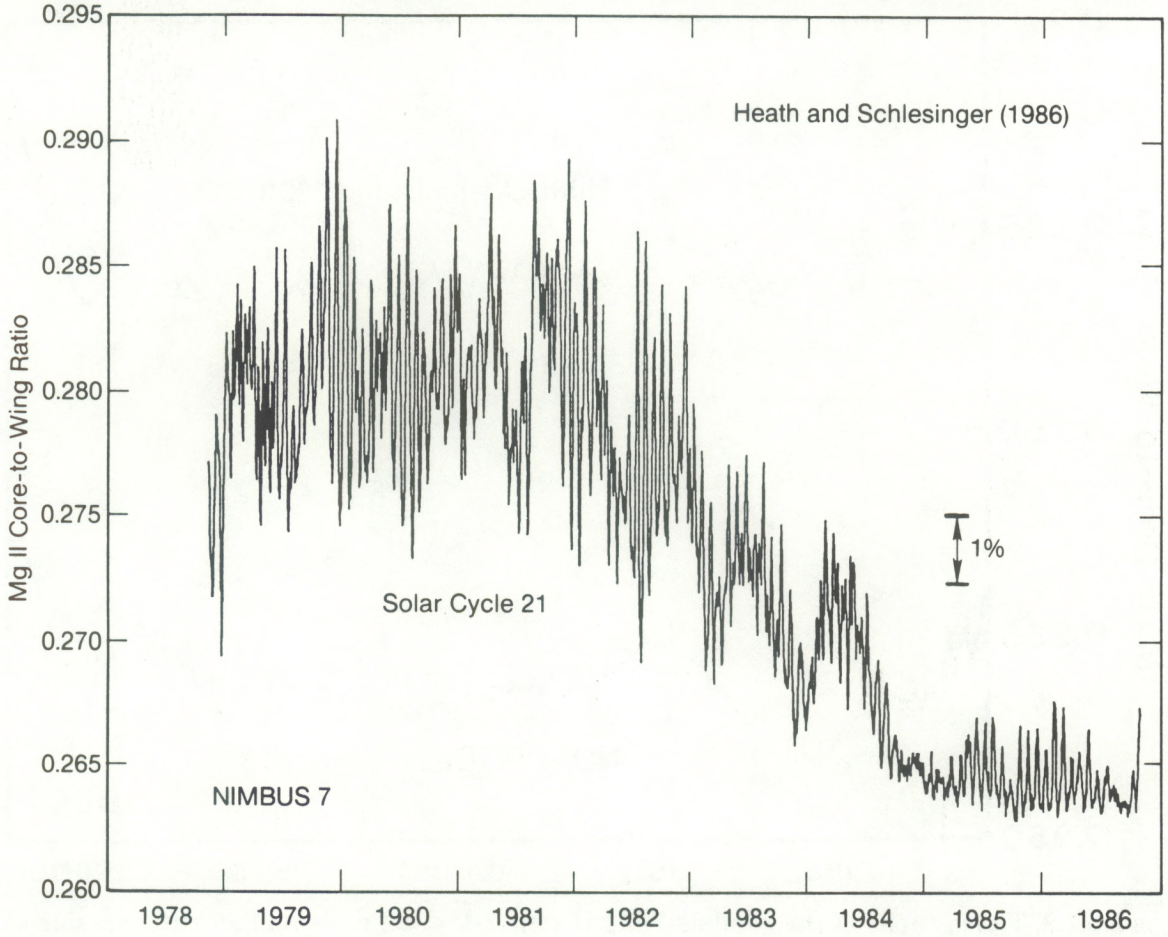

Figure 6.1.1 The Mg II core-to-wing ratio based on Nimbus-7 SBUV measurements and the original equation of Heath and Schlesinger (1986).

of Nimbus 7 from its first day of observations). As comparisons are made with more accurate measurements in the future, corrections may be developed for improving the original Nimbus-7 results; but in the meantime, this is our reference data set.

Although Nimbus-7 R_{MgII} values extend into early March 1987, the last Nimbus-7 data that we have received ends on October 28, 1986. The NOAA9 measurements of the solar Mg II h and k lines in the discrete-wavelength mode started May 27, 1986. Figure 6.1.1 shows that the small overlap period of same-day data for those NOAA9 and Nimbus-7 measurements involves values near the minimum of the solar cycle, when the solar rotational variations were quite small, and the highest values attained were during the rise of the rotational variation in October 1986.

Figure 6.1.2 shows the Nimbus-7 and NOAA9 data for the overlap period. The NOAA9 data shown here are the classical ratio based on equation (4.7), before we had incorporated temporal interpolations of the wing measurements to determine the effective wing output for the same instant in time (or the same Sun angles) as that of the core measurement (see Sect. 4.2). The solar signal is weak, and the noise in the NOAA9 data is obviously strong. Daily means, medians, and means of the middle data sets (see Figure 4.2.5), such as sets 3, 4, and 5, were all examined. Regression analyses, as shown in Figure 6.1.3, were computed. The cor-

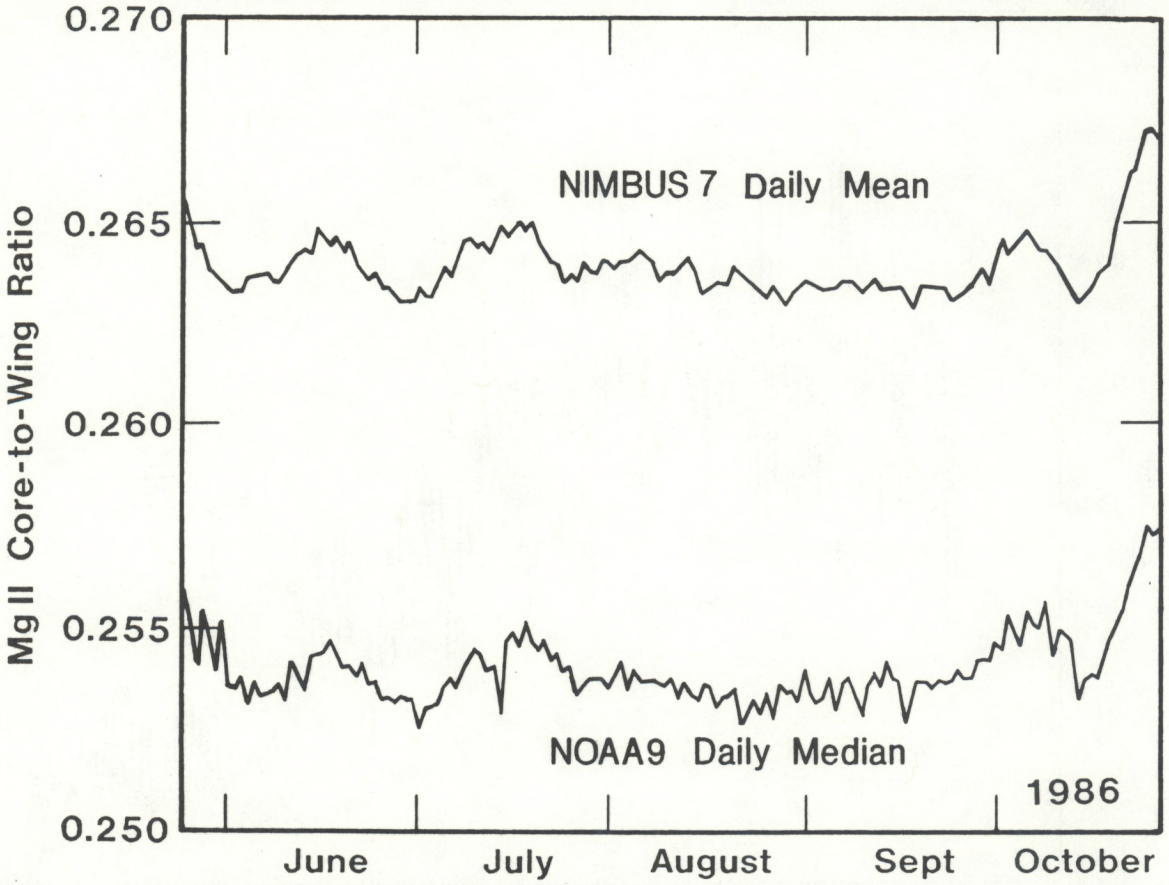

Figure 6.1.2. Time graphs of the Nimbus-7 Mg II center-to-wing ratio and an early version of the NOAA9 Mg II ratio for the discrete-wavelength mode for the overlap period of same-day available data. For these NOAA9 results no temporal interpolations of the wing measurements were made and bad data were not identified.

relation coefficient of 0.75 was unacceptably low; or the uncertainty in the regression relation, indicated in the figure by the large difference in the two regression lines, was unacceptable.

The variance in these data that is not explained by the straight line relation amounts to 44% of their total variance. The correlation of the Nimbus-7 results shown in Figure 6.1.1 with the same-day Ottawa 10.7 cm solar radio flux (F10), corrected to 1 AU, has a coefficient r=0.956; so it would have been better to use the radio data to extend the Nimbus-7 R_{MgII} values to later times than to use the NOAA9 results shown in Figure 6.1.3. On the basis of the results in Figures 6.1.2 and 6.1.3 we decided to return to the NOAA9 data to determine how our ratio of solar signal to observational noise could be improved.

Figure 6.1.4 shows similar classical R_{MgII} results after the temporal interpolations between adjacent wing measurements were applied in order to estimate their value at the same time as the core measurements. (See Section 4.2 and equations (4.4)-(4.6).) Also, bad data were removed as discussed in Chapter 4; this process involved excluding stuck full-counter values, isolated wild points, and the first sunlit measurement set (when the Sun was partly occulted by the satellite), and correcting for counter overflows. Much of the improvement was gained by using the NOAA9 daily median rather than the mean of sets 3, 4, and 5. Although the correlation coefficient is better, it is still too low for the regression results to be useful.

The time graph for NOAA9 in Figure 6.1.4 shows too much day-to-day jitter, so the raw data was again studied to determine the origin of this noise. We discovered a lot of noise in the

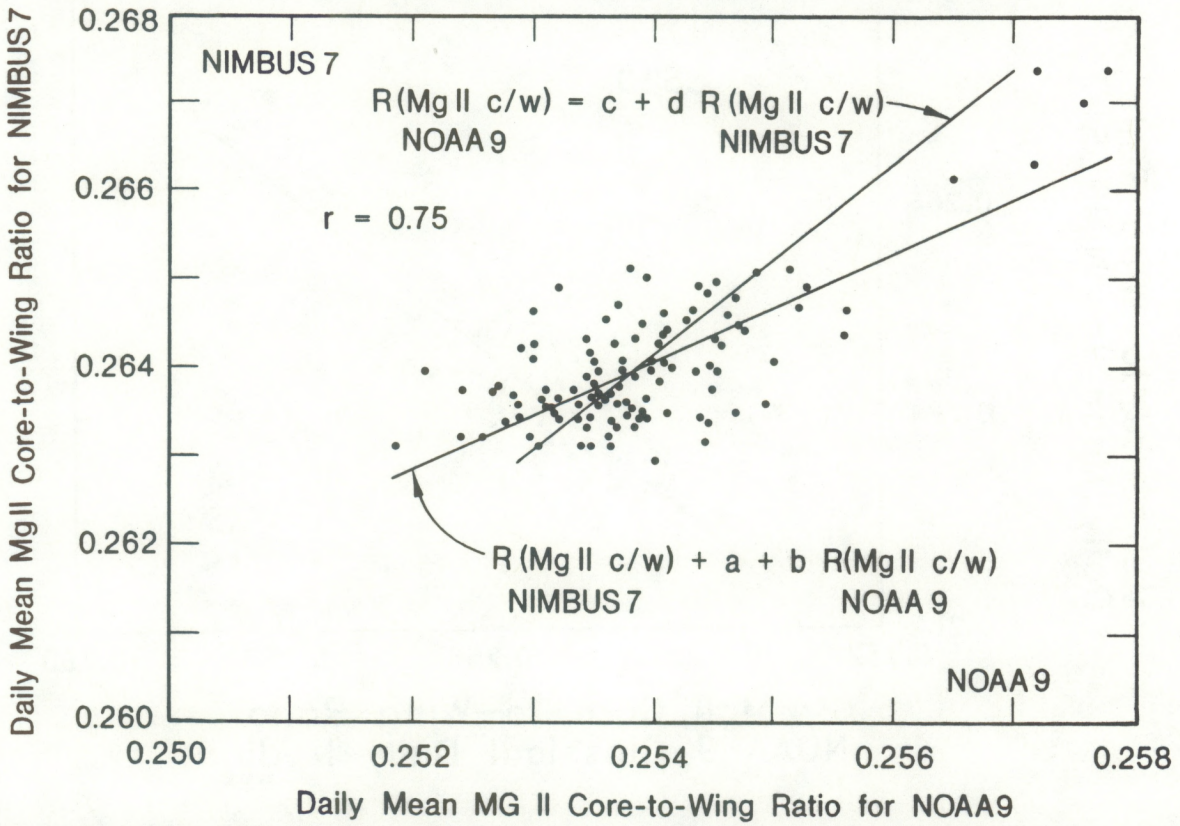

Figure 6.1.3. Scatter diagram of same-day paired Mg II center-to-wing ratios for Nimbus 7 versus the daily mean for discrete-mode sets 3-5 with regression lines. The correlation coefficient, dynamic range, and number of independent values are all too low for these results to adequately define the relation between the NOAA9 and Nimbus-7 results.

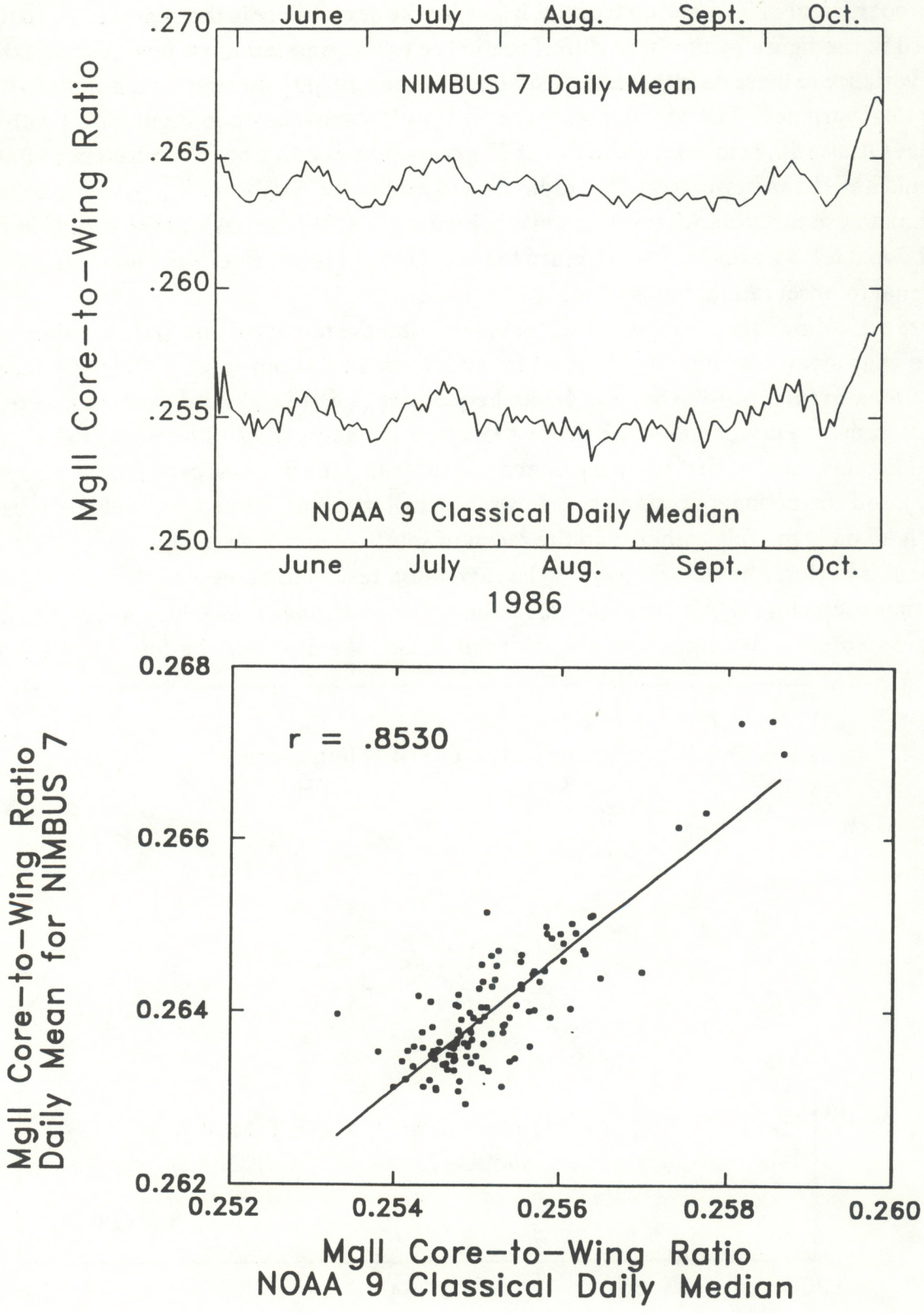

Figure 6.1.4. Time graphs (top) and scatter diagram (bottom) for the classical NOAA9 and Nimbus-7 Mg II center-to-wing ratios; bad data have been corrected.

range-3 output values, relative to their corresponding range-2 values, and decided to use only range-2 values and the modified ratio of equation (4.8).

Figure 6.1.5 shows the subsequent results for the modified NOAA9 Mg II ratio. The correlation coefficient has risen to a worthwhile value, but it is still only comparable to that for F10 for the entire Nimbus-7 data set. The regression line has moved inside the group of the five highest values, and the variance of these points relative to the straight line has diminished. Nevertheless, considering Figure 6.1.1, the dynamic range involved in Figure 6.1.5 is still only about 15% of that involved from solar cycle minimum to maximum. Therefore, using the results in Figure 6.1.5 to convert the modified Mg II ratio to equivalent Nimbus-7 values in order to extend those values through solar cycle 22 would amount to a gross extrapolation! Furthermore, there are only five values in the upper half of Figure 6.1.5 (too few values with clear solar signals to provide sufficient confidence in this conversion relation). A better way to determine the conversion relation is still needed.

If we include the final Nimbus 7 data in this type of analysis for the months of November 1986, through February 1987, we can improve upon the results shown in Figure 6.1.5; this is worth doing because it should improve the correlation coefficient and the error estimates for the linear regression relations. However, since those values are also from solar minimum, we would not increase the dynamic range; the gross extrapolation problem would remain unsolved. So we still need to find a better solution to this conversion problem, which will be discussed further in Section 6.3. Nevertheless, the progression of improving results from Figure 6.1.2 through 6.1.5 shows the value of temporal interpolations for the wing measurements, the removal or correction of certain bad data, and the avoidance of range-2 to range-3 conversion jitter and drift.

The regression coefficients a–d as defined in Figure 6.1.3 are summarized in Table 6.1. The central columns for a' and b' are derived from the c and d coefficients; a' and b' simply convert the latter equation, which was derived with the NOAA9 data as the dependent variable, into the same form as that for the a and b coefficients, which were derived with Nimbus-7 data as the dependent variable. The a' and b' coefficients are included to allow easy comparison of the two regression equations. The lack of close agreement between a and a', and b and b', illustrates the inadequacy of these conversion factors.

The change in coefficients from the first two cases (first two rows) in Table 6.1 to those in the last case for the modified ratio is simply a consequence of the modified ratio using wavelengths in the absorption line wall rather than in the far wings; this is not an indication of error for any of the three rows. Although we recommend that none of these regression relations be used to convert NOAA9 results to equivalent Nimbus-7 values, their progression of increasing agreement among them shows the value of making our data processing revisions that led to the modified ratio results. For further information on the relation between Nimbus-7 and NOAA9 Mg II ratios, see Section 6.3.

Note in Figures 6.1.2 and 6.1.4 that there is an absolute offset between the Nimbus-7 and NOAA9 ratios, with NOAA9 values being about 0.01 (4%) lower than Nimbus-7 values. Neglecting the relative wavelength dependence of the K_F and X_{23} of equation (1.2) and neglect-

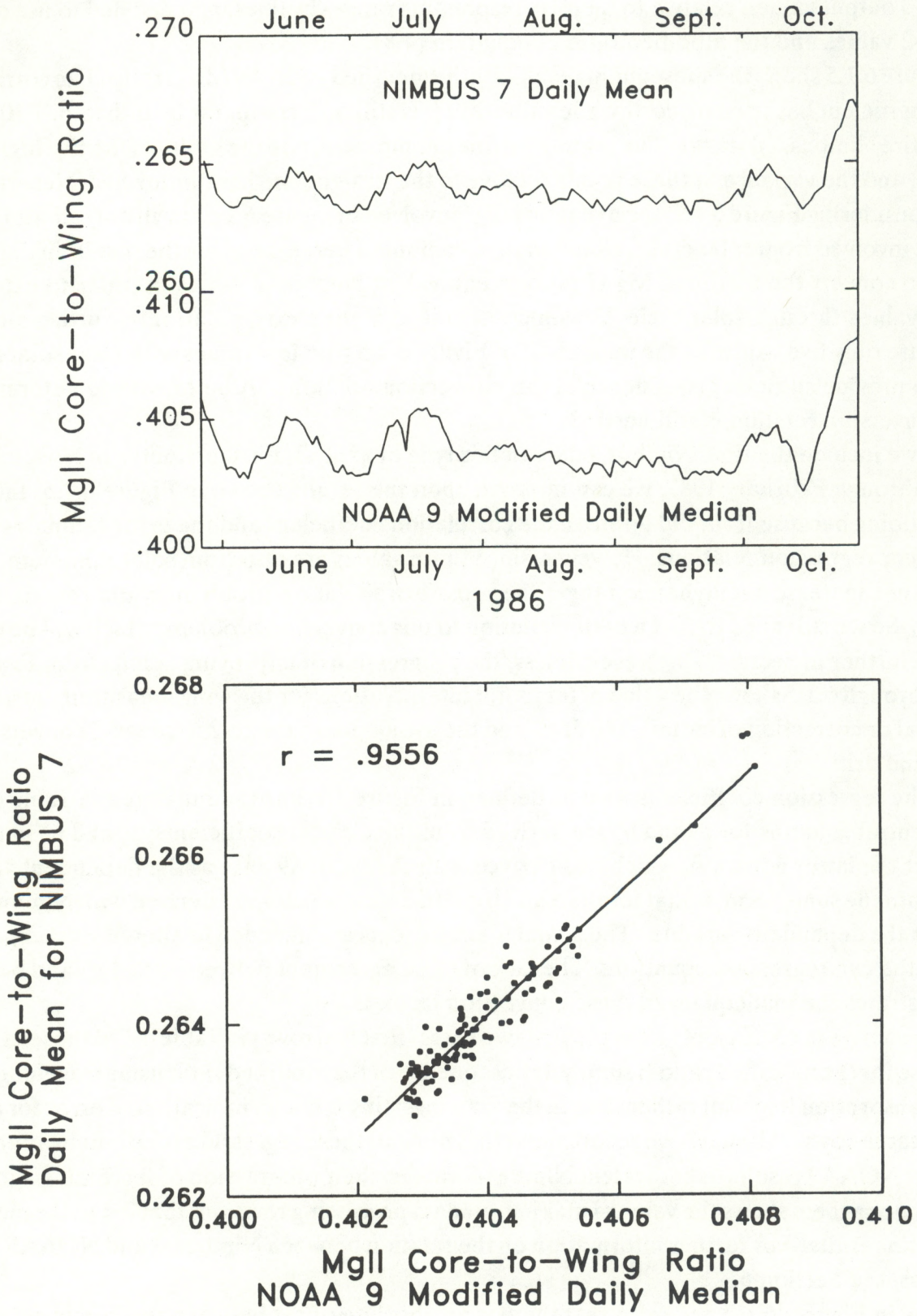

Figure 6.1.5. Same as in Figure 6.1.4, except for the modified Mg II ratio.

Table 6.1 Regression coefficients for direct comparisons of NOAA9 and Nimbus-7 Mg II core-to-wing ratios.

Related Figure	NOAA9 R_{MgII} Data Used	Coefficients (See Fig. 6.1.3) a	b	a'	b'	c	d
6.1.3	Daily mean of sets # 3, 4, & 5; classical	0.1091	0.610	-0.0090	1.075	0.0084	0.9301
6.1.4	Daily median, bad data removed, classical ratio	0.0656	0.7775	-0.0087	1.0687	0.0081	0.9357
6.1.5	Modified ratio.	-0.0220	0.7081	-0.0492	0.7754	0.0634	1.2897

a, a' and c are the intercepts of the respective straight lines while b, b', and d are the slopes; a' = -c/d, and b'= 1/d;
a' and b' are based on the c and d coefficients derived with the NOAA9 values as the dependent variable;
a' and b' are used to convert the latter equation to the same form as that for the a and b coefficients to aid in comparing the two equations. The correlation coefficient r = 0.753, 0.853, and 0.9556 for rows 1, 2, and 3, respectively.

ing the goniometric corrections of equation (1.5) in equation (4.7) did not cause this offset. Nimbus-7 may have had a higher level of scattered light than did NOAA9; this would affect the flux measurements in the core of the line more than in the wing measurements and thereby raise the core-to-wing ratio, which might help to explain the offset. However, laboratory measurements of scattered light for Nimbus-7 indicate otherwise. The NOAA9 core wavelength (no. 7) fits the minimum-flux center of the unresolved Mg II h & k absorption lines a little better than in the case of Nimbus-7. The smaller wavelength spacing for adjacent wavelengths (0.148 nm) means that the three core wavelengths fit further down into the bottom of the absorption line for NOAA9 than for Nimbus-7. This, together with slight differences in wing wavelengths, can explain ratio shifts of about 1.5 to 2%, or almost half of the 4% offset. However, the slightly wider bandpass of NOAA9 (1.14 nm) than for Nimbus-7 (1.1 nm) reduces this effect somewhat. When concurrent range-2 and range-3 values for NOAA9 are compared, the nominal value that we used for X_{23} (104.22), based on Frederick et al. (1986), appears to be about 2.6% too high for the time of the overlap of Nimbus-7 and NOAA9 discrete wavelengths. This would affect the wing measurements for the classical ratio but not the core measurements and would cause the NOAA9 ratios to be about 2.6% too low, explaining the remainder of the offset.

We are not so concerned that offsets exist; the regression relations correct for them. Our main concern about such offsets is whether they are an indication of some unknown problem in the data that may cause other problems, and that they increase our dependence on large data overlaps.

6.2. Fine Wavelength Resolution Measurements of the Mg II Lines

Donald Heath (private communication, 1983) hoped that it would be possible to use earlier rocket flight measurements of the Mg II core-to-wing ratio to derive values of the Mg II core-

to-wing ratio that could then be combined with the Nimbus-7 values to provide information before the start of the satellite measurements. Hall and Anderson (1988) showed that their balloon-flight data gave ratios that were about 0.006 to 0.010 (2–4%) lower than same-day Nimbus-7 values (see section 2.4). They also noted problems with probable differences in wavelength scales and that the Mg II ratios were sensitive to the instrument bandwidth. In principle, measurements with high wavelength resolution can use the numerous narrow absorption lines together with laboratory determinations of their wavelengths, to calibrate the wavelength scale. Several spectra have been studied, and the results are presented below.

6.2.1 AFGL Measurements

(L. C. Puga)

Hall and Anderson (1988) reported their observations of the Mg II h & k absorption lines near 280 nm, made with 0.01 nm resolution from balloon flights near 40 km in altitude. Figure 6.2.1.1 shows their observations for two flights made before the beginning of the Nimbus-7 observations. The solid line is higher in the h & k emission cores than is the dashed line curve because of the higher level of solar activity. The higher values of the dashed line than for the solid line outside of the h and k emission cores are thought to be due not to solar activity but to differences in observational conditions, either in the instrument (1 year's difference in time) or in the observing conditions (i. e. the balloon altitude, solar zenith angle, and net columnar ozone along the sun-balloon path).

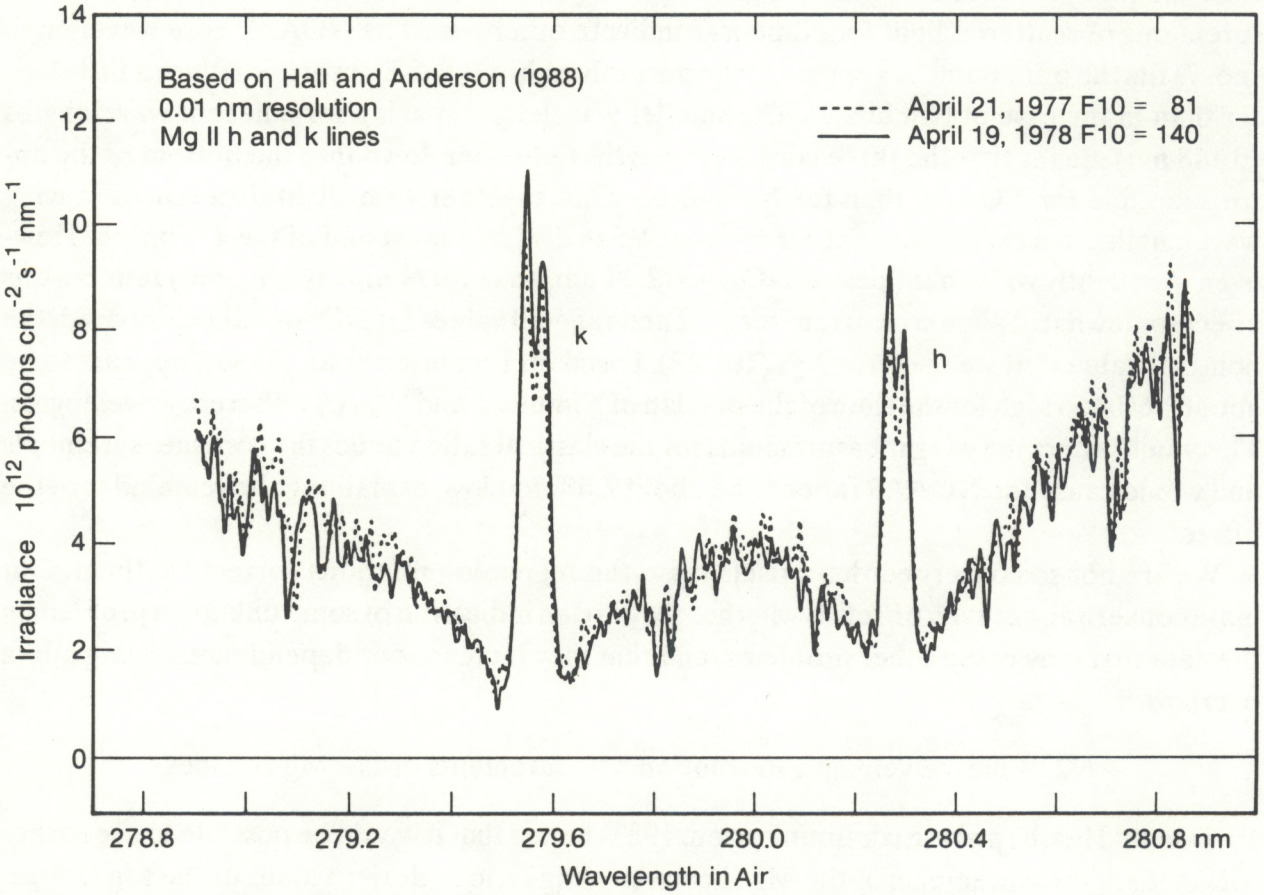

Figure 6.2.1.1. Balloon flight observations of the Mg II h & k lines. of the higher level of solar activity.

Hall and Anderson (1988) corrected their data for terrestrial ozone absorption and convolved them with the bandpass of the Nimbus-7 instrument to derive a core-to-wing ratio based on Heath and Schlesinger's (1986) equation (4.1). Hall and Anderson obtained a value of 0.256 for 21 April 1977 (when the Ottawa 10.7 cm flux adjusted to 1 AU (F10) was 81) which was after the solar minimum between cycles 20 and 21 and during the early rise of cycle 22.

Figure 6.1.1 shows that the Nimbus-7 ratios sank to only about 0.263 for the minimum between cycles 21 and 22. Using the regression relation between long-term averages of F10 and R_{MgII}, we would expect that the Nimbus-7 value would have been above 0.265 for 21 April 1977. So there is an offset of about 0.007 to 0.009 between these data, similar to what Hall and Anderson (1988) concluded from same-day comparisons with Nimbus-7 observations for two of their later flights, on 22 April 1981 and 20 April 1983, where the offsets were Nimbus 7−Hall=0.010 and 0.060, respectively. They concluded that to compare Mg II data from different instruments one should accurately know each instrument's bandpass function. They also showed that much of the difference between the Nimbus-7 data and theirs could be explained by shifting the Nimbus-7 data by .1 nm to shorter wavelengths.

We analyzed Hall and Anderson's (1988) data to see what we could learn about the Nimbus-7 wavelength scale and the spectral shape of the Mg II h and k lines; we agree with all of their conclusions, especially that it may be impossible to resolve the inter-instrument normalization factors when data sets do not overlap in time.

Figure 6.2.1.2 is based on Figure 3 of Hall and Anderson (1988). It shows their spectrum after filtering their observations with a 1.1 nm bandpass (NOAA9's bandpass is 1.14 nm) and also the approximate locations of the NOAA9 discrete mode measurements. We don't know the exact NOAA9 wavelengths because they may have changed slightly from the time of the preflight laboratory measurements to the time when solar UV irradiances were being measured. Changes may have been caused by problems with the in-flight calibration lamp on NOAA9 and because the main spectral lines of that lamp are not at the Mg II line wavelengths. However, we do know from Figure 4.3.1 that the minimum flux for the NOAA9 observations of the unresolved solar Mg II h & k lines is near 279.9155−279.920 nm; this is slightly longer than that for wavelength no. 7, for which our nominal value is 279.9152 nm. We used data files provided by Dr. L. A. Hall (1988, private communication) of the Air Force Geophysics Laboratory (AFGL), Hanscom AFB, Bedford, Massachusetts, for their balloon-flight measurements on 19 April 1978 and 20 April 1983, and then filtered them with a triangular passband with a half-max bandwidth of 1.14 nm. We found the minimum of the Mg II h and k lines for the AFGL wavelength scale, converted to vacuum wavelengths to be 279.838 nm and 279.982 nm; this differs from the MgII h and k lines for wavelength no. 7 by about -0.8 Å and +0.64 Å, respectively. So a unique wavelength correction for the NOAA9 data cannot be confidently made on the basis of these balloon flight data.

Figure 6.2.1.3 shows the spectrum for 20 April 1983 after being filtered for the NOAA9 triangular bandpass. The wavelengths have been converted from values in air to wavelengths in a vacuum using the corrections given in Allen (1963); a linear interpolation is made with respect to wavelength in order to better compare Hall and Anderson's (1988) spectra with the

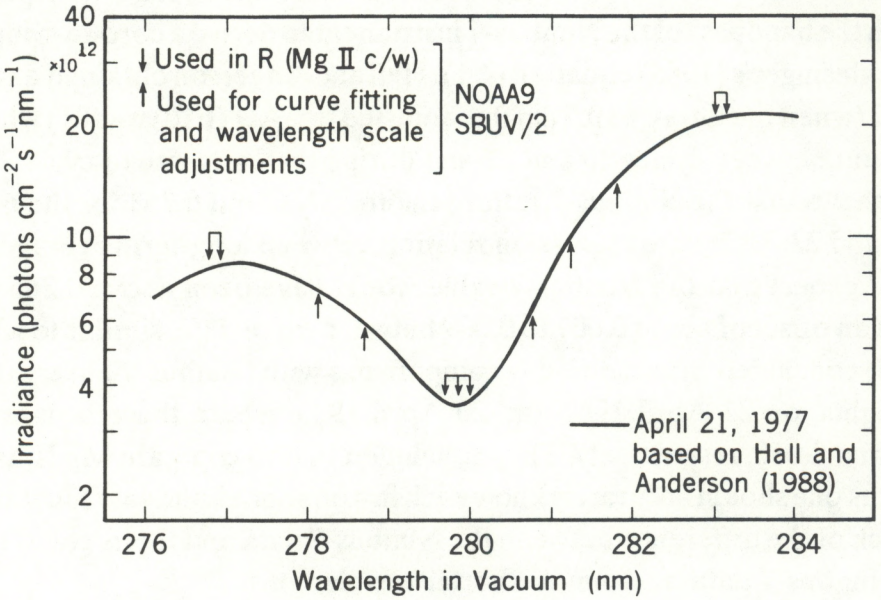

Figure 6.2.1.2. The balloon-flight spectrum for the Mg II h and k lines after being filtered with the half-max 1.1 nm triangular bandwidth of Nimbus-7, with arrows marking the approximate wavelength positions of the NOAA9 discrete-wavelength mode measurements, based on Figure 3 of Hall and Anderson (1988).

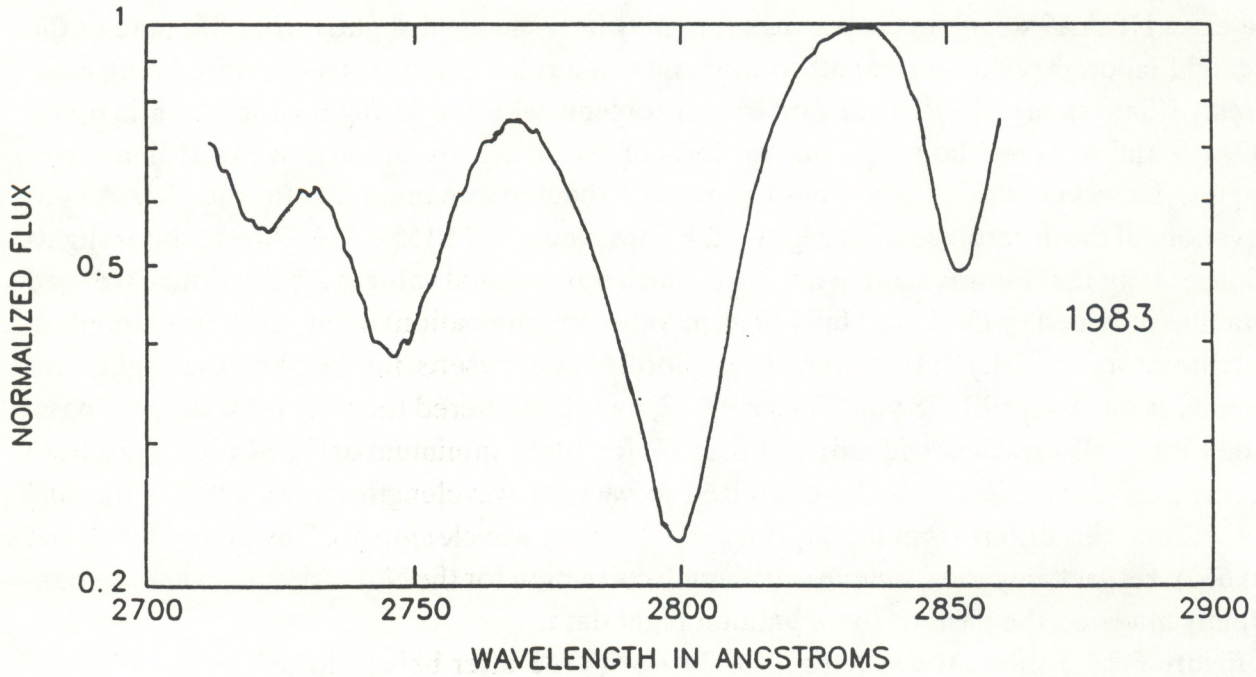

Figure 6.2.1.3. Solar UV spectra from a balloon flight of 20 April 1983 of Hall and Anderson (1988).

vacuum wavelengths that we use for the NOAA9 satellite. For the 1983 data, the file contained fluxes with a wavelength resolution of .1 nm, listed every .05 nm; for the 1978 data, the file gave the flux with .012 nm resolution, listed every .002 nm. Similar calculations were made for each data set for the triangular Nimbus-7 data, with a 1.1 nm half-max bandwidth. Our analysis of the Mg II data of Hall and Anderson are still in progress and the detailed quantitative results will be reported in a later progress report.

Our main conclusions so far are the following: (1) differences in wavelength scales for two different instruments are an important source of error in comparing R_{MgII} values from two different instruments, (2) corrections for terrestrial ozone for balloon-flight measurements may also be an important source of error in comparing R_{MgII} results, (3) the core wavelengths of the NOAA9 discrete-wavelength-mode observations fit the minimum of the unresolved Mg II h & k lines better than the Nimbus-7 wavelength steps do, and (4) the Nimbus-7 wavelength step that is considered closest to the minimum of the Mg II h & k lines is roughly .1 nm longer in wavelength than is wavelength no. 7 in the NOAA9 data.

6.2.2. Harvard Measurements

L. C. Puga and S. D. Bouwer

Kohl and Parkinson (1976) observed the solar spectrum of the Mg II h and k lines with a half-max bandwidth of .0028 nm scanning between 225 nm and 320 nm from a rocket flight on 15 May 1974. The peak altitude of the rocket flight was 281.2 km, so terrestrial atmospheric absorption was not a problem. However, the instrument viewed portions of the Sun, with an angular resolution of 184" by 1.5", rather than the full-disk flux (namely the quiet Sun at the center of the disk and a region just inside the solar limb). We expect such regional observations to differ from full-disk measurements because of their spectral shape and its relation to the Mg II core-to-wing ratio (R_{MgII}) for full-disk measurements. The quiet-Sun region should have a core-to-wing ratio slightly smaller than the full-disk ratio at the minimum of the solar cycle. The minimum of a solar cycle involves the slow decline of old cycle activity and the rise of new cycle activity; some solar activity still exists at the minimum between cycles. More importantly, even if the entire visible Sun were quiet, the upper-photospheric wing radiation would decrease more with increasing solar central angle toward the limb of the Sun than would the chromospheric h and k emission cores. So R_{MgII} for that quiet, full-disk flux would be slightly higher than that for the Sun-center, quiet-Sun emission because of the weak limb emission's contribution to the full-disk flux, with its effectively higher ratio (see Figure 4 of Kohl and Parkinson (1976) and Figure 3 of Doschek and Feldman (1977)). This same effect causes 13-day periodicity (produced by two peaks roughly 180° apart in the distribution of solar active regions as a function of solar longitude) to be weaker, relative to nearby 27-day periodicity in the chromospheric Mg II h and k emission cores, than in the upper photospheric UV emission at most other wavelengths in the 170–290 nm range (Donnelly and Puga, 1990).

Figure 6.2.2.1 shows a graph of the quiet Sun-center spectrum. The numerous vertical lines in the 275–278.5 and 281–285 nm ranges are real and are caused by the narrow absorption lines present at most UV wavelengths. The influence of these weak absorption lines, formed in the upper-photosphere, temperature minimum region, and lower chromosphere, is suppressed in the 279–281 nm range, where the Mg II h and k line absorption dominates. Figure

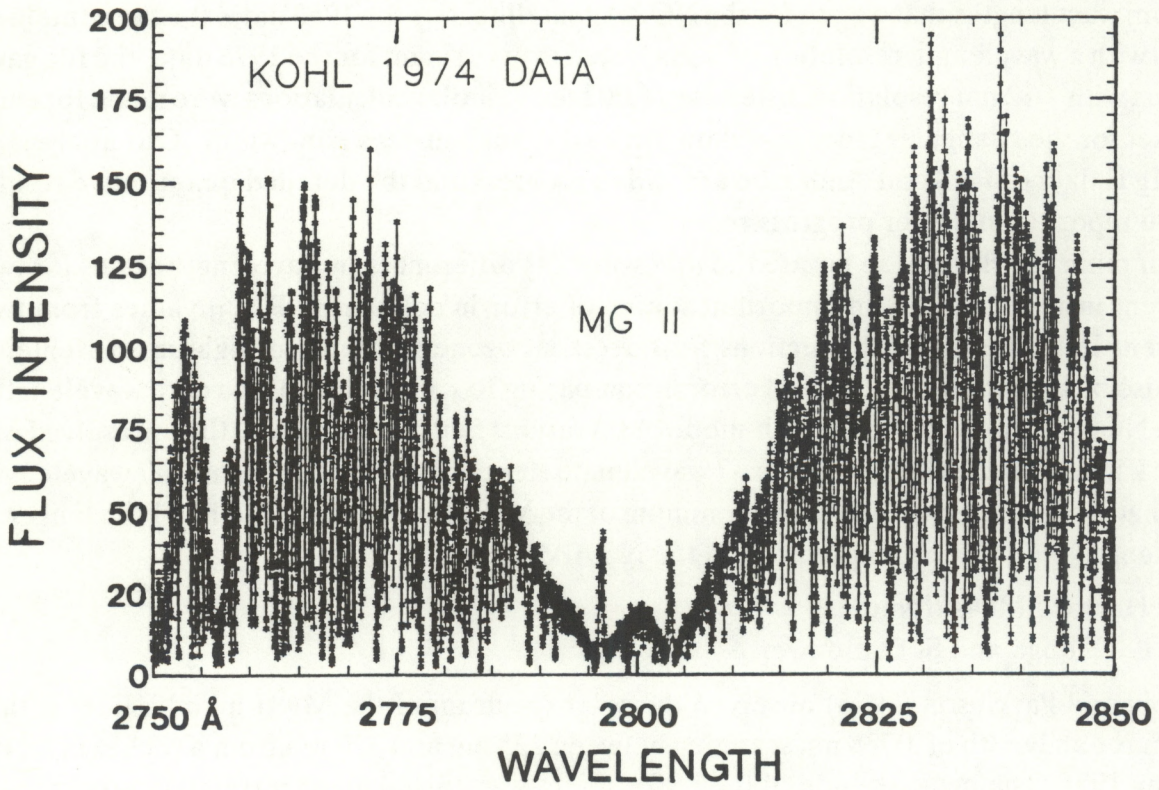

Figure 6.2.2.1. The quiet Sun-center spectrum of the Mg II h and k lines observed with fine wavelength resolution by Kohl and Parkinson (1976) with a high-altitude rocket flight, on 15 May 1974, during moderate levels of solar activity in the decline of solar cycle 20.

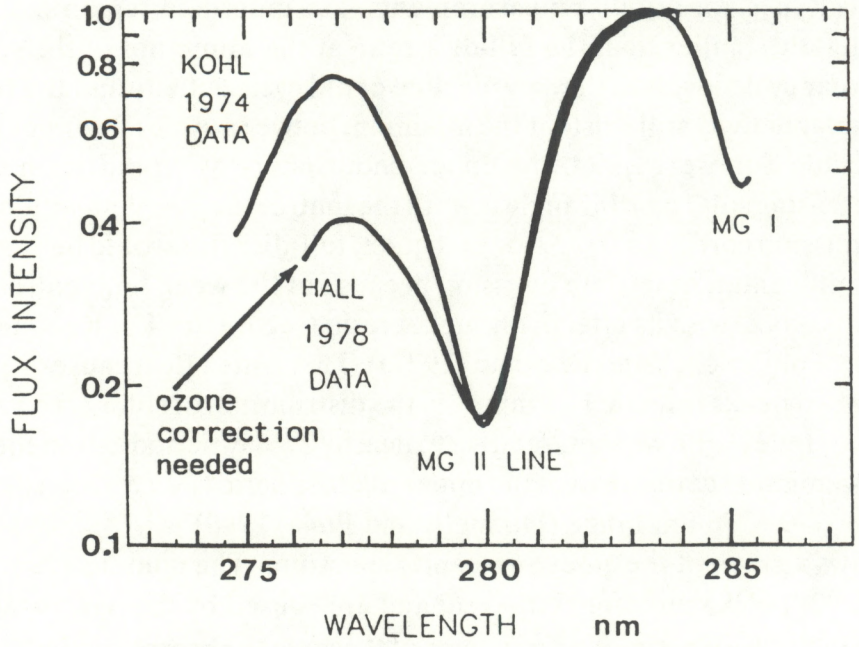

Figure 6.2.2.2. Mg II h and k line spectra from 15 May 1974 (Kohl and Parkinson, 1976) and from 19 April 1978 (Hall and Anderson, 1988) after being filtered with the NOAA9 band-pass function.

6.2.2.2 shows the Kohl and Parkinson (1976) Sun-center spectrum after it has been integrated with the triangular NOAA9 filter which has a 1.14 nm half-max band width. Both the spectrum based on Kohl and Parkinson (1976) and that of Hall and Anderson (1988) have been normalized by dividing by their maximum values in the long-wavelength wing to aid in comparing spectral shapes. Note the large difference in shape with respect to the filtered spectrum of Hall and Anderson (1988).

Considering Figure 4.6.8, the ratio of flux at NOAA9 wavelength no. 12 (near the peak in the short-wavelength wing) to that at no. 1 (near the long-wavelength peak) is about 0.757; this agrees well with the spectrum of Kohl and Parkinson but not with that of Hall and Anderson, presumably because the latter must be corrected for terrestrial ozone. The ratio of the flux in the short- wavelength peak to that in the long wavelength peak is also too low in Figures 2.3 and 6.2.1.2 to agree with the NOAA9 data (Figure 4.6.8), but Figure 6.2.1.3 agrees fairly well.

Table 6.2.1 lists in Angstroms the intensity as a function of wavelength in a vacuum for the quiet Sun-center spectrum of Kohl and Parkinson (1976). These data have been filtered, with a triangular bandpass, with a half-maximum width of 1.14 nm, like that for the SBUV2 monitor on NOAA9. These results are included here for future use by others, in studying the shape of the Mg II h and k lines as a function of wavelength to improve our understanding of the SBUV2 observations of this doublet.

Figure 6.2.2.3 shows the values of $R_{Mg\ II}$ computed from the Sun-center spectrum of Kohl and Parkinson (1976), as if the full-disk spectrum for that day were the same relative shape as that of the emission from the quiet center of the Sun, as a function of a uniform shift in all the NOAA9 wavelength positions. For the nominal NOAA9 wavelengths (shift=0), R_{MgII} is near 0.198, which is expectably lower than the solar minimum values in Figure 6.1.1. The minimum as a function of wavelength shift is only .01 nm to shorter wavelengths from the nominal values. Figure 6.2.2.4 shows the same results expressed as a percentage error with respect to the R_{MgII} value for the nominal NOAA9 wavelengths.

A wavelength shift of a few thousandths of an nm, like those in Figure 4.3.1, would produce a negligible error in R_{MgII} according to Figure 6.2.2.4. Shifts as small as .05 nm, especially those to longer wavelengths (where the correction is larger), would require corrections for wavelength drift because the solar cycle variability seen in Figure 6.1.1 is of the order of only 10%. An error of 1% is therefore quite large; a shift of only +.01 nm or -.02 nm produces a 0.1% error in R_{MgII}, which is of the order of 1% of the solar cycle signal in R_{MgII}. Before applying such a correction, we need a better estimate of its magnitude and how well it is determined.

Figure 6.2.2.5 shows the spectrum derived from an average of Kohl and Parkinson's (1976) near-limb spectrum ($\mu=0.23=\cos\theta$, or $\theta=77°$) and a quiet Sun-center spectrum as a crude approximation of a second estimate for a full- disk flux spectrum, one that includes some of the effects of the limb spectrum. An arithmetic average is equivalent to assuming that the Sun-center spectrum applies for disk radii from zero out to 71% of the solar radius (or solar central angle θ out to 45°); the limb spectrum applies outside of that, which probably gives too much weight to the limb spectrum. The slightly higher peak in the h emission core than in the k emission core appears to be a spurious consequence of the wavelength samples plotted. The lower

Table 6.2.1 The quiet Sun-center spectrum after being filtered by the NOAA9 bandpass function and normalized by dividing by the maximum value in the long-wavelength wing.

Wavelength	0.0	0.2	0.4	0.6	0.8 Å
2761 Å	.66766	.67134	.67494	.67773	.68083
2762	.68310	.68588	.68794	.69056	.69308
2763	.69499	.69722	.70038	.70344	.70539
2764	.70887	.71164	.71520	.71817	.72076
2765	.72459	.72798	.73096	.73570	.73802
2766	.74047	.74153	.74359	.74515	.74715
2767	.74950	.75123	.75138	.75292	.75428
2768	.75471	.75567	.75602	.75578	.75530
2769	.75464	.75386	.75287	.75172	.75119
2770	.74971	.74916	.74704	.74574	.74417
2771	.74270	.74215	.74144	.73968	.73899
2772	.73834	.73545	.73389	.73157	.72908
2773	.72680	.72404	.72159	.71998	.71692
2774	.71557	.71227	.70925	.70600	.70213
2775	.69848	.69398	.68931	.68467	.67984
2776	.67488	.67019	.66410	.66064	.65484
2777	.65137	.64440	.63940	.63449	.62898
2778	.62419	.61922	.61372	.60908	.60386
2779	.59919	.59390	.58850	.58289	.57741
2780	.57252	.56746	.56200	.55696	.55192
2781	.54679	.54141	.53645	.53083	.52580
2782	.51998	.51485	.50917	.50426	.49863
2783	.49361	.48880	.48330	.47775	.47302
2784	.46775	.46266	.45771	.45276	.44815
2785	.44272	.43731	.43190	.42673	.42164
2786	.41694	.41107	.40600	.40121	.39600
2787	.39127	.38585	.38107	.37573	.37038
2788	.36557	.36007	.35499	.34983	.34471
2789	.34015	.33503	.32981	.32452	.31926
2790	.31478	.31021	.30584	.30150	.29669
2791	.29189	.28689	.28213	.27765	.27266
2792	.26829	.26385	.25958	.25512	.25035
2793	.24591	.24165	.23760	.23351	.22942
2794	.22547	.22130	.21729	.21370	.21009
2795	.20668	.20348	.20048	.19769	.19479
2796	.19208	.18920	.18677	.18407	.18180
2797	.17964	.17775	.17607	.17454	.17328
2998	.17193	.17091	.17017	.16956	.16928
2799	.16902	.16925	.16949	.16994	.17073
2800	.17168	.17278	.17387	.17514	.17636

Table 6.2.1. Continued

Wavelength	0.0	0.2	0.4	0.6	0.8Å
2801 Å	.17767	.17916	.18081	.18258	.18451
2802	.18664	.18904	.19140	.19375	.19618
2803	.19897	.20206	.20509	.20853	.21223
2804	.21641	.22038	.22487	.22939	.23410
2805	.23904	.24419	.24955	.25512	.26081
2806	.26659	.27268	.27897	.28523	.29170
2807	.29794	.30425	.31056	.31709	.32401
2808	.33090	.33862	.34610	.35354	.36113
2809	.36858	.37662	.38424	.39222	.40043
2810	.40851	.41691	.42498	.43360	.44141
2811	.44957	.45776	.46610	.47465	.48315
2812	.49156	.50019	.50824	.51645	.52444
2813	.53297	.54186	.55072	.55988	.56911
2814	.57798	.58714	.59620	.60550	.61404
2815	.62238	.63055	.63831	.64594	.65344
2816	.66084	.66818	.67603	.68275	.68023
2817	.69663	.70375	.70985	.71723	.72377
2818	.72990	.73687	.74353	.74961	.75623
2819	.76204	.76895	.77529	.78210	.78760
2820	.79349	.79884	.80410	.81035	.81574
2821	.82170	.82720	.83190	.83731	.84157
2822	.84540	.85010	.85527	.85973	.86441
2823	.86918	.87442	.87822	.88326	.88748
2824	.89180	.89655	.90080	.90544	.90950
2825	.91246	.91614	.91828	.92083	.92263
2826	.92473	.92678	.92978	.93190	.93518
2827	.93810	.94209	.94478	.94820	.95097
2828	.95443	.94785	.96120	.96346	.96616
2829	.96951	.97180	.97575	.97842	.98021
2830	.98232	.98486	.98645	.98680	.98808
2831	.98927	.99043	.99227	.99373	.99535
2832	.99580	.99680	.99880	.99826	.99879
2833	.99993	.99922	.99861	.99826	.99771
2834	.99756	.99785	.99634	.99669	.99552
2835	.99534	.99286	.99215	.99091	.98883
2836	.98670	.98517	.98356	.98217	.98152
2837	.98109	.97961	.97854	.97733	.97491
2838	.97413	.97177	.96805	.96470	.96144
2839	.95805	.95321	.94880	.94490	.94065
2840	.93537	.92925	.92322	.91773	.91160

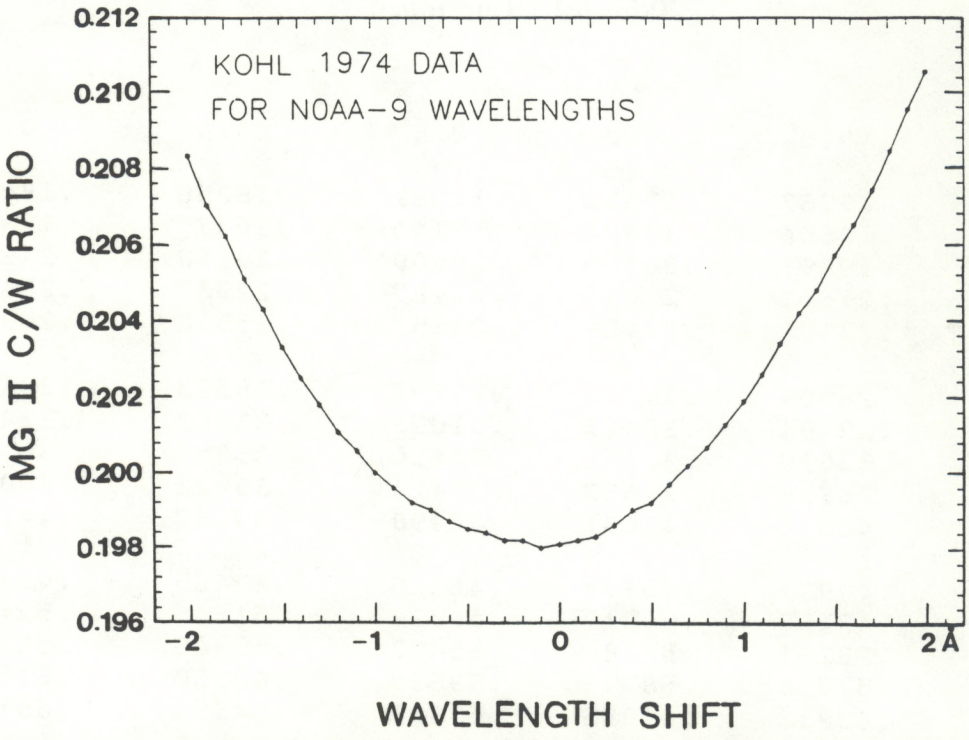

Figure 6.2.2.3. The Mg II core-to-wing ratio as a function of wavelength shift in the NOAA9 discrete-wavelength mode for the quiet Sun-center spectrum of Kohl and Parkinson (1976).

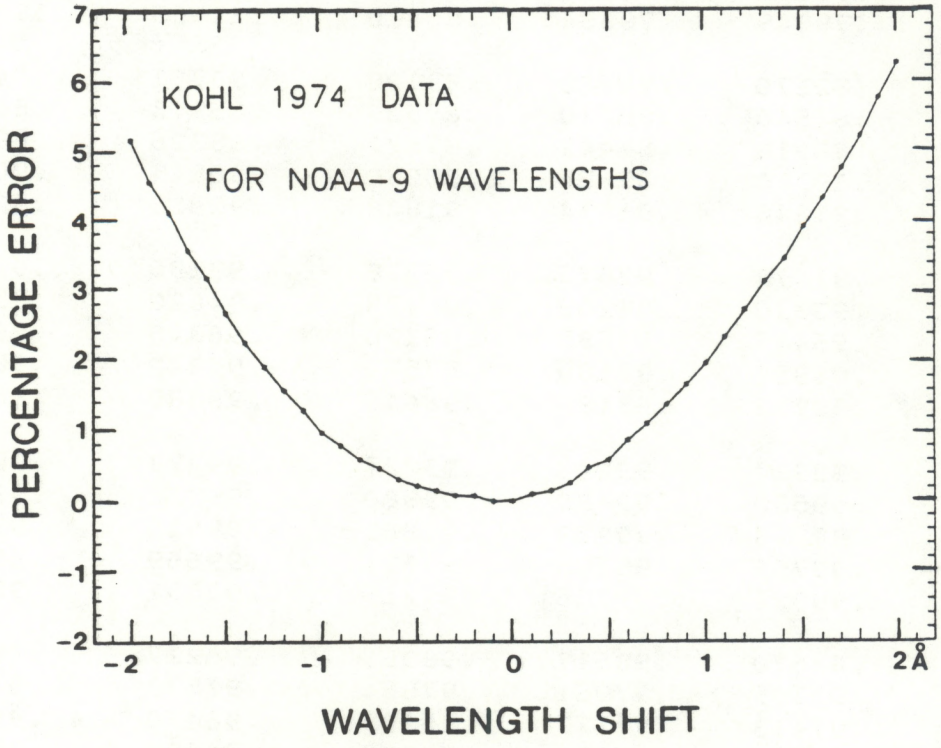

Figure 6.2.2.4. The same as figure 6.2.2.3 expressed as a percent error relative to the R_{MgII} value for no shift in wavelength.

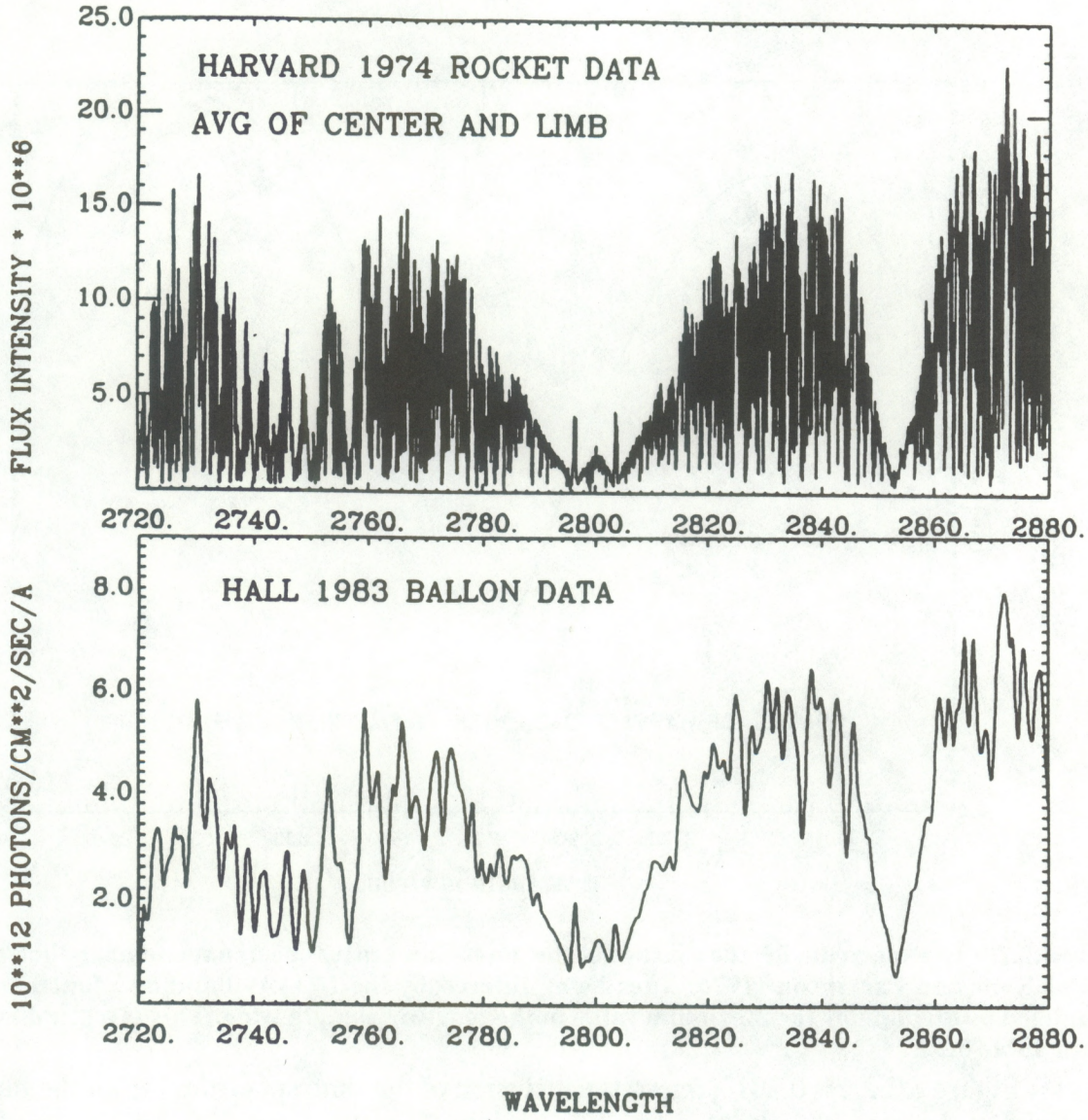

Figure 6.2.2.5. Solar UV energy-flux spectrum with very fine wavelength resolution derived from an average of Kohl and Parkinson's (1976) near-limb spectrum and quiet-Sun-center spectrum, observed on 15 May 1974 (top), and a moderate resolution photon-flux spectrum of Hall and Anderson (1988), observed on 20 April 1983 (bottom).

resolution file of Hall and Anderson's (1988) balloon-flight observations discussed in Section 6.2.1 and shown in Figures 6.2.1.3, 6.2.1.6, and 6.2.1.7 are also shown in Figure 6.2.2.5 for comparison.

Figure 6.2.2.6 shows this average limb and center spectrum after filtering it with the bandpass function for the SBUV2 monitor on the NOAA9 satellite and after normalizing it to the peak intensity in the long-wavelength wing. All the fine structure in Figure 6.2.2.5 is smoothed out in Figure 6.2.2.6. The short-wavelength wing peaks at a vacuum wavelength of 276.853 nm with a relative intensity of 0.761, which agrees well with Figures 4.6.8 and 6.2.1.3 and with the Sun-center spectrum in Figure 6.2.2.2. The minimum in the line core occurred at 279.908 nm, which is about 0.01 nm below the NOAA9 estimates in Figure 4.3.1. The classical NOAA9

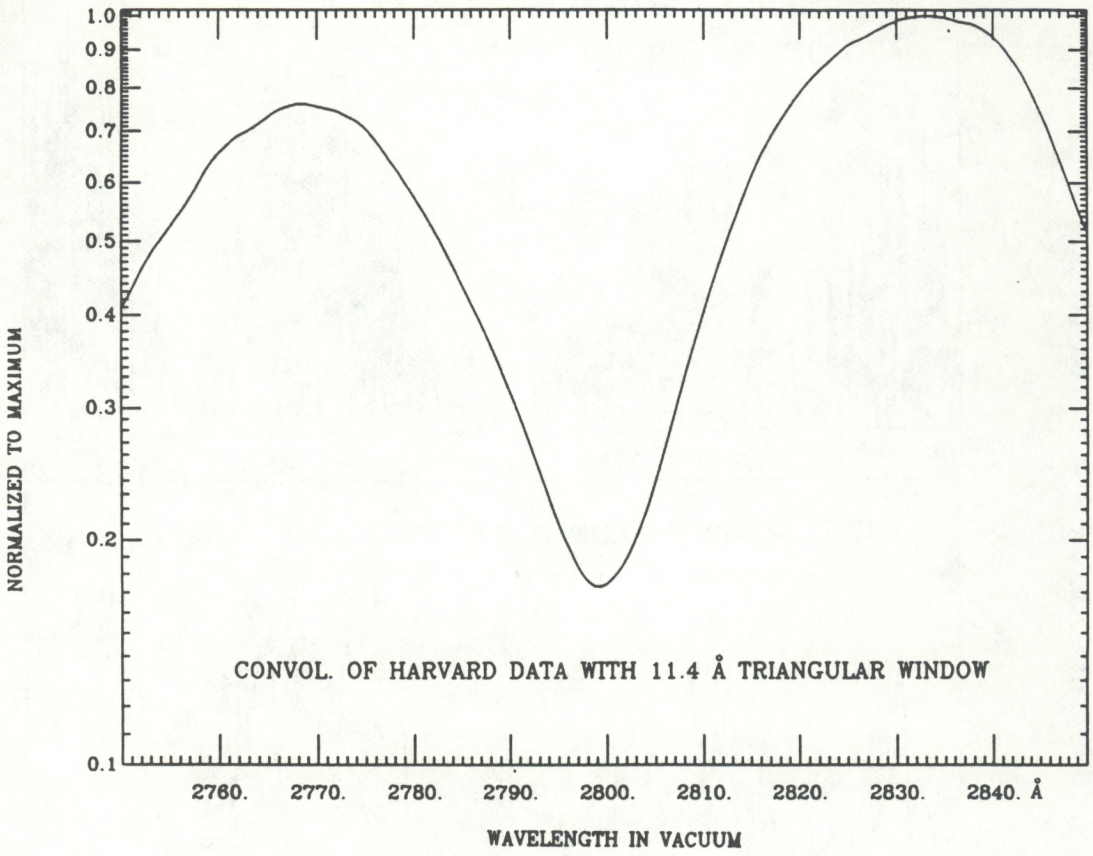

Figure 6.2.2.6 The spectrum for the average of the quiet-Sun-center spectrum and near-limb spectrum of Kohl and Parkinson (1976) after being filtered by the NOAA9 bandpass function and normalized by dividing by the maximum value in the long-wavelength wing. This is a graph of the data in Table 6.2.2.

R_{MgII} for Figure 6.2.2.6 is 0.2018 nm, so the inclusion of the limb spectrum raised the ratio by about 0.002 (1%) more than the Sun-center spectrum alone did. Since the solar cycle variation in Figure 6.1.1 is only about 10%, this 1% shift suggests that it would be difficult to estimate the full-disk spectrum from spatially resolved spectra to the accuracy needed for comparing R_{MgII} data. However, this value is still low in comparison to that of the solar cycle minimum seen in Figure 6.1.1.

Table 6.2.2 gives this average center and limb spectrum for the NOAA9 passband function, for use in further studies of the relative wavelength dependence of the solar Mg II h and k lines, for applications to the SBUV2 monitoring measurements. Note that in Figure 6.2.2.6 the minimum is very smooth and nearly parabolic in shape, which is consistent with using a second-order polynomial to fit the minimum discussed in Section 4.3, or that in equation (4.9).

Figure 6.2.2.7 shows the change in R_{MgII} for the spectrum in Figure 6.2.2.6 or Table 6.2.2. This change is produced by adding to each of the NOAA9 wavelengths involved in equation (4.2) an amount called wavelength shift (or $\Delta\lambda$), where the change is with respect to the original value $R_{MgII}=0.201813$ at $\Delta\lambda= 0$. The minimum of this curve is at $\Delta\lambda=+.02$ nm even though the minimum of the spectrum in Figure 6.2.2.6 is at 279.908 nm. This latter spectrum is about 0.007 nm shorter than the center wavelength no.7; i. e. the combined effects of the shifts for the

Table 6.2.2. The spectrum for the average of the quiet-Sun-center spectrum and near-limb spectrum of Kohl and Parkinson (1976) after being filtered by the NOAA9 bandpass function and normalized by dividing by the maximum value in the long-wavelength wing

Wavelength	0.0	0.2	0.4	0.6	0.8 Å
2761 Å	0.67296	0.67684	0.68048	0.68372	0.68652
2762	0.68903	0.69129	0.69342	0.69556	0.69785
2763	0.70035	0.70281	0.70541	0.70830	0.71142
2764	0.71466	0.71798	0.72109	0.72424	0.72741
2765	0.73071	0.73433	0.73789	0.74098	0.74384
2766	0.74637	0.74854	0.75035	0.75216	0.75372
2767	0.75507	0.75637	0.75763	0.75895	0.75999
2768	0.76068	0.76088	0.76093	0.76097	0.76061
2769	0.75996	0.75918	0.75828	0.75725	0.75614
2770	0.75511	0.75402	0.75300	0.75199	0.75106
2771	0.75012	0.74902	0.74783	0.74685	0.74565
2772	0.74414	0.74237	0.74034	0.73804	0.73561
2773	0.73331	0.73122	0.72913	0.72692	0.72454
2774	0.72177	0.71881	0.71557	0.71201	0.70810
2775	0.70390	0.69951	0.69484	0.68990	0.68507
2776	0.68007	0.67496	0.66979	0.66434	0.65888
2777	0.65341	0.64797	0.64269	0.63757	0.63263
2778	0.62754	0.62230	0.61691	0.61137	0.60583
2779	0.60018	0.59476	0.58939	0.58406	0.57876
2780	0.57330	0.56789	0.56249	0.55710	0.55183
2781	0.54662	0.54132	0.53582	0.53026	0.52464
2782	0.51904	0.51347	0.50803	0.50264	0.49723
2783	0.49169	0.48618	0.48067	0.47514	0.46970
2784	0.46439	0.45915	0.45382	0.44834	0.44289
2785	0.43758	0.43247	0.42754	0.42251	0.41743
2786	0.41242	0.40754	0.40261	0.39764	0.39274
2787	0.38782	0.38287	0.37788	0.37290	0.36788
2788	0.36284	0.35780	0.35281	0.34784	0.34283
2789	0.33785	0.33289	0.32800	0.32323	0.31858
2790	0.31402	0.30943	0.30485	0.30018	0.29552
2791	0.29092	0.28632	0.28173	0.27718	0.27275
2792	0.26833	0.26389	0.25949	0.25519	0.25100
2793	0.24683	0.24274	0.23870	0.23473	0.23074
2794	0.22689	0.22314	0.21952	0.21603	0.21269
2795	0.20952	0.20652	0.20359	0.20081	0.19822
2796	0.19578	0.19345	0.19109	0.18864	0.18623
2797	0.18404	0.18209	0.18036	0.17879	0.17743
2798	0.17627	0.17530	0.17453	0.17389	0.17344
2799	0.17323	0.17325	0.17348	0.17390	0.17448
2800	0.17519	0.17608	0.17706	0.17809	0.17924

Table 6.2.2 Continued

Wave-length	0.0	0.2	0.4	0.6	0.8Å
2801Å	0.18054	0.18199	0.18358	0.18531	0.18718
2802	0.18921	0.19138	0.19374	0.19629	0.19894
2803	0.20171	0.20464	0.20780	0.21109	0.21451
2804	0.21813	0.22198	0.22615	0.23055	0.23519
2805	0.24006	0.24506	0.25028	0.25568	0.26128
2806	0.26702	0.27292	0.27888	0.28499	0.29123
2807	0.29755	0.30391	0.31033	0.31680	0.32352
2808	0.33050	0.33755	0.34469	0.35194	0.35921
2809	0.36646	0.37382	0.38129	0.38895	0.39668
2810	0.40459	0.41265	0.42071	0.42875	0.43685
2811	0.44492	0.45301	0.46117	0.46925	0.47738
2812	0.48555	0.49375	0.50200	0.51032	0.51862
2813	0.52688	0.53525	0.54380	0.55249	0.56121
2814	0.56992	0.57874	0.58771	0.59676	0.60566
2815	0.61437	0.62273	0.63087	0.63876	0.64639
2816	0.65391	0.66117	0.66837	0.67567	0.68279
2817	0.68983	0.69662	0.70330	0.70995	0.71664
2818	0.72333	0.72981	0.73617	0.74263	0.74911
2819	0.75560	0.76194	0.76827	0.77467	0.78111
2820	0.78728	0.79332	0.79948	0.80540	0.81132
2821	0.81712	0.82275	0.82827	0.83356	0.83867
2822	0.84354	0.84827	0.85313	0.85801	0.86290
2823	0.86783	0.87271	0.87766	0.88258	0.88747
2824	0.89221	0.89693	0.90178	0.90636	0.91057
2825	0.91430	0.91753	0.92048	0.92319	0.92570
2826	0.92785	0.93000	0.93239	0.93524	0.93825
2827	0.94147	0.94484	0.94818	0.95147	0.95453
2828	0.95735	0.96016	0.96300	0.96597	0.96893
2829	0.97180	0.97449	0.97699	0.97956	0.98225
2830	0.98449	0.98642	0.98836	0.99008	0.99142
2831	0.99244	0.99335	0.99447	0.99558	0.99663
2832	0.99778	0.99861	0.99912	0.99962	0.99984
2833	0.99983	0.99981	0.99994	0.99992	0.99957
2834	0.99903	0.99831	0.99768	0.99687	0.99591
2835	0.99475	0.99340	0.99187	0.99022	0.98845
2836	0.98655	0.98464	0.98294	0.98169	0.98069
2837	0.97972	0.97871	0.97785	0.97678	0.97517
2838	0.97304	0.97068	0.96791	0.96462	0.96103
2839	0.95733	0.95369	0.94980	0.94548	0.94074
2840	0.93570	0.93042	0.92484	0.91898	0.91280

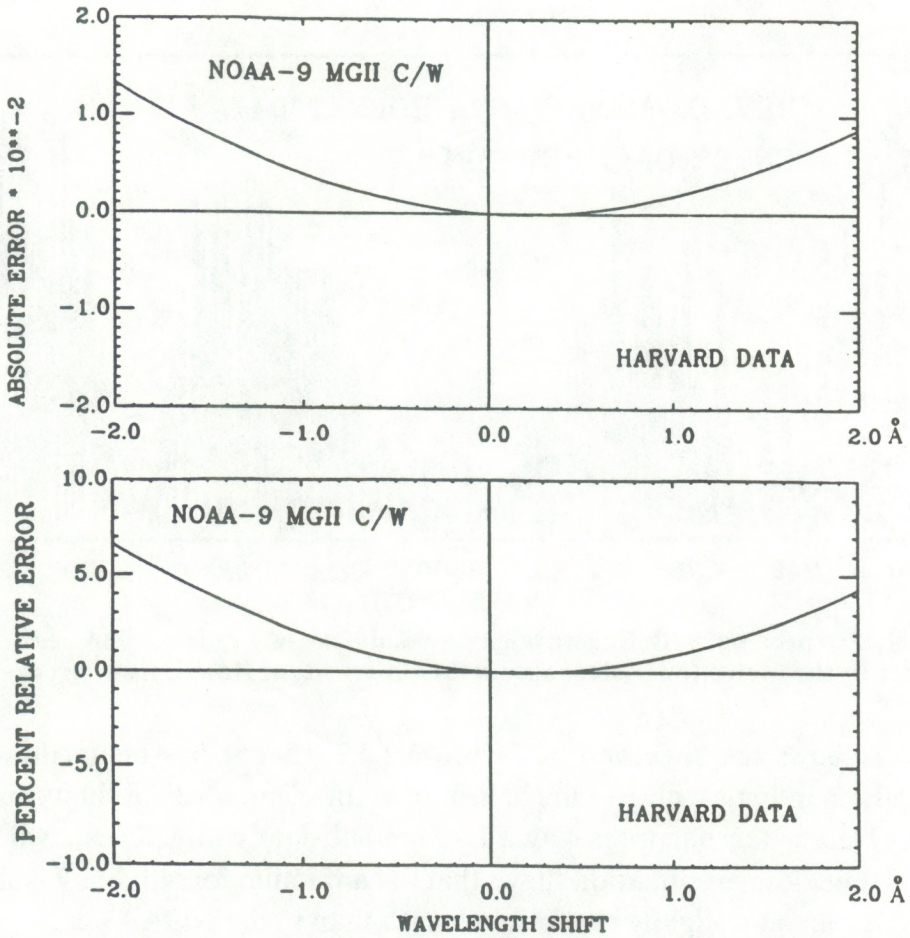

Figure 6.2.2.7. The absolute error (top) and percentage error (bottom) in R_{MgII} as a function of a shift in wavelength added to each of the nominal wavelengths of the NOAA9 discrete-wavelength mode of observations for the spectrum shown in Figure 6.2.2.6.

other six terms in equation (4.2) dominate over the effect due to wavelength no. 7 alone. For shifts between -.02 to+.05 nm the errors are negligible, but small corrections would be appropriate for larger shifts. The wavelength shifts found in Figures 4.3.1 and 4.3.6 would have a negligible effect.

6.2.3. Hawaii Measurements

S. D. Bouwer

Figure 6.2.3.1 shows a broader wavelength range, for the same spectrum as shown in Figure 2.1, for data obtained by the Institute of Astronomy of the University of Hawaii from a rocket flight on 19 June 1974. The portion of the Sun used in deriving this spectrum was a fairly quiet area, with angular view 7" × 130", located near the center of the Sun. Notice the close resemblance of this figure to Figures 6.2.2.5 and 6.2.2.1. The spectrum was measured with .0005 nm wavelength steps and the corrected wavelength scale was accurate to ± .003 nm. Intercomparisons with the Kohl and Parkinson's data (1976) over .5 nm intervals were used to correct the wavelength-dependent intensity sensitivity of these University of Hawaii data, recorded using photographic film; so, at least in terms of broad-wavelength dependence, these data are not completely independent of the results of Kohl and Parkinson (1976).

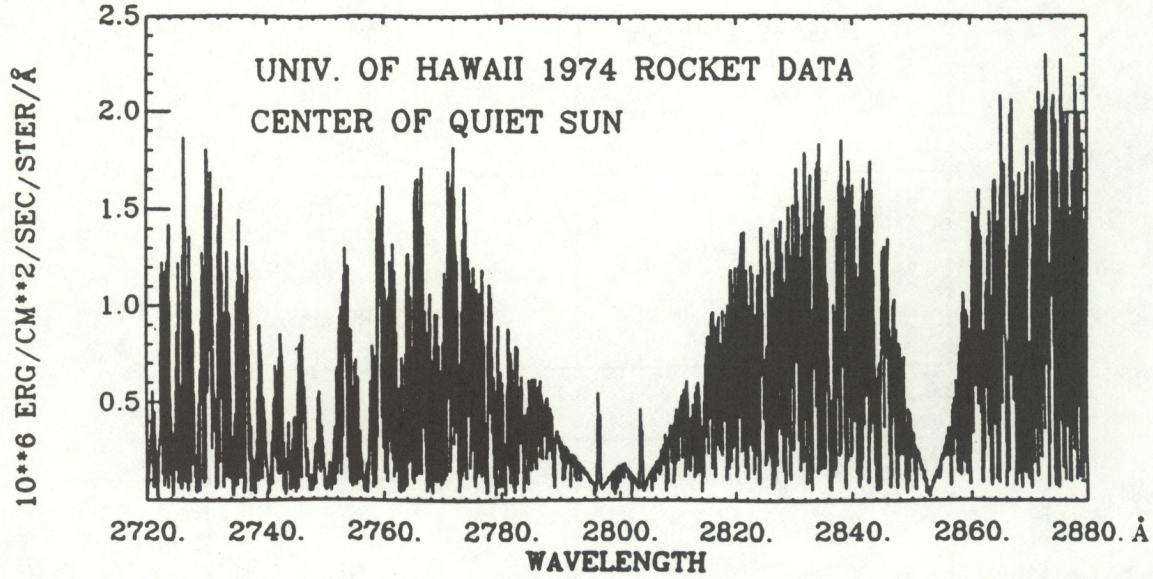

Figure 6.2.3.1. Solar spectrum with fine wavelength resolution of a quiet region near the center of the Sun, recorded by the Institute of Astronomy at the University of Hawaii from a rocket flight of 19 June 1974.

Figure 6.2.3.2 shows the spectrum of Figure 6.2.3.1 after it has been filtered with the NOAA9 triangular bandpass with 1.14 nm half-max width; Figure 6.2.3.3 shows similar results for the Nimbus-7 triangular bandpass with a 1.10 nm half-max width. These two figures look almost identical, but close examination shows that the minimum for Nimbus 7 is slightly lower in intensity and occurs at a slightly lower wavelength than in the NOAA9 case.

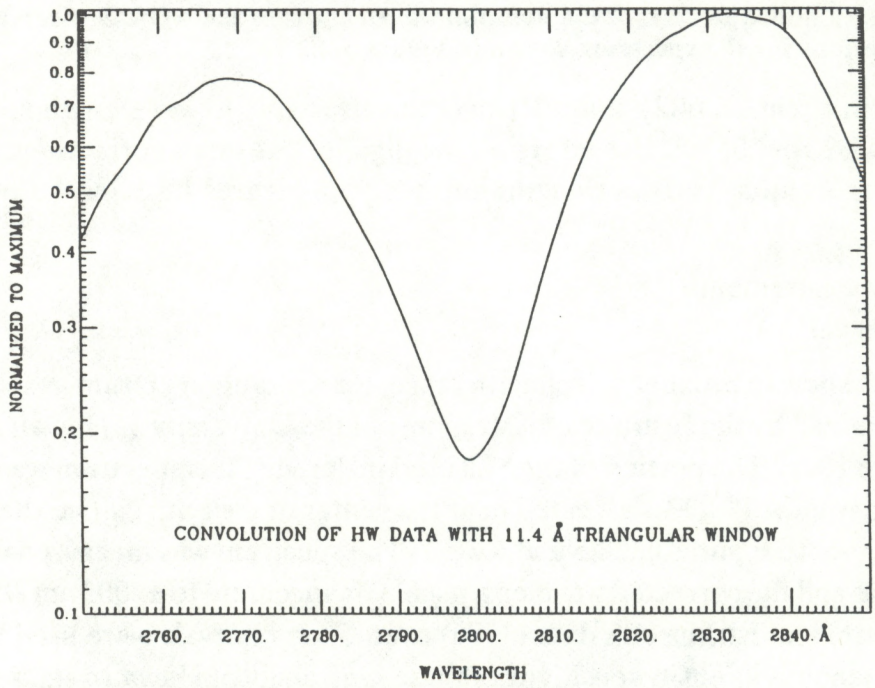

Figure 6.2.3.2. The spectrum for the quiet center of the Sun from the University of Hawaii (Allen et al., 1978) after being filtered by the NOAA9 band-pass function and normalized by dividing by the maximum value in the long-wavelength wing. This is a graph of the data in Table 6.2.3.

Table 6.2.3 presents the spectral normalized intensity, as a function of wavelength in a vacuum for the NOAA9 case, for use in future studies. Assuming that the spectra for the full-disk flux for a quiet Sun would be similar to the spectra in Figures 6.2.3.2 and 6.2.3.3, we compute the MgII core-to-wing ratios to be $R_{MgII}=0.2082$ for NOAA9 from equation (4.2) and $R_{MgII}=0.2090$ for Nimbus 7 from equation (4.1). These values are roughly 0.01 higher than the values for the Sun-center spectrum of Kohl and Parkinson (1976) and are more like the results for the spectrum derived from the average of Kohl and Parkinson's limb and Sun-center spectra. See the no-shift value in Figure 6.2.2.3. Both of these values are, however, clearly lower than the solar cycle minimum values in Figure 6.1.1. We do not expect these two results to be identical because of the differences in wavelength positions and bandwidths involved in equations (4.1) and (4.2), but we would expect their temporal variations with changing solar activity to be linearly related. The Nimbus-7 R_{MgII} value is higher than that for NOAA9, despite the fact that the minimum is slightly lower for Nimbus-7 in Figure 6.2.3.3 than for NOAA9 in Figure 6.2.3.2, because the central wavelength for NOAA9 fits better with the minimum of the unresolved Mg II h & k lines than does the central wavelength of Nimbus-7.

Figures 6.2.3.4–6.2.3.7 show the sensitivity of R_{MgII} to uniform shifts in the NOAA9 discrete-mode wavelengths or to errors in the NOAA9 wavelength scale, relative to that for the University of Hawaii data, in absolute error in R_{MgII} and also in percent error with respect to

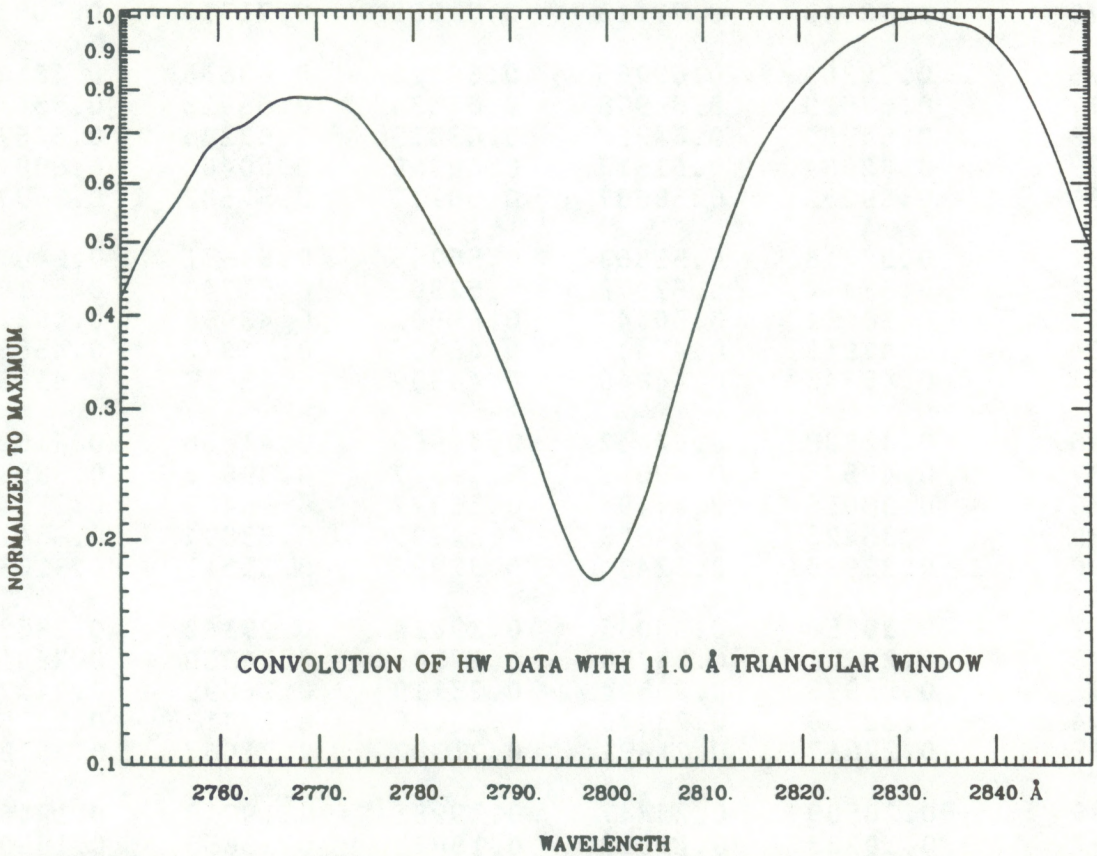

Figure 6.2.3.3. The spectrum for the quiet center of the Sun, from the University of Hawaii (Allen et al., 1978), after being filtered by the Nimbus-7 bandpass function and normalized by dividing by the maximum value in the long-wavelength wing.

Table 6.2.3. The quiet Sun-center spectrum of Allen et al. (1978) after being filtered by the NOAA9 triangular bandpass function with a 1.14 nm half-max width and then normalized by dividing by the maximum value in the long-wavelength wing

Wave-length	0.0	0.2	0.4	0.6	0.8Å
2761Å	0.69455	0.69795	0.70112	0.70398	0.70641
2762	0.70858	0.71055	0.71244	0.71452	0.71686
2763	0.71947	0.72214	0.72493	0.72801	0.73130
2764	0.73472	0.73810	0.74120	0.74433	0.74749
2765	0.75087	0.75462	0.75838	0.76165	0.76467
2766	0.76730	0.76950	0.77129	0.77302	0.77450
2767	0.77576	0.77705	0.77827	0.77959	0.78061
2768	0.78129	0.78158	0.78178	0.78203	0.78199
2769	0.78172	0.78136	0.78088	0.78028	0.77962
2770	0.77910	0.77851	0.77802	0.77765	0.77744
2771	0.77723	0.77675	0.77611	0.77566	0.77483
2772	0.77352	0.77188	0.76988	0.76758	0.76510
2773	0.76270	0.76050	0.75824	0.75583	0.75328
2774	0.75015	0.74662	0.74279	0.73856	0.73398
2775	0.72913	0.72413	0.71889	0.71352	0.70831
2776	0.70301	0.69765	0.69226	0.68658	0.68102
2777	0.67539	0.66978	0.66434	0.65913	0.65413
2778	0.64900	0.64368	0.63819	0.63246	0.62670
2779	0.62084	0.61517	0.60958	0.60400	0.59840
2780	0.59262	0.58687	0.58112	0.57532	0.56971
2781	0.56418	0.55853	0.55265	0.54671	0.54071
2782	0.53474	0.52879	0.52305	0.51742	0.51182
2783	0.50611	0.50047	0.49502	0.48956	0.48425
2784	0.47913	0.47411	0.46896	0.46372	0.45854
2785	0.45346	0.44840	0.44359	0.43877	0.43388
2786	0.42908	0.42442	0.41969	0.41486	0.41008
2787	0.40525	0.40033	0.39537	0.39036	0.38530
2788	0.38016	0.37494	0.36977	0.36463	0.35947
2789	0.35428	0.34908	0.34393	0.33894	0.33410
2790	0.32938	0.32464	0.31992	0.31511	0.31031
2791	0.30558	0.30086	0.29614	0.29142	0.28680
2792	0.28221	0.27758	0.27300	0.26850	0.26413
2793	0.25975	0.25544	0.25119	0.24699	0.24278
2794	0.23868	0.23470	0.23085	0.22713	0.22356
2795	0.22017	0.21691	0.21372	0.21067	0.20780
2796	0.20509	0.20247	0.19981	0.19718	0.19460
2797	0.19223	0.19012	0.18825	0.18653	0.18504
2798	0.18376	0.18270	0.18187	0.18123	0.18081
2799	0.18066	0.18077	0.18112	0.18169	0.18242
2800	0.18333	0.18444	0.18566	0.18693	0.18830

Table 6.2.3. Continued

Wave-length	0.0	0.2	0.4	0.6	0.8
2801	0.18981	0.19146	0.19323	0.19513	0.19713
2802	0.19927	0.20156	0.20401	0.20660	0.20929
2803	0.21209	0.21502	0.21812	0.22130	0.22461
2804	0.22813	0.23191	0.23600	0.24035	0.24496
2805	0.24979	0.25476	0.25995	0.26532	0.27088
2806	0.27656	0.28236	0.28823	0.29424	0.30038
2807	0.30659	0.31282	0.31908	0.32538	0.33196
2808	0.33879	0.34583	0.35289	0.36004	0.36717
2809	0.37430	0.38150	0.38881	0.39627	0.40381
2810	0.41142	0.41914	0.42680	0.43443	0.44206
2811	0.44960	0.45720	0.46492	0.47260	0.48037
2812	0.48819	0.49607	0.50395	0.51200	0.52000
2813	0.52805	0.53625	0.54462	0.55301	0.56133
2814	0.56960	0.57797	0.58654	0.59530	0.60397
2815	0.61253	0.62075	0.62872	0.63643	0.64388
2816	0.65122	0.65828	0.66527	0.67239	0.67935
2817	0.68633	0.69302	0.69966	0.70628	0.71292
2818	0.71958	0.72609	0.73248	0.73902	0.74562
2819	0.75230	0.75880	0.76530	0.77174	0.77820
2820	0.78441	0.79048	0.79668	0.80264	0.80861
2821	0.81450	0.82014	0.82574	0.83110	0.83640
2822	0.84150	0.84644	0.85160	0.85681	0.86190
2823	0.86683	0.87174	0.87674	0.88174	0.88669
2824	0.89135	0.89597	0.90066	0.90506	0.90908
2825	0.91283	0.91635	0.91977	0.92302	0.92594
2826	0.92836	0.93074	0.93328	0.93629	0.93947
2827	0.94292	0.94657	0.95015	0.95364	0.95687
2828	0.95978	0.96266	0.96551	0.96849	0.97140
2829	0.97430	0.97702	0.97953	0.98205	0.98465
2830	0.98678	0.98857	0.99021	0.99160	0.99265
2831	0.99343	0.99415	0.99514	0.99614	0.99712
2832	0.99823	0.99898	0.99939	0.99986	0.99998
2833	0.99992	0.99966	0.99957	0.99938	0.99883
2834	0.99806	0.99718	0.99644	0.99544	0.99427
2835	0.99290	0.99137	0.98975	0.98810	0.98637
2836	0.98460	0.98282	0.98119	0.97993	0.97886
2837	0.97779	0.97681	0.97606	0.97509	0.97369
2838	0.97170	0.96954	0.96684	0.96351	0.95988
2839	0.95621	0.95265	0.94884	0.94459	0.93994
2840	0.93499	0.92984	0.92433	0.91850	0.91244

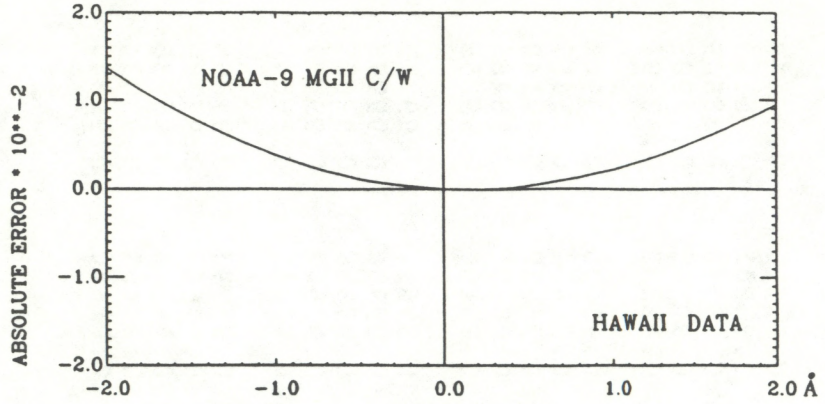

Figure 6.2.3.4

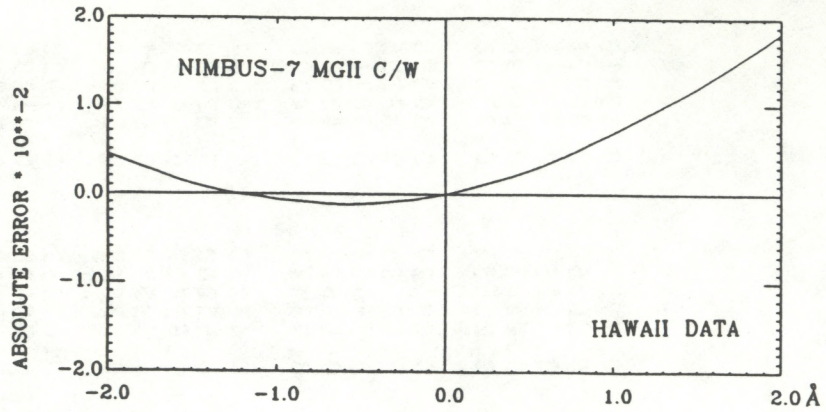

Figure 6.2.3.5

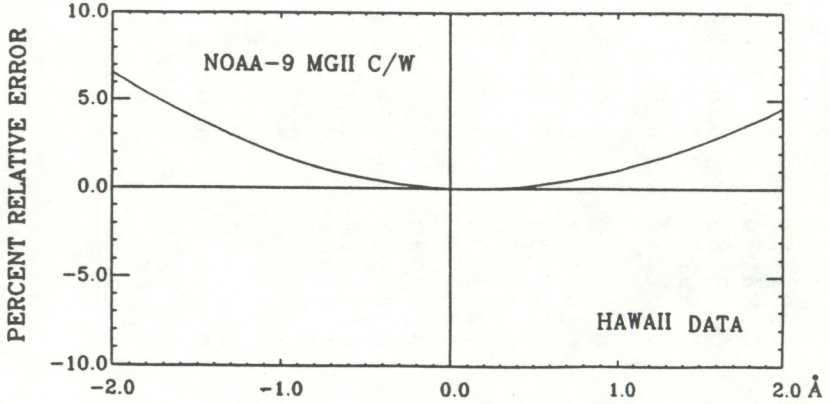

Figure 6.2.3.6

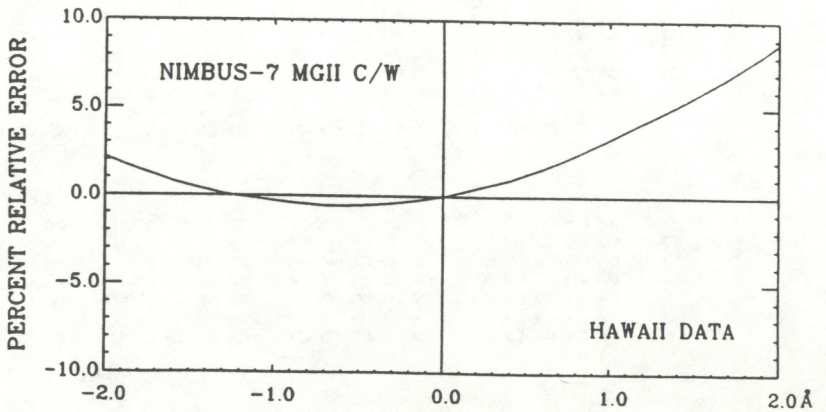

Figure 6.2.3.7

the core-to-wing ratio for no shift. Notice the close similarity between Figure 6.2.3.4 and 6.2.3.7 (top), and also that between Figures 6.2.3.6 and 6.2.3.7 (bottom). The Nimbus-7 results in Figures 6.2.3.5 and 6.2.3.7 attain their minimum R_{MgII} values if the Nimbus-7 wavelengths are shifted by .07 nm to shorter wavelengths.

6.2.4. Summary of Studies of R_{MgII} for Fine-Wavelength-Resolution Spectra

The results presented above are just the beginning of our studies of R_{MgII} for fine-wavelength-resolution observations of the solar Mg II h and k lines. Improved analyses of full-disk spectra with fine wavelength resolution are needed. So, what have we learned so far and what should we do next?

Hall and Anderson's (1988) full-disk spectrum, shown in Figure 6.2.1.2 is so affected by the large wavelength-dependent corrections for atmospheric transmission to the balloon altitude that we are uncertain how well their spectra of 21 April 1977 and 19 April 1978 can be used to model the Mg II line shape for the low-resolution NOAA9 observations. However, their 1983 spectrum, taken on a day when Nimbus-7 observations were made, is worth studying further. The analysis reported in Section 6.2.1 should be improved by using the preflight laboratory measurements of the NOAA9 and Nimbus-7 passbands rather than the oversimplified triangular function. The photon flux should be converted to an energy flux since the Mg II index is based on a ratio of energy fluxes and not photon fluxes. (The spectra of Kohl and Parkinson (1976) and that of Allen et al. (1978) were energy flux spectra.)

The solar radiance spectra from quiet portions of the Sun are not sufficiently representative of the full-disk flux spectrum for our studies of the influence of the Mg II h and k line shape on the NOAA9 SBUV2 measurements; the center-to-limb effect causes the full-disk or irradiance spectrum to differ sufficiently from the quiet Sun-center spectrum to significantly affect R_{MgII}. Although we have qualitative information on the center-to-limb dependence of the Mg II h and k line shape, we do not have sufficiently accurate quantitative information to derive the full-disk spectrum from the radiance observations for use in determining R_{MgII} precisely from such observations. It may nevertheless be interesting to attempt such a "quiet-Sun" derivation because the results may be representative of the Maunder-minimum values for R_{MgII}, which was probably lower than our recent solar cycle minimum values; however, such a result would be highly speculative and probably inaccurate.

The results in Figures 6.2.2.4, 6.2.2.7, and 6.2.3.6 provide information about the percent error in R_{MgII} as a function of either wavelength drifts or errors in the wavelength scale for the NOAA9 data. However, these results are not highly accurate since we now know that these quiet-Sun radiance spectra are not quite the same as the full-disk spectrum. Their relative wave- length shape probably is appropriate but we plan to study other full-disk spectra in an attempt to obtain a better result. In the meantime, we will use the results presented here as our best-estimate guideline. We see no need to revise the wavelength scale for NOAA9.

Figure 6.2.4 summarizes the spectral shape for the NOAA9 observations derived from solar radiance observations. Comparison of the flux ratios shown in Figures 4.6.7 and 4.6.8 with the spectra and NOAA9 wavelength positions in Figure 6.2.4 shows good agreement, but the central minimum is a little lower in the latter case. Similarly, Figures 4.6.1 to 4.6.5 agree with

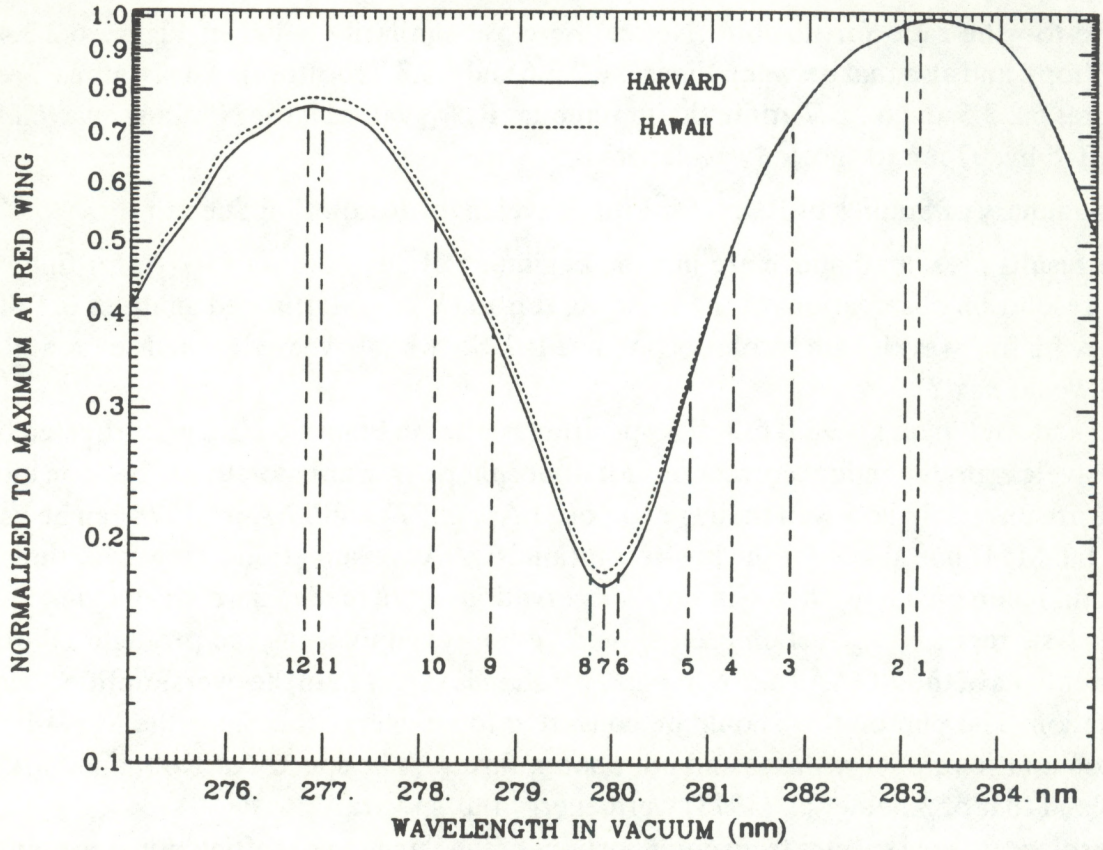

Figure 6.2.4. Comparison of the average of the quiet Sun-center and limb spectra of Kohl and Parkinson (1976) and the quiet Sun-center spectrum of the University of Hawaii (Allen et al., 1978). See Figures 6.2.2.6 and 6.2.3.2, respectively. Each spectrum is normalized to its maximum value in its long-wavelength wing. The dashed vertical lines mark the positions of our nominal values for the twelve wavelengths in the discrete-wavelength mode observations of the solar Mg II h and k lines.

the results in Figure 6.2.4. Note that the impressions one obtains from the older Figure 6.2.1.2 (for example that the flux at wavelength no. 10 is lower than that at wavelength no. 4) can be misleading. Figure 6.2.4 provides a greatly improved representation of the shape of the Mg II h and k lines and the wavelength locations for NOAA9 discrete-wavelength mode observations. Quantitative comparisons of spectra and flux ratios for the NOAA9 measurements will be presented in future reports in this series.

6.3. Ca-K 1Å Index

S. D. Bouwer and J. Barrett

In Chapter 2 we reviewed the close relationship between measurements of the Mg II h and k lines (like those made by the Nimbus 7 and NOAA9 satellites) and the Ca II H and K line observations from mountaintop observatories. Because of this known close relationship, we compared same-day Ca-K 1Å index values of White and Livingston (1981) and White et al. (1992) with the Nimbus- 7 R_{MgII} values and, separately, with both the NOAA9 classical and modified Mg II core-to-wing ratios. This was done to determine the relation of each of these Mg II indices to the Ca K 1Å index and also to use these relations to improve our knowledge of

the relationship between the Nimbus-7 and NOAA9 Mg II indices. The advantage of such comparisons over the results in Section 6.1 is that they use data representative of the entire time series and also of the full dynamic range of data, as seen in Figure 6.1.1. The main disadvantage of the Ca K 1Å index is that it is typically recorded on about 3 to 4 consecutive days per month; therefore it lacks the full coverage of daily samples. The main results and details of this study are being published elsewhere (Donnelly, White and Livingston, 1994; Donnelly et al., 1994) and will not be repeated here except for a brief summary. First, we present a result that shows a problem with the classical NOAA9 ratio and is not being published elsewhere.

Figure 6.3 shows a scatter diagram and linear regression line for the NOAA9 classical Mg II core-to-wing ratio derived from equation (4.7) versus same-day values of White and Livingston's (1981) Ca K 1Å index. The NOAA9 time series of classical R_{MgII} data were normalized to an estimate of their solar cycle minimum value based on the monthly average of daily values for September 1986. The data included in Figure 6.3 are from the interval June 1986–July 1988, from solar minimum to about halfway to the peak of solar cycle 22.

Although the correlation coefficient for Figure 6.3 was 0.97, which is quite high, there is a serious problem in this figure. There is a nearly linear trend in which intensity increases above the solar cycle minimum values, then the linear trend falls below the line shown for the Ca K 1Å index up to about 0.0895 Å. Near Ca K=0.090 the classical NOAA9 values of R_{MgII} rise

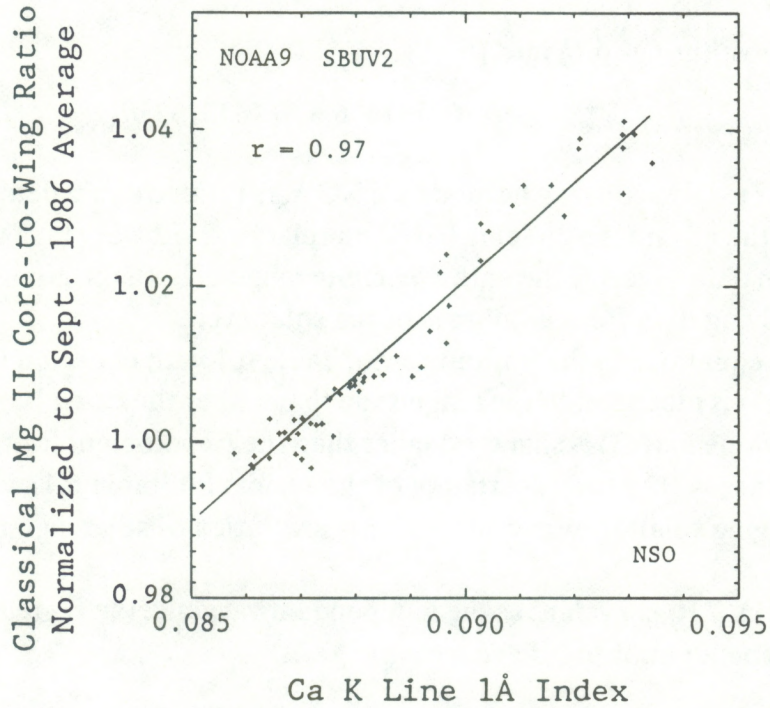

Figure 6.3. A scatter diagram of the classical NOAA9 Mg II ratio as a function of same day values of the Ca K 1Å index observed by White and Livingston (1981) at the National Solar Observatory on Kitt Peak. The NOAA9 data were normalized to their monthly average value for September 1986. The straight line is the linear regression relation of R_{MgII} as a function of Ca K for the entire data set.

abruptly to a second linear trend for higher values; the slope of this second linear trend is similar to the first. R_{MgII} appears to have had 0.9% added to it above this transition. Since the main temporal trend in the data in Figure 6.3 is the rise of the solar cycle, this shift as a function of intensity can also be interpreted as a change that occurred in time, near December 1987, when the rate of rise of monthly averages of intensity increased about fourfold. So, there was a shift in the relationship of the classical NOAA9 ratio with respect to the Ca K index.

The NOAA9 data were studied to determine whether there was a problem in the data related to this shift. This study led first to the studies in Sections 4.3, 4.4, and 4.7, and then to the abandonment of the classical NOAA9 Mg II ratios and the adoption of the modified Mg II ratio in equation (4.8). The modified ratio has no such shift in its relation with the Ca K 1Å index (Donnelly et al., 1994).

Returning to the review of comparisons of R_{MgII} being published elsewhere (Donnelly, White and Livingston, 1994; Donnelly et al., 1994), we give the linear regression relations derived from comparing NOAA9 data for May 27, 1986 through March 31, 1990:

$$I_{CaK1\text{Å}\ predicted} = -0.1092458 + 0.484681\ R_{MgII\ NOAA9,\ modified}(m\text{Å}) , \qquad (6.1)$$

where the correlation coefficient is r=0.9901 for 109 same-day pairs. Similarly, comparing the Nimbus-7 data shown in Figure 6.1.1 with Ca K 1Å values for 177 same-day pairs gives

$$R_{MgII\ Nimbus7\ predicted} = 0.143908 + 1.38882\ I_{CA\ K\ 1\text{Å}} , \qquad (6.2)$$

where r=0.976. Substituting (6.1) into (6.2) gives

$$R_{MgII\ equivalent\ Nimbus7\ value} = -0.00781416 + 0.673133\ R_{MgII\ NOAA9,\ modified} . \qquad (6.3)$$

Equation (6.3) is used to convert the modified NOAA9 ratio to equivalent Nimbus-7 values. This equation has the advantage of being based on relations with very high correlation coefficients derived from data covering the entire dynamic range of both the Nimbus-7 and NOAA9 data sets and involving data from all phases of the solar cycle.

Comparing the equations in the bottom row of Table 6.1 with equation (6.3), we note that the intercept in (6.3) is much smaller in magnitude than either the *a* or *a* ' coefficients in Table 6.1; similarly, the slope in (6.3) is slightly smaller than the *b* coefficient for the modified ratio. These differences are within the uncertainty of the results for Table 6.1, which are based on small data sets having small dynamic ranges with low ratios of solar signal to observational noise.

Using the Nimbus-7 R_{MgII} values as the independent variable, the regression with the Ca K 1Å index as the dependent or predicted variable gives

$$I_{Ca\ K\ 1\text{Å}\ predicted} = -0.0942175 + 0.685768\ R_{MGII\ Nimbus7} . \qquad (6.4)$$

Equation (6.4) allows one to estimate the Ca K index for most of the days each month when Ca K is not measured. If we solve for the Nimbus-7 variable and put (6.4) in the same form as (6.2), we get

$$R_{MGII\ Nimbus7} = 0.137390 + 1.45822\ I_{Ca\ K\ 1Å} \quad . \tag{6.5}$$

Equation (6.5) places (6.4) into a form where we can better compare the coefficients with (6.2) to see the differences in these two lines, which also provides some indication of the uncertainty in (6.2). For example, the slope in (6.5) is higher than that in (6.2) by about 5%, despite the large correlation coefficient. So we do not have as high a precision conversion as is desirable.

One approach to avoiding accumulative errors as data from future NOAA satellites are combined into one common time series would be to convert each satellite's data to the Kitt Peak Ca K 1Å index. A recent revision to the Kitt Peak instruments may have affected their Ca K 1Å time series, so tests must be conducted; but it is easier to perform such tests than to test (calibrate) an aging satellite instrument. Using the Ca K 1Å index as one reference data set means that the long-term cycle-to-cycle variation would be set by the Ca K data and the Mg II ratio would fill in the missing day-to-day data.

The next two sections were written in 1989. They use classical NOAA9 R_{MgII} values and a conversion Nimbus-7 value that predates our adoption of the modified Mg II ratio and derivation of the results in equation (6.3). Those earlier NOAA9 results cause part (but only part) of the hysteresis or relatively low values in time period 3 during the rise of cycle 22. They are included here for the sake of completeness and because they point out many interesting features that will continue to be discussed in this series of reports.

6.4 COMPARISON OF R(MgIIc/w) TO 10.7 cm RADIO FLUX

W. Kent Tobiska

6.4.1 10.7 cm Radio Flux ($F_{10.7}$) Data

$F_{10.7}$, which was previously called the Covington index F, is a mixed emission produced in the chromosphere, chromosphere-corona transition region, cool corona, and hot corona. Because of the coronal input, it's temporal variation reflects different solar processes than solely chromospheric region lines such as the R(MgIIc/w). A number of mechanisms are suspected for the creation of the low-energy $F_{10.7}$ emission. Among them include gyroresonance absorption and emission in small bright emission cores as proposed by Alissandrakis *et al.* [1980] and thermal bremsstrahlung emission in large active regions as interpreted by Felli *et al.* [1981]. However, the ratio of production by one mechanism to another is still uncertain.

Solar 10.7 cm radio flux has been recorded daily since February 14, 1947 [Covington, 1948], and is reported on a regular basis adjusted to 1 AU. It is observed at radio wavelengths (2800 MHz) at the Earth's surface and collected by a receiver at the Ottawa, Canada observatory. The World Data Center A (WDC) in Boulder now makes available a complete record of $F_{10.7}$ daily flux variations which covers 42 years (1947-1988) between the decline of cycle 18 into the rise of cycle 22. The measured flux, in units of $\times 10^{-22}$ W m^{-2} Hz^{-1}, is shown in Figure 6.4.1 for October 28, 1981 through July 30, 1988. These 10.7 cm flux values are based on measurements at 1700 UT. A quadratic linear fit to the data is overplotted in the dataset as the dotted line.

There are several items in this dataset which deserve recognition. First, the decline from high to low solar activity for the $F_{10.7}$ is roughly a factor of 4, from 300 to 70 $\times 10^{-22}$ W m^{-2} Hz^{-1}. Valley to peak variations in short-term features can change by a factor of 2. Second, there is a slower decline from high to low solar activity than the rise from low to high solar conditions. Third, there is a relatively flat period of solar minimum where emissions from active regions occasionally rise above the "quiet" sun baseline emission level of about 70. Fourth, there are clear 27-day solar rotation modulations which are especially evident during higher solar activity but also exist during solar minimum. There are also periodicities on longer time scales, both from Figure 6.4.1 and the normalized power spectrum in Figure 6.4.2. The $F_{10.7}$ dataset used for the power spectrum presentation in Figure 6.4.2 was first detrended by subtracting the quadratic fit in Figure 6.4.1.

6.4.2 Comparison of R(MgIIc/w) and $F_{10.7}$

The NIMBUS 7 - NOAA 9 MgII core-to-wing ratio, R(MgIIc/w), and $F_{10.7}$ datasets overlap between November 7, 1978 through July 30, 1988. However, for comparison to the Lyman-α data in section 6.5, the overlapping data were chosen between October 28, 1981 through July 30, 1988. All the datasets have been divided into three smaller sets. These correspond to the decline of solar cycle 21 (October 28, 1981 through September 18, 1984), cycle 21 minimum (September 19, 1984 through December 11, 1987), and the rise of cycle 22 (December 12, 1987 through July 30, 1988). Although sunspot minimum was in September

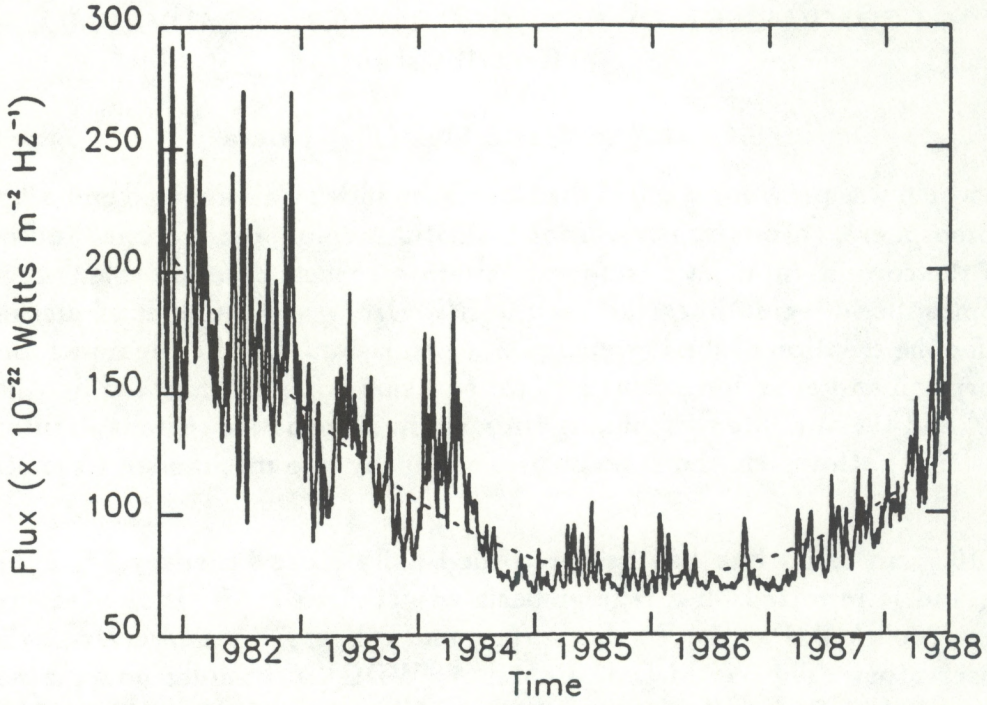

Fig. 6.4.1. 10.7 cm radio flux from October 28, 1981 through July 30, 1988.

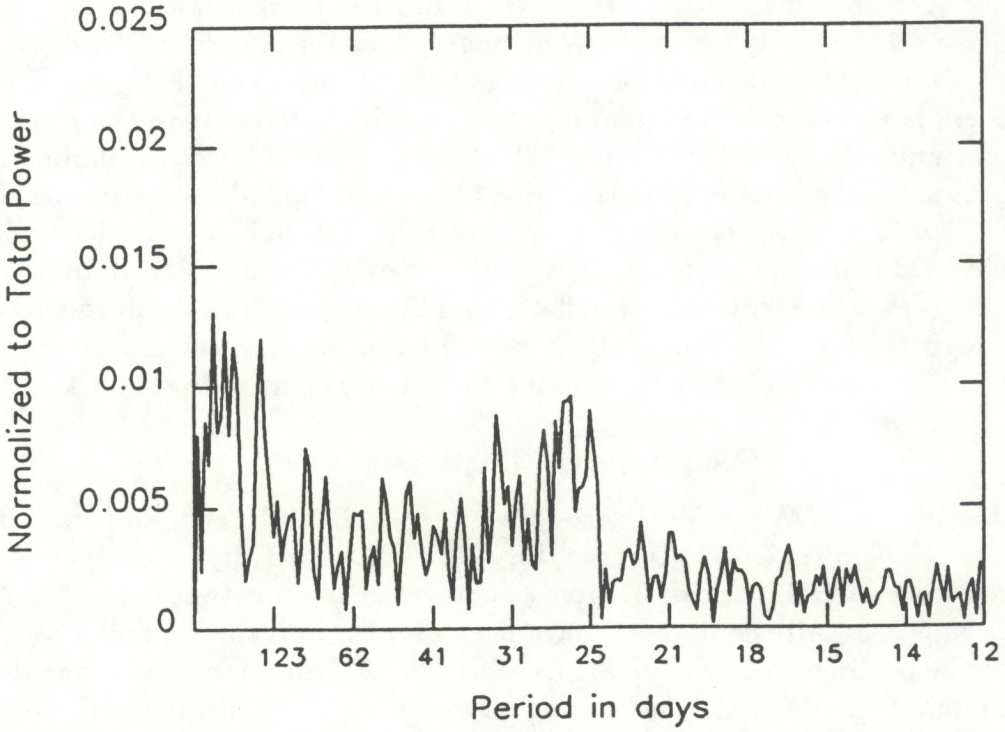

Fig. 6.4.2. 10.7 cm radio flux power spectrum normalized to the total power.

1986, and some observers may consider that date as the beginning of cycle 22, a longer cycle 21 minimum period is extracted from these data which corresponds to observed features described below. There are no missing data in the $F_{10.7}$ while R(MgIIc/w) missing data have been filled using a cubic spline and modified as described below.

The two datasets are compared quantitatively and qualitatively. Figure 6.4.3 and Table 6.4.1 both quantitatively describe the three periods of cycle decline, minimum, and rise. The large segment of data in the cycle decline phase has a linear correlation coefficient of 0.91 between day 301, 1981 and day 262, 1984. The slope of the cycle decline data is slightly steeper than for the solar minimum period of day 263, 1984 through day 345, 1987 where the correlation coefficient is 0.66. The weaker correlation during minimum arises from the fact that $F_{10.7}$ almost never varies below 70 of its units and defines a flat baseline. However, R(MgIIc/w) continues a slow decline in solar minimum. The rise of cycle 22, from day 346, 1987 through the end of the data on day 212, 1988, has a similar slope to the decline of cycle 21. For the rising data, the correlation coefficient is 0.90. The differences between the data are enhanced during solar minimum conditions where the R(MgIIc/w) contains a greater number of 27-day and longer period solar features compared to $F_{10.7}$.

TABLE 6.4.1 $F_{10.7}$ and R(MgIIc/w) Comparison

Solar Activity Period	Dates	Intercept[a]	Slope[b]	Correlation Coefficient
1 Decline	28 Oct 81 - 18 Sep 84	.977	5.52×10^{-4}	.91
2 Minimum	19 Sep 84 - 11 Dec 87	.976	3.66×10^{-4}	.66
3 Rise	12 Dec 87 - 30 Jul 88	.975	4.33×10^{-4}	.90

[a] Intercept in R(MgIIc/w) = $a + bF_{10.7}$.
[b] Slope in R(MgIIc/w) = $a + bF_{10.7}$.

A qualitative comparison is made between the R(MgIIc/w) and $F_{10.7}$ datasets in Figure 6.4.4. In this figure, $F_{10.7}$ is plotted on the same scale as the MgII c/w ratio data. The solid line is the R(MgIIc/w) time series and the dotted line is the $F_{10.7}$ time series. The overall correlation between the datasets for the entire period of time from October 28, 1981 through July 30, 1988 is 0.91 and is strongly influenced by the long-term trends. The three solar activity periods are marked and the good correspondence between the data for the decline of cycle 21, the separation of R(MgIIc/w) from $F_{10.7}$ during solar minimum, and the similar increase of both R(MgIIc/w) and $F_{10.7}$ during the rise of cycle 22 are apparent. Figures 6.4.5 and 6.4.6 show a more detailed view of the solar minimum and rise of cycle 22 data in the time periods described above.

An interesting feature in Figure 6.4.3 is the hysteresis effect during solar minimum and the rise of cycle 22. Line 2 (solar minimum relationship) and the low end of line 3 (beginning of cycle 22 rise) are both considerably offset from the relationship depicted in line 1 (cycle 21 decline). Two potential reasons exist for this discrepancy between $F_{10.7}$ and R(MgIIc/w). Either 1) there is a decrease in R(MgIIc/w) relative to $F_{10.7}$ from measurement degradation on both the NIMBUS 7 and NOAA 9 satellites or 2) there is a

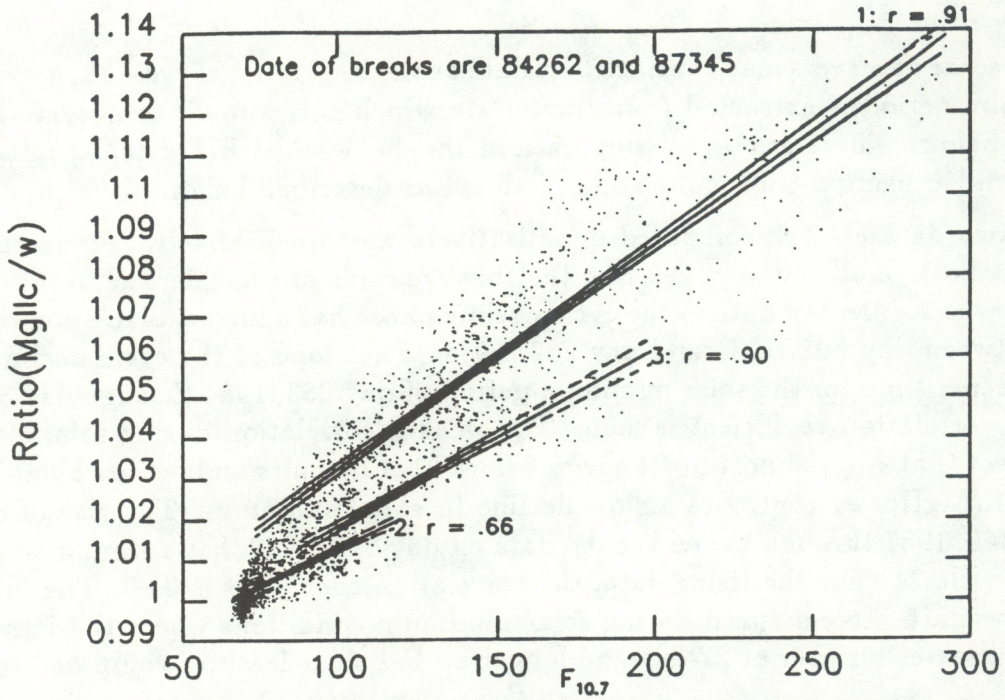

Fig. 6.4.3. $F_{10.7}$ and R(MgIIc/w) compared for October 28, 1981 through July 30, 1988. 1 = solar cycle 21 decline; 2 = cycle 21 minimum; 3 = cycle 22 rise. $\pm 3\sigma$ scatter in the linear regression between the two datasets is shown by the dotted lines on either side of a solid line during each of the three periods. r is the coefficient of linear correlation.

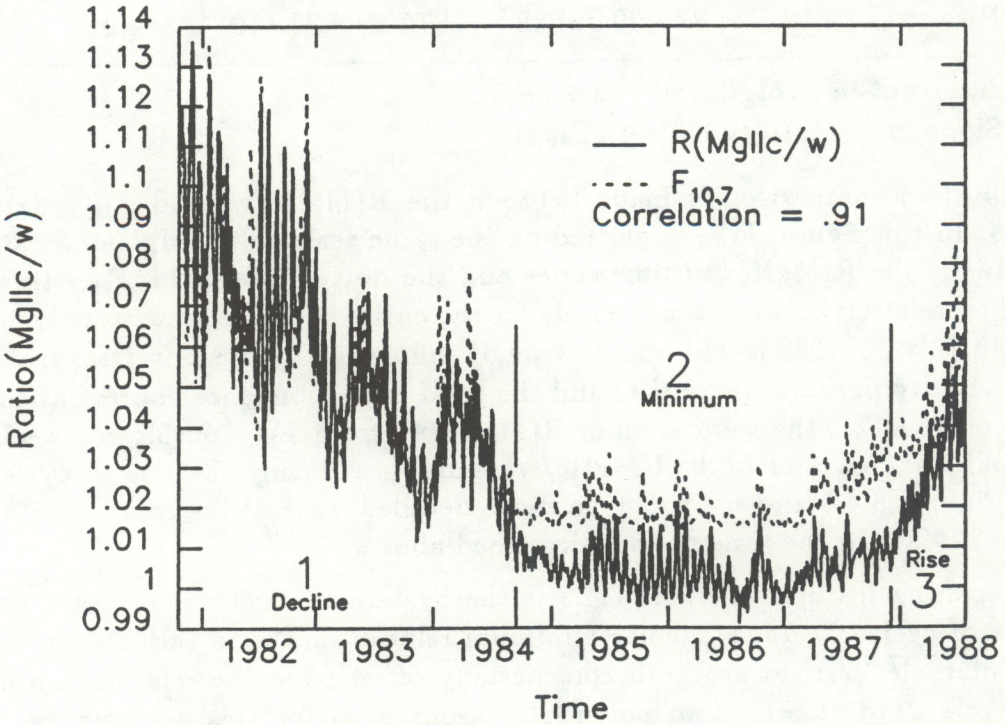

Fig. 6.4.4. $F_{10.7}$ and R(MgIIc/w) compared for October 28, 1981 through July 30, 1988 with the phases of the solar cycle marked in the time series. The correlation is for the entire dataset.

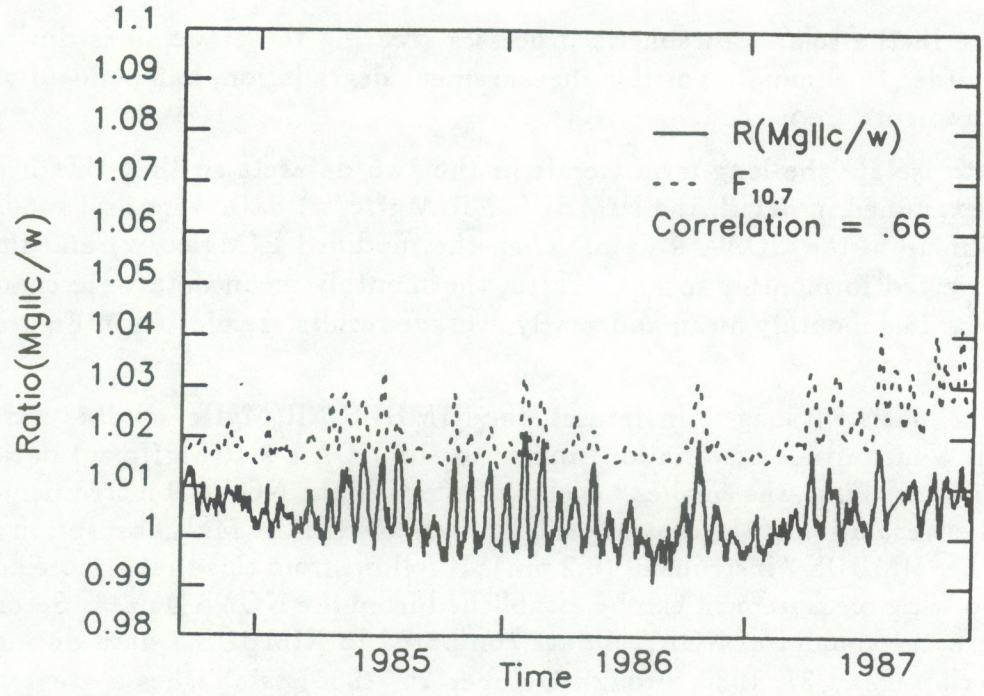

Fig. 6.4.5. $F_{10.7}$ and R(MgIIc/w) compared for September 19, 1984 through December 11, 1987 during solar minimum conditions. The correlation is for the solar minimum phase.

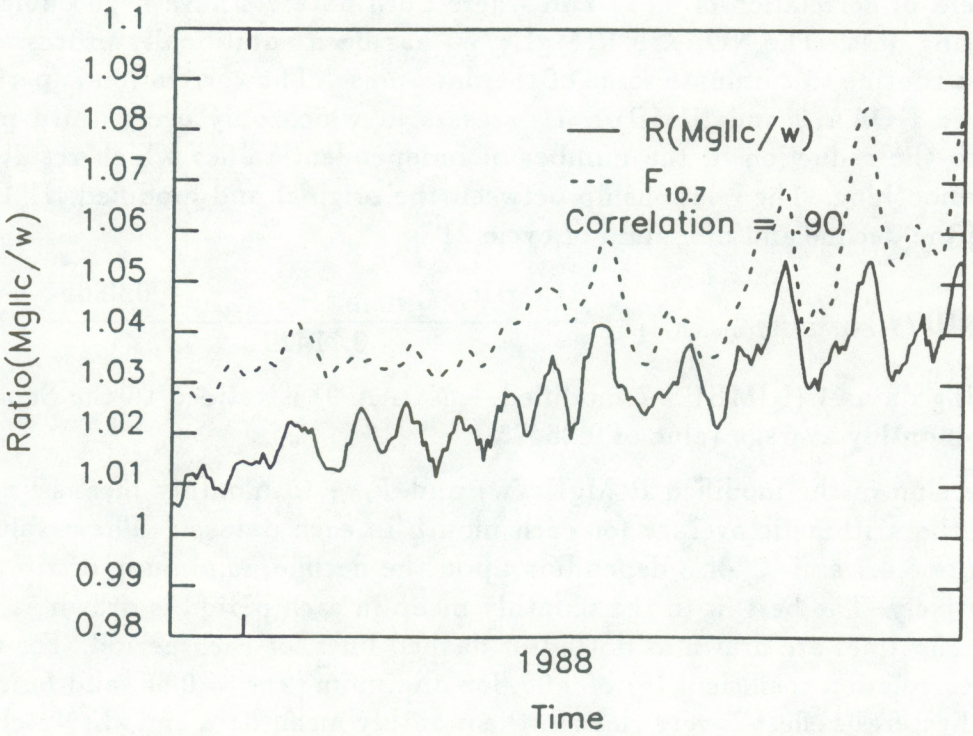

Fig. 6.4.6. $F_{10.7}$ and R(MgIIc/w) compared for December 12, 1987 through July 30, 1988 during solar cycle rise conditions. The correlation is for the rising phase.

distinct change in the solar atmospheric processes creating these two lines during solar minimum. In order to eliminate possible measurement degradation, independent chromospheric measurements are needed.

In order to isolate the long-term trends in the two datasets so that this hysteresis effect can be examined in detail, the NIMBUS 7 R(MgIIc/w) data were first modified to make them similar to the NOAA 9 data. Then the modified R(MgIIc/w) and the $F_{10.7}$ data were converted to monthly means. Third, the monthly mean data were changed to yearly averages. The monthly mean and yearly average results are plotted in Figures 6.4.7 and 6.4.8, respectively.

To create a consistent long-term dataset, the NIMBUS 7 R(MgIIc/w) data were modified to exhibit a magnitude of variation similar to the NOAA 9 R(MgIIc/w) data based on two assumptions. First, the smaller wavelength steps of the NOAA 9 instrument (0.148 nm) gives a finer resolution of the central peak further down in the MgII absorption feature compared to the NIMBUS 7 instrument (0.2 nm). It follows from this that a more accurate ratio of core-to-wing measurement can be established from the NOAA 9 data. Second, the significantly greater amount of NOAA 9 data compared to NIMBUS 7 data during the 5 months of overlap (May 27, 1986 through October 26, 1986) establishes a greater confidence in using NOAA 9 R(MgIIc/w) as the independent data in a linear correlation with the NIMBUS 7 R(MgIIc/w). The relationship between the NOAA 9 and NIMBUS 7 data during the period of overlap is

$$\mathrm{R(MgIIc/w)_{NIMBUS7}} = 0.28654 + 0.71429\mathrm{R(MgIIc/w)_{NOAA9}}$$

with a coefficient of correlation of 0.877 and where both datasets have been cubic spline filled over missing data. The NOAA 9 R(MgIIc/w) has been additionally processed with a 3-day smooth routine to eliminate some of the data noise. The correlation is performed with compressed NOAA 9 and NIMBUS 7 datasets in which only every third point is retained due to the reduction in the number of independent values which results from the NOAA 9 smoothing. The relationship between the original and modified NIMBUS 7 dataset during the decline and minimum of cycle 21 is

$$\mathrm{R(MgIIc/w)_{NIMBUS7(modified)}} = \frac{\mathrm{R(MgIIc/w)_{NIMBUS7(original)}} - 0.28654}{0.71429}$$

and the resulting dataset (NIMBUS 7 modified + NOAA 9) is ratioed to the September 1986 NOAA 9 monthly average value of 0.25475.

The conversion of the modified R(MgIIc/w) and $F_{10.7}$ to monthly means was done by calculating the arithmetic average for each month in each dataset. These values are plotted in Figure 6.4.7 as 1, 2, or 3 depending upon the decline, minimum, or rise period of time, respectively. The best fit to the monthly mean in each period is drawn as a solid line while the $\pm 3\sigma$ lines are drawn as dotted or dashed lines for each period. For decline (1), there is a correlation coefficient (r) of 0.96, for minimum (2) $r = 0.68$, and for rise (3) $r = 0.96$. The hysteresis effect is very clear in the monthly mean data and absolutely clear in the yearly averages plotted in Figure 6.4.8. The yearly average values were obtained by

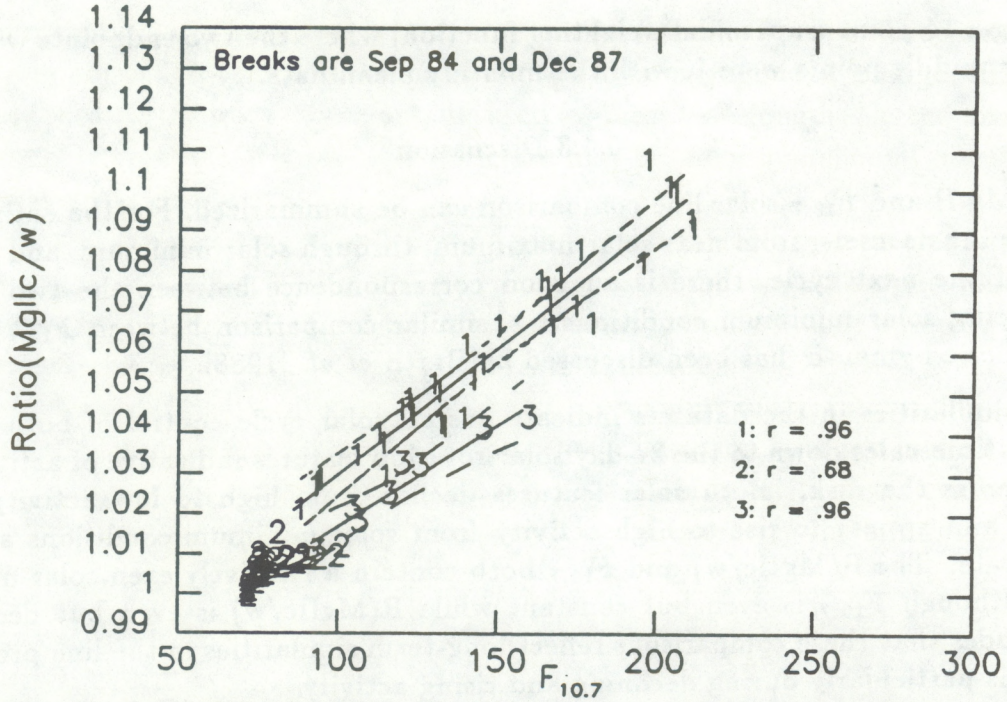

Fig. 6.4.7. $F_{10.7}$ and R(MgIIc/w) monthly averages compared for three phases of the solar cycle (1 = decline, 2 = minimum, and 3 = rise). r is the coefficient of linear correlation.

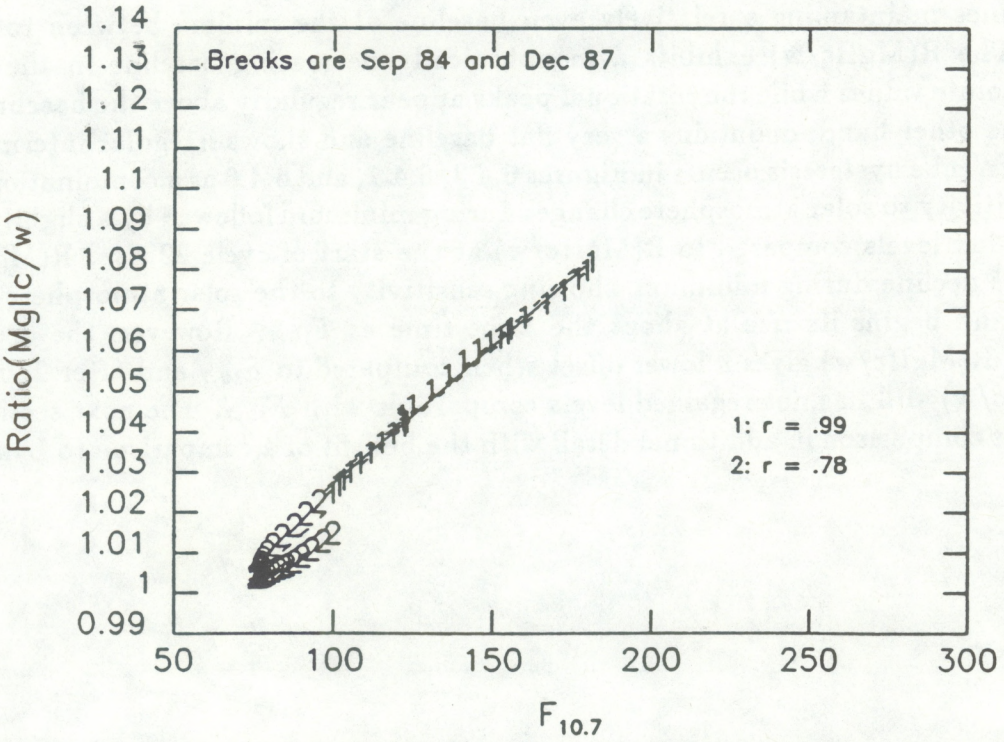

Fig. 6.4.8. $F_{10.7}$ and R(MgIIc/w) yearly averages compared for two phases of the solar cycle (1 = decline and 2 = minimum). r is the coefficient of linear correlation.

convolving a 14-point trapezoidal weighting function, where the two endpoints were $\frac{1}{2}$ and the twelve middle points were 1, with the monthly mean data.

6.4.3 Discussion

The Mg II and $F_{10.7}$ solar line comparison can be summarized. For the entire period of overlapping datasets, from near solar maximum, through solar minimum, and well into the rise of the next cycle, there is an good correspondence between the two datasets except during solar minimum conditions. A similar comparison between $F_{10.7}$ and the chromospheric Lyman-α has been discussed by Barth *et al.* [1988].

The similarities in the datasets indicate overall solar cycle control of both lines on solar cycle timescales down to the 27-day solar rotation features indicative of active region passage across the disk. Both solar features decline from high to low activity at the same rate and appear to rise to high activity from solar minimum conditions at nearly the same rate. The R(MgIIc/w) and $F_{10.7}$ both contain a relatively even solar minimum baseline although $F_{10.7}$ is even but constant while R(MgIIc/w) is even but decreasing. One concludes that these comparisons reflect long-term similarities in the line production mechanisms particularly during declining and rising activity.

The differences between the datasets may illustrate some important solar phenomena. The most prominent distinctions are during solar minimum and are shown in Figures 6.4.4, 6.4.5, 6.4.7, and 6.4.8. In this period, the R(MgIIc/w) and $F_{10.7}$ are clearly dissimilar, especially in the monthly mean and yearly average plots, although there still exists a weak correlation. This is based upon both lines showing the larger solar rotational features and both lines maintaining a relatively even baseline at the minima between rotational features. The R(MgIIc/w) exhibits a monotonically decreasing baseline in the 27-day minima absolute values while the rotational peaks appear regularly above the baseline. The $F_{10.7}$, on the other hand, maintains a very flat baseline and shows irregular intermediate-term periods. The hysteresis occurs in Figures 6.4.3, 6.4.7, and 6.4.8 as a combination of the $F_{10.7}$ insensitivity to solar atmosphere changes during minimum followed by a slightly faster increase in flux levels compared to R(MgIIc/w) at the start of cycle 22 rise. R(MgIIc/w) continues its decline during minimum, showing sensitivity to the solar atmosphere energy variations, and begins its rise at about the same time as $F_{10.7}$. However, the decreased flux level in R(MgIIc/w) gives a lower offset when compared to $F_{10.7}$ and after 22 months the R(MgIIc/w) still has not regained levels comparable with $F_{10.7}$. The next section will discuss these comparison in additional detail with the benefit of a comparison to Lyman-α.

6.5 COMPARISON OF R(MgIIc/w) TO SME LYMAN ALPHA

W. Kent Tobiska

6.5.1 Solar Mesosphere Explorer (SME) data

SME is a NASA Explorer series satellite operated by the Laboratory for Atmospheric and Space Physics (LASP) at the University of Colorado (CU) in Boulder. The primary scientific mission of SME, described by Thomas *et al.* [1980] is to provide a comprehensive study of mesospheric ozone creation and depletion. This includes observations of solar UV flux variations. SME was launched from the Western Test Range into a polar, sun-synchronous, 3 pm ascending node orbit on October 6, 1981. The nearly circular orbit had an initial eccentricity of 0.0032 with an altitude near 540 km. The 97.5 degree inclination allows for orbit precession of approximately 1 degree per day. Science and engineering data are received daily at the Project Operations Control Center located at CU. This site houses the SME mission control, mission planning, and data analysis teams.

The SME satellite has acquired a substantial dataset of solar Lyman-α daily-averaged fluxes between October 8, 1981 and April 13, 1989. The Lyman-α data, available from LASP, consist of daily-averaged values of the full-disk flux adjusted to 1 AU. It is regularly observed by a wavelength scanning solar ultraviolet spectrometer with a 7.5 Å bandpass described by Rottman *et al.* [1982]. Figure 6.5.1 is a plot of the observed daily-averaged Lyman-α flux absolute intensities with an accuracy of $\pm 5\%$ from October 28, 1981 through July 30, 1988.

The time series has several distinct characteristics which are immediately recognizable. First, the absolute fluxes vary in the range of 3 $(\pm 1) \times 10^{11}$ photons cm^{-2} sec^{-1} as described by Rottman [1983]. It is apparent that there is a strong solar cycle modulation and that the overall decline from high to low solar activity reduces Lyman-α by about a factor of 2, i.e., from over 4×10^{11} to 2.3×10^{11} photons cm^{-2} sec^{-1}. This decreasing trend was also described by Rottman [1987]. It is not yet clear whether Lyman-α reached higher levels in 1981 prior to SME. A minimum in the data exists in August 1986, potentially indicating a quiet sun background value near 2.3×10^{11} photons cm^{-2} sec^{-1}. Next, there are strong periodicities in the dataset. The detrended Lyman-α shows a power spectrum with a substantial 27-day periodicity [Rottman, 1983] due to solar rotational effects. The quadratic line fit to the data in Figure 6.5.1 is used to detrend this dataset. Figure 6.5.2 depicts the periodicities in the time frame described above. The power in Figure 6.5.2 has been normalized and is plotted as a function of period in days. There are longer periods in the data on the order of several solar rotations. Additionally, there is a moderate 13-day period, as distinct from $F_{10.7}$, which supports the observations of Donnelly *et al.* [1986] who indicate that 13-day periodicities are strong, moderate, and weak in the photosphere, chromosphere, and corona, respectively.

6.5.2 Comparison of R(MgIIc/w) and Lyman-α

The NIMBUS 7 - NOAA 9 MgII core-to-wing ratio, R(MgIIc/w), and SME Lyman-α datasets overlap between October 28, 1981 through July 30, 1988. Both of the datasets

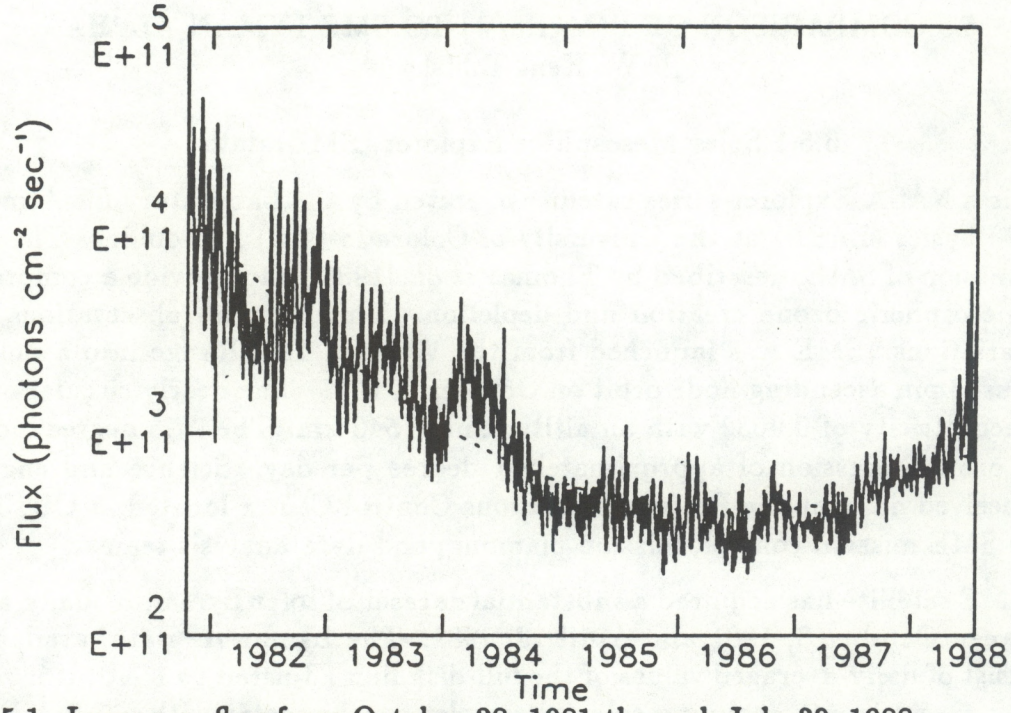

Fig. 6.5.1. Lyman-α flux from October 28, 1981 through July 30, 1988.

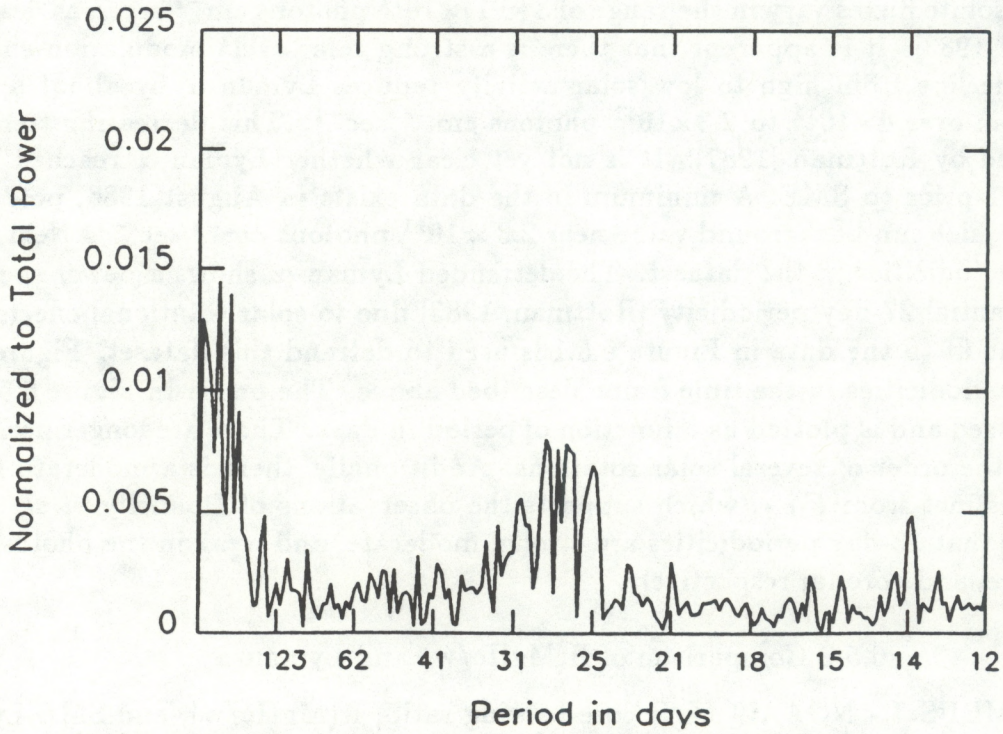

Fig. 6.5.2. Lyman-α flux power spectrum normalized to the total power.

have been divided into three smaller sets as in the $F_{10.7}$ and R(MgIIc/w) comparison. These correspond to the decline of solar cycle 21 (October 28, 1981 through September 18, 1984), cycle 21 minimum (September 19, 1984 through December 11, 1987), and the rise of cycle 22 (December 12, 1987 through July 30, 1988). There are no missing Lyman-α data and the long-term R(MgIIc/w) is modified as described in section 6.4.2.

The two datasets are compared quantitatively and qualitatively. Figure 6.5.3 and Table 6.5.1 both quantitatively describe the three periods of cycle decline, minimum, and rise. The large segment of data in the cycle decline phase has a linear correlation coefficient of 0.95 between day 301, 1981 and day 262, 1984. The slope of the cycle decline data is more pronounced than the solar minimum period of day 263, 1984 through day 345, 1987 where the correlation coefficient is 0.66. There is a slightly steeper slope during the rise of cycle 22 from day 346, 1987 through the end of the data on day 212, 1988. For the latter data, the correlation coefficient is 0.84. The main distinction between the datasets is that during solar minimum conditions the R(MgIIc/w) declines somewhat slower than the Lyman-α. Both solar features decline from high to low activity and rise from low to high activity at nearly the same rate.

TABLE 6.5.1 Lyman-α and R(MgIIc/w) Comparison

Solar Activity Period	Dates	Intercept[a]	Slope[b]	Correlation Coefficient
1 Decline	28 Oct 81 - 18 Sep 84	.820	6.91×10^{-13}	.95
2 Minimum	19 Sep 84 - 11 Dec 87	.924	3.09×10^{-13}	.66
3 Rise	12 Dec 87 - 30 Jul 88	.859	5.78×10^{-13}	.84

[a] Intercept in R(MgIIc/w) $= a + b\mathrm{Ly}_\alpha$.
[b] Slope in R(MgIIc/w) $= a + b\mathrm{Ly}_\alpha$.

A qualitative comparison is made between the R(MgIIc/w) and Lyman-α datasets in Figure 6.5.4. In this figure, Lyman-α is plotted on the same scale as the MgII c/w ratio data. The solid line is the R(MgIIc/w) time series and the dotted line is the Lyman-α time series. The overall correlation for the entire period of time between October 28, 1981 and July 30, 1988 between the datasets is 0.95 which is strongly influenced by the long-term trends. The three activity periods are marked. Figures 6.5.5 and 6.5.6 show the same data in detailed views for the solar minimum and cycle 22 rise periods.

The datasets are also shown as monthly mean and yearly average comparisons in Figures 6.5.7 and 6.5.8, respectively. The conversion of these data are described in section 6.4.2. In each plot, the $\pm3\sigma$ lines are drawn as short or long dashes relative to the solid best fit line for each period of solar activity. The 1, 2, and 3 indicate the averaged values for decline, minimum, and rise in the R(MgIIc/w) and Lyman-α. The breaks in the data are the same dates discussed above, September 1984 and December 1987, which correspond to slope changes observed in the R(MgIIc/w) dataset.

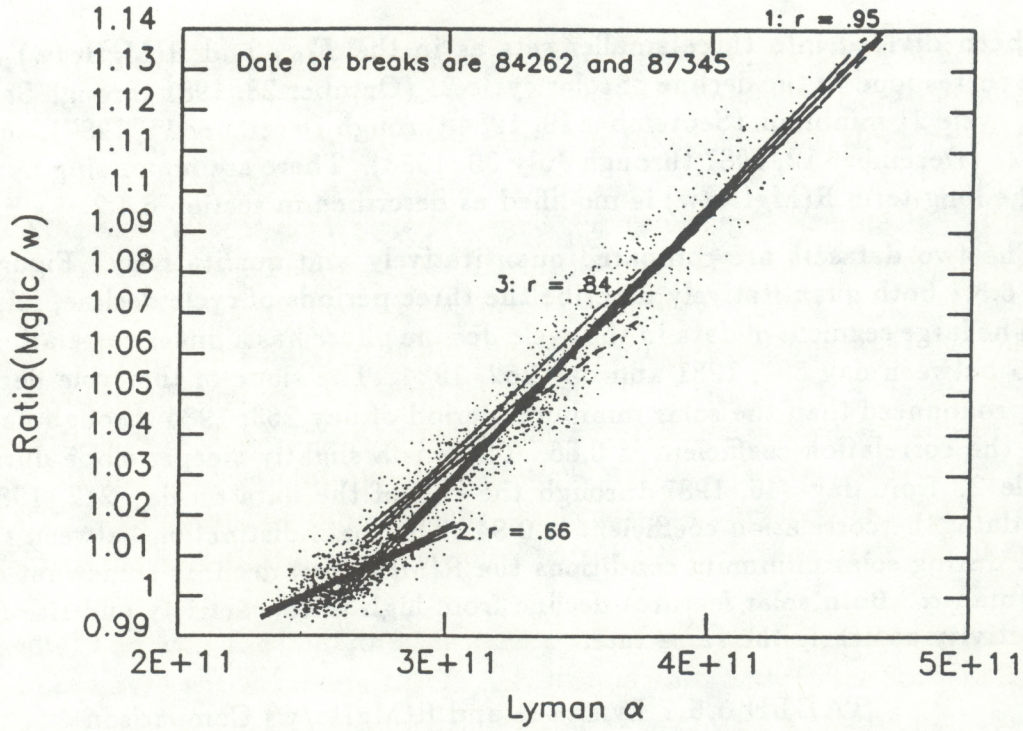

Fig. 6.5.3. Lyman-α and R(MgIIc/w) compared for October 28, 1981 through July 30, 1988. 1 = solar cycle 21 decline; 2 = cycle 21 minimum; 3 = cycle 22 rise. $\pm 3\sigma$ scatter in the linear regression between the two datasets is shown by the dotted lines on either side of a solid line during each of the three periods. r is the coefficient of linear correlation.

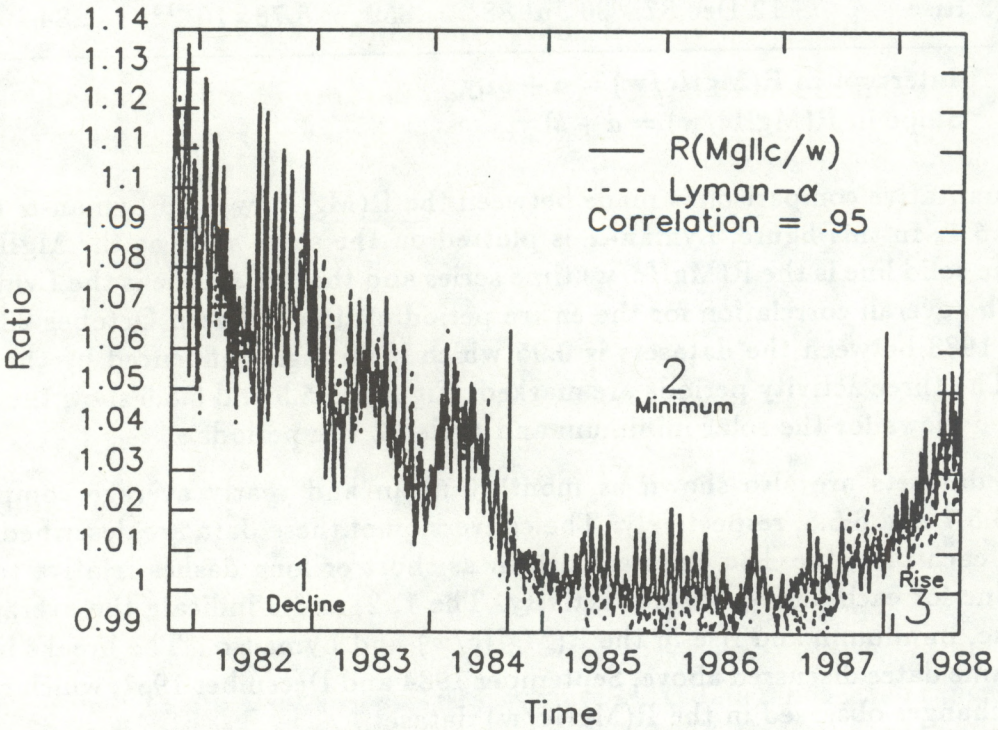

Fig. 6.5.4. Lyman-α and R(MgIIc/w) compared for October 28, 1981 through July 30, 1988 with the phases of the solar cycle marked in the time series. The correlation is for the entire dataset.

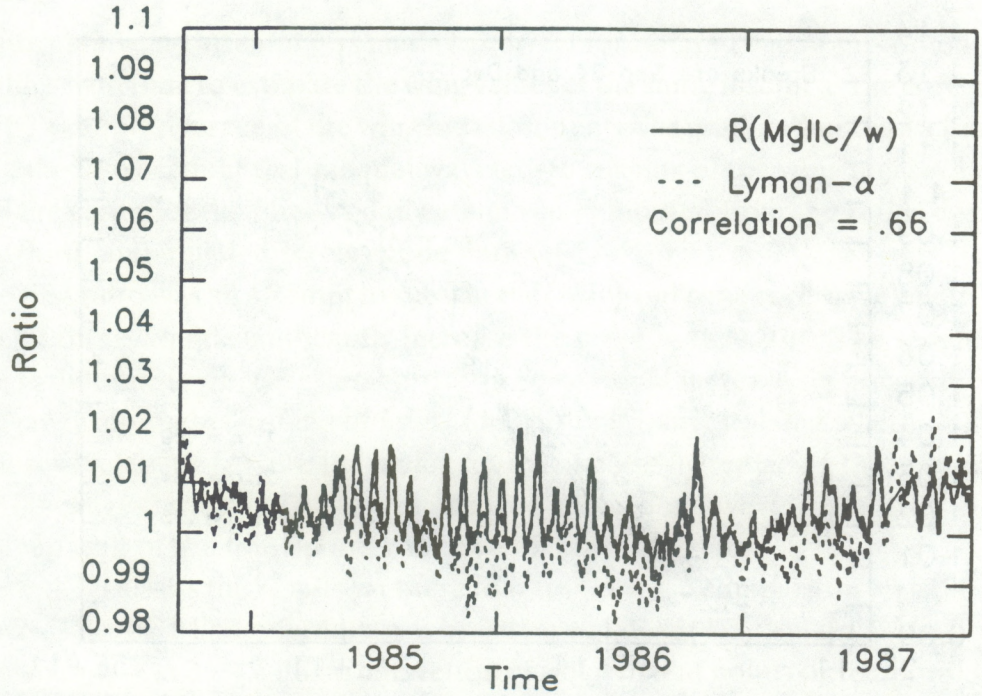

Fig. 6.5.5. Lyman-α and R(MgIIc/w) compared for September 19, 1984 through December 11, 1987 during solar minimum conditions. The correlation is for the solar minimum phase.

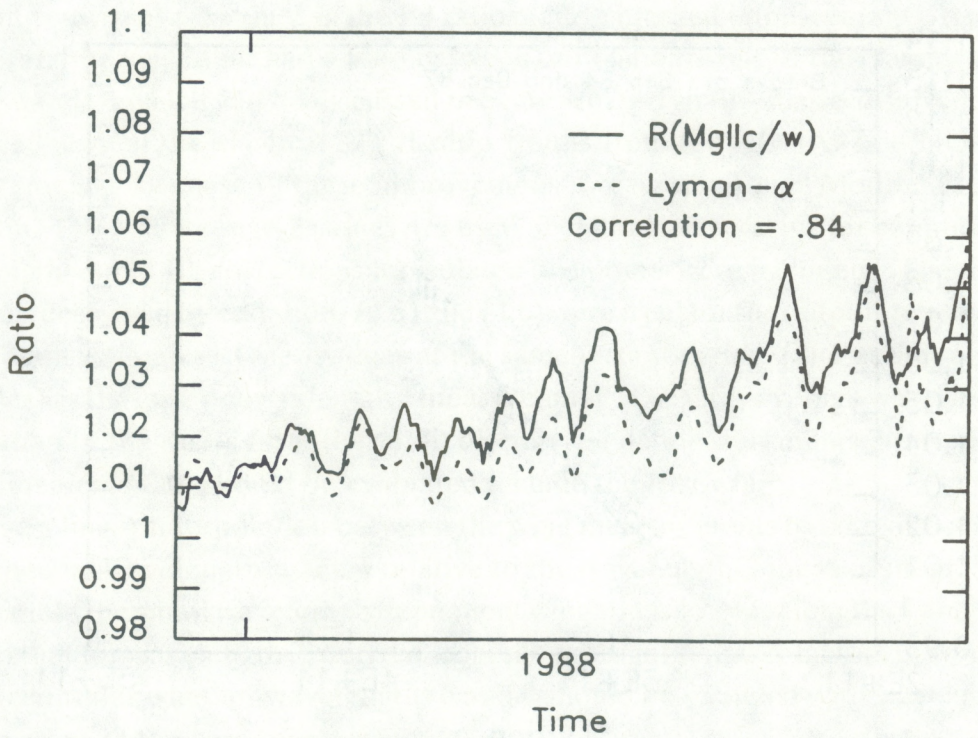

Fig. 6.5.6. Lyman-α and R(MgIIc/w) compared for December 12, 1987 through July 30, 1988 during solar cycle rise conditions. The correlation is for the rising phase.

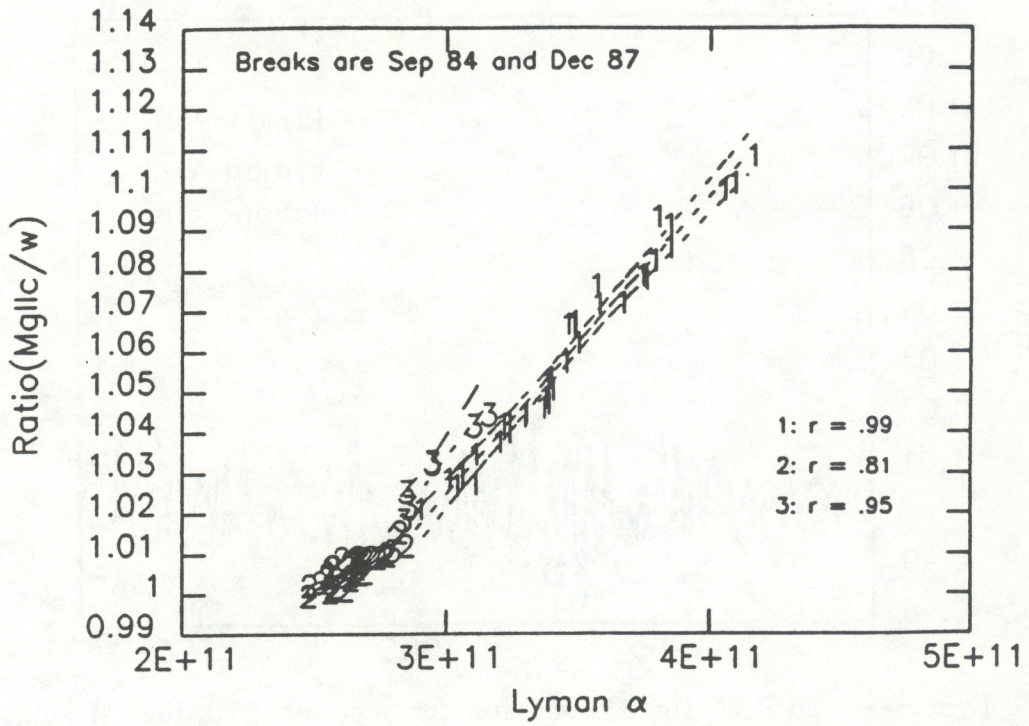

Fig. 6.5.7. Lyman-α and R(MgIIc/w) monthly averages compared for three phases of the solar cycle (1 = decline, 2 = minimum, and 3 = rise). r is the coefficient of linear correlation.

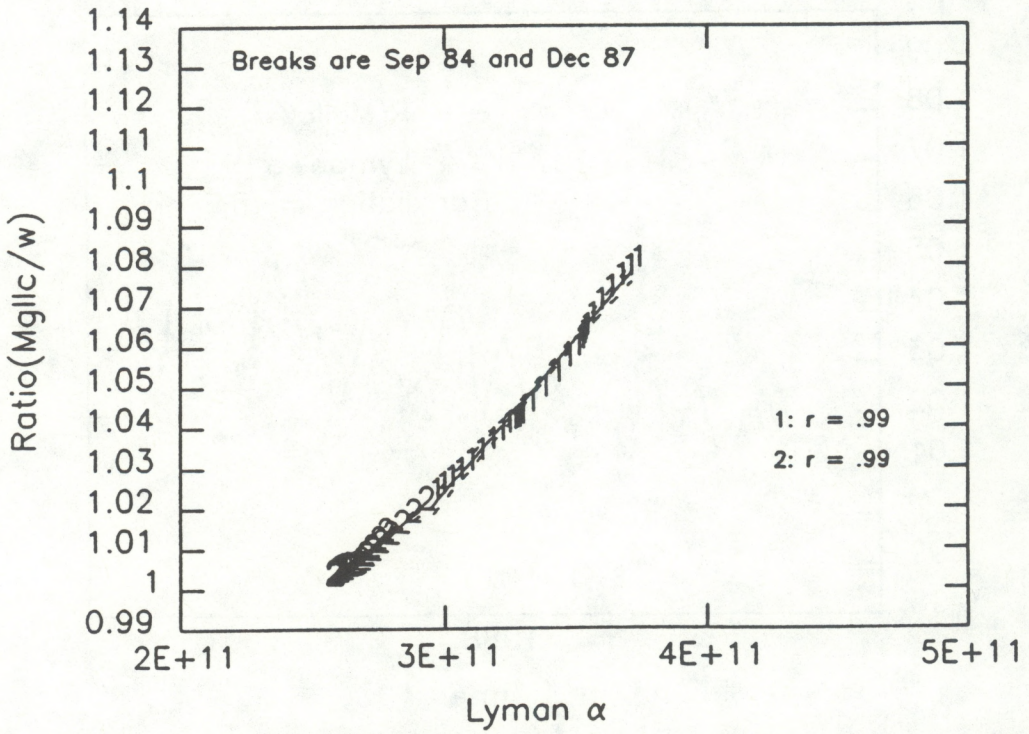

Fig. 6.5.8. Lyman-α and R(MgIIc/w) yearly averages compared for two phases of the solar cycle (1 = decline and 2 = minimum). r is the coefficient of linear correlation.

6.5.3 Discussion

The Mg II and II Lyman-α solar line comparison can be summarized. For the entire period of overlapping datasets, from near solar maximum, through solar minimum, and well into the rise of the next cycle, there is an excellent correspondence between the two datasets during all levels of activity. In fact, Lyman-α compares much better with R(MgIIc/w) for this period than does $F_{10.7}$ with R(MgIIc/w) or $F_{10.7}$ with Lyman-α. The latter comparison has been discussed by Barth *et al.* [1988]. In general, this excellent correlation (0.95) between R(MgIIc/w) and Lyman-α occurs because of similar origins within the solar atmosphere for these two lines. The SME Lyman-α is the integrated measurement of the peak and wings of the line and therefore the measurements sample the middle and upper chromosphere. The R(MgIIc/w) measurements sample the lower chromosphere. The similarity is most pronounced for the decline and rise of solar activity where the slopes and intercepts are nearly identical. The slight offset is due to the lower Lyman-α values obtained during minimum. It is notable that the hysteresis effect seen in the R(MgIIc/w) and $F_{10.7}$ comparison does not exist here. Either both of the Lyman-α and R(MgIIc/w) measurements degrade at nearly the same rate or the decline and rise solar periods have comparable temporal processes producing these lines. It is unlikely that the former occurs. Thus, this high correlation on solar cycle timescales tends to indicate that both lines are experiencing similar time-varying production mechanisms. The high correlation also gives high weight to the claims of good relative magnitude variation accuracy in the SME, NIMBUS 7, and NOAA 9 measurements. In particular, the slope changes in the R(MgIIc/w) in September 1984 and December 1987 are probably real, given the excellent decline and rise correlations with Lyman-α before and after those dates, respectively.

The differences between the datasets illustrate important solar features. The most prominent distinctions are during solar minimum as shown in Figure 6.5.5. In this period, there is a weak correlation based upon both lines maintaining a decline as well as both lines showing solar rotational features. The weak correlation strengthens in the yearly average plot of Figure 6.5.8 and therefore indicates that the short-term and intermediate-term variations are the most dissimilar during solar minimum. As mentioned in section 6.4.3, the R(MgIIc/w) exhibits a monotonically decreasing baseline in the rotational minima absolute values while the rotational features themselves appear quite regularly above the baseline. The Lyman-α, on the other hand, not only continues a sharper decline than the R(MgIIc/w) but shows irregular minima absolute levels between the rotational features with no hint of a baseline. In this, the R(MgIIc/w) is more like $F_{10.7}$ than Lyman-α. Since the Lyman-α and R(MgIIc/w) approach the relative magnitude of each other during the rise of cycle 22, one concludes that the differences during solar minimum do not reflect instrumental changes but indicate temporal distinctions in the solar chromospheric regions.

6.5.4 Conclusions

The comparisons of R(MgIIc/w) with Lyman-α and $F_{10.7}$, as well as the Lyman-α comparison with $F_{10.7}$ by Barth *et al.* [1988] shown in Figure 6.5.9, lead to the conclusion that $F_{10.7}$ does not represent the UV lines of R(MgIIc/w) nor Lyman-α during periods

of low solar activity. The UV lines show distinct daily, 27-day, and intermediate-term variations while $F_{10.7}$ does not. During solar minimum, or low activity, $F_{10.7}$ reaches a threshold level below which the flux shows no temporal variations. This can be considered a quiet sun threshold for $F_{10.7}$.

However, both R(MgIIc/w) and Lyman-α have exceptional correlations during high declining and rising activity and relatively good correlations during low minimum activity. It is clear that solar temporal variations still occur based on the observations of the R(MgIIc/w) and Lyman-α variations and that the continual decline of solar UV activity, especially in the chromosphere, is not a result of measurement degradation but is a result of changes in real solar processes. This is supported by the same hysteresis effect in the two independent datasets of R(MgIIc/w) and Lyman-α compared to $F_{10.7}$. Figures 6.5.10, 6.5.11, and 6.5.12 show the Lyman-α and $F_{10.7}$ correlations for the full dataset, monthly means, and yearly averages, respectively.

The $F_{10.7}$ has chromospheric, transition region, and coronal components, as opposed to the R(MgIIc/w) and Lyman-α which are chromospherically-produced lines. The temporal differences of the $F_{10.7}$ flat baseline and irregular 27-day activity versus the UV continual decline and regular 27-day activity during solar minimum may be attributed to the $F_{10.7}$ flux component produced in the corona. This $F_{10.7}$ time series suggests that the dominant production mechanism must be non-chromospheric in origin during solar minimum, i.e., probably coronal. It also suggests that the corona reaches a quiet sun condition but that the chromosphere does not during solar minimum. The dominant mechanism of $F_{10.7}$ production, i.e., thermal bremsstrahlung, gyroresonance, or another method, is not clearly determined by this analysis. However, the widespread use of $F_{10.7}$ as a general UV index must certainly be questioned as a result of these data comparisons, especially for periods of low solar activity.

6.5.5 Acknowledgements

The efforts of Dr. Gary Rottman and Barry Knapp of LASP in updating and calibrating the SME Lyman-α dataset are much appreciated. Dr. Oran White has also assisted in this and his efforts are acknowledged in helping produce this extremely valuable dataset. The R(MgIIc/w) dataset was developed from Dr. Don Heath's NIMBUS 7 SBUV measurements and the NOAA 9 SBUV dataset. The work in this study is supported by a CIRES cooperative agreement with NOAA.

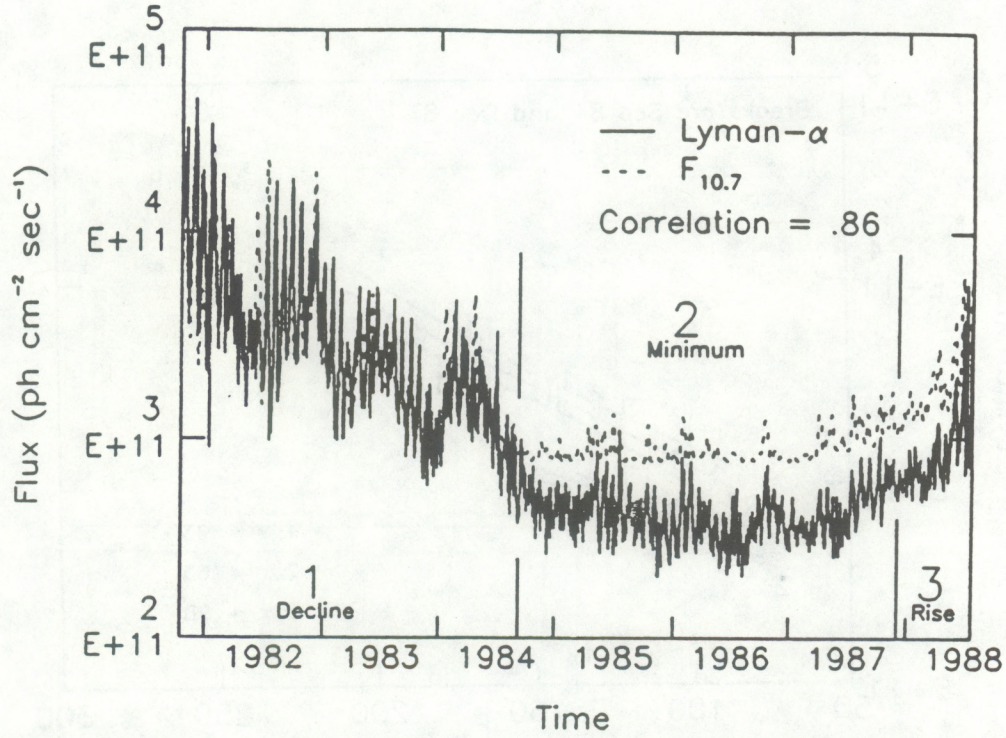

Fig. 6.5.9. Lyman-α and $F_{10.7}$ compared for October 28, 1981 through July 30, 1988 with the phases of the solar cycle marked in the time series. The correlation is for the entire dataset.

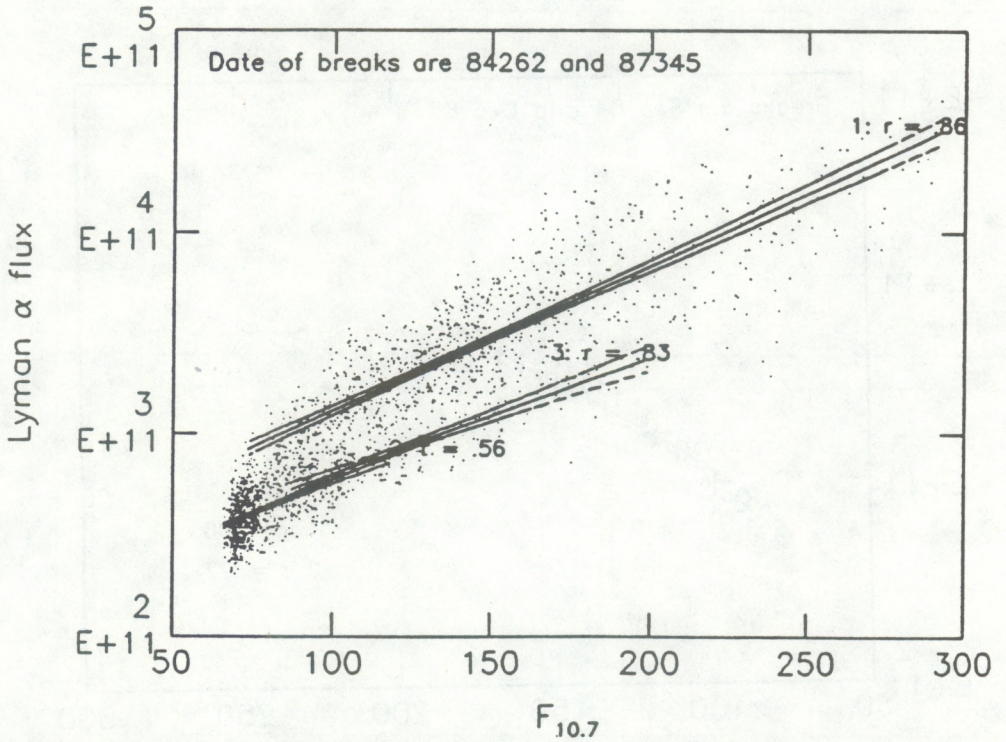

Fig. 6.5.10. Lyman-α and $F_{10.7}$ compared for October 28, 1981 through July 30, 1988. 1 = solar cycle 21 decline; 2 = cycle 21 minimum; 3 = cycle 22 rise. $\pm 3\sigma$ scatter in the linear regression between the two datasets is shown by the dotted lines on either side of a solid line during each of the three periods. r is the coefficient of linear correlation.

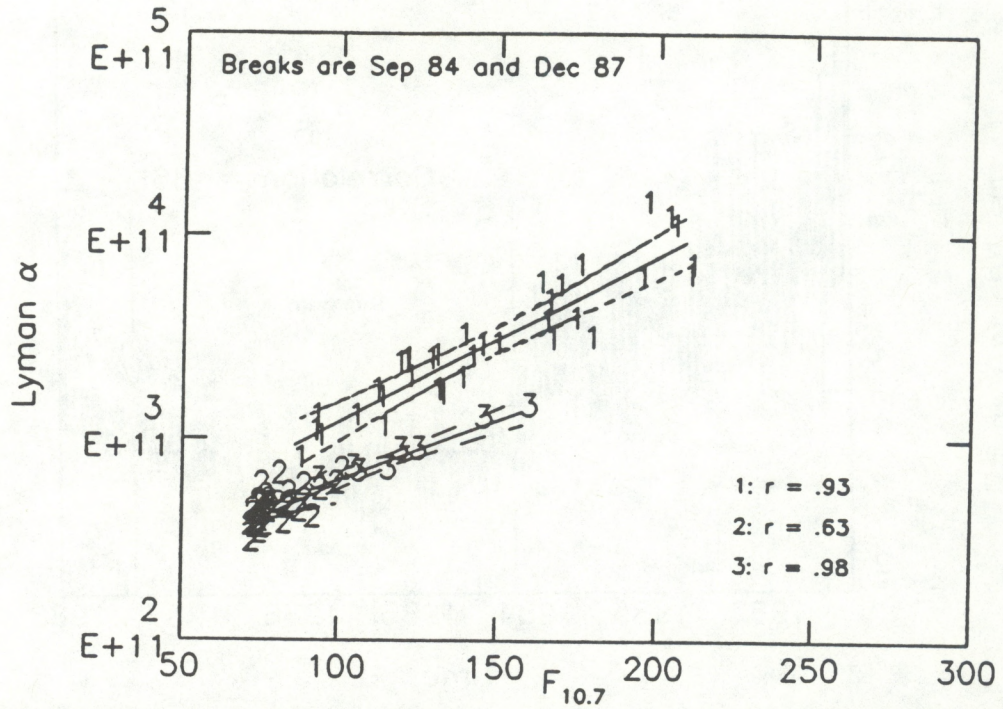

Fig. 6.5.11. Lyman-α and $F_{10.7}$ monthly averages compared for three phases of the solar cycle (1 = decline, 2 = minimum, and 3 = rise). r is the coefficient of linear correlation.

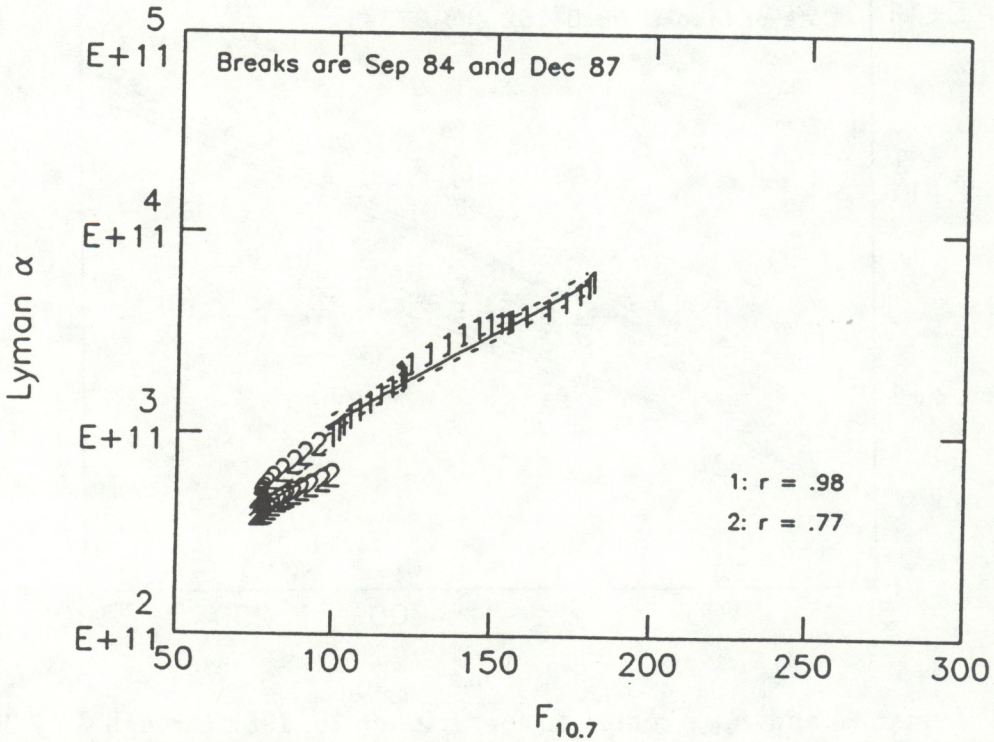

Fig. 6.5.12. Lyman-α and $F_{10.7}$ yearly averages compared for two phases of the solar cycle (1 = decline and 2 = minimum). r is the coefficient of linear correlation.

7. DISCUSSION

This report has discussed our exploratory studies, during 1987-1989, of the NOAA9 discrete-mode measurements of the solar Mg II h & k lines near 280 nm. We had previously tried to derive the Mg II core-to-wing ratio (R_{MgII}) from the wavelength-scan mode of observations; however, we abandoned that effort because the results were too noisy, relative to those that could be achieved using either the Canadian solar 10.7 cm radio flux (F10) or the National Solar Observatory's equivalent-width (EW) measurements for the solar He I absorption line at 1083 nm, despite known real differences between the temporal variations of these latter measures of solar activity and R_{MgII}. Much of the 1987-1989 work involved discovering problems in the classical Mg II ratio derived from the discrete-mode data; we did not develop the modified ratio and verify its value until 1989 because we did not expect that using measurements from the steep walls of the unresolved absorption lines would work so well as a range-2 replacement for the range-3 far wing measurements. The next step is to refine this ratio by including some of the corrections for instrumental effects that were not incorporated in these early exploratory studies. Some of the candidate refinements are discussed below.

7.1. Corrections for Nonlinearity

Table 7.1 is a subset of data from Table 2-1b of Ball Reference 3, which reports Ball Aerospace's linearity calibrations. Figure 3.4.9 shows that the range-2 output for the wavelength nearest the center of the h & k unresolved absorption lines had values from about 14,000 to 34,000 during 1986-1987. Similarly, the wall wavelengths nos. 4 and 10 had range-2 values from about 31,500 to 85,500 (See Figures 3.4.6 and 3.4.18). This means that, at least for 1986-1987 data, the modified Mg II ratio involved data within the range between rows 2 and 5 of Table 7.1. Using the five rows of observed and expected data pairs and applying linear regression analysis, we obtain the following:

$$\text{Predicted Linear Value} = 142 + 0.9812\ \text{Background} - \text{Corrected Observed Signal}, \quad (7.1)$$

where the correlation coefficient is r= 0.99999881. Using equation (7.1) gives the predicted values in the column for equation (7.1) in Table 7.1. The remaining percentage of nonlinearity in the adjacent column is given by equation (7.2).

$$\text{Percent Nonlinearity} = \frac{\text{Predicted Linear Signal} - \text{Linear Signal}}{\text{Linear Signal}} \times 100\%. \quad (7.2)$$

The percentage of nonlinearity is displayed in Table 7.1. The high correlation coefficient and the small residual nonlinearities show that the portion of range 2 used by the modified Mg II core-to-wing ratio is very linear, much more so than is suggested by the overall system results discussed in section 1.3.2. The slope between the observed outputs and the instrument input will be slightly different for this local range, used by the modified Mg II index, than is that given by the calibration constant K_F^c. This is not a problem since the K_F^c factor cancels out in the core-to-wing ratio, except for the weak wavelength-dependent component discussed in the

Table 7.1 Linearity Calibrations for Part of Range 2

Background Corrected Observed Output	Expected Output Based on Input	Percent Non-Linearity	Five-Point Fit Predicted Linear Output	Five-Point Fit Percent Non-Linearity	Four-Point Fit Predicted Linear Output	Four-Point Fit Percent Non-Linearity
5,147	5,133	0.29	5,192	1.16		
10,384	10,323	0.59	10,331	0.08	10,364	0.40
20,826	20,629	0.96	20,577	-0.25	20,604	-0.12
42,542	41,934	1.45	41,886	-0.11	41,899	-0.08
84,646	83,168	1.78	83,200	0.04	83,187	0.02

next section. The intercept in equation 7.1 is very small for the range-2 outputs encountered in the modified Mg II core-to-wing ratio, but it is not completely negligible. Using (7.1) to correct for the nonlinearity in the Mg II discrete-mode data would mean that the intercept term would have the same effect as would modifying C_{o2}.

How well determined are the slope and intercept in (7.1)? First, note that the largest nonlinearity of 1.16%, listed in Table 7.1, occurs for the lowest output level; this is more than a factor of 2 lower than the range-2 outputs encountered in 1986-1988. If we use just the four higher-intensity rows of Table 7.1 to determine the best-fit line, the results are as follows:

$$\text{Predicted Linear Value} = 182 + 0.9806\ \text{Background} - \text{Corrected Observed Signal}, \quad (7.3)$$

where the correlation coefficient, r=0.99999937, has half the unexplained (nonlinear) variance of the previous case. The two columns on the right side of Table 7.1 give the predicted linear values based on this locally fit linear-correction function in equation (7.3) and the corresponding percentage nonlinearity based on (7.2). In this case, the largest nonlinearity is only 0.4% and occurs again at the low-intensity end of the range. The slope changed little from (7.1), but the intercept changed more.

The above results indicate that the portion of range 2 used in the modified Mg II ratio derived from NOAA9 SBUV2 measurements, made in the discrete-wavelength mode, is very linear. This analysis does not take into account any error bars in either the linear signal-input terms or the instrument background-corrected output terms. Consequently, we are uncertain whether the remaining small deviations from unity are real or a consequence of calibration errors; i. e. we are uncertain as to how well determined are equations (7.1) and (7.3). How the nonlinearity evolves with the age of the instrument is also undetermined. It is not clear whether applying this small linearity correction would provide a real improvement to the Mg II ratios. Further evaluation of the effect of such a correction should be made. More importantly, since the deviations from linearity increase for decreasing range-2 values below 10,000, the outputs for the core wavelength (no. 7) should be examined for such lower values in data from more recent years.

7.2. Corrections for Wavelength Dependence

K_F in equation (1.2) is a function of wavelength, albeit a weak variation over the 3 nm wavelength range from wavelength no. 4 to no. 10. We can use the K_F^c calibration data and equation (1.8) to determine most of this wavelength dependence, but equation (1.4) shows that we should consider the diffuser reflectance as a function of wavelength and the Sun angles θ and $\emptyset$, i. e. $R(\lambda, t, \theta, \emptyset)$. So far we have avoided using θ and $\emptyset$ by using temporal interpolations of the discrete-wavelength wall measurements to determine the wall output values for the same instant in time (and same Sun angles) as the interim core measurement and then neglecting the weak wavelength dependence of $R(\lambda,t,\theta,\emptyset)/R(\lambda,t_c,\theta,\emptyset)$. We think a potential source of errors due to insufficient accuracy in deriving θ and $\emptyset$ has been avoided. So, what are these weak wavelength dependencies and how sensitive are our Mg II ratio results to them?

Equation (1.8) says that, for the long-wavelength wall measurement in the modified Mg II ratio at wavelength no. 4 (λ_4), $K_F^c(\lambda_4)$ is 0.85% smaller than for the center-of-the line $K_F^c(\lambda_7)$. Similarly, for the short-wavelength wall measurement, $K_F^c(\lambda_{10})$ is about 1% higher than $K_F^c(\lambda_7)$. The $K_F^c(\lambda_7)$ portion cancels in the modified Mg II core-to-wing ratio, and all that would remain would be a weighting factor of 0.9915 for the $(C_2(\lambda_4)-C_{o2})$ denominator term and 1.010 for the λ_{10} term. These two partially canceling weighting factors would cause both a slight shift of a few tenths of a percent in the solar minimum value of R_{MgII} and also in the slope with respect to varying solar activity. However, the consequent revised regression relations, with respect to the Ca K line data and the revised conversion to equivalent Nimbus-7 values, would remove most of this shift in the final equivalent Nimbus-7 values. Nevertheless, a demonstration of the effects of these small corrections for wavelength dependence needs to be conducted. Note that the irradiance calibration data used to derive equation (1.8) were for the discrete-wavelength mode and for range 2 outputs, the very same conditions as those encountered in all of the data used in the modified Mg II core-to-wing ratio. In the case of the classical discrete-mode ratio, the effects of the relative wavelength dependence of K_F^c are larger than for the modified ratio, -2.2% at λ_1 and +1.65% at λ_{12}.

A second source of refining corrections for wavelength dependence may be the goniometric terms. Using Ball Aerospace Division's preflight goniometric calibration published in Section 9 of Ball Reference No. 3 (i. e. the calibration of the Sun-angle dependence of $g(\lambda, \theta, \emptyset)$ in equation (1.7) at wavelengths of 250, 300, 350 and 400 nm), we derived estimates of the wavelength dependence of g. Those results show a negligible wavelength dependence at 300 nm and longer but a complicated wavelength dependence as a function of θ and $\emptyset$ at 280 nm. However, an examination of the errors involved shows that this latter result is probably all a consequence of large calibration errors ($\pm$2.2%) at 250 nm. Therefore, we have not been able to estimate the wavelength dependence of $g(\lambda, \theta, \emptyset)$ over the Mg II discrete-mode wavelength range. Perhaps unpublished calibration results nearer 280 nm exist, or measurements can be made near 280 nm for an SBUV2 monitor that hasn't flown yet. Since the variations of g with θ are quite large (about $\times$3 for θ ranging from 20° to 0), and fairly large with $\emptyset$ (about $\times$1.5 for $\emptyset$ ranging from 65° to 34°), these goniometric calibrations are probably adequate for determining the θ

and $\emptyset$ dependencies of g for wavelengths longer than 300 nm. However, they are inadequate for our attempt to determine the weak wavelength dependence of g near 280 nm.

Only in the case of the classical discrete-wavelength mode Mg II index, where the wing measurements are converted from range-3 values to equivalent range-2 values, is there a third source of refining corrections for wavelength dependence, namely that for the wavelength dependence of X_{23}. (The modified Mg II core-to-wall ratio that uses all range-2 values is independent of X_{23}.) In the case of NOAA9, the unknown temporal variations of X_{23} appear to make the classical ratio unsatisfactory. Assuming for the moment that these temporal problems could somehow be overcome, how large would the corrections for wavelength dependence be? Based on Table 2, Cebula (1988), the X_{23} at wing wavelength no. 1 (λ_1) would be about +0.3% higher than that for the line center (λ_7), while that for λ_{12} would be about 0.3% lower. These corrections are smaller than and in the opposite direction from those for K_F^c, discussed above. These X_{23} results have two problems. First, they are based on Earth view data and not Sun view data and supposedly the X_{23} varies with the type of data as well as with wavelength and time. Secondly, these results used for wavelengths near 280 nm are based on an extrapolation from data in the 305.7-339.8 nm range. Furthermore, Frederick et al. (1986) showed results for Sun view data where X_{23} was a more complicated function of both the wavelength and the intensity of the output signal (i. e. the nonlinearity is a function of wavelength); their results were too sparse in wavelength to use for accurately deriving $X_{23}(\lambda)$. So we do not yet have a good correction for this third source of wavelength dependence; fortunately, it does not apply to the modified Mg II ratio.

7.3 Revisions for Wavelength Weighting in the Wing Background

In the exploratory modified Mg II ratio given in equation (4.8), we used a simple arithmetic average ($\times$ ½) of the two wall measurements in the denominator. In effect, this ties our relative intensity scale to a part of the solar spectrum that varies little with solar activity so that we can then obtain a relative measure of a part of the solar spectrum that varies greatly with solar activity, i. e. the center-of-line measurement. Drifts in instrument sensitivity that are nearly constant with wavelength and can be described by a multiplying factor will cancel out in the ratio. Heath and Schlesinger's (1986) original Nimbus 7 Mg II ratio (equation (4.1)) used wing wavelengths equally spaced in wavelength with respect to the center-of-line to make the ratio independent of drifts that had either a weak or nearly linear dependence on wavelength. Actually, because the flux level for the short-wavelength wing measurements are clearly lower than (and not approximately equal) to the flux level for the long-wavelength wing, their ratio is not completely insensitive to instrumentation drifts that are linear functions of wavelength (Donnelly et al., 1987, p. 6). This could be compensated for by including a weighting function for just the shorter wavelength, which would bring their combined weights of the wings up to the level of the long-wavelength wing fluxes. Nevertheless, Heath and Schlesinger's (1986) Mg II ratio does include an estimate at the center-of-line wavelength of the background flux if the absorption line were not there. In the NOAA9 discrete mode measurements, λ_4 and λ_{10} are not equally spaced about the center-of-line wavelength λ_7. See Table 4.1.1

. If equation (4.8) were modified so that the denominator provided a linearly interpolated estimate of the flux at the center-of-line wavelength, then the equation would become

$$\frac{R(i)}{MgII} = \frac{C(7,i)}{\left[\frac{\lambda_4-\lambda_7}{\lambda_4-\lambda_{10}}\ C_{E7}(\lambda_{10}) + \frac{\lambda_7-\lambda_{10}}{\lambda_4-\lambda_{10}}\ C_{E7}(\lambda_4)\right]} \tag{7.4}$$

All the above C values are range 2 outputs reduced by the Co2 value of 65.4. Substituting the wavelengths from Table 4.1.1 gives

$$\frac{R(i)}{MgII} = \frac{C(7,i)}{0.429\ C_{E7}\ (10,i) + 0.571\ C_{E7}(4,i)} \tag{7.5}$$

In equation (4), the weighting factors for both denominator terms are 0.5; in 7.4 the weighting is now a little higher for wavelength 4 than for no. 10, where wavelength no. 4 unfortunately includes a weak solar signal from the h & k emission cores from the wings of the SBUV2 instrument's broad passband. The shift from equation (4.8) to (7.5) would cause a slight reduction in the solar minimum value and a slight reduction in the slope with respect to changing solar activity. Most of these shifts would be removed by the revised linear regression with respect to the Ca K index and the subsequent conversion to equivalent Nimbus 7 values. Some gain in reduced sensitivity to multiplicative instrument degradation functions that are a linear function of wavelength should be gained at a cost of reduced solar signal-to-noise ratio. It is not clear without further evaluation whether (7.5) provides a small improvement or reduces quality. For example, Figure 6 of Cebula et al. (1989) suggests that the degradation of the NOAA9 SBUV2 instrument sensitivity during 1986-1988 is a large and nearly linear function of wavelength in the 200-260 nm range but is small and fairly constant for wavelengths longer than 262 nm, including the Mg II wavelengths near 280 nm. In that case, equation (7.5) would be inferior to (4.8).

7.4 Future Analyses

The next report in this series will cover research of NOAA9 and NOAA11 SBUV2 data conducted through 1993, including intercomparisons and applications to modeling solar EUV and UV fluxes. Future work should evaluate the suggestions for refinements given above.

Another modified Mg II index that should be examined involves replacing the measurement at wavelength no. 4 with that at wavelength no. 3. Table 4.1.1 shows that wavelengths 3 and 10 are more nearly equally spaced in wavelength with respect to the center-of-line wavelength no. 7 than are wavelengths 4 and 10. The main advantage this would provide is that wavelength no.3 is free of any significant solar signal from the h and k emission cores, while no. 4 is complicated by a weak core signal. (See Figure 4.6.7.) The main disadvantage is that several of the discrete mode sets per day would have to be removed from the analysis because the range-2 values for wavelength no. 3 are in the high-count saturation region, as shown in Figure

4.4.2. Another problem may be that some days have no unsaturated range-2 values for wavelength 3.

7.5 Differences in Absolute and Relative Photometry Viewpoints

To encourage discussions early drafts of this report were sent to several scientists and engineers involved in the design, calibration, operation, and analysis of the SBUV2 monitor and associated data. Most of their corrections and suggestions have already been incorporated in this report, and comments received too late for this publication will be discussed in the next report in this series. Matthew DeLand and Richard Cebula provided extensive comments that involve a perspective that differs from ours: We take a relative photometry viewpoint; theirs is an absolute photometry viewpoint. If both groups thoroughly understood the SBUV2's actual performance and all the transfer functions and corrections needed to interpret the data, their results should agree. Because they do not, we hope that discussing these differences in viewpoint will promote future convergence.

The Mg II core-to-wing ratio is a relative measurement of solar variability in which the percentage solar variability is much stronger in the core than in the wings of the combined Mg II h and k solar absorption lines. We therefore applied a relative photometry viewpoint in our interpretation of the SBUV2 measurements. We assume that any solar UV spectrometer will drift with respect to the preflight calibrations in various unknown ways. We look for ways to derive relative measures of solar variability that will minimize the effects of instrumentation variations. In effect, we try to precisely determine the intensity of the core of the line relative to the average of the two wing intensities for each set of twelve-wavelength measurements. We think of the instrument transfer function as being a Taylor series expansion as a function of time and wavelength difference. We take the time of the core wavelength (no. 7) to be $t=0$, and the wavelength difference is with respect to wavelength 7, i. e., $\Delta=\lambda-\lambda_7$. The constant term in the Taylor series is just the instrument transfer function for the core wavelength measurement. After dividing all terms in the Taylor series by the constant term, then the constant term cancels out in the Mg II ratio. The Sun angles for the solar rays incident on the diffuser are functions of time over the 4 minutes of each day's group of measurements. We are mainly interested in the variation of the instrument transfer function over the 12 seconds in time and over the 3 nm wavelength interval as the instrument steps from wavelength 4 to wavelength 10.

The absolute flux viewpoint involves using the best available preflight and inflight calibrations, together with estimates of the Sun-diffuser angles, to convert each Sun-view measurement to a solar flux value for the associated wavelength and time. The Mg II ratio is then derived using these absolute flux values.

Because of the high correlation we find between our modified ratio and the Ca K 1Å index (See Section 6.3), we now use those comparisons as our main verification of the accuracy of our results. We use the regression relations with the Ca K 1Å index to convert NOAA9 modified Mg II ratios to equivalent Nimbus 7 values. In effect, the Ca K 1Å data set the long-term relative temporal variations while the Mg II data fill in the day-to-day variations. We see our current efforts to include additional corrections (Sections 7.1 – 7.4) as being an attempt to reduce

the 2% of the variance not yet explained by the linear regression relation between the modified Mg II ratio and the Ca K 1Å index. Changing the weighting given to the two wing wavelengths, for example, would change the absolute values of the NOAA9 modified Mg II ratio. After a new regression relation with respect to the Ca K 1Å index is computed, and after a new conversion to equivalent Nimbus 7 Mg II ratios is derived, the new equivalent Mg II ratios based on the revised NOAA9 Mg II ratios are expected to have a much smaller change than that for the NOAA9 ratios.

In the comments below, "DC" signifies input from Matthew DeLand and Richard Cebula. "Authors' Comments" presents the reply of the authors of this report. Similarly, the section numbers used below refer to sections numbers in this report.

DC General Comment 1. . . . . "given your use of extremely overrange Range-2 data and issues related thereto, we have serious reservations as to the quality of the input data set."

Authors' Comments: We use the linear portion of range 2 above the first counter overflow but below the nonlinear, or what we call the "saturation" part, of the upper end of range-2 for the wall wavelengths numbers 4 and 10. The first counter overflow is a minor ambiguity problem that is easily solved by looking at the associated range-3 value. One main purpose of the study in Section 4.4 was to establish from the data how high the range-2 values can go while remaining nearly linear. We do not use range-2 values above 90,000 for NOAA9, which is below the nonlinear and saturation (or counter countdown) portion of range 2. Therefore, the range-2 values we have used in computing the modified Mg II ratio are not "extremely overrange."

DC General Comment 2. "After extensive review, we find significant problems with many facets of the SBUV/2 instrument understanding presented in this report. The documentation of this work is a valuable service to the user community, but we feel that significant revisions are needed to prevent misconceptions and errors from being circulated. While we have commented on several aspects of your instrument description and data handling, we recommend a thorough review of this report by Ball Aerospace Systems Division SBUV/2 personnel."

Authors' Comments: An early draft of this report was sent to 27 persons who are involved in some aspect of the design, testing, calibration, operation or data processing of the NOAA9 SBUV2 monitor and its data, including several members of Ball Aerospace. Constructive criticism received before the end of February 1994 has been incorporated or discussed in this report. Comments received later will be discussed in subsequent reports in this series. We continue to welcome clarifying comments and suggestions.

DC General Comment 3. "We are troubled that you have apparently ignored many of our previous discussions regarding SBUV/2 instrument issues, as well as the numerous memoranda, reports, and refereed papers for which reprints have been furnished."

R. F. Donnelly's Comments: First, this is a progress report for work conducted in 1987–1989, which predates most of the papers to which you refer. Secondly, our relative photometry approach differs from your overall-system, absolute photometry approach. For example, we are most interested in the linearity, noise, and drift for the small portion of the dynamic range involved in the outputs from the Mg II core wavelength and the wall wavelengths num-

bers 4 and 10, rather than for the full dynamic range or wavelength range of the instrument. Third, and most important, because you continue to describe your results, shown in Figure 3 of Cebula et al. (1992), as showing that the "classical Mg II index constructed from sweep mode data is consistent with the first Mg II index product from Nimbus–7 SBUV . . ." (DeLand and Cebula, 1994), we suspect the accuracy of all your analysis results. Through comparisons with the solar 10.7 cm radio flux and also the equivalent width of the He I line at 10830Å, our interpretation of Figure 3 is that about 75% of the variance in your classical NOAA9 Mg II ratio is due to instrumentation noise and drift and not due to solar variations. We consider your classical sweep-mode Mg II ratio to be an unacceptable result by a large margin, which is the reason we switched from studying the sweep-mode Mg II data to the discrete-wavelength Mg II measurements in 1987.

DC General Comment 4. "We strongly recommend that an appropriately edited version of this work be submitted to a refereed scientific journal for publication. Technical reports provide a useful method of presenting extensive details regarding techniques and methods. However, the refereed literature has been accepted as the appropriate method of disseminating research results to the scientific community, and should be used. It is especially important for you to do this because, so far as we know, your work in this area has not as yet been reported in the refereed literature."

Authors' Comments: Our modified Mg II core-to-wing ratio has been published in a refereed journal (Donnelly, 1991) and accepted for publication in a refereed journal (Donnelly et al., 1994). Any criticism of those data can be sent as a letter to either of those journals. We use the reviewed and edited NOAA ERL SEL Technical Memoranda series for the following purposes: (1) to report progress, (2) to present minor science research results of interest to a small audience, (3) to describe analyses in detail too lengthy for journal papers, and (4) to serve as a tool to promote discussion and criticism that can lead to improvements. Eventually, after the detailed discussions are completed, a summary journal paper would be appropriate.

DC General Comment 5. "Significant portions of the work described in this report seem to have been completed some time ago, but publication in 1994 implies to the reader that the contents are up to date, and that other related work has been acknowledged. There are numerous papers in the refereed literature dealing with both SBUV and SBUV/2 instrumentation issues . . . which are relevant to this report, but are not mentioned."

Authors' Comments: We referenced your inputs used in our 1987–1989 research reported here. Since we strongly disagree with some of your references, we cannot simply provide them as general references without including our criticisms of that work. The proper place to criticize those publications is in the journals where they are published. Your comment reminds us that it is time to do so.

DC General Comment 6. "The report reads as if it is an amalgamation of several separate works, written throughout the past few years, rather than a single, unified report. We recommend that the report be revised so as to delete redundant discussions."

Authors Comments: Yes, the entire report was not written by only one of the authors. Although the editorial review process will homogenize the final version to some extent, we hope the different writing styles will still be evident.

DC General Comments 7. "We suggest that internal memoranda (e. g. your references Cebula [1988], Lienesch [1989]) should be cited in the text as private communications. Using the same form as a published reference is misleading to the reader. Even more important, these communications are not widely available to the user community."

Authors' Comments: The final report will use the SEL editor's format. The first draft reflected our preference for using a reference to an item in the list of references, where a more complete mailing address could be included without disrupting the text so that interested readers could contact the source.

In the detailed comments given below, S denotes "section," P indicates paragraph, E refers to "equation" and s signifies sentence numbered from the beginning of the paragraph.

1. DC: Refer to S1.2.4, P4, s1: "The reference for the Nimbus-7 SBUV diffuser degradation should be Cebula et al., (1988)." Authors: No comment.

2. DC: Refer to S1.2.4, P4: "The degradation of the NOAA-9 SBUV/2 PMT gain with time is explicitly noted and expected by Frederick et al. [1986], so that the term X1r in Equation (1.2) should be understood to implicitly contain a time dependence. The suggestion that instrument throughput change can be determined through direct observations of the mercury calibration lamp is critically dependent on a stable lamp output over both short and long time scales. Frederick et al. [1986] demonstrate that this condition is not met for NOAA-9 SBUV/2, and Weiss et al. [1991] have shown significant long-term changes in lamp output which are greater than the total instrument throughput change including diffuser degradation." Authors: No comment.

3. DC: S1.3.1, P1: "The method used to derive calibration constants for each of the Mg II wavelengths is questionable. Forcing a polynomial fit to match two endpoints with only one intervening input data point, as well as constraining the slope of the fit at an endpoint, seems rather contrived. The impact of the method should be small for the limited wavelength range of the Mg II data, but use of a spline fit to the full calibration data set seems more appropriate. In addition, why is this method discussed when all later results use raw counts only?"

Authors' Comments: Our smooth curve fit to the calibration is a good fit for the portion of the wavelength range of interest for studies of the Mg II h and k lines and should not be questioned without first graphing both the curve and the calibration data. This comment is an example of the overall systems viewpoint as opposed to our interest in selected portions of the instrument, in this case a small portion of the wavelength range. As noted in Section 1.3.1, the wavelength dependence at 283.1 nm and to longer wavelengths is a fairly linear trend, which justifies setting the slope at 283.1 nm. Although this curve is not incorporated in the results presented in this report, it was a first step in evaluating the wavelength dependence corrections; you will see more of that work in subsequent reports in this series.

4. DC: S1.3.2, P1: "The interpretation of Dr. R. P. Cebula's non-linearity study is incorrect. The increase in the magnitude of the Range-2 non-linearity term (on a logarithmic intensity

scale) hardly implies that high levels of Range-2 counts are more linear than lower levels. Furthermore, the nominal maximum value for Range-2 counts is 65,535, and Ball Aerospace recommends that the counter-overflowed values can only be safely used to approximately 10–15% above this level (i.e. $C_{max}(\text{Range 2}) \leq 75{,}000$) before significant additional sources of nonlinearity come into play. The presence of a raw count value of approximately 84,000 in the non-linearity study is a consequence of the pre-launch test procedure, in which input count levels were doubled for each step. We do not understand the justification for ignoring the results derived by Ball Aerospace Systems Division personnel and Dr. Cebula, based on careful prelaunch testing, and using instrument outputs which are far beyond the recommended limits."

Authors' Comments: Our statements are correct. The limited portion of the dynamic range involved in the solar Mg II discrete-wavelength measurements is locally more linear than corrections of +1.7% and +2.9% imply. Our studies of NOAA11, which are discussed in the next report in this series, indicate that an upper limit for range-2 values of 75,000 would be appropriate for that instrument; however, the results presented in Section 4.4 show that an appropriate upper limit for NOAA9 is more like 95,000. (The intensity ranges for NOAA11 were shifted with respect to those for NOAA9). In our data analyses we do not use values above 90,000. The analysis in Section 4.4 illustrates the linearity of the range-3 output as a function of the range-2 output for the same input, which is not the same as the linearity of the output as a function of the spectral irradiance input. However, suppose there were an output versus input nonlinearity for range-2 values above 75,000. The linearity of range-3 values, with respect to same-input range-2 values from 75,000 to 95,000, means that the range-3 outputs from 780 to about 970 must also have a problem with output versus input nonlinearity. Nonsense! We would rather use range-2 values in the 75,000 to 90,000 range for the wall wavelengths nos. 4 and 10 than have to use range-3 values and deal with their low counts, high noise and range-2/range-3 drifts.

5. DC: S3.4: "The figures in this section do include long-term changes due to diffuser degradation. However, the method of presentation, where no correction is made for goniometric effects and an extremely large dynamic range is plotted, prevents this fact from being recognized. The casual reader would interpret this statement to imply that the diffuser degradation is unimportant, when in fact it is critically important to interpreting SBUV/2 irradiance measurements. The failure to apply any sort of goniometric correction to the raw irradiance data constitutes a major flaw in this analysis.

Authors' Comments: We love to show the raw data and let them speak to us in all their glory! Sure, there are long-term changes due to diffuser degradation; but let us rejoice that they are miniscule compared to those of Nimbus 4 SBUV and small compared to those of Nimbus 7 SBUV. We are confident that even casual readers will note that we do not claim them to be negligible. The diffuser correction affects both the numerator and denominator of the Mg II ratio. If the SBUV2 monitors were perfectly linear, the diffuser correction would completely cancel out in the Mg II ratio; so its only affect on the Mg II ratio is through a weak coupling caused by the very small nonlinearity of the instrument for the small portion of the dynamic

range that is used. It would be inappropriate for your absolute flux viewpoint to exaggerate the diffuser degradation effect on the Mg II ratio, where it is a very weak if not negligible correction. If the diffuser degradation were large, the effect of the small nonlinearity would be increased. For our relative photometry work, we are not so concerned with accurately determining a correction for the diffuser degradation; that degradation will simply cause the raw counts to be lower. So we mainly need to correct for the weak nonlinearity for whatever the output levels are. Your statement about not applying any goniometric correction and that being a major flaw is incorrect. The temporal interpolation used for each set of twelve-wavelength measurements, to determine the outputs for the wall wavelengths 4 and 10 for the same time as that for the core wavelength measurement, corrects for most of the goniometric corrections except for a weak coupling between the small wavelength dependence over the wavelength 4 to 10 range with the Sun-diffuser angles. The difference between your goniometric-correction approach and our temporal-interpolation approach can be analyzed. We suspect that the Sun-angle inputs may actually introduce noise into the derivation of the Mg II ratio because to the actual Sun angles differ slightly from those used in the goniometric corrections. Consequently, one appropriate test of the merits of the two approaches for the discrete-mode measurements would be to determine which approach gave the smallest yearly average of the daily standard deviation of the six daily values of RMgII from the discrete wavelength sets 2–7, normalized to the daily mean. This test simply assumes that, on average, the solar UV irradiance at the wavelengths involved in the Mg II ratio is constant with time over the 3-minute interval of the discrete-wavelength mode measurements 2–7.

6. DC: S4.2, item 3 below Figure 4.2.4: The "stuck counter" situation related to the use of inordinately overflowed data, could be avoided by using only recommended range data.

Authors' Comments: Such values are very rare and were first noticed in the core wavelength measurements that are well within the range DC considers to be recommended.

7. DC: S4.2, item 4 after Figure 4.2.4: "How many standard deviations from an average linear regression fit on a single day of data does a 2% difference represent? This cut-off should be justified. Also, if a "bad" point is replaced by the result of a linear regression fit to the remaining data rather than simply discarded, this introduces a bias by artificially reducing the statistical noise of the resulting Mg II index values. This type of "filling" should be explicitly noted for users of these data.

Author's Comments: The 2% criteria is rather conservative and catches really bad points. Whenever such isolated bad points are corrected, a message of the incident is printed. Since the daily Mg II value is a median rather than a mean of the ratios derived from Sun-lit discrete-wavelength sets 2–7, the corrected point has an effect on the daily median only if it ranks either third or fourth when the daily values are placed in monotonically increasing order (which means it can have only a minimal effect). The effect of this process can be tested simply by comparing the results for good data sets with those for the same data and purposely changing a few isolated points to represent isolated bad points. Bad-data events such as the loss of data in the fall of 1988, are first seen as an inordinate number of bad-data messages. The next report in this series discusses cases with unusual amounts of missing or bad data.

8. DC: E4.4–4.6: "The assumption of constant angles [α, β] corresponding to wavelength #7 for all samples in a given data set introduces an elevation angle error of $\Delta\alpha \simeq 0.5°$ for wavelengths #1 and 12. This is not a trivial error for the SBUV/2 instrument viewing geometry because $\theta_{incidence} = \alpha + 62°$, and since the measured signal is proportional to cos θ_i, the error can be greater than 2% at $\theta_i = 70°$.

Authors' Comments: We do not assume that α and β are constant. We assume they change with time from one wavelength to the next and from one set of 12 wavelengths to the next. On the basis of the behavior of the raw output values with time, we assume that the goniometric correction as a function of α and β, which are themselves functions of time, is a smoothly varying function of time that can be approximated piecewise at wavelength i by a linear function of time from one measurement at wavelength i to the next measurement at that wavelength. So we use these piecewise linear segments to estimate what the raw output would be for wavelength i if it were measured at the same time as the measurement that is actually made for wavelength 7. Within the accuracy to which the piecewise linear fit agrees with the actual goniometric curve as a function of time, this is equivalent to determining what the raw output would be for wavelength if it were measured at the same α and β angle as those occurring when wavelength 7 is measured.

These discussions will be continued in the next report in this series, which will include comments that have not yet been received.

8. REFERENCES

Alissandrakis, C. E., M. R. Kundu, and P. Lantos, 1980, A model for sunspot associated emission at 6 cm wavelength, *Astron. Astrophys.*, **82**:30.

Allen, C. W., 1963. *Astrophysical Quantities*, Athlone Press, U. of London, 79.

Allen, M. S., H. C. McAllister, and J. T. Jefferies, 1978, *High Resolution Atlas of the Solar Spectrum 2678-2931 A.,* Inst. Astron., U. Hawaii, Honolulu, Hawaii, 58 pp.

Ball Ref. 1, April 1, 1984, *SBUV/2 Technical Description (Final Phase Design)*, Document No. 6802–10, Revision C., Ball Aerospace Systems Division, Boulder, CO.

Ball Ref. 2, M. Kirk and B. H. Brandreth, February 25, 1985, *Specification Compliance and Calibration Data Book, Vol. I for Solar Backscatter Ultraviolet Spectral Radiometer, Mod. 2 (SBUV/2 Flight 1)*, Document No. B6802–71, Rev. A, Ball Aerospace Systems Division, Boulder, CO, pp. 17-1 to 17–3.

Ball Ref. 3, B. H. Brandreth and M. Kirk, December 1, 1987, *Specification Compliance and Calibration Data Book, Vol. II for Flight Model No. 1, Serial No. 002, Solar Backscatter Ultraviolet Spectral Radiometer, Mod. 2*, Document No. B6802–71, Ball Aerospace Systems Division, Boulder, CO, pp. 6-1 to 6–65.

Ball Ref. 4, February 1, 1986, *SBUV/2 Final Engineering Report for Flight #1*, (S/N002), Document No. B6802–91, Ball Aerospace Systems Division, Boulder, CO, pp. 6-1 to 6–3.

Ball Ref. 5, July 30, 1987, B. H. Brandreth and M. Kirk, *Specification Compliance and Calibration Data Book, Vol. I for Solar Backscatter Ultraviolet Spectral Radiometer, Mod. 2 (SBUV/2 Flight 1)*, Document No. B6802–71, Rev. C, Ball Aerospace Systems Division, Boulder, CO, pp. 7-1 to 7–2.

Barth, C. A., W. K. Tobiska, and G. J. Rottman, 1988, Comparison of the solar Lyman alpha flux with the solar 10.7-cm radio flux, *EOS Trans. AGU*, **69**:1354.

Bouwer, S. D., 1992, Periodicities of solar irradiance and solar activity indices, II, *Solar Phys.*, **142**:365–389.

Bouwer, S. D., J. Pap, and R. F. Donnelly, 1990, Dynamic power spectral analysis of solar measurements from photospheric, chromospheric and coronal sources. In *Climate Impact of Solar Variability*, NASA Conf. Proc. 3086 (eds. K. H. Schatten and A. Arking), NASA GSFC, Greenbelt, MD, 125–132.

Cebula, R. P., H. Park, and D. F. Heath, 1988. Characterization of the Nimbus-7 SBUV radiometer for the long-term monitoring of stratospheric ozone, *J. Atmos. Oceanic Tech.*, **5**:215–227.

Cebula, R. P., M. T. DeLand, and B. M. Schlesinger, 1989, *A Status Report on the Analysis of the NOAA-9 SBUV/2 Sweep Mode Solar Irradiance Data*, ST Systems Corp., Lanham, Maryland 20706, 22 pp. (See Cebula et al., 1990.)

Cebula, R. P., M. T. DeLand, B. M. Schlesinger, and R. D. Hudson, 1990, A status report on the analysis of the NOAA-9 SBUV/2 sweep mode solar irradiance data. In *NOAA-9 Solar Backscatter Ultraviolet (SBUV/2) Instrument and Derived Ozone Data: A Status Report Based on a Review on January 29, 1990*, NOAA Tech. Rpt. NESDIS 53 (ed. W. G. Planet), Satellite Research Lab., Office of Research and Applications, NOAA NESDIS, Washington, D. C., pp. 4–1 to 4–22.

Cebula, R. P., M. T. DeLand, and B. M. Schlesinger, 1992. Estimates of solar variability using the Solar Backscatter Ultraviolet (SBUV)2 MgII index from the NOAA-9 satellite, *J. Geophys. Res.*, **97**:11613–11620.

Covington, A. E., 1948, Solar noise observations on 10.7 centimeters, *Proc. of the I.R.E.*, **36**:454.

DeLand, M. T. and R. P. Cebula, 1994. Comparisons of the MgII index products from the NOAA-9 and NOAA-11 SBUV/2 instruments, *Solar ys.*, in press.

Donnelly, R. F., 1987, Temporal trends of solar EUV and UV full-disk fluxes, *Solar Phys.*, **109**: 37–58.

Donnelly, R. F., 1988a, The solar UV MgII core-to-wing ratio from the NOAA9 satellite during the rise of solar cycle 22, *Adv. Space Res.*, **8**:(7)77–(7)80.

Donnelly, R. F., 1988b, Uniformity in solar UV flux variations important to the stratosphere, *Annales Geophys.*, **6**:417–424.

Donnelly, R. F., 1988c, The Solar Electromagnetic Radiation Flux Study (SERFS). In *STP Newsletter*, World Data Center A for Solar-Terrestrial Physics, Boulder, CO, **88–1**:34–36.

Donnelly, R. F., 1989, Solar UV variability. In *MAP Handbook 29, Proceedings of the IAGA Symposium for Solar Activity Forcing of the Middle Atmosphere* (ed. J. Lastovicka), available from SCOSTEP Secretariat, U. of Ill., Urbana, IL, **29**:1–8.

Donnelly, R. F., 1990a, Solar UV temporal variations during solar cycle 22 & the twentieth century. In *Climate Impact of Solar Variability* NASA Conf. Proc. 3086 (eds. K. H. Schatten and A. Arking), NASA GSFC, Greenbelt, MD, 328–335.

Donnelly, R. F., 1990b, Temporal variations of solar UV, EUV and X-ray fluxes, sunspot number and F10. In *Solar-Terrestrial Predictions: Proceedings of a Workshop at Leura, Australia, October 16-20, 1989, Volume 1. Working Group Reports, Invited Papers, and Contributed Solar Papers*, (eds. R. J. Thompson et. al.), NOAA ERL, Boulder, CO, 381–385.

Donnelly, R. F., 1991, Solar UV spectral irradiance variations, *J. Geomagn. & Geoelect.*, **43**, Suppl., 835–842.

Donnelly, R. F, and J. Barrett, 1990, Analysis of SBUV2 measurements of solar UV irradiance variations. In *NOAA-9 Solar Backscatter Ultraviolet (SBUV/2) Instrument and Derived Ozone Data: A Status Report Based on a Review on January 29, 1990,* NOAA Tech. Rept. NESDIS 53 (ed. W.

G. Planet), Satellite Res. Lab., Office of Research and Applications, NOAA NESDIS, Washington, D. C., pp. 12-1 to 12-5.

Donnelly, R. F, and L. C. Puga, 1990, Thirteen-day periodicity and the center-to-limb dependence of UV, EUV, and X-ray emission of solar activity, *Solar Phys.*, **130**:369–390.

Donnelly, R. F., D. E. Stevens, J. Barrett, and K. Pfendt, 1987, *Short-Term Temporal Variations of Nimbus-7 Measurements of the Solar UV Spectral Irradiance,* NOAA Tech. Memo. ERL ARL–154, NOAA ERL, Boulder, CO, 59 pp.

Donnelly, R. F., D. F. Heath, B. M. Schlesinger, S. F. Keil, W. C. Livingston and O. R. White, 1994, *SERF3 Model of the Temporal Variations of the Solar Spectral Irradiance*, Part I, Solar UV Irradiance, in preparation for publication as a NOAA ERL SEL Tech. Memo.

Donnelly, R. F., D. F. Heath, J. L. Lean, and G. J. Rottman, 1983, Differences in the temporal variations of solar UV flux, 10.7-cm solar radio flux, sunspot number, and Ca-K plage data caused by solar rotation and active region evolution, *J. Geophys. Res.*, **88**:9883–9888.

Donnelly, R. F., H. E. Hinteregger, and D. F. Heath, 1986, Temporal variations of solar EUV, UV and 10830-A radiations, *J. Geophys. Res.*, **91**:5567–5578.

Donnelly, R. F., J, W. Harvey, D. F. Heath, and T. P. Repoff, 1985, Temporal characteristics of the solar UV flux and the He I line at 1083 nm, *J. Geophys. Res.*, **90**:6267–6273.

Donnelly, R. F, L. C. Puga, T. P. Repoff, and J. L. Lean, 1984, *The NOAA-ERL-ARL Solar UV Radiation and Climate Research Project Program Description and Progress Report*, NOAA Tech. Memo. ERL ARL–126, Air Resources Lab., NOAA ERL, Boulder, CO, 142 pp.

Donnelly, R. F., O. R. White, and W. C. Livingston, 1994, The solar Ca II K index and the Mg II core-to-wing ratio, accepted for publication in *Solar Physics.*

Doschek, G. A., and U. Feldman, 1977, High-resolution spectra of the solar Mg II h and k lines from SKYLAB. *Astrophys. J., Suppl. Ser.*, **35**:471–482.

Felli, M., K. R. Lang, and R. F. Willson, 1981, VLA observations of solar active regions. I. The slowly varying component, *Astrophys. J.*, **247**:325.

Foukal, P., 1990, *Solar Astrophysics,* John Wiley & Sons, Inc., New York, NY, 475.

Frederick, J. E., R. P. Cebula, and D. F. Heath, 1986, Instrument characterization for the detection of long-term changes in stratospheric ozone: an analysis of the SBUV/2 radiometer, *J. Atmosph. & Oceanic Tech.*, **3**:472–480.

Fredga, K., 1971, A comparison between MgII and CaII spectroheliograms, *Solar Phys.*, **21**:60–81.

Fredga, K., 1969, Spectroheliograms in the Mg II line at 2795.5 Å. *Solar Phys.*, **9**:358–371.

Gouttebroze, P., 1977, Velocity gradients in the solar chromosphere and Mg II line profiles, *Astron. Astrophys.*, **54**:203–211.

Hall, L. A., and G. P. Anderson, 1988, Instrumental effects on a proposed Mg II index of solar activity, *Ann. Geophys.*, **6**:531–534.

Heath, D. F., 1980, A review of observational evidence for short and long term ultraviolet flux variability of the sun. In *Sun and Climate*, Centre National D'Etudes Spatiales, Toulouse, France, pp.447–471.

Heath, D. F., and B. M. Schlesinger, 1986, The Mg 280-nm doublet as a monitor of changes in solar ultraviolet irradiance. *J. Geophys. Res.*, **91**:8672–8682.

Heath, D. F., A. J. Krueger, H. A. Roeder, and B. D. Henderson, 1975, The solar backscatter ultraviolet and total ozone mapping spectrometer (SBUV/TOMS) for NIMBUS G, *Optical Eng.*, **14**: 323–331.

Heath, D. F., T. P. Repoff, and R. F. Donnelly, 1984, *NIMBUS-7 Observations of Solar UV Spectral Irradiance Variations Caused by Solar Rotation and Active-Region Evolution for the Period November 7, 1978-November 1, 1980*, NOAA Tech. Memo. ERL ARL–129, Air Resources Lab., NOAA/ERL, Boulder, CO, 75 pp.

Kohl, J. L., and W. H. Parkinson, 1976, The Mg II h and k lines. I. Absolute center and limb measurements of the solar profiles. *Astrophys. J.*, **205**:599–611.

Lean, J. L., and T. P. Repoff, 1987, A statistical analysis of solar flux variations over time scales of solar rotations: 1978–1982, *J. Geophys. Res.*, **92**:5555–5563.

Lemaire, P., 1970, Resonance lines in the solar chromosphere. In *Ultraviolet Stellar Spectra and Ground-Based Observation* (eds. Houziaux and Butler), IAU, 250–255.

Lemaire, P., 1984, Increasing solar chromosphere line intensities with solar activity, *Adv. Space Res.* **4**:(8)29–(8)35.

Livingston, W., R. F. Donnelly, V. Grigoryev, M. L. Demidov, J. Lean, M. Steffen, O. R. White, and R. L. Willson, 1991, Sun-as-a-star spectrum variability. In *Solar Interior and Atmosphere*, (eds. A. N. Cox, W. C. Livingston, and M. S. Matthews), U. Arizona Press, Tucson, 1135.

Moore, C. E., R. Tousey, and C. M. Brown, 1982, *The Solar Spectrum 3069A-2095A*. NRL Report 8653, Naval Res. Lab., Washington, D. C., 169 pp.

Pap, J., H. S. Hudson, G. J. Rottman, R. C. Willson, R. F. Donnelly, and J. London, 1990a, Modeling solar Lyman alpha irradiance. In *Climate Impact of Solar Variability*, NASA Conf. Proc. 3086, (eds. K. H. Schatten and A. Arking), NASA GSFC, Greenbelt, MD, 189–196.

Pap, J., W. K. Tobiska, and S. D. Bouwer, 1990b, Periodicities of solar irradiance and solar activity indices, I, *Solar Phys.*, **129**:165–189.

Planet, W. G., ed., 1990, *NOAA-9 Solar Backscatter Ultraviolet (SBUV/2) Instrument and Derived Ozone Data: A Status Report Based on a Review on January 29, 1990*, NOAA Tech. Rept. NESDIS 53, NOAA NESDIS, Washington, D. C.,1-1 to 13-15.

Puga, L. C., R. F. Donnelly, J. Barrett, G. Falcon, K. Pfendt, D. Stevens, and M. Gao, 1987, *The NOAA-ERL-ARL Solar UV Radiation and Climate Research Project, Program Description and Progress Report*, NOAA Tech. Memo. ERL ARL-159, Boulder, CO, 117 pp.

Purcell, J. D., A. Boggess III, and R. Tousey, 1958, A high resolution ultraviolet spectrogram of the sun. Paper 6.6. In *Experimental Results of the U. S. Rocket Program for the International Geophysical Year to 1 July 1958*, (eds. J Hanessian, Jr., and I. Guttmacher), IGY Rocket Report Series No. 1, IGY World Data Center A for Rockets and Satellites, National Academy of Sciences, Washington, D. C., 198-199.

Purcell, J. D., D. L. Garrett, and R. Tousey, 1963, Solar spectra from 3500 to 2200 Å at 30 mÅ resolution. In *Space Res. III,* (ed. W. Priester), North Holland Publ. Co., Amsterdam, 781-785.

Rottman, G. J., 1983, 27-day variations observed in solar U. V. (120-300 nm) irradiance, *Planet. Space Sci.*, **31**:1001.

Rottman, G. J., 1987, Results from space measurements of solar UV and EUV flux. In *Solar Radiative Output Variation* (ed. P. Foukal), Cambridge Research and Instrumentation, Inc., Cambridge, MA, 71-86.

Rottman, G. J., C. A. Barth, R. J. Thomas, G. H. Mount, G. M. Lawrence, D. W. Rusch, R. W. Sanders, G. E. Thomas, and J. London, 1982, Solar spectral irradiance, 120 to 190 nm, *Geophys. Res. Lett.*, **9**:587.

Schlesinger, B. M., R. P. Cebula, D. F. Heath, and A. J. Fleig, 1988, *Nimbus 7 Solar Backscatter Ultraviolet (SBUV) Spectral Scan Solar Irradiance and Earth Radiance Product User's Guide*. NASA Ref. Publ. 1199, NASA Code NTT-4, Washington, D. C. 20546-0001, 67 pp.

Solar Geophysical Data, September 1988, No. 529, Part II, 74-75.

Solar Geophysical Data, September 1989, No. 541, Part II, 178-180.

Solar Geophysical Data, October 1989, No. 542, Part II, 82-91.

Solar Geophysical Data, October 1991, No. 566, Part II, 84-87.

ST Systems Corp., 1987, SBUV/2 Flight Unit #1 (S/N 002) Nonlinearity Correction Determination, prepared for R. D. Hudson, NASA GSFC, Greenbelt, MD, by ST Systems Corp., Lanham, MD, 81 pp.

Thomas, G. E., C. A. Barth, E. R. Hansen, C. W. Hord, G. M. Lawrence, G. H. Mount, G. J. Rottman, D. W. Rusch, A. I. Stewart, R. J. Thomas, J. London, P. L. Bailey, P. J. Crutzen, R. E. Dick-

inson, J. C. Gille, S. C. Liu, J. F. Noxon, and C. B. Farmer, 1980, Scientific objectives of the Solar Mesosphere Explorer mission, *Pageoph.*, **118**:591.

Tobiska, W. K., and S. D. Bouwer, 1989, Intermediate-term variations of chromospheric and coronal solar flux during high solar cycle 21 activity, *Geophys. Res. Let.*, **16**:779–782.

Tousey, R., E. F. Milone, J. D. Purcell, W. P. Schneider, and S. G. Tilford, 1974, *An Atlas of the Solar Ultraviolet Spectrum Between 2226 and 2992 Angstroms*. NRL Report 7788, Naval Research Lab., Washington, D. C., 87.

Weiss, H., R. P. Cebula, K. Laamann, and R. D. Hudson, 1991. Evaluation of the NOAA-11 Solar Backscatter Ultraviolet radiometer, mod 2 (SBUV/2): inflight calibration, *Proc. SPIE, 1493*, 80–90.

White, O. R., and W. C. Livingston, 1981, Solar luminosity variations, III, Calcium K variation from solar minimum to maximum in cycle 21, *Astrophys. J.*, **249**:798–816.

White, O. R., W. C. Livingston, and S. L. Keil, 1992, Solar CaII measurements and activity cycles in solar-type stars. In *Proc. of the Solar Electromagnetic Radiation Study for Solar Cycle 22* (ed. R. F. Donnelly), NOAA ERL SEL, Boulder, CO, 160–165.

Zirin, H., 1966, *The Solar Atmosphere*, Blaisdell Publ. Co., Waltham, MA, 228–232.

Zirin, H., 1988, *Astrophysics of The Sun,* Cambridge U. Press, Cambridge, England, 166–168.

APPENDIX I

Tabulations of R(MgIIc/w) for 1986–1988

Table A1-1 presents the core-to-wing ratio (RMgII) for the Mg II h and k lines derived from the NOAA9 SBUV2 discrete-wavelength mode measurements using equations (4.4–4.6 and 4.8). These values have been converted to equivalent Nimbus-7 values using equation (6.3). All the data tests and corrections discussed in Chapter 4 were applied to these data, namely: (1) counter overflow corrections, (2) stuck full-counter bad points, (3) 2% off linearity tests for isolated bad points, (4) piece-wise linear temporal interpolation, etc. Daily medians of the ratios derived from discrete-wavelength sets no. 2–7 were used except for the several cases marked with an asterisk (*); those marked cases involved fewer than the full group of sets no. 2–7 but at least four usable sets per day. These asterisk cases were our first attempt to fill in missing days of data when problems occurred with some of the measurements; the next progress report will include several other techniques and a quality factor to keep track of what technique was used to derive the R_{MgII} result.

The results in Table A1-1 were published in Solar Geophysical Data (1991). Table A1-2 identifies the dates when no results are presented in Table A1-1 because of various problems with the data. The large gap starting September 20, 1988, was caused by part of the satellite unexpectedly blocking the view of the Sun for the SBUV2 instrument.

TABLE A1-1.

MgII Core to Wing Ratio

NIMBUS7 Equivalent Values Derived from NOAA9 Measurements

Date	Value	Date	Value	Date	Value	Date	Value	Date	Value
86 5 27	0.2654	86 7 6	0.2637	86 8 18	0.2636	86 9 28	0.2633	86 11 7	0.2648
86 5 28	0.2650	86 7 7	0.2639	86 8 19	0.2637	86 9 29	0.2634	86 11 8	0.2642
86 5 29	0.2648	86 7 8	0.2638	86 8 20	0.2637	86 9 30	0.2636	86 11 9	0.2636
86 5 30	0.2644	86 7 10	0.2646	86 8 21	0.2636	86 10 1	0.2640	86 11 10	0.2634
86 5 31	0.2642	86 7 11	0.2646	86 8 22	0.2635	86 10 2	0.2642	86 11 11	0.2632
86 6 1	0.2639	86 7 12	0.2648	86 8 23	0.2634	86 10 3	0.2644	86 11 12	0.2634
86 6 2	0.2636	86 7 13	0.2646	86 8 24	0.2635	86 10 4	0.2641	86 11 13	0.2634
86 6 3	0.2636	86 7 14	0.2639	86 8 25	0.2633	86 10 5	0.2644	86 11 14	0.2637
86 6 4	0.2635	86 7 15	0.2649	86 8 26	0.2634	86 10 6	0.2643	86 11 15	0.2640
86 6 5	0.2633	86 7 16	0.2650	86 8 27	0.2636	86 10 7	0.2643	86 11 16	0.2645
86 6 6	0.2634	86 7 17	0.2651	86 8 28	0.2636	86 10 8	0.2645	86 11 17	0.2647
86 6 7	0.2633	86 7 18	0.2650	86 8 29	0.2636	86 10 9	0.2646	86 11 18	0.2649
86 6 8	0.2635	86 7 19	0.2651	86 8 30	0.2633	86 10 10	0.2642	86 11 19	0.2651
86 6 9	0.2638	86 7 20	0.2649	86 8 31	0.2633	86 10 11	0.2642	86 11 20	0.2652
86 6 10	0.2638	86 7 21	0.2649	86 9 1	0.2637	86 10 12	0.2640	86 11 21	0.2651
86 6 11	0.2638	86 7 22	0.2648	86 9 2	0.2636	86 10 13	0.2636	86 11 22	0.2652
86 6 12	0.2641	86 7 23	0.2645	86 9 3	0.2635	86 10 14	0.2631	86 11 23	0.2653
86 6 13	0.2641	86 7 24	0.2643	86 9 4	0.2637	86 10 15	0.2629	86 11 24	0.2655
86 6 14	0.2642	86 7 25	0.2640	86 9 5	0.2636	86 10 16	0.2631	86 11 25	0.2653
86 6 15	0.2645	86 7 26	0.2639	86 9 6	0.2635	86 10 17	0.2634	86 11 26	0.2651
86 6 16	0.2649	86 7 27	0.2637	86 9 7	0.2637	86 10 18	0.2640	86 11 27	0.2651
86 6 17	0.2648	86 7 29	0.2639	86 9 8	0.2638	86 10 19	0.2643	86 11 28	0.2651
86 6 18	0.2648	86 7 31	0.2639	86 9 10	0.2635	86 10 20	0.2645	86 11 29	0.2648
86 6 19	0.2647	86 8 1	0.2639	86 9 11	0.2638	86 10 21	0.2649	86 11 30	0.2644
86 6 20	0.2646	86 8 2	0.2639	86 9 12	0.2638	86 10 22	0.2654	86 12 1	0.2645
86 6 21	0.2643	86 8 3	0.2640	86 9 13	0.2635	86 10 23	0.2659	86 12 2	0.2643
86 6 22	0.2641	86 8 4	0.2641	86 9 14	0.2635	86 10 24	0.2663	86 12 3	0.2641
86 6 23	0.2644	86 8 5	0.2640	86 9 15	0.2636	86 10 25	0.2667	86 12 4	0.2641
86 6 24	0.2640	86 8 6	0.2641	86 9 16	0.2636	86 10 26	0.2668	86 12 5	0.2638
86 6 25	0.2639	86 8 7	0.2641	86 9 17	0.2632	86 10 27	0.2668	86 12 6	0.2634
86 6 26	0.2638	86 8 8	0.2642	86 9 18	0.2632	86 10 28	0.2669	86 12 7	0.2633
86 6 27	0.2634	86 8 9	0.2637	86 9 19	0.2634	86 10 29	0.2667	86 12 8	0.2634
86 6 28	0.2634	86 8 10	0.2638	86 9 20	0.2634	86 10 30	0.2667	86 12 9	0.2633
86 6 29	0.2636	86 8 11	0.2640	86 9 21	0.2633	86 10 31	0.2663	86 12 10	0.2636
86 6 30	0.2634	86 8 12	0.2637	86 9 22	0.2634	86 11 1	0.2664	86 12 11	0.2638
86 7 1	0.2634	86 8 13	0.2638	86 9 23	0.2634	86 11 2	0.2665	86 12 12	0.2640
86 7 2	0.2633	86 8 14	0.2638	86 9 24	0.2634	86 11 3	0.2661	86 12 13	0.2643
86 7 3	0.2633	86 8 15	0.2639	86 9 25	0.2633	86 11 4	0.2658	86 12 14	0.2644
86 7 4	0.2634	86 8 16	0.2639	86 9 26	0.2635	86 11 5	0.2656	86 12 15	0.2642
86 7 5	0.2634	86 8 17	0.2639	86 9 27	0.2634	86 11 6	0.2651	86 12 16	0.2645

Date	Value	Date	Value	Date	Value	Date	Value	Date	Value
86 12 17	0.2645	87 1 27	0.2639	87 3 10	0.2637	87 4 19	0.2662	87 5 29	0.2643
86 12 18	0.2647	87 1 28	0.2637	87 3 11	0.2635	87 4 20	0.2652	87 5 30	0.2646
86 12 19	0.2644	87 1 29	0.2637	87 3 12	0.2636	87 4 21	0.2649	87 5 31	0.2644
86 12 20	0.2643	87 1 30	0.2637	87 3 13	0.2635	87 4 22	0.2649	87 6 1	0.2647
86 12 21	0.2645	87 1 31	0.2638	87 3 14	0.2636	87 4 23	0.2647	87 6 2	0.2649
86 12 22	0.2645	87 2 2	0.2635	87 3 15	0.2641	87 4 24	0.2650	87 6 3	0.2649
86 12 23	0.2643	87 2 3	0.2636	87 3 16	0.2639	87 4 25	0.2649	87 6 4	0.2651
86 12 24	0.2641	87 2 4	0.2634	87 3 17	0.2641	87 4 26	0.2645	87 6 5	0.2655
86 12 25	0.2643	87 2 5	0.2635	87 3 18	0.2643	87 4 27	0.2643	87 6 6	0.2657
86 12 26	0.2643	87 2 6	0.2635	87 3 19	0.2644	87 4 28	0.2643	87 6 7	0.2659
86 12 27	0.2640	87 2 7	0.2633	87 3 20	0.2647	87 4 29	0.2644	87 6 8	0.2662
86 12 28	0.2640	87 2 8	0.2635	87 3 21	0.2649	87 4 30	0.2646	87 6 9	0.2660
86 12 29	0.2638	87 2 9	0.2637	87 3 22	0.2649	87 5 1	0.2650	87 6 10	0.2657
86 12 31	0.2634	87 2 10	0.2637	87 3 23	0.2647	87 5 2	0.2649	87 6 11	0.2658
87 1 1	0.2636	87 2 11	0.2636	87 3 24	0.2648	87 5 3	0.2648	87 6 12	0.2658
87 1 2	0.2635	87 2 12	0.2639	87 3 25	0.2647	87 5 4	0.2649	87 6 13	0.2660
87 1 3	0.2634	87 2 13	0.2640	87 3 26	0.2646	87 5 5	0.2654	87 6 14	0.2661
87 1 4	0.2636	87 2 14	0.2639	87 3 27	0.2645	87 5 6	0.2660	87 6 15	0.2662
87 1 5	0.2636	87 2 15	0.2643	87 3 28	0.2644	87 5 7	0.2665	87 6 16	0.2660
87 1 6	0.2637	87 2 16	0.2642	87 3 29	0.2644	87 5 8	0.2668	87 6 17	0.2661
87 1 7	0.2636	87 2 17	0.2640	87 3 30	0.2642	87 5 9	0.2672	87 6 18	0.2662
87 1 8	0.2636	87 2 18	0.2640	87 3 31	0.2642	87 5 10	0.2675	87 6 19	0.2667
87 1 9	0.2638	87 2 19	0.2642	87 4 1	0.2641	87 5 11	0.2677	87 6 20	0.2665
87 1 10	0.2635	87 2 20	0.2640	87 4 2	0.2639	87 5 12	0.2676	87 6 21	0.2668
87 1 11	0.2636	87 2 21	0.2643	87 4 3	0.2642	87 5 13	0.2670	87 6 22	0.2667
87 1 12	0.2638	87 2 22	0.2642	87 4 4	0.2638	87 5 14	0.2665	87 6 23	0.2662
87 1 13	0.2636	87 2 23	0.2641	87 4 5	0.2640	87 5 15	0.2665	87 6 24	0.2659
87 1 14	0.2638	87 2 25	0.2639	87 4 6	0.2644	87 5 16	0.2666	87 6 25	0.2656
87 1 15	0.2641	87 2 26	0.2641	87 4 7	0.2645	87 5 17	0.2666	87 6 27	0.2654
87 1 16	0.2644	87 2 27	0.2643	87 4 8	0.2652	87 5 18	0.2666	87 6 28	0.2652
87 1 17	0.2644	87 2 28	0.2642	87 4 9	0.2656	87 5 19	0.2668	87 6 29	0.2651
87 1 18	0.2648	87 3 1	0.2641	87 4 10	0.2665	87 5 20	0.2666	87 6 30	0.2653
87 1 19	0.2647	87 3 2	0.2643	87 4 11	0.2668	87 5 21	0.2664	87 7 1	0.2651
87 1 20	0.2647	87 3 3	0.2641	87 4 12	0.2669	87 5 22	0.2666	87 7 2	0.2650
87 1 21	0.2647	87 3 4	0.2643	87 4 13	0.2676	87 5 23	0.2666	87 7 3	0.2652
87 1 22	0.2650	87 3 5	0.2642	87 4 14	0.2678	87 5 24	0.2667	87 7 4	0.2654
87 1 23	0.2651	87 3 6	0.2641	87 4 15	0.2678	87 5 25	0.2664	87 7 5	0.2652
87 1 24	0.2648	87 3 7	0.2642	87 4 16	0.2675	87 5 26	0.2660	87 7 6	0.2650
87 1 25	0.2643	87 3 8	0.2642	87 4 17	0.2673	87 5 27	0.2653	87 7 7	0.2651
87 1 26	0.2642	87 3 9	0.2641	87 4 18	0.2668	87 5 28	0.2647	87 7 8	0.2649

Date	Value *	Date	Value	Date	Value	Date	Value	Date	Value
87 7 9	0.2648	87 8 23	0.2674	87 10 3	0.2665	87 11 13	0.2673	87 12 24	0.2674
87 7 10	0.2646	87 8 24	0.2671	87 10 4	0.2664	87 11 14	0.2674	87 12 25	0.2672
87 7 13	0.2648	87 8 25	0.2668	87 10 5	0.2667	87 11 15	0.2672	87 12 26	0.2675
87 7 14	0.2648	87 8 26	0.2665	87 10 6	0.2670	87 11 16	0.2671	87 12 27	0.2674
87 7 15	0.2653	87 8 27	0.2663	87 10 7	0.2670	87 11 17	0.2670	87 12 28	0.2676
87 7 16	0.2656	87 8 28	0.2660	87 10 8	0.2669	87 11 18	0.2674	87 12 29	0.2679
87 7 17	0.2659	87 8 29	0.2659	87 10 9	0.2671	87 11 19	0.2677	87 12 30	0.2686
87 7 18	0.2662	87 8 30	0.2658	87 10 10	0.2672	87 11 20	0.2677	87 12 31	0.2685
87 7 20	0.2667	87 9 1	0.2662	87 10 11	0.2675	87 11 21	0.2679	88 1 1	0.2685
87 7 21	0.2673	87 9 2	0.2660	87 10 12	0.2675	87 11 22	0.2684	88 1 2	0.2682
87 7 22	0.2680	87 9 3	0.2662	87 10 13	0.2677	87 11 23	0.2691	88 1 3	0.2685
87 7 23	0.2686	87 9 4	0.2664	87 10 14	0.2683	87 11 24	0.2692	88 1 4	0.2684
87 7 24	0.2691	87 9 5	0.2664	87 10 15	0.2688	87 11 25	0.2691	88 1 5	0.2687
87 7 25	0.2690	87 9 6	0.2664	87 10 16	0.2688	87 11 26	0.2689	88 1 6	0.2688
87 7 26	0.2688	87 9 7	0.2664	87 10 17	0.2684	87 11 27	0.2687	88 1 7	0.2689
87 7 27	0.2685	87 9 8	0.2663	87 10 19	0.2681	87 11 28	0.2679	88 1 8	0.2685
87 7 29	0.2680	87 9 9	0.2663	87 10 20	0.2678	87 11 29	0.2678	88 1 9	0.2681
87 7 30	0.2679	87 9 10	0.2666	87 10 21	0.2673	87 11 30	0.2676	88 1 10	0.2683
87 7 31	0.2675	87 9 11	0.2670	87 10 22	0.2665	87 12 1	0.2676	88 1 11	0.2685
87 8 1	0.2671	87 9 12	0.2670	87 10 23	0.2658	87 12 2	0.2674	88 1 12	0.2692
87 8 2	0.2663	87 9 13	0.2670	87 10 24	0.2657	87 12 3	0.2673	88 1 13	0.2697
87 8 3	0.2661	87 9 14	0.2669	87 10 25	0.2658	87 12 4	0.2673	88 1 14	0.2701
87 8 4	0.2659	87 9 15	0.2670	87 10 26	0.2663	87 12 5	0.2670	88 1 15	0.2700
87 8 5	0.2653	87 9 16	0.2669	87 10 27	0.2669	87 12 7	0.2668	88 1 16	0.2702
87 8 6	0.2652	87 9 17	0.2671	87 10 28	0.2673	87 12 8	0.2666	88 1 17	0.2702
87 8 7	0.2652	87 9 18	0.2669	87 10 29	0.2678	87 12 9	0.2668	88 1 18	0.2699
87 8 8	0.2653	87 9 19	0.2670	87 10 30	0.2680	87 12 10	0.2668	88 1 19	0.2699
87 8 9	0.2654	87 9 20	0.2668	87 10 31	0.2682	87 12 11	0.2665	88 1 20	0.2697
87 8 11	0.2661	87 9 21	0.2666	87 11 1	0.2683	87 12 12	0.2662	88 1 21	0.2693
87 8 12	0.2661	87 9 22	0.2658	87 11 2	0.2688	87 12 13	0.2664	88 1 22	0.2690
87 8 13	0.2664	87 9 23	0.2656	87 11 3	0.2688	87 12 14	0.2670	88 1 23	0.2686
87 8 14	0.2670	87 9 24	0.2655	87 11 4	0.2687	87 12 15	0.2676	88 1 24	0.2686
87 8 15	0.2675	87 9 25	0.2654	87 11 5	0.2686	87 12 16	0.2682	88 1 25	0.2678
87 8 16	0.2679	87 9 26	0.2652	87 11 6	0.2681	87 12 17	0.2682	88 1 26	0.2678
87 8 17	0.2679	87 9 27	0.2651	87 11 7	0.2680	87 12 18	0.2682	88 1 29	0.2677
87 8 18	0.2681	87 9 28	0.2649	87 11 8	0.2681	87 12 19	0.2680	88 1 30	0.2681
87 8 19	0.2679	87 9 29	0.2655	87 11 9	0.2680	87 12 20	0.2682	88 1 31	0.2686
87 8 20	0.2679	87 9 30	0.2657	87 11 10	0.2680	87 12 21	0.2681	88 2 1	0.2693
87 8 21	0.2680	87 10 1	0.2659	87 11 11	0.2677	87 12 22	0.2679	88 2 2	0.2701
87 8 22	0.2676	87 10 2	0.2661	87 11 12	0.2676	87 12 23	0.2677	88 2 3	0.2705

Date	Value	Date	Value	Date	Value	Date	Value	Date	Value
88 2 4	0.2705	88 3 15	0.2696	88 4 26	0.2698	88 6 5	0.2744	88 7 15	0.2724
88 2 5	0.2706	88 3 16	0.2697	88 4 27	0.2696	88 6 6	0.2758	88 7 16	0.2723
88 2 6	0.2702	88 3 17	0.2703	88 4 28	0.2698	88 6 7	0.2758	88 7 17	0.2730
88 2 7	0.2698	88 3 18	0.2701	88 4 29	0.2696	88 6 8	0.2760	88 7 18	0.2733
88 2 8	0.2697	88 3 19	0.2706	88 4 30	0.2698	88 6 9	0.2764	88 7 19	0.2736
88 2 9	0.2694	88 3 20	0.2702	88 5 1	0.2700	88 6 10	0.2751	88 7 20	0.2726
88 2 10	0.2690	88 3 21	0.2705	88 5 2	0.2702	88 6 11	0.2738	88 7 21	0.2722
88 2 11	0.2688	88 3 22	0.2698	88 5 3	0.2701	88 6 12	0.2730	88 7 22	0.2720
88 2 12	0.2688	88 3 23	0.2689	88 5 4	0.2701	88 6 13	0.2717	88 7 23	0.2727
88 2 13	0.2688	88 3 24	0.2690	88 5 5	0.2706	88 6 14	0.2706	88 7 24	0.2733
88 2 14	0.2689	88 3 25	0.2690	88 5 6	0.2709	88 6 15	0.2705	88 7 25	0.2731
88 2 15	0.2694	88 3 26	0.2696	88 5 7	0.2712	88 6 16	0.2706	88 7 26	0.2737
88 2 16	0.2697*	88 3 27	0.2700	88 5 8	0.2716	88 6 17	0.2706	88 7 27	0.2745
88 2 17	0.2699	88 3 28	0.2707	88 5 9	0.2724	88 6 18	0.2707	88 7 28	0.2752
88 2 18	0.2701	88 3 29	0.2712	88 5 10	0.2727	88 6 19	0.2712	88 7 29	0.2759
88 2 19	0.2700	88 3 30	0.2715	88 5 11	0.2729	88 6 20	0.2713	88 7 30	0.2766
88 2 20	0.2699	88 3 31	0.2719	88 5 12	0.2723	88 6 21	0.2716	88 8 1	0.2768
88 2 21	0.2694	88 4 1	0.2717	88 5 13	0.2717	88 6 22	0.2720	88 8 2	0.2763
88 2 22	0.2688	88 4 2	0.2713	88 5 14	0.2709	88 6 23	0.2721	88 8 3	0.2756
88 2 23	0.2685	88 4 3	0.2708	88 5 15	0.2703	88 6 24	0.2720	88 8 4	0.2747
88 2 24	0.2682	88 4 4	0.2702	88 5 16	0.2699	88 6 25	0.2723	88 8 5	0.2737
88 2 25	0.2677	88 4 5	0.2695	88 5 17	0.2692	88 6 26	0.2727	88 8 6	0.2734
88 2 26	0.2677*	88 4 6	0.2684	88 5 18	0.2688	88 6 27	0.2729	88 8 7	0.2738
88 2 27	0.2673	88 4 7	0.2685	88 5 19	0.2685	88 6 28	0.2736	88 8 8	0.2742
88 2 28	0.2679	88 4 8	0.2695	88 5 20	0.2689	88 6 29	0.2742	88 8 9	0.2745
88 2 29	0.2687	88 4 9	0.2708	88 5 21	0.2693	88 6 30	0.2748	88 8 10	0.2741
88 3 1	0.2689	88 4 10	0.2720	88 5 22	0.2703	88 7 1	0.2750	88 8 11	0.2741
88 3 2	0.2691	88 4 11	0.2727	88 5 23	0.2709	88 7 2	0.2757	88 8 12	0.2738
88 3 3	0.2697	88 4 13	0.2737	88 5 24	0.2716	88 7 3	0.2760	88 8 13	0.2738
88 3 4	0.2697	88 4 14	0.2736	88 5 25	0.2718	88 7 4	0.2760	88 8 14	0.2735
88 3 5	0.2693	88 4 15	0.2737	88 5 26	0.2721	88 7 5	0.2757	88 8 15	0.2734
88 3 6	0.2691	88 4 16	0.2735	88 5 27	0.2724	88 7 6	0.2748	88 8 16	0.2730
88 3 7	0.2691	88 4 17	0.2735	88 5 28	0.2722	88 7 7	0.2737	88 8 17	0.2724
88 3 8	0.2689	88 4 18	0.2729	88 5 29	0.2724	88 7 8	0.2722	88 8 19	0.2711
88 3 9	0.2683	88 4 19	0.2719	88 5 30	0.2721	88 7 9	0.2711	88 8 20	0.2710
88 3 10	0.2680	88 4 20	0.2711	88 5 31	0.2725	88 7 10	0.2707	88 8 21	0.2711
88 3 11	0.2675	88 4 22	0.2708	88 6 1	0.2724	88 7 11	0.2710	88 8 22	0.2712
88 3 12	0.2681	88 4 23	0.2701	88 6 2	0.2726	88 7 12	0.2711	88 8 23	0.2720
88 3 13	0.2686	88 4 24	0.2700	88 6 3	0.2730	88 7 13	0.2716	88 8 24	0.2726
88 3 14	0.2690	88 4 25	0.2697	88 6 4	0.2735	88 7 14	0.2717	88 8 25	0.2742

Date	Value	Date	Value	Date	Value	Date	Value	Date	Value
88 8 25	0.2742	88 9 9	0.2731	88 11 18	0.2761	88 12 8	0.2756	88 12 26	0.2776
88 8 26	0.2751	88 9 10	0.2733	88 11 20	0.2744	88 12 9	0.2762	88 12 27	0.2779
88 8 27	0.2766	88 9 11	0.2731	88 11 21	0.2749	88 12 10	0.2769	88 12 28	0.2778
88 8 28	0.2776	88 9 12	0.2733	88 11 26	0.2735	88 12 11	0.2775	88 12 29	0.2778
88 8 29	0.2782	88 9 13	0.2731*	88 11 27	0.2737	88 12 12	0.2782	88 12 30	0.2777
88 8 30	0.2778	88 9 14	0.2726*	88 11 28	0.2744	88 12 13	0.2789	88 12 31	0.2764
88 8 31	0.2776	88 9 15	0.2723*	88 11 29	0.2746	88 12 14	0.2802		
88 9 1	0.2770	88 9 16	0.2717*	88 11 30	0.2752	88 12 15	0.2807		
88 9 2	0.2770	88 9 17	0.2720*	88 12 1	0.2760	88 12 16	0.2809		
88 9 3	0.2768	88 9 18	0.2731*	88 12 2	0.2760	88 12 17	0.2810		
88 9 4	0.2765	88 9 19	0.2723*	88 12 3	0.2753	88 12 20	0.2797		
88 9 5	0.2764	88 11 14	0.2759	88 12 4	0.2751	88 12 21	0.2786		
88 9 6	0.2755	88 11 15	0.2759	88 12 5	0.2754	88 12 22	0.2787		
88 9 7	0.2746	88 11 16	0.2762	88 12 6	0.2756	88 12 24	0.2782		
88 9 8	0.2734	88 11 17	0.2766	88 12 7	0.2757	88 12 25	0.2780		

TABLE A1-2. Dates of missing data.

July 9, 1986	July 19, 1987	Sept. 20 - Nov. 13, 1988
July 28, 1986	July 28, 1987	Nov. 19, 1988
July 30, 1986	Aug. 10, 1987	Nov. 22 - 25, 1988
Sept. 9, 1986	Aug. 31, 1987	Dec. 18 - 19, 1988
Dec. 30, 1986	Dec. 6, 1987	Dec. 23, 1988
Feb. 1, 1987	Jan. 27, 1988	
Feb. 24, 1987	Jan. 28, 1988	
June 26, 1987	Apr. 12, 1988	
July 11, 1987	Apr. 21, 1988	
July 12, 1987	Aug. 18, 1988	

APPENDIX II

Alternative Forms for R(MgIIc/w) for NIMBUS7 Data

Abstract

Two alternative forms of the Mg II core-to-wing ratio are compared with the ratio of arithmetic averages used by Heath and Schlesinger (1986), namely a ratio of geometric averages and a combination of arithmetic and geometric averages. The results are very similar except for a slight constant offset and a very small linear drift of the two new ratios relative to the original ratio. The small drift is suggested to be a consequence of a slight difference in the weak coupling or the aging of instrument sensitivity into the Mg II core-to-wing ratio.

1. Introduction

The core-to-wing ratio R(MgIIc/w) for the combined solar Mg II h and k lines that was developed by Heath and Schlesinger (1986) has several minor problems. For example, R(MgIIc/w) is a little weaker in 13-day periodicity than is the UV flux at most wavelengths in the 175-290 nm range because the Mg II h and k lines are from the middle chromosphere, rather than from the upper photosphere, and have a center-to-limb dependence of active-region emission that decreases less with increasing solar central angle. This is a problem when R(MgIIc/w) is used to estimate the temporal variations of UV fluxes at other wavelengths in the 175-290 nm range (with a simple linear regression relation) because the estimated values are too weak in 13-day periodicity. This can be overcome by using the UV flux measurements to determine their short-term variations and using R(MgIIc/w) to estimate their long-term variations.

The minor problem explored below is caused by the UV flux in the short-wavelength wing being lower in amplitude than in the long-wavelength wing. This causes quite a weak coupling of the wavelength dependent drift in instrument sensitivity, which will be demonstrated below. The analyses discussed below were conducted to explore alternative ways to derive the Mg II core-to-wing ratio to try to decrease this weak coupling.

2. Heath and Schlesinger's Mg II UV Index

Heath and Schlesinger (1986) defined the center-to-wing ratio for the Mg II h and k solar absorption lines (not resolved into two lines because the spectrometer bandwidth is too broad) by the following equation:

$$R0(MgII,t) = \frac{4[F(279.8\ nm,t) + F(280.0\ nm,t) + F(280.2\ nm,t)]}{3[F(276.6,t) + F(276.8,t) + F(283.2,t) + F(283.4,t)]} \qquad \text{(A2-1)}$$

where $F(\lambda,t)$ is the measured solar flux at wavelength λ and time t. We consider this ratio to be extremely important to measurements of solar UV flux variations. Since we consider three versions of R(MgIIc/w), the original version in (1) will be denoted here by $R0$. The numerator and denominator in (1) involve arithmetic averages of fluxes, so $R0$ is also called the arithmetic average core-to-wing ratio.

The numerator in (1) gives the flux at the center of the line, where it is lower than in the wings of the line, but the percent variation with solar activity is very high. The average of three flux values is used because this average is much less sensitive to the effects of any small jitter in the wavelength drive system, i. e. small fluctuations in wavelength locations from one spectral scan to another. The denominator includes an average of two fluxes in the far wing of the short-wavelength side and two fluxes in the long-wavelength wing, where their spacing in wavelength is symmetrical, about 280 nm and they are located at wavelengths of very low-percentage variation. See Section 6.2 of this report for figures showing the shape of the Mg II *h* and *k* lines.

3. Weak Coupling to Wavelength-Dependent Drifts in Instrument Sensitivity

*R*0 is insensitive to drifts in instrument sensitivity, slowly varying functions of wavelength over the 276.6−283.4 nm range, as demonstrated by the following: Let the measured flux values *Fm* be represented by the separated functions of the real solar flux $Fr(\lambda, t)$ and the instrumentation drift function $D((\lambda, t)$, where λ represents wavelength and $Fm = FrD$. As long as *D* is a weakly varying function of wavelength over the 276.6−283.4 nm range (possibly a large change with time), then the substitution of *FrD* values for the *Fm* values in equation (1) allows the factoring out of *D* in the numerator and denominator; this means that Heath's MgII ratio is an accurate measure of the true center-to-wing ratio.

If the wavelength dependence of *D* is not so small, then the drift has a weak affect on *R*0. Assume *D* is a nearly linear function of wavelength for the seven wavelengths involved over the 276.6−283.4 nm range, such as the following:

$$D(\lambda, t) = a\,(t)[1 + (\lambda - 280\ \text{nm})\, b(t)] \ . \qquad \text{(A2-2)}$$

Substituting (2) into (1) and canceling out the common factor $a(t)$ from each term in the numerator and denominator gives the following:

$$R(MgII) = \frac{Fc(t) + 0\,.\,2b[Fr(280\,.\,2,t) - \mathrm{Fr}(279.8,\mathrm{t})]/3}{Fw(t) + \{3.4b[Fr(283\,.\,4 - Fr(276\,.\,6+)] + 3\,.\,2b[Fr(283\,.\,2) - Fr(276\,.\,8)]\}/4} \qquad \text{(A2-3)}$$

where the real wavelength-averaged center-line flux *Fc* is given by

$$Fc(t) = [Fr(279.8,t) + Fr(280.0,t) + Fr(280.2,t)]/3 \quad , \qquad \text{(A2-4)}$$

and the real wavelength-averaged wing flux *Fw* is given by

$$Fw(t) = [Fr(276.6,t) + Fr(276.8) + Fr(283.2,t) + Fr(283.4,t)]/4 \ . \qquad \text{(A2-5)}$$

Since $Fr(280.2) \simeq Fr(279.8)$ and *b* is much smaller than unity for these wavelengths, then the terms in the numerator other than *Fc* are negligible. From Section 6.2 of this report, one can see that the fluxes in the short-wavelength wing are roughly twenty percent lower than those in the long-wavelength wing, so the remaining terms in the denominator other than *Fw* do not cancel to zero. However, considering that *b* is small relative to unity and there are two subtractions, these residual drift terms are small relative to *Fw*. Consequently, *R*(MgII) is fairly insensitive to instrumentation drift, including drifts that are nearly linear functions of wavelength

within the 276.6−283.4 nm range. If the short-wavelength wing had flux intensities equal those in the long-wavelength wing, $R0$ would be completely insensitive to instrument drifts with a linear wavelength dependence; however, because the flux intensity in the short-wavelength wing is distinctly lower than in the long-wavelength wing, a weak coupling of the wavelength dependence of the instrument drift into $R0$ occurs. Can we modify the way the ratio is taken, so as to maintain its strong measure of solar variability and yet further reduce this weak coupling?

4. Alternative Core-to-Wing Ratios for the Mg II *h* and *k* Lines

Two other ratios were examined; the first is labeled $R1$. It differs from (1) in the denominator by using a combination of arithmetic averages for the two fluxes in the short-wavelength wing and similarly an arithmetic average for the two fluxes in the long-wavelength wing, but a geometric average is then used for these two averages.

$$R1(MgII,t) = \frac{2[(279.8\ nm,t) + F(280.0\ nm,t) + F(280.2\ nm,t)}{3\{[F(276.6,t) + F(276.8,t)] \times [F(283.2t) + F(283.4,t)]\}^{1/2}} \quad \text{(A2-6)}$$

The second new ratio, R2, involves all geometric averages as follows:

$$R2(MgII,t) = \frac{[F(279.8\ nm,t) \times F(280.0\ nm,t) \times F(280.2\ nm,t)]^{1/3}}{[F(276.6,t) \times F(276.8,t) \times F(283.2,t) \times F(283.4,t)]^{1/4}} \quad \text{(A2-7)}$$

Because $R0$ varies by only about 10% over a whole solar cycle, we expect from perturbation theory that the results for $R0$, $R1$ and $R2$ will be very similar.

5. Comparison of Observational Results

Figures A2-1 through A2-4 show daily values for all three ratios for 1979−1982. Straight lines are used to connect the results on consecutive days; gaps in the line indicate missing days. The three ratios are nearly the same; the differences in ordinate scales indicate that $R1$ and $R2$ are nearly identical and both are about 1% higher than $R0$. This is a consequence of the short−wavelength wing being smaller than the long-wavelength wing and the arithmetic mean being slightly higher than the geometric mean. For example, if the intensity of the short-wavelength wing were 75% (See Section 6.2.2) of that in the long-wavelength wing, the arithmetic average would be 0.875 and the geometric average would be 0.866 which is about 1% lower and produces a ratio about 1% higher than for $R0$. Figure A2-5 shows the three functions with a combined time scale; again the results appear to be identical except for the 1% offset.

Figure A2-6 shows the ratios $R1/R0$, $R2/R0$ and $R1/R2$, which in effect removes the common solar signal and magnifies the differences. In the bottom graph, the range between the two scale numbers given is extremely small, 10^{-4}. If the solar cycle minimum-to-maximum increase in R(MgIIc/w) is of the order of 10%, then most of the variations in the bottom graph are smaller than 0.1% of the signal being measured, and can therefore be neglected. The top two graphs are nearly identical. The short-term noise in these top two graphs is also small enough (±0.1% of solar cycle signal) that it can be neglected as well.

The most important result in Figure A2-6 is the linear, long-term upward drift in the top two figures. This is a difference of about 0.001 in 7 years and is equivalent to 1% of the solar cycle

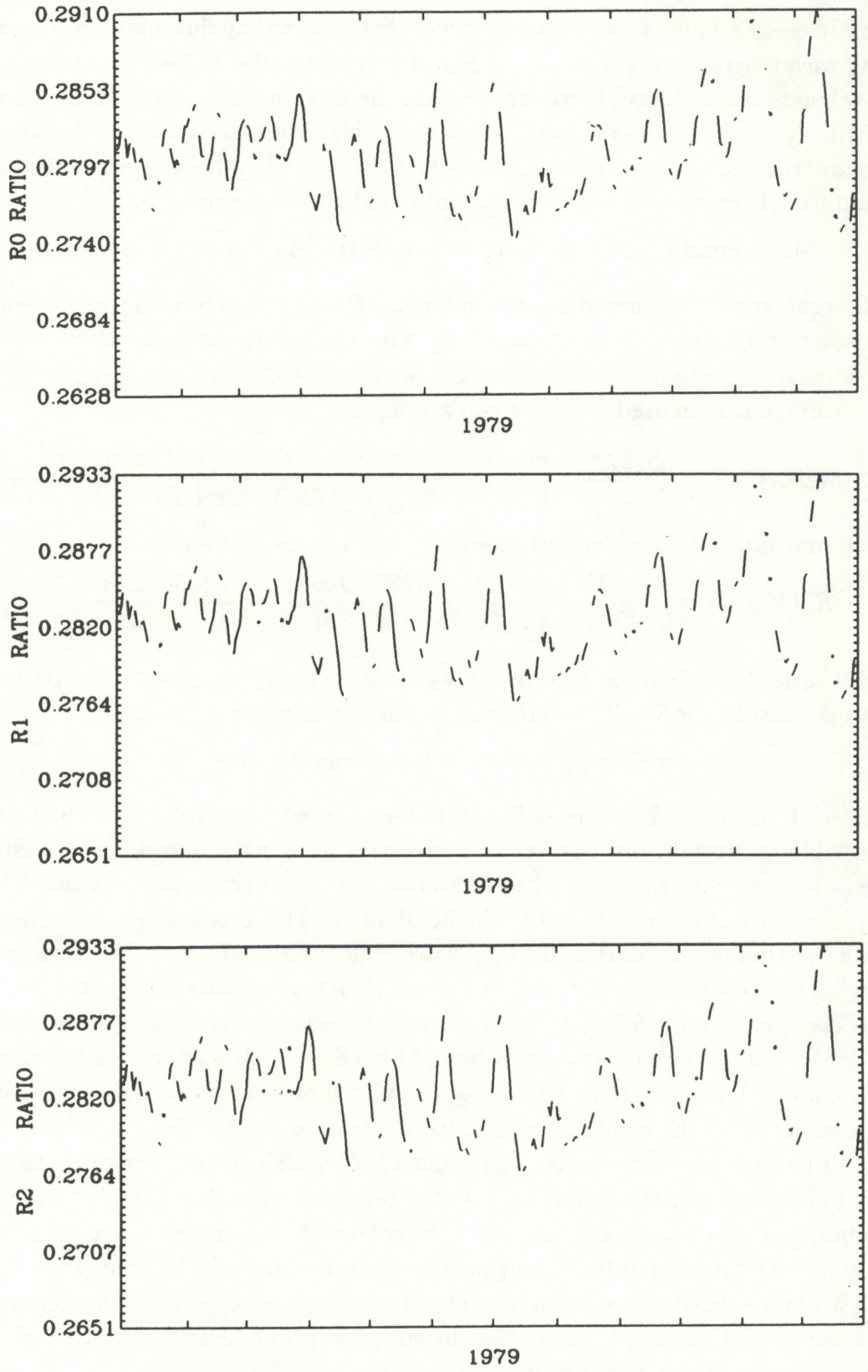

Figure A2-1. The original and two test ratios for 1979 based on measurements from the SBUV instrument on the NIMBUS7 satellite (Heath, 1980).

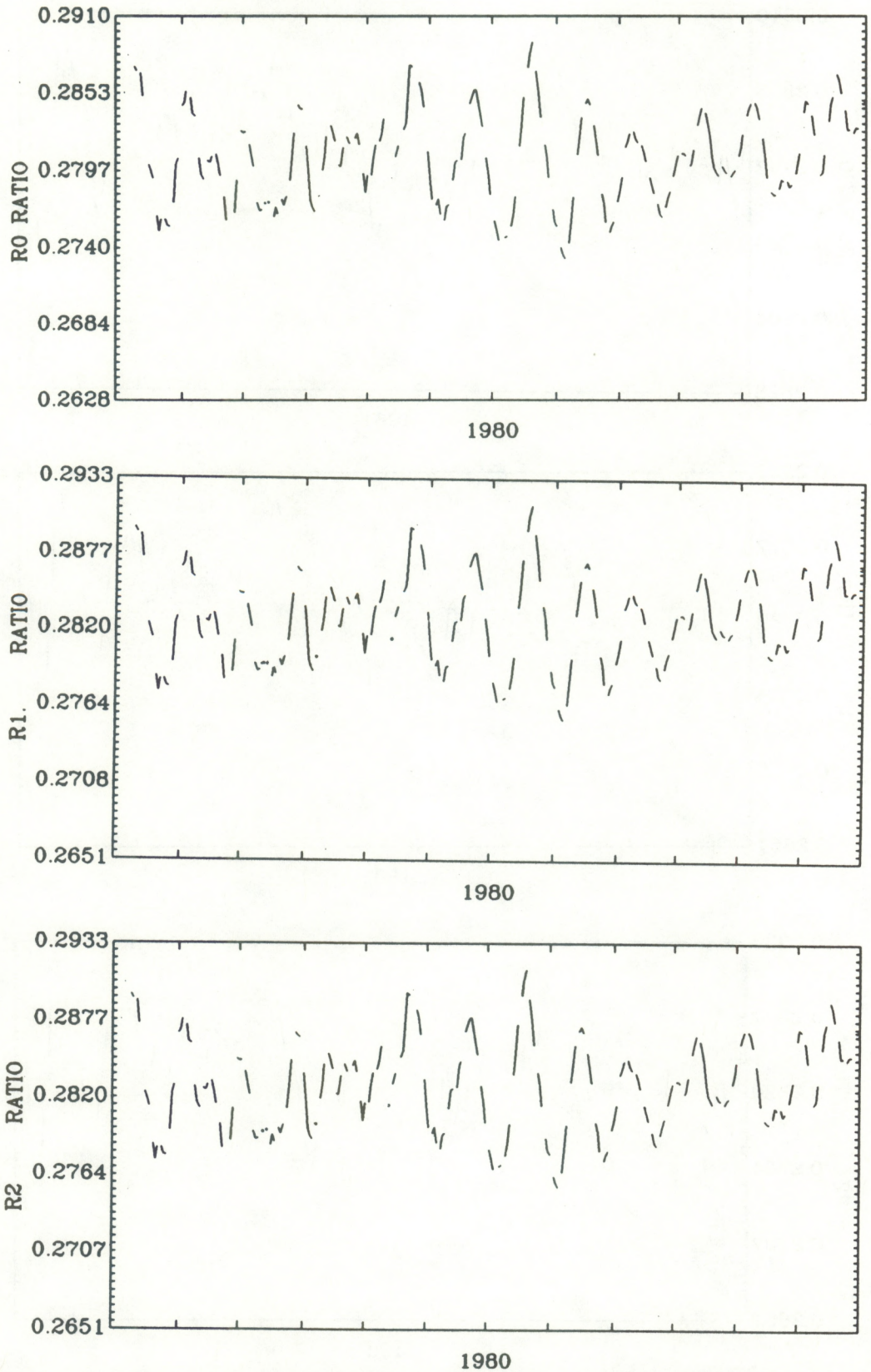

Figure A2-2. *R*0, *R*1 and *R*2 as a function of time for 1980, based on NIMBUS7 data. Lines connect results only on consecutive days.

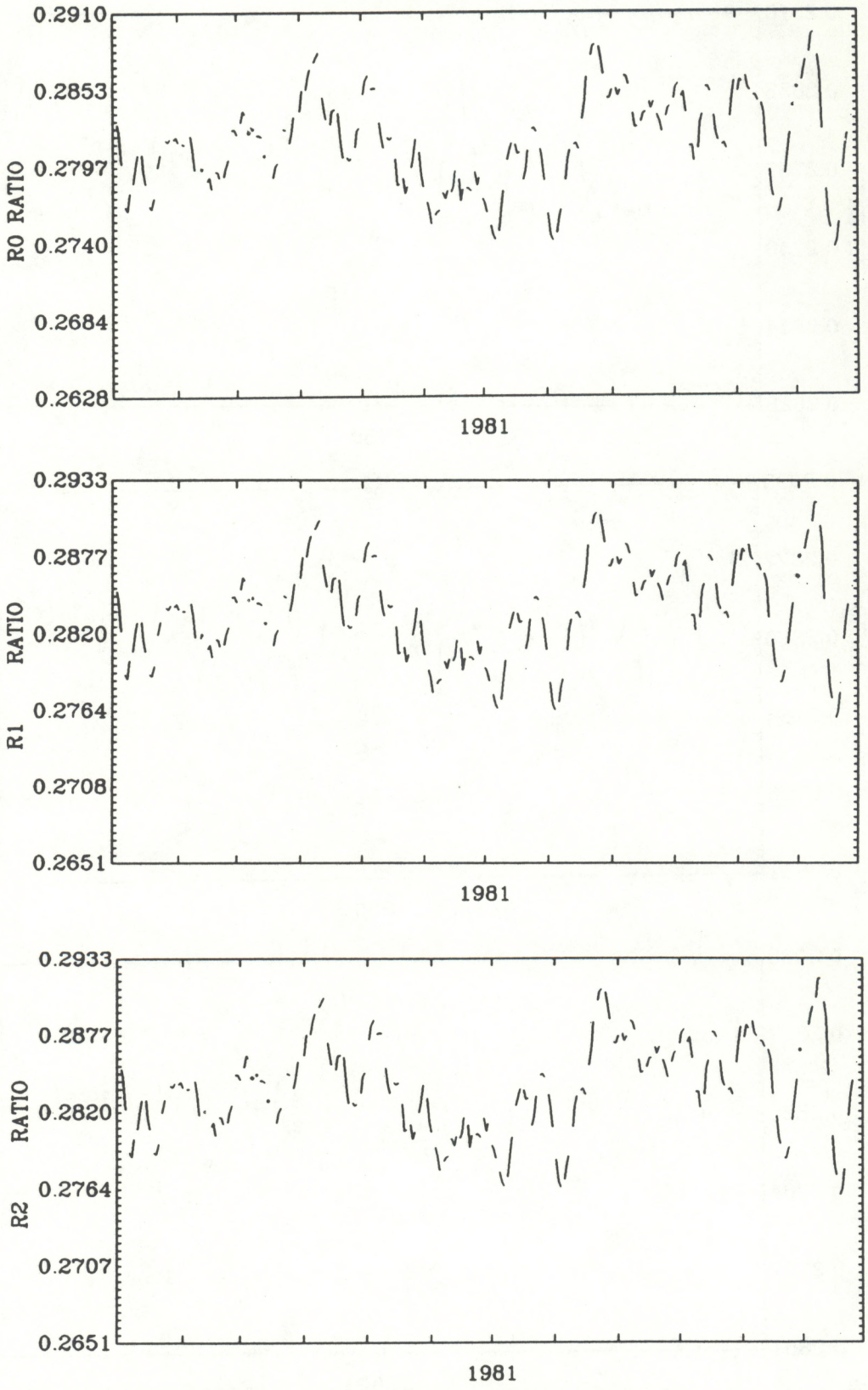

Figure A2−3. The arithmetic ratio *R*0, the combination-average ratio *R*1, and the geometric average *R*2 versus time for 1981, for NIMBUS7 data.

signal. This minor problem is not completely negligible but certainly not large enough to warrant aggresive pursuit.

6. Discussion

The solar signals in Figures A2-1through A2-5 look alike for the three forms of the ratio, as well they should. Those results should not be highly sensitive to the way the averaging is conducted, but should be dominated by the strong solar signal in the numerator's core wavelength terms. All three ratios are insensitive to drifts in instrument sensitivity if those drifts are weak functions of wavelength in the 276.6−283.4 nm range. The minor problem being considered here involves drifts in instrumentation that are not weak functions of wavelength. Whatever the cause of the long-term trend in Figure A2-6, it suggests an error in *R*0 (or *R*1 and *R*2) that increases in magnitude with time (either a decrease for *R*0 or an increase for *R*1 and *R*2 or some combination of the two) to roughly 0.12 % in 8 years (about 1% of the solar cycle amplitude in *R*0).

Our *R*(MgII*c*/*w*) values do not include any correction for a nearly linear but quite small increase in wavelength of the instrument's wavelength steps of about 0.3 Å near 280 nm in 8 years of observations reported by Schlesinger et al. (1988). According to Section 6.2.3 of this report, such a wavelength error would cause our 1986 values of *R*0 to be about 0.16% too large, a little larger in magnitude and **opposite in sign** (considering that *R*0 is in the denominator) relative to the long-term drift in the top graphs of Figure A2-6, (about 0.12% in 8 years). Furthermore, these same wavelength drifts would induce increases in *R*1 and *R*2 similar to those in *R*0, which would then produce little or no drift in their ratios. In summary, although there must be a small drift in *R*0 caused by a small drift in the wavelength positions of the spectrometer, it is not the main cause of the trend in *R*1/*R*0 or *R*2/*R*0.

Since *R*1 and *R*2 are nearly identical, the main effect must be caused by the difference in using either an arithmetic or geometric average of the long- and short-wavelength wings. Therefore, to simplify the analysis, consider one "average" flux measurement in the core of the combined lines called *Fc*; one in the long-wavelength wing, *Flw;* and one in the short-wavelength wing, *Fsw*; wavelength spacing *W* is equal. Then (1) reduces to the following:

$$R0 = \frac{2Fc}{Flw + Fsw} \tag{A2-8}$$

and both *R*1 and *R*2 reduce to the common form:

$$R1 = R2 = \frac{Fc}{[Flw \times Fsw]^{1/2}} \tag{A2-9}$$

Again, assuming an instrument drift with a linear wavelength dependence as in (2), using a subscript *r* to denote the real solar fluxes and equations (8) and (9) for the measured fluxes gives the following:

$$R0 = \frac{2Fcr}{Flw_r + Fsw_r + bW[Flw_r - Fswr]} \tag{A2-10}$$

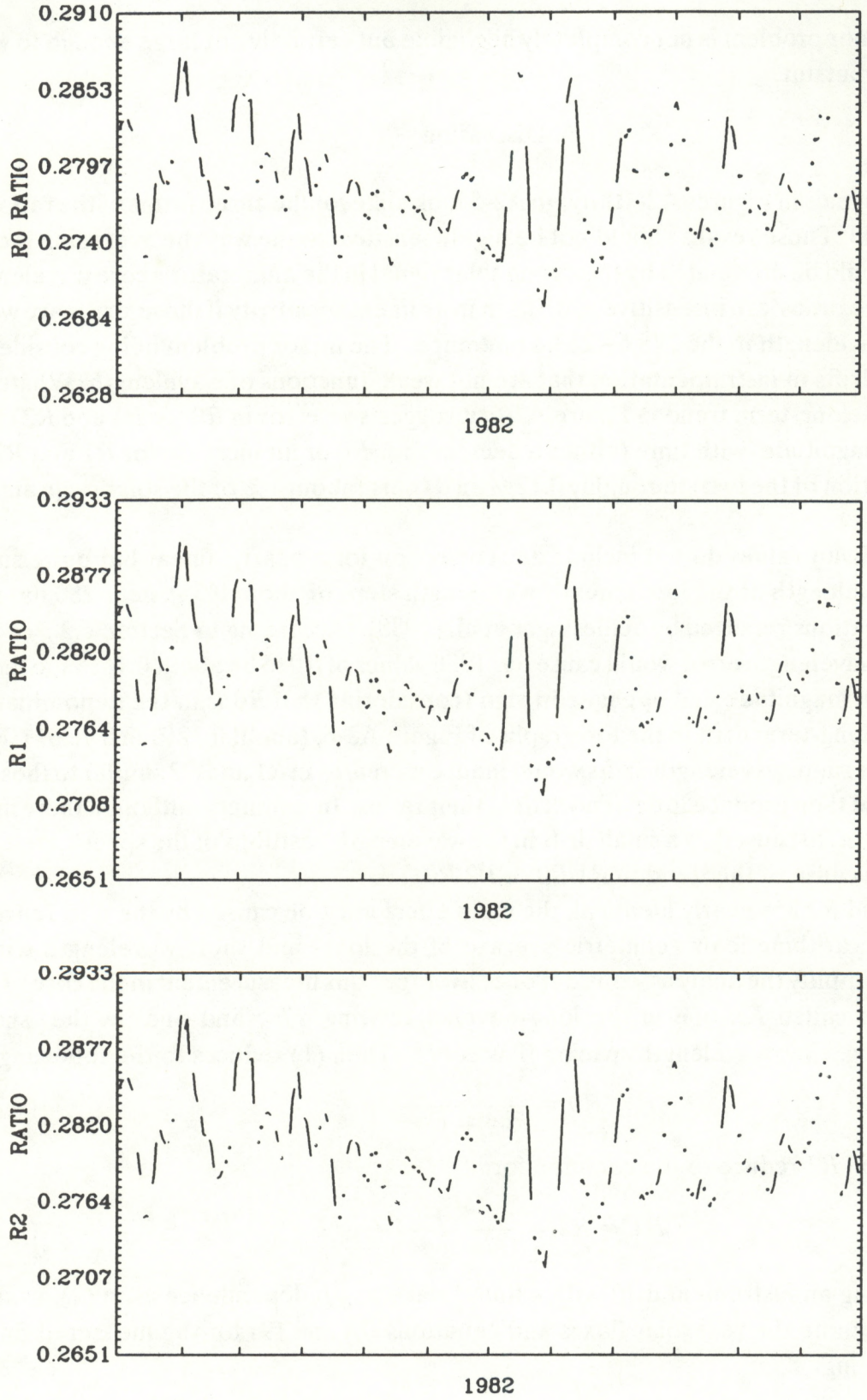

Figure A2-4. *R*0(t), *R*1(*t*) and *R*(*t*) for 1982, based on NIMBUS7 data. Connecting lines are used only for consecutive days; gaps and isolated data points indicate adjacent days when data are missing.

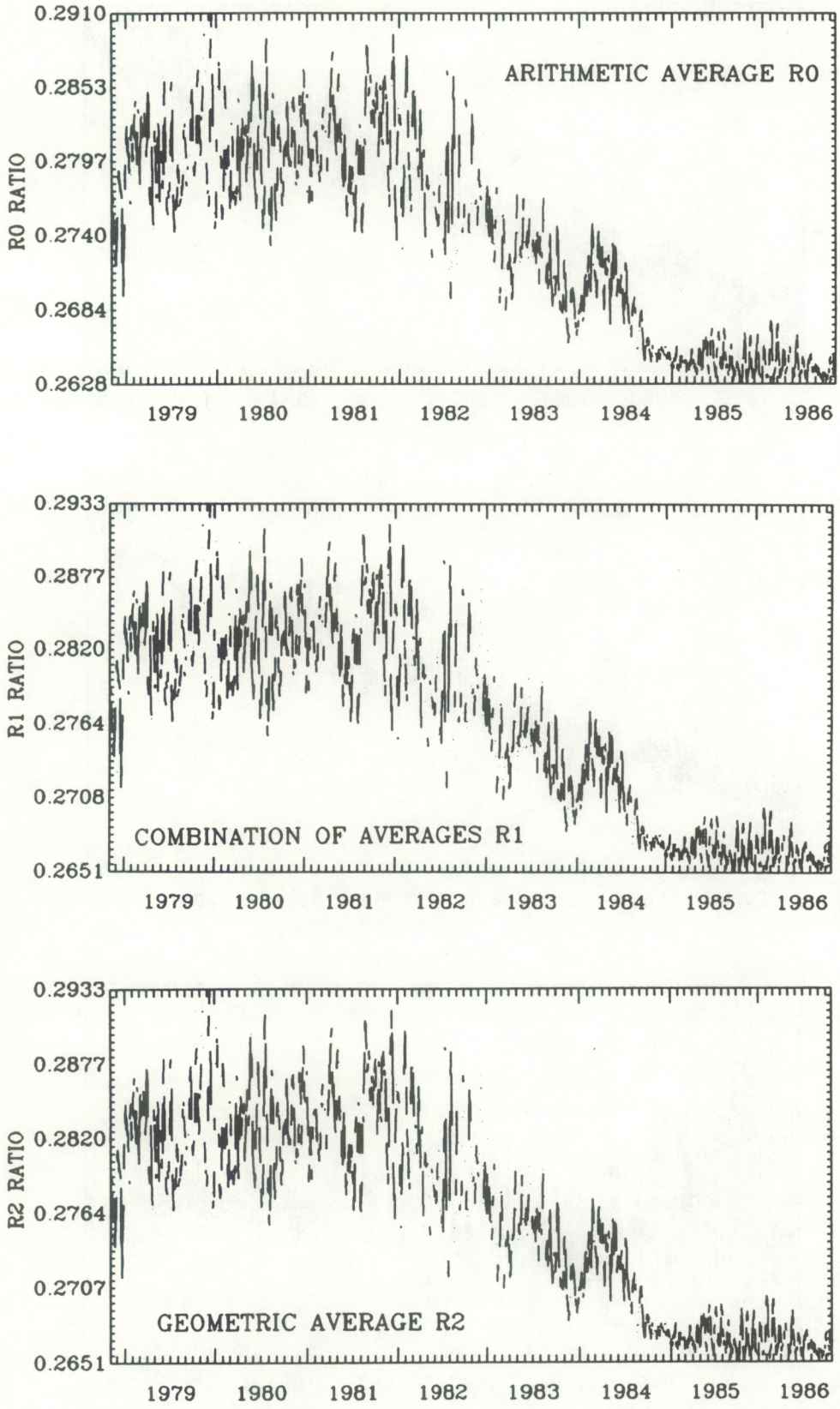

Figure A2-5. *R*0, *R*1 and *R*2 as a function of time for November 1978–September 1986, based on NIMBUS7 data (Heath and Schlesinger, 1986).

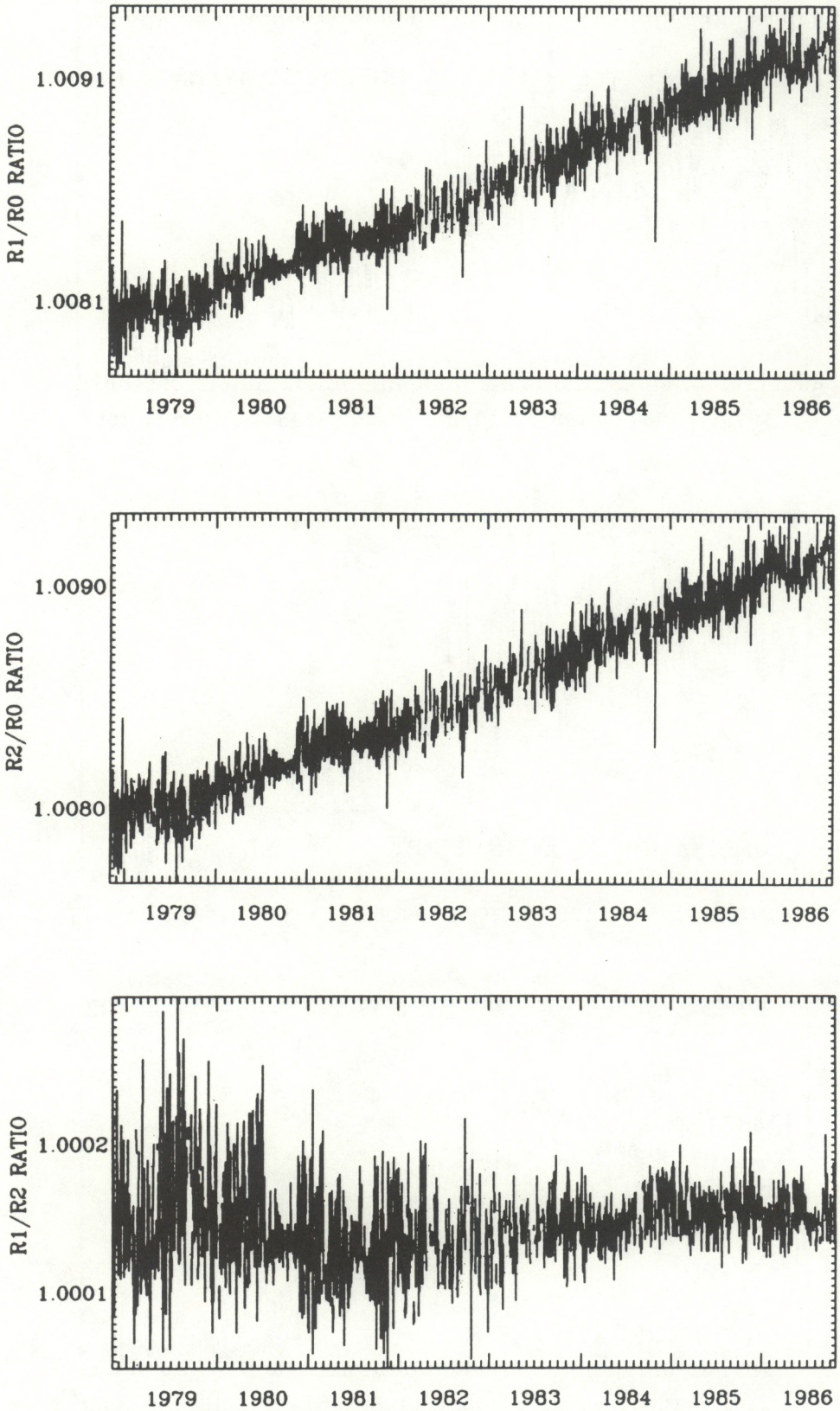

Figure A2-6. Ratios *R*1/*R*0, *R*2/*R*0 and *R*1/*R*2 versus time. Note that the ratio scale range on the bottom figure is extremely small and the range of the long-term linear trend in the top two graphs is fairly small.

Assuming that the last term in the denominator is small compared to the first two, expanding in a series and neglecting higher than first order terms gives:

$$R0 \simeq R0'\left\{1 - bW\frac{[Flwr - Fswr]}{[Flwr + Fswr]}\right\} \qquad \text{(A2-11)}$$

where $R0'$ is the value of (8) when $b=0$. For $Fsw=0.75\ Flw$, this last term simplifies to $bW/7$, where W is about 3.4 nm. Similarly, (9) gives

$$R1 \simeq R1'\left\{1 - 1/2[bW]^2\right\} \qquad \text{(A2-12)}$$

which means the first-order terms have dropped out and the first correction is a second-order term. As long as bW is much smaller than 1/7, then the drift term in (12) is smaller than in (11). Based on Figure 2.8 of Schlesinger et al. (1988), b near 280 nm is probably about 0.001. This implies that the drift in $R1$ would be about 1 % of that in $R0$ for a drift with a linear wavelength dependence in the 276.6−283.4 nm range. In conclusion, there appears to be a minor advantage in using either $R1$ or $R2$ rather than $R0$ decreasing the influence of $Fsw=0.75\ Flw$ and its consequent weak coupling to wavelength dependent drift.

APPENDIX III

The Dependence of the 10.7-cm Solar Flux on both Plage and Sunspots

Abstract

The temporal variations of the 10.7-cm solar radio flux (F10) are better fit by a linear regression with respect to two variables, the Ca-K plage index, P, and the net projected sunspot area, S_A, than by either variable alone; coefficients range from 0.89 for solar cycle 21 to 0.96 for cycle 19. Adding the S_A term may provide improvement through better representation of the gyroresonance emission component of F10. Variations among the linear equation coefficients from one cycle to another are large enough that the accuracy of predicting F10(t) from $S_A(t)$ and P(t) is much lower than suggested by the high correlation coefficients.

1. Introduction

Oster (1983) concluded that the temporal variations of the full-disk solar 10.7-cm flux (F10) could be well explained using the temporal variations of Ca-K plage data. At that time, we were studying some of the systematic differences between temporal variations of F10 and solar UV flux measurements (Donnelly et al., 1983); we considered the latter to be closely related to the Ca-K plage data (Lean et al., 1982). The short-term variations (days, weeks) of F10 are more like those of the coronal EUV lines of Fe XV at 28.4 nm, and Fe XVI at 33.5 nm, than like chromospheric EUV or UV emissions. For example, during episodes of strong 27-day variations caused by a major group of active regions, F10 tended to rise more quickly, peak earlier, and decay faster than the chromospheric EUV fluxes (Donnelly et al., 1986). Solar radio astronomy with high spatial resolution has shown that gyroresonance emission is important at centimeter wavelengths (Marsh and Hurford, 1982), as is thermal bremsstrahlung emission. Gyroresonance emission depends on the strong magnetic fields of sunspots and was suspected as a contributor to the faster rise, earlier peak and faster decay of F10 during episodes of major activity. Sunspots also peak and decay faster than the associated plages. This gyroresonance component may be roughly proportional to S_A, the net projected sunspot area summed over the visible disk.

Since solar soft X-rays also rose, peaked, and decayed quickly during these episodes of major activity, in comparison to the solar UV flux measurements, we concluded that the hot coronal emission measure from the sum of all coronal loops and flux tubes over the visible disk and limb corona also rose and decayed similarly. Perhaps part of the 10.7-cm emission comes from thermal bremsstrahlung from the corona as well as from the chromosphere, where the coronal component may behave differently than the chromospheric component. In this case, the strong magnetic fields of sunspots contribute to the closed emerging dense magnetic flux loops with high coronal emission measure, by containing the plasma. So this second possible source of F10(t) differing from the chromospheric EUV fluxes may also be proportional to S_A through a structural link to the coronal loops.

On the other hand, Rybansky et al. (1988) showed that the coronal green line ($T \geq 2\times10^6$ K) has a solar cycle dependence with a much higher peak in late 1981, relative to the level in late 1979, than in the case of F10. Similarly, Wagner (1988) showed that coronal 1–8 Å soft X-ray flux ($T \geq 3\times10^6$ K) was much higher in late 1981 than it had been in late 1979. These results suggest that coronal bremsstrahlung at $T \geq 2\times10^6$ can't be a major contributor to the 10.7-cm full-disk flux or F10 would have a solar cycle dependence somewhere between that for the chromospheric Mg II core-to-wing ratio (or the Ca-K index, or the He I 1083 nm equivalent width) and the coronal green line or 1–8 Å flux. This reduces potential contributors to either thermal bremsstrahlung from the corona below 2×10^6 K and the transition region (in addition to chromospheric thermal bremsstrahlung) or gyroresonance emission. Harvey's (1989) full-disk magnetic flux intensity index has a solar cycle dependence much like that for F10, which means that the gyroresonance component does not conflict with the solar cycle shape of F10.

The following analysis was conducted in early 1987, before the conclusions in this paragraph were made.

2. Linear Regression Analysis for Two Variables

Two mechanisms in which F10(t) may differ from chromospheric EUV and UV fluxes:

(1) Gyroresonance emission related to the strong fields of sunspots.

(2) Thermal bremsstrahlung from above the chromosphere.

Both were assumed to be approximately proportional to S_A. Chromospheric emission was assumed to be proportional to P. The question was whether linear regression analysis with respect to the two variables, P and S_A, gave a much better fit to F10(t) than did either variable alone. The equations considered were the following:

$$F'(t) = a + bP(t) + cS_A(t) \quad , \tag{1}$$

$$F'(t) = d + fS_A(T) \quad , \tag{2}$$

and

$$F'(t) = g + hP(t) \quad , \tag{3}$$

where $F'(t)$ are the linear-regression's best fit values for F10. Since S_A and P are themselves correlated, linear regression analysis was conducted to determine the portion of S_A that was correlated to P, namely

$$S_A(t)Predicted = A + B{:}P(t) \quad . \tag{4}$$

The uncorrelated portion of $S_A(U)$ was computed from (4)

$$U_A(t) = S_A(t) - S_A(t)Predicted \quad ,$$

and the linear relation was derived for

$$F10(t) = C + D{:}P(t) + E{:}U(t) \quad . \tag{5}$$

These equations were evaluated for the four data sets of daily values listed in Table A3-1. Each of these data sets starts on the first day of the initial year and ends on the last day of the final year.

3. Discussion

The correlation coefficients are distinctly higher for the two-variable equations (1) or (5) than for the single-variable equations, which is what we expected. This does not prove that F10 has a strong gyroresonance component (or transition region and cool coronal component) in addition to a chromospheric component, or that S_A is representative of the former while P is representative of the latter; that is still speculative. A better fit may be achieved simply because more parameters are being considered. F10 has correlated highly with other solar parameters, but values as high as 0.96 have involved annually smoothed data and values above 0.9 usually involve at least 81-day averages. The results in Table A3-1 involve daily values; those for cycles 19 and 20 involve whole cycles and the results for cycles 18 and 21 involve most of those cycles.

The correlations of F10 with respect to S_A are higher than those with respect to P in three out of four data sets (equations (2) and (3)). Note that the correlation of S_A and P (equation (4)) are the lowest in Table A3-1, (much lower than for the other four equations), which means that 30% to 57% of the variance in S_A cannot be explained by a linear relation with P. The variation in coefficients from one data set to another is quite large, much larger than the linear regression's standard deviations for the estimated equation coefficients; this is especially true for P. Therefore, the plage data may be inhomogeneous in quality, and the physical relation between $F10(t)$, $S_A(t)$ and $P(t)$ may not be as simple as is suggested by the high correlation coefficients and our introductory discussion of the possible physical links.

4. Postscript

The above analysis was conducted in 1987. Recently, Oster (1990) studied the 10.7-cm flux enhancement above the quiet-Sun background from individual active regions. He discovered that the 10.7-cm active-region flux was better correlated with the associated sunspot area ($t = 0.93$) than with the active region's plage area ($r = 0.84$), where the combination of plages and sunspot area in a two-variable regression gave $r = 0.96$. The above results are full-disk equivalents of Oster's studies of individual active regions. Gelfreikh (1990) showed that non-thermal emission near sunspots contributes significantly to the 11-cm solar radio flux of active regions, so the physical link between sunspots and F10 may be more complicated than simply the dependence of gyroresonance radio emission on magnetic field strength.

5. References

Gelfreikh, G. B., Inner corona from solar radio observations, to be published in *Advances of Space Res.*, the Proc. of COSPAR Symp. 9 on Space Observations of the solar Corona and Origin of the Solar Wind, held June 27–29, 1990, in The Hague, Netherlands.

Oster, L., Reconstructing the emission at 10.7-cm from individual active regions in terms of optical data, *J. Geophys. Res.*, **95**, A5, 6247–6262, 1990.

TABLE A3–1. Linear Regression Analysis Results

Solar Cycle Number:		18	19	20	21
Years in Data Set:		1942–1954	1955–1964	1965–1975	1976–1983
Equation Number	Equation Coefficient				
(1)	a	79.69	70.70	73.14	89.73
	b	0.2410	0.8158	0.9668	1.041
	c	0.02877	0.02519	0.01877	0.02877
	r	0.945	0.960	0.953	0.893
(2)	d	84.18	83.01	84.49	109.64
	f	0.03990	0.04108	0.03574	0.04484
	r	0.899	0.930	0.885	0.825
(3)	g	97.73	68.59	73.11	95.07
	h	0.5076	1.709	1.597	1.840
	r	0.807	0.907	0.905	0.798
(4)	A	627.2	–83.81	–1.40	185.54
	B	9.265	35.47	33.56	27.77
	r	0.654	0.831	0.767	0.655
(5)*	C	97.73	68.59	73.11	95.07
	D	0.5076	1.709	1.597	1.840
	E	0.02877	0.02519	0.01877	0.02877
	r	0.945	0.960	0.953	0.893

* Note that the results for (5) are related to those in (1)–(4), where $C = a + A{:}E$, $D = b + B{:}E$, and $E = c$ and r for (5) $= r$ for (1). A linear transformation of one of the variables does not change r.

APPENDIX IV

13-Day Periodicity of the Aluminum Edge Ratio

Richard F. Donnelly and David E. Stevens

Abstract

The ratio of power in 13-day periodicity to that at 27 days usually is distinctly higher for the Al I ratio than for the UV flux measurements at any wavelength in the 160-300 nm range. This strong 13-day periodicity occurs because the Al I edge ratio is sensitive to the 13-day solar signal's slightly weaker amplitude, relative to the 27-day signal, at wavelengths longer than that of the Al I edge than at wavelengths shorter than the edge. Consequently, although the Al I edge ratio may be less sensitive to the effects of long-term drifts in instrument sensitivity than are the UV flux measurements, it overemphasizes the 13-day periodicity relative to that in the solar UV flux. Changing the key wavelengths selected by Heath and Schlesinger for the Al I edge ratio does not remove this amplifying effect for the 13-day periodicity, but moderate improvements can be made.

1. Introduction

Power spectra of the NIMBUS 7 solar UV flux measurements have a strong peak at periods in the 27–28 day range and also a second strong peak at periods in the 13–14 day range. Ratios of the peak power in the 13-day line to that in the 27-day line, called $P13/P27$ below, were studied (Donnelly et al., 1987) in UV measurements from the NIMBUS 7 satellite, as a function of wavelength in the 160-400 nm wavelength range for several different 2-year intervals. The variations in magnitude of $P13/P27$ from one 2-year interval to another depended on the episodes of strong 13-day or 27-day periodicity occurring in each interval, but the relative wavelength dependence of this ratio was quite similar from case to case. $P13/P27$ ratios were fairly constant in the 175–260 nm range, but the ratios in the 190–210 nm range tended to be a little higher than those in the 210–235 nm range. $P13/P27$ was, on average, about 17% higher for 205–210 nm than for 210-215 nm. In Figures 5.3–5.10 in Donnelly et al. (1987), $P13/P27$ for the Al I edge ratio [R(AlI)] was always higher than the corresponding ratio for the 210–215 nm range (about 69% higher on average). This anomalous behavior is significant because if R(AlI) is used with a simple linear regression relation to estimate the solar flux at nearby wavelengths, the 13-day periodicity in the flux will be overestimated.

2. Al I Edge Ratio

There is a rapid change in solar variability over a short change in wavelength at the Al I absorption edge near 208 nm. Ratios of the flux at wavelengths just shortward of the Al I edge to the flux at wavelengths just longward of the edge are used to obtain a relative measure of solar variability that is less sensitive to the drifts in instrument sensitivity that are slowly varying functions of wavelength in the small wavelength range involved in the ratio. Heath and Schlesinger (1986) defined their Al I edge ratio as follows:

$$R(A1I,t) = B(t)\left[\frac{F(208.6,t) + F(208.8,t) + F(209.0,t)}{F(211.2,t) + F(211.4,t) + F(211.6,t)}\right] . \qquad \text{(A4-1)}$$

this is primarily a ratio of an average of flux at three wavelengths at the short wavelength side of the edge to a similar average from the long-wavelength side. The corresponding terms in the numerator and denominator are 2.6 nm apart in wavelength. The B term attempts to correct for the wavelength dependence of the instrumentation drift function over this 2.6 nm interval by taking the average of two similar ratios with wavelength separations of 2.6 nm as follows:

$$B(t) = 2/\left[\frac{F(203.4,t) + F(203.6,t) + F(203.8,t)}{(F(206.0,t) + F(206.2,t) + F(206.4,6)} + \frac{F(213.8,t) + F(214.0,t) + F(214.2,t)}{F(216.4,t) + F(216.6,t) + F(216.8,t)}\right],$$

where the percent variation due to solar activity is essentially the same in the numerator as that in the denominator for each fraction in B. Any flux measurement includes a small amount of random noise; so considering that R(AlI) involves 18 flux measurements, we should expect R(AlI) to have a higher random noise content. On the basis of 27-day solar rotational variations, the solar signal percentage variation at 208.8 nm is only about 65% higher than that at 211.4 nm; so the solar signal in R(AlI) is significantly weaker than in the flux measurement at 208.8 nm. Consequently, the ratio of solar signal to random observational noise would be expected to be much poorer in R(AlI) than in the core-to-wing ratio for the Mg II h and k lines R(MgIIc/w). We also expect a more frequent occurrence of noise spikes, with respect to time, in the Al I edge ratio than in the Mg II center-to-wing ratio. Indeed, Heath and Schlesinger (1986) found the residuals, obtained by subtracting the values estimated from R(MgIIc/w) from the observed Al I edge ratio, to be rich in short-term noise. The following analyses examine whether simple modifications to R(AlI) can reduce its overestimation of 13-day periodicity from the solar signal, where short-term noise complicates the results.

3. Alternative Aluminum Edge Ratios

The 13-day periodicity in R(AlI) comes mainly from flux measurements near 208.8 nm and those near 211.4 nm. The main question examined was whether the choice of these two particular wavelengths contributed to the overemphasis of 13-day periodicity. Figure A4-1 shows the location of the wavelengths in equation (1) and (2) relative to the aluminum absorption edge. In the bottom graph of Figure A4-1, these wavelengths are shown in relation to the NIMBUS7 SBUV flux measurements of Heath (1980). In the top graph the wavelengths used in the A1I ratio are shown relative to the wavelength dependence of the 27-day fractional variations derived from an average of the eight solar rotational variations discussed in Chapter 2 of Heath, Repoff, and Donnelly (1984). The R_n and R_d arrows indicate the wavelengths of the main terms that produce the solar variation signal in R(AlI); i.e., they are the numerator and denominator in (1). The B arrows in Figure A4-1 mark the wavelengths of the numerator and denominator terms within the braces of (2). Figure A4-1 suggests that the wavelengths used in R(AlI) may not be the best choices; for example, moving them several tenths of a nm to shorter wavelengths should produce a slight increase in the solar signal amplitude because of the higher signal at R_n.

The B term in (2) has a weak solar signal and is used to correct for any linear wavelength dependence in the long-term drift in instrument sensitivity. For the current analysis problem, where we are trying to reduce the sensitivity of R(AlI) to 13-day solar variations, we are not concerned with long-term instrumentation drifts. Therefore, we neglect the B term in (1) in our analyses of short-term variations below.

Alternative ratios for the aluminum absorption edge were computed as follows:

$$R_{A1I}(\lambda_1,t) = \frac{F(\lambda_1,t)}{F(\lambda_2,t)} \quad , \qquad \text{(A-3)}$$

where $\lambda_1 = 209.4 - 0.2n$ and $\lambda_2 = 211 + 0.2n$ nm, for $n = 0, 1, 2, \ldots 24$. So $\lambda_2 = \lambda_1 + 1.6 + 0.4n$. In other words, the short wavelength in the numerator and the long wavelength in the denominator were equally spaced with respect to 210.2 nm (which is near the central wavelength in (1)) they moved away from each other, by 0.2 nm steps, from a separation of 0.6 nm up to 11.2 nm. For each of these 25 wavelength pairs, the time series R_{AlI} was computed from the NIMBUS7 observations for two intervals, each of 2 year duration. Long-term trends were removed, autocorrelations were computed, and power spectra were estimated, using the techniques described by Lean and Repoff (1987).

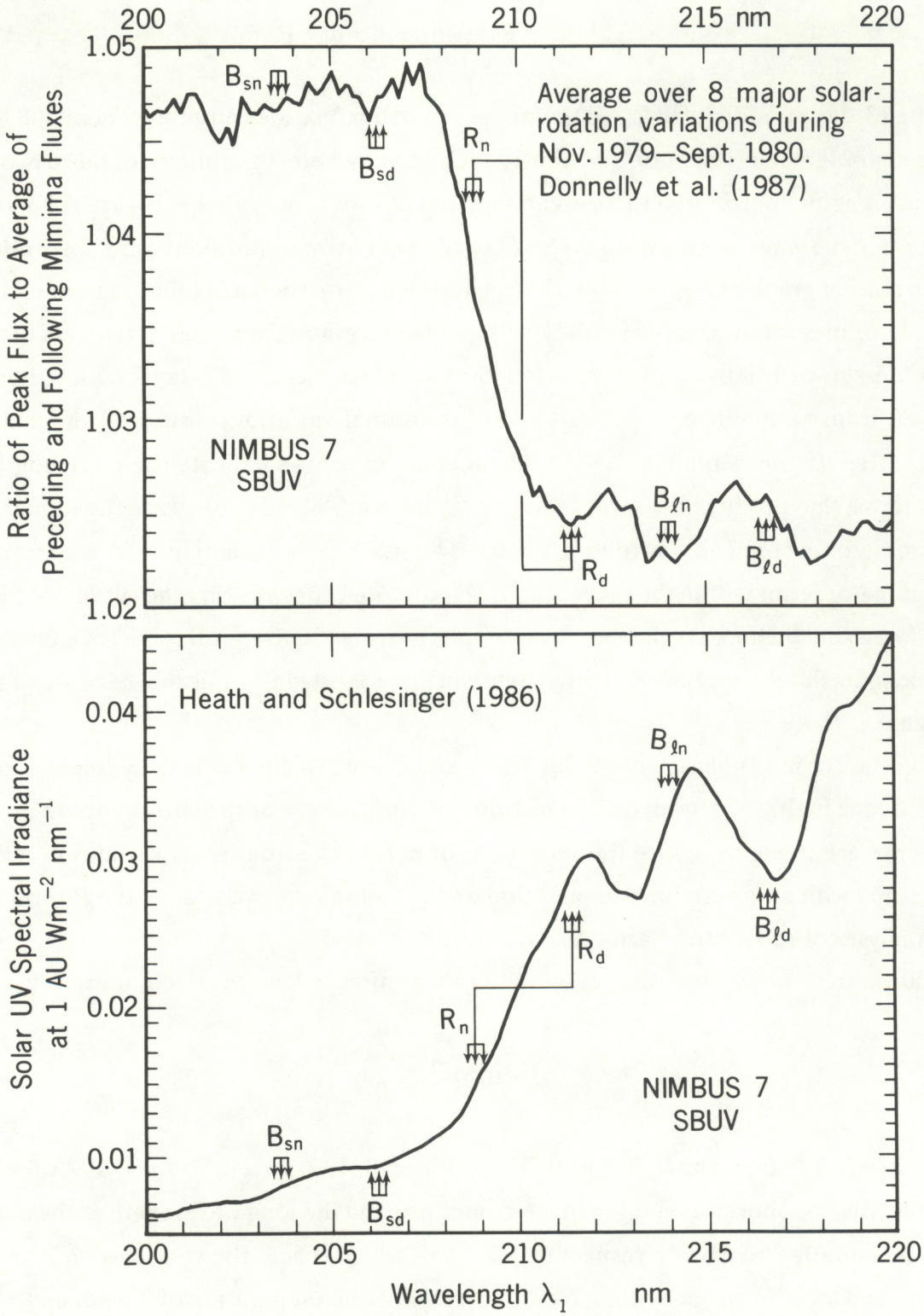

A4-1. Fractional variation of the solar UV flux produced by 27-day solar rotation (top graph) and the solar UV flux (bottom) as a function of vacuum wavelength near the Al I absorption edge. The arrows mark the wavelengths used by Heath and Schlesinger (1986) in their Al I edge ratio.

Figure A4-2 shows the results of these analyses, where all six graphs have λ_1 as the independent variable. The top three graphs of Figure A4-2 viewed from the right side, are for 1979-1980 data and the bottom three are for 1982-1983. Those on the left side show the power in the 27-day periodicity (*P*27). As λ_1 and λ_2 move away from the center of the Al I edge, i. e., λ_1 decreases below 209.4 nm, the solar signal in R_{AlI} increases; consequently, the power in the 27-day periodicity generally increases as λ_1 decreases until just below 208 nm, where it levels out (except for some fine structure in the results). This behavior is consistent with our expectations based on Figure A4-1. The center two graphs show similar results for 13-day periodicity, where the increase from 209.4 to 208.6 nm is relatively more rapid with decreasing wavelength than in the 27-day case. The two graphs at the right give P13/P27 as a function of λ_1. Very high *P*13/*P*27 values occur for the wavelengths used by Heath and Schlesinger (1986), but there are no wavelength pairs that give *P*13/*P*27 values as low as those observed in the UV fluxes in the 160−300 nm range.

We conclude that a simple revision in the choice of wavelengths will not completely solve the problem of high *P*13/*P*27. On the other hand, using λ_1 at 207.6 and λ_2 at 212.8 nm would provide somewhat better results than do the wave-lengths currently used. Figure A4-1 shows that those wavelengths are off the steep portions of the Al I edge; this would cause the results to be less sensitive to instrument jitter in wavelength positions and, therefore, less sensitive to short-period noise.

4. The Cause of the Overemphasis of 13-day Periodicity

Assume that both $F(\lambda_1)$ and $F(\lambda_2)$ can be approximated by a constant term (F_o) and two small perturbations, one a sinusoid with a 13-day period and the other with a 27-day period, as follows:

$$F(\lambda_1) = F_0(\lambda_1)[1 + a_1 \sin\left(\frac{2\pi t}{13}\right) + b_1 \sin\left(\frac{2\pi t}{27}\right)] \qquad \text{(A-4)}$$

and

$$F(\lambda_{2)} = F_0(\lambda_2)[1 + a_2 \sin\left(\frac{2\pi t}{13}\right) + b_1 \sin\left(\frac{2\pi t}{27}\right)] , \qquad \text{(A-5)}$$

where time t is in days. $a_1 << 1$, and the same is true of the amplitudes of the other three perturbation signals, then the time series for the alternate aluminum absorption-edge ratio would be approximately the following:

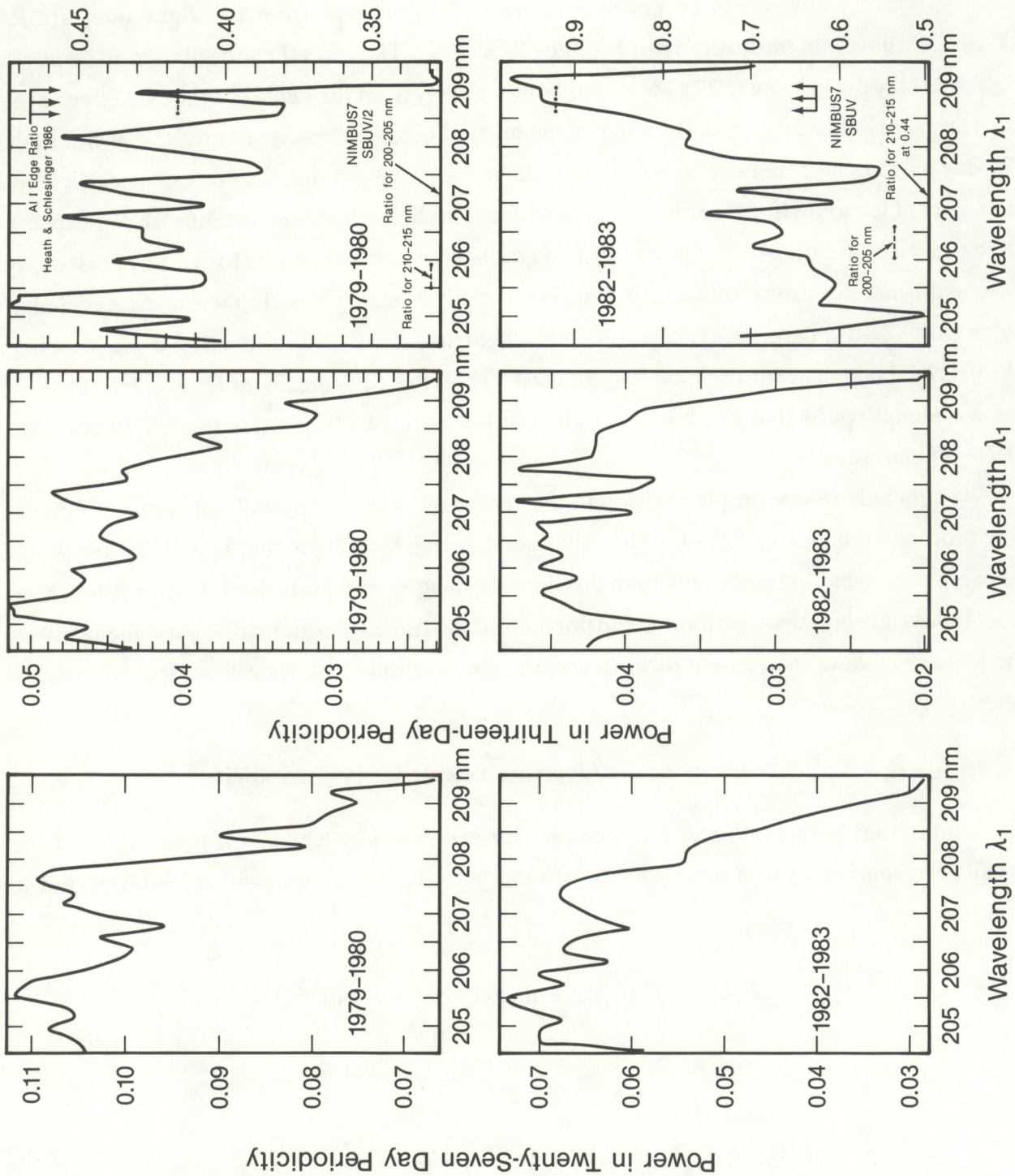

Figure A4-2. Peak power at lines in the power spectra of the modified Al I edge ratio at periods in the 13-14 day range and the 27-28 day range, and the ratio of these peak powers as a function of vacuum wavelength λ_1 for two intervals, each of 2-year duration. The dashed line denotes the ratio level only; the corresponding wavelength range is given by the associated label and not by the λ_1 scale. The dash-dot line gives the ratio for the Heath and Schlesinger equation for *R*(AlI).

$$R_{AlI} = R_0[1 + (a_1 - a_2)\sin\left(\frac{2\pi t}{13}\right) + (b_1 - b_2)\sin\left(\frac{2\pi t}{27}\right)] , \qquad \text{(A4-6)}$$

For the UV fluxes, the power would be proportional to a^2 and b^2 for periods of 13 days and 27 days, respectively; the aluminum edge ratio, the power would be proportional to $(a_1\text{-}a_2)^2$ and $(b_1\text{-}b_2)^2$ for periods of 13 days and 27 days, respectively. For example, for 1979–1980, Figure 5.3 gives P13/P27=0.36 for 205-210 nm and 0.33 for 210-215 nm, which is only slightly lower than in the first case. Using these values to approximate $P13/P27$ for λ_1 and λ_2, respectively, gives $a_1 = 0.6b_1$ and $a_2 = 0.574b_2$. The top graph in Figure A4-1 suggests that for λ_1=208.8 nm, b_2=0.67b_1. These values would give $P13/P27$ for (6) to be 0.425, which is in rough agreement with the 1979-1980 value for Heath and Schlesinger's equation of 0.417.

The important feature of this oversimplified explanation is that the small difference between $P13/P27$ for the two fluxes (0.36 versus 0.33) contributed to a much higher $P13/P27$ for R_{AlI}. The difference terms in the perturbation amplitudes in (6) produce an amplifying effect.

5. Discussion

We cannot eliminate the overemphasis of 13-day periodicity in the Al I edge ratio by a simple revision of the wavelengths used. Moderate improvements can be made, but will be awaiting the arrival of extensive results demonstrating the improvement as well as further need for Al I edge results.

Anyone trying to apply these results to data from other instruments should keep in mind that the vacuum wavelengths used here are those used in the NIMBUS7 data. They may be inaccurate with regard to absolute wavelengths or to the wavelength scale used by another experiment. The structural shape of the bottom spectrum in Figure A4-1 should serve as a guide data from other instruments are used.

APPENDIX V

Correlation between the 10.7-cm radio flux variability and sunspot development

by
Judit Pap
Cooperative Institute for Research in Environmental Sciences
University of Colorado, Campus Box 216
Boulder, CO 80309

Abstract

Most of the sunspot-related short-term variability of solar emission at 10.7 cm is related to the formation and development of sunspot groups. The correlation coefficient between the daily means of 10.7-cm radio flux and projected areas of all sunspots, after removing the solar cycle variability from the data sets, is 0.87. The correlation coefficient is only 0.36 for old, decaying sunspots but is 0.76 for developing, active sunspot groups.

1. Introduction

A good correlation between sunspots and 10.7-cm radio flux has been established for more than four decades (Covington, 1947). The solar emission at 10.7 cm is divided into three components: (1) quiet-Sun emission, (2) the active-region contribution, and (3) the background component that is distributed widely over active regions and activity complexes (Tapping, 1987). Stevens and Donnelly (1989) have recently pointed out that variability of 10.7-cm radio flux is better explained by two variables, the Ca-K plage index and sunspot areas, than by either variable alone (see Appendix III).

There is also good correlation between the dips in total irradiance, measured by the SMM/ACRIM radiometer (Willson et al., 1981), and the peaks in the 10.7-cm radio flux (e.g. Willson, 1982). The temporary dips in total irradiance, on a daily/weekly time scale and with an amplitude up to 0.25%, are caused by sunspots (Willson et al, 1981; Hudson et al., 1982). These sunspot-related irradiance dips occur mainly during the formation and developing phase of sunspot groups (Pap, 1985; 1986); the old, decaying groups do not reduce the total irradiance. A good correlation was found between sunspots and coronal activity (Pap, 1987) by using the daily observations of radio flux measured at 260 MHz (Tlamicha, 1985).

The relation between the temporal variability of 10.7-cm radio flux and the evolution of sunspot groups is discussed in this report with emphasis on two particular subsets of sunspots, namely those in active and passive groups. The newly formed and developing sunspot groups with complex structure (gamma and/or delta magnetic configurations) are called "active" groups. Note that during the years near solar maximum (between 1979 and 1982) roughly 62% of all sunspots appear in newly formed active regions or in old active regions showing new activity. Most of these spots are short-lived (a few days), their area is small (<400 millionths of the solar disk), and they do not show any complexity. Only about 21% of these spots develop into

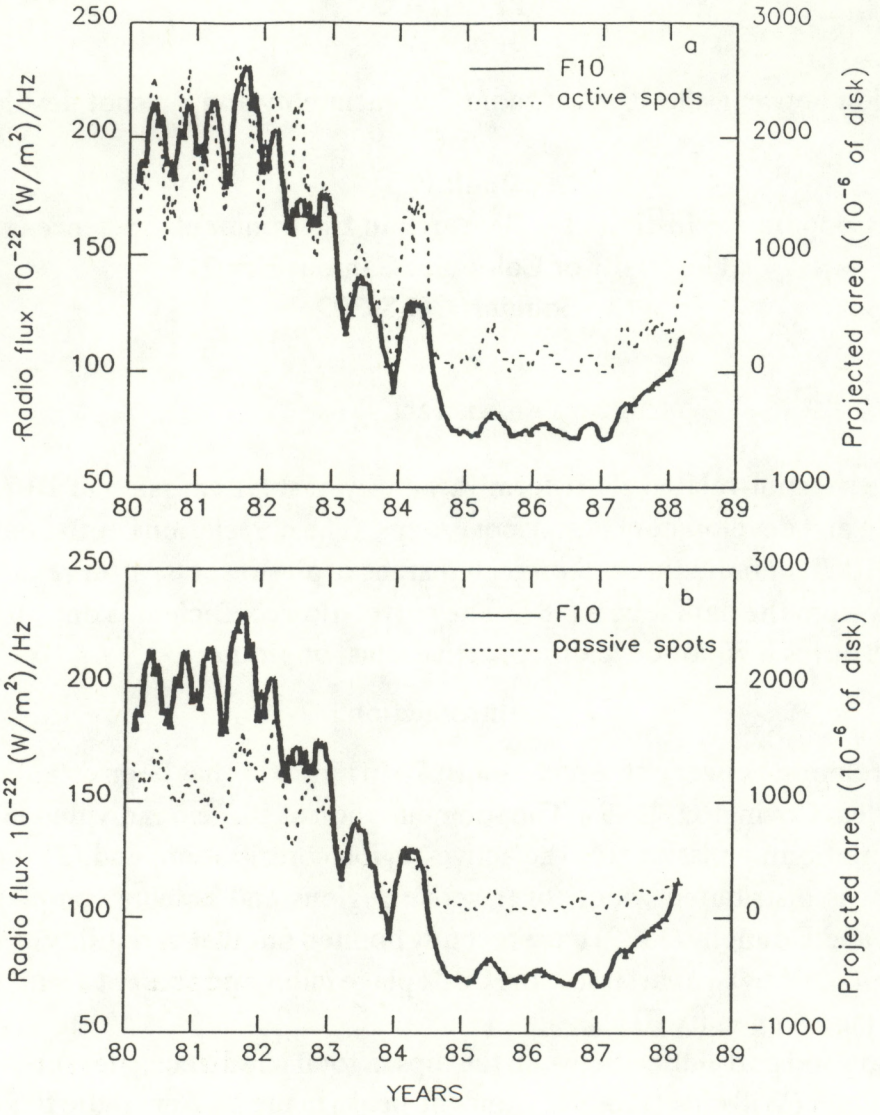

Figure 1. 81-day running means of 10.7-cm radio flux (heavy lines) and projected areas of active (dashed lines (a)) and passive (dashed lines (b)) sunspot groups, January 1980 through May 1988.

large, complex sunspots. Nearer solar minimum this ratio is lower, with only 10% of all sunspots showing complex structure and area larger than 400 millionths of the disk. More details on active and passive spots are given in other papers (Pap, 1985; 1986).

2. Results of Linear Regression Analysis

Figure 1 shows the relation between the 81-day running means of 10.7-cm radio flux (hereafter F10) and projected areas of active (a) and passive (b) sunspot groups. As can be seen, peaks in the active spot areas and F10 correspond well to each other. The correlation coefficient is rather high: 0.96 between the 81-day running means of F10 and the projected sunspot areas (both active and passive). However, a significant part of this high correlation arises from

the long-term trend (variation over the solar cycle), mainly in the case of the passive sunspot groups. As can be seen from Figure 1, the data show a continuous decrease from 1982 to 1985. There is a little variability near the time of solar minimum, between 1985 and 1987. Both types of sunspot areas as well as F10 start to increase in early 1987, with the growing new solar activity. The correlation coefficient for F10 and the projected areas of all sunspots, both young, developing and old, decaying sunspots, is 0.98 for their 81-day running means. The correlation coefficients, calculated between F10 and projected areas of each kind of sunspot group, are summarized in Table 1.

Table 1. Correlation Coefficients

Projected areas	Non-detrended Data Sets		
	Daily means	27-day r.m.*	81-day r.m.*
All Spots	0.91	0.96	0.98
Active Spots	0.78	0.89	0.96
Passive Spots	0.77	0.90	0.96
	Detrended Data Sets		
All Spots	0.87	0.88	0.88
Active Spots	0.76	0.79	0.79
Passive Spots	0.36	0.44	0.57

*r.m.=running means

The solar-cycle related long-term trends have been removed from the data sets by means of a 4th-degree polynomial fit. The detrended data sets are seen in Figure 2. Figure 2a shows the 81-day running means of F10 and the projected areas of active sunspot groups. Figure 2b shows the same for the passive spot areas. As can be seen, peaks in F10 and active spot areas correlate well; every peak has a corresponding one in the other data set. The correlation coefficient in this case is 0.79, which is lower than that above because of the reduction in the dynamic range in the data when the long-term trend was removed. The correlation drops even more (from 0.96 to 0.57) in the case of passive spots. For all spots the correlation coefficient is 0.88 (see Table 1).

Results of linear regression analysis are reproduced in Figure 3. Figure 3a gives the daily means of F10 against the projected areas of all sunspot groups for 1980–1988. The correlation-coefficient value (0.87) is written in the figure. Figures 3b and 3c show the daily means of F10 against the daily projected areas of active and passive groups, the correlation coefficients are 0.76 and 0.36, respectively. As can be seen, in the case of passive spot areas the scatter of data points is much larger than for the active areas; there is no clear linear relationship between the passive spot areas and F10 variability. In the case of active spots, Figure 3b shows that the value of F10 increases in parallel to the growing sunspot areas. This figure also shows that the developing sunspot groups are much larger in area than the old, decaying ones.

The above results indicate that most of the short-term variation of F10 is related to sunspots, especially the developing, complex groups of sunspots. However, we should note that

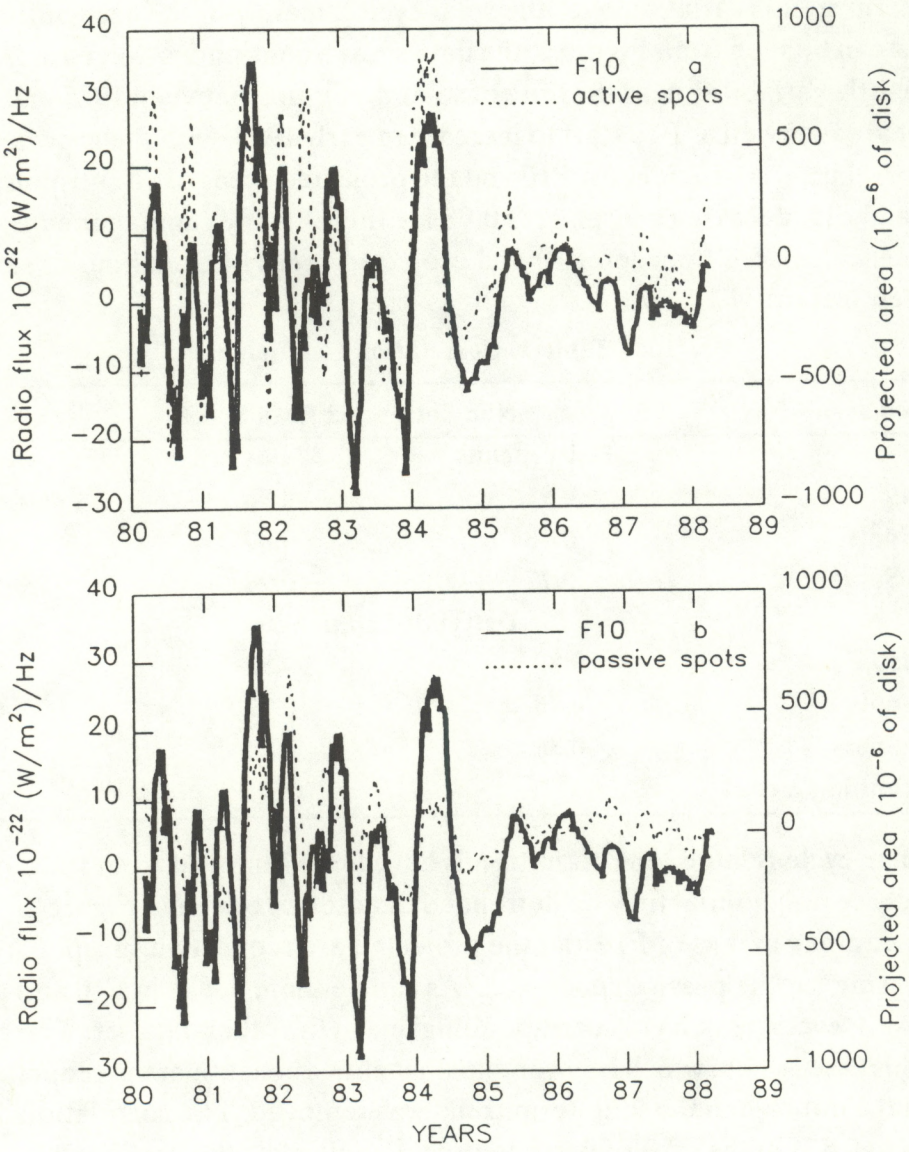

Figure 2. 81-day running means of 10.7-cm radio flux (heavy lines) and projected sunspot areas (dashed lines) after the long-term trends are removed by means of a 4th-degree polynomial fit. Fig. 2a shows the relation between the 10.7-cm flux and projected areas of active groups; Fig. 2b shows the same for the passive groups. Both figures 2a and 2b shown data from January 1980 to May 1988.

the relationship of F10 and sunspots is somewhat different from that of total solar irradiance and projected areas of active sunspot groups. The correlation between total solar irradiance and projected areas is higher if we consider only the active spots rather than all sunspots (e.g. Pap, 1985, 1986; Fröhlich and Pap, 1989). This is because the value of total irradiance sometimes tends to increase when mainly old sunspots are on the Sun. This effect is due to the increased excess flux of faculae surrounding the old spots. On the other hand, newly formed small spots with simple structure, whose lifetime does not exceed a few days, are not considered as active spots (see Pap, 1985; 1986). Thus we can expect higher correlation between the

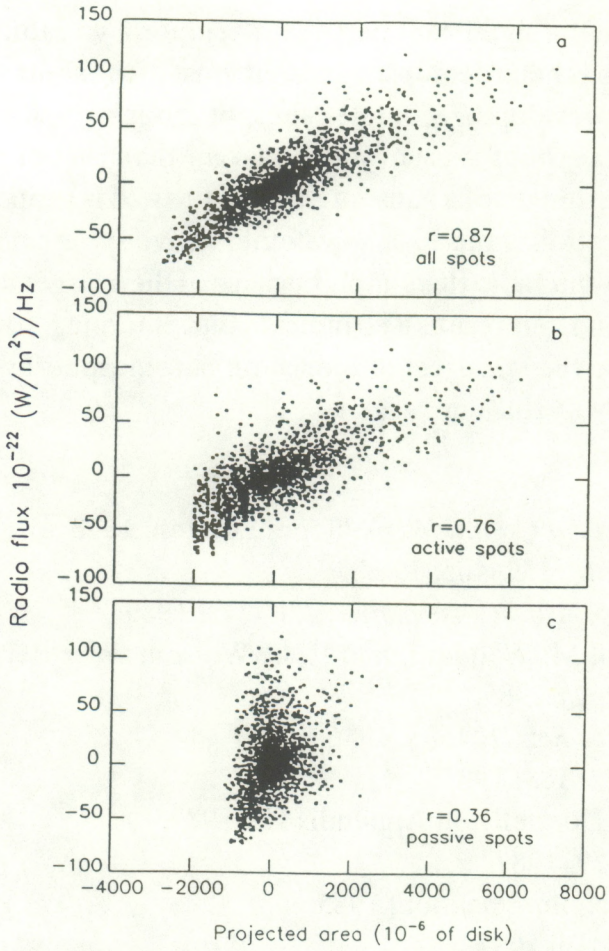

Figure 3. Daily values of the 10.7-cm radio flux are plotted against the daily values of projected areas of active (a), passive (b), and all (c) sunspots, after removing the solar cycle-related long-term trends from the data sets. The analysis is from January 1980 to May 1988.

variation of total irradiance and sunspot areas if we do not consider those spots whose effect is probably overcompensated by facular radiation or which cannot modify significantly the total irradiance because of their small area and short lifetime. However, this situation may be quite different for F10. Although the developing, complex groups contribute the most to short-term variations of F10, the correlation between F10 and projected areas of all spots is somewhat higher than for the active spots. This means that magnetic fields concentrated in old as well as in new, small spots or pores can modify the value of radio flux, especially at 10.7 cm.

3. Discussion

The strong temporal variability of solar emission at 10.7 cm is thought to be related to localized activity in strong magnetic fields. Two physical mechanisms are usually applied in modeling the 10.7-cm radio flux variability: the gyroresonant absorption and free-free (bremsstrahlung) emission (Tapping, 1987). The latter is supposed to be related to weaker fields, for example in plages; the former is related to strong magnetic fields concentrated in sunspots (e.g. Tapping, 1987). More details on this topic are discussed in Appendix III.

Our results show that a significant part of the temporal variability of 10.7-cm radio flux is related to sunspots. It has been demonstrated that most of the short-term variability of 10.7-cm radio flux is caused by developing, complex sunspot groups. It should be noted that the area of developing, complex groups is usually much larger than that of the old, decaying spots. It is well known that the strength of a sunspot's magnetic field is proportional to its size (e.g. Allen, 1973). Thus a question is raised as to whether active spots cause most of the sunspot-related variability of 10.7-cm radio flux simply because of their larger area and stronger magnetic fields. On the other hand, our results also indicate that emerging, strong magnetic fields, forming sunspots, may have the strongest influence on chromospheric/coronal emission at radio wavelengths, especially at 10.7 cm.

4. References

Allen, C. W., *Astrophysical Quantities,* Athlone, London, 1973.

Covington, A. E., *Nature*, **159**, 405, 1947.

Fröhlich, C. and J. Pap, *Astron. Astrophys.*, **220**, 272, 1989.

Hudson, H. S., S. Silva, M. Woodard, and R. C. Willson, *Solar Phys.*, **76**, 211, 1982.

Pap, J., *Solar Phys*., **97**, 21 1985.

Pap, J., *Astrophys. Space Sci.*, **127**, 55, 1986.

Pap, J., *Solar Phys*., **112**, 183, 1987.

Stevens, D. E. and R. Donnelly, in Appendix III, 1989.

Tapping, K. F., *JGR*, 829, 1987.

Tlamicha, A., private communication, 1985.

Willson, R. C., *JGR*, **4319**, 1982.

Willson, R. C., S. Gulkis, M. Janssen, H. S. Hudson, and G.A. Chapman, *Science 211*, **700**, 1981.

*U.S. GOVERNMENT PRINTING OFFICE:1995-673-018/00067